Bayesian joint detection-estimation in functional MRI with automatic parcellation and functional constraints

Mohanad Albughdadi

THÈSE

En vue de l'obtention du

DOCTORAT DE L'UNIVERSITÉ DE TOULOUSE

Délivré par :

Institut National Polytechnique de Toulouse (INP Toulouse)

Discipline ou spécialité :

Signal, Image, Acoustique et Optimisation

Présentée et soutenue par :

M. MOHANAD ALBUGHDADI

le vendredi 16 septembre 2016

Titre :

BAYESIAN JOINT DETECTION-ESTIMATION IN FUNCTIONAL MRI WITH AUTOMATIC PARCELLATION AND FUNCTIONAL CONSTRAINTS

Ecole doctorale :

Mathématiques, Informatique, Télécommunications de Toulouse (MITT)

Unité de recherche :

Institut de Recherche en Informatique de Toulouse (I.R.I.T.)

Directeur(s) de Thèse :

M. JEAN YVES TOURNERET

M. LOTFI CHAARI

Rapporteurs :

M. ANDRE FERRARI, UNIVERSITE DE NICE SOPHIA ANTIPOLIS

M. DIMITRI VAN DE VILLE, UNIVERSITE DE GENEVE

Membre(s) du jury :

M. LOTFI SENHADJI, UNIVERSITE RENNES 1, Président

M. JEAN YVES TOURNERET, INP TOULOUSE, Membre

M. LOTFI CHAARI, INP TOULOUSE, Membre

Mme FLORENCE FORBES, INRIA GRENOBLE - RHONE ALPES, Membre

M. PHILIPPE CIUCIU, CEA SACLAY, Membre

Abstract

Brain parcellation into a number of hemodynamically homogeneous regions (parcels) is a challenging issue in fMRI analyses. An automatic inference for the parcels from the fMRI data was proposed in the framework of the joint parcellation detection estimation (JPDE) model. However, this model still requires appropriate prior information about the number of parcels and their shapes provided through an initial parcellation, which is a challenging task since it generally depends on the subject. In this thesis, we present novel approaches for hemodynamic brain parcellation. These approaches are motivated by the fact that the hemodynamic response function varies across brain regions and sessions within subjects, and even among subjects and groups. The proposed approaches belong to one of two main categories, the subject-level and group-level fMRI data analysis models. For the subject-level fMRI data analysis, we propose three models to automatically estimate the optimum number of parcels and their shapes directly from fMRI data. The first one is formulated as a model selection procedure added to the framework of the classical JPDE model in which we compute the free energy for the candidate models, each with different number of parcels, and then select the one that maximizes this energy. To overcome the computational intensity associated with the first approach, we propose a second method which relies on a Bayesian non-parametric model where a combination of a Dirichlet process mixture model and a hidden Markov random field is used to allow for unlimited number of parcels and then estimate the optimal one. Finally to avoid the computational complexity associated with the estimation of the interaction parameter of the Markov field in the second approach, we make use of a well known clustering algorithm (the mean shift) and embed it in the framework of the JPDE model to automatically infer the number of parcels by estimating the modes of the underlying multivariate distribution. All the proposed subject-level approaches are validated using synthetic and real data. The obtained results are consistent across approaches in terms of the detection of the elicited activity. Moreover, the second and the third approaches manage to discriminate the hemodynamic response function profiles according to different criteria such as the full width at half maximum

and the time to peak.
Regarding the group-level fMRI analysis, we propose two new models that are able to estimate group-level parcellation and hemodynamic response function profiles. The JPDE model is extended to allow for this group-level estimation by considering data coming from all the subjects resulting in a multi-subject joint parcellation detection estimation model. However, in real data experiment, it is noticed that the smoothness of the estimated HRFs is sensitive to one of the hyperparameters. Hence, we resort to the second model that performs inter and intra subject analysis providing estimation at both the single and group-levels. A thorough comparison is conducted between the two models at the group-level where the results are coherent. At the subject-level, a comparison is conducted between the proposed inter and intra subject analysis model and the JPDE one. This comparison indicates that the HRF estimates using our proposed model are more accurate as they are closer to the canonical HRF shape in the right motor cortex. Finally, the estimation of the unknown variables, the parameters and the hyperparameters in all of the proposed approaches is addressed from a Bayesian point of view using a variational expectation maximization strategy.

Résumé

La parcellisation du cerveau en un certain nombre de régions hémodynamiques homogènes est toujours un défi majeur en analyse des données d'imagerie par résonance magnétique fonctionnelle (IRMf). Une inférence automatique pour les parcelles à partir des données d'IRMf a été proposée dans le cadre du modèle de parcellisation détection estimation conjointe (joint parcellation detection estimation: JPDE). Toutefois, ce modèle requiert toujours des informations préalables sur le nombre de parcelles ainsi que leurs formes, généralement renseignées à partir d'une parcellisation initiale, ce qui constitue un défi car cela dépend généralement du sujet. Dans cette thèse, de nouvelles approches pour la parcellisation hémodynamique du cerveau sont présentées. Ces approches sont motivées par le fait que la réponse hémodynamique varie selon les régions du cerveau, les sujets, les différentes sessions pour chaque sujet ainsi que les groupes de sujets. Les approches proposées appartiennent à l'une des deux catégories suivantes : les modèles d'analyse de données d'IRMf au niveau d'un sujet et au niveau d'un groupe de sujets. Pour l'analyse de données d'IRMf au niveau d'un sujet, trois modèles pour estimer automatiquement le nombre optimal de parcelles ainsi que leurs formes (directement) à partir des données d'IRMF sont proposés. La première approches est élaborée comme une procédure de sélection de modèle ajoutée à la structure du modèle JPDE dans lequel l'énergie libre pour les modèles candidats est calculée, chacun avec un nombre différent de parcelles, puis celui qui maximise cette énergie est retenu. Afin de surmonter l'intensité du calcul associé à cette approche, une seconde méthode est proposée. Elle repose sur un modèle bayésien non-paramétrique dans lequel une combinaison d'un processus de Dirichlet et d'un champ de Markov caché aléatoire est utilisée pour permettre un nombre illimité de parcelles et enfin en estimer le nombre optimal. Finalement, pour éviter la complexité du calcul associé à l'estimation du paramètre d'interaction du champ de Markov dans la seconde méthode, un algorithme de clustering est utilisé (le mean shift). Il est intégré dans la structure du modèle JPDE afin de déduire automatiquement le nombre de parcelles en estimant les modes de la distribution multivariée sous-jacente. Les approches proposées au niveau du sujet sont validées à l'aide de données

synthétiques et réelles. Les résultats d'analyse obtenus sont cohérents en termes de détection de l'activité évoquée. De plus, les deux derniers approches parviennent à distinguer les profils de la réponse hémodynamique en fonction de différents critères tels que la largeur à mi-hauteur et le temps de montée. En ce qui concerne les analyses au niveau d'un groupe de sujets, deux modèles capables d'estimer la parcellisation ainsi que les profils de réponse hémodynamique sont proposés. Le modèle JPDE est modifié pour permettre l'estimation au niveau du groupe en considérant les données provenant de tous les sujets ce qui a abouti à un modèle multi-sujet d'estimation-détection de parcellation conjointe. Cependant, les essais sur des données réelles démontrent que la régularité de la FRH est sensible à l'un des hyperparameters. Par conséquent, le deuxième modèle qui effectue une analyse inter et intra sujet et qui fourni une estimation à la fois au niveau du sujet et au niveau du groupe est privilégié. Une comparaison approfondie entre les deux modèles est menée au niveau du groupe et les résultats sont cohérents. Au niveau du sujet, une comparaison est effectuée entre le modèle d'analyse inter et intra sujet proposé et le modèle JPDE. Cette comparaison démontre que les estimations du FRH utilisant le modèle proposé sont plus précises car plus proches de la forme canonique de la FRH dans le cortex moteur droit. L'estimation des variables inconnues et des paramètres dans les approches proposées est traitée en utilisant une stratégie d'espérance-maximisation variationnelle.

Contents

Acronyms

AMS	Adaptive Mean Shift
AMS-JPDE	Adaptive Mean Shift-based Joint Parcellation Detection Estimation
AR	Autoregressive
ASL	Arterial Spin Labeling
BIC	Bayesian Information Criterion
BOLD	Blood Oxygen Level-Dependent
CBF	Cerebral Blood Flow
CBV	Cerebral Blood Volume
$CMRO_2$	Cerebral Metabolic Rate of Oxygen
DeoxyHB	Deoxygenated Hemoglobin
DP	Dirichlet Process
DPMM	Dirichlet Process Mixture Model
DTI	Diffusion Tensor Imaging
E	Oxygen Extraction Fraction
EEG	Electroencephalography
EPI	Echo Planar Imaging
FFT	Fast Fourier Transform
FMRI	Functional Magnetic Resonance Imaging
FOV	Field of View
FWHM	Full Width at Half Maximum
GLM	General Linear Model
GLS	Generalized Least Squares
HB	Hemoglobin
HMRF	Hidden Markov Random Field
HRF	Hemodynamic Response Function
IFT	Inverse Fourier Transform
II-JPDE	Inter and Intra Subject Joint Parcellation Detection Estimation
JDE	Joint Detection Estimation
JPDE	Joint Parcellation Detection Estimation
MCMC	Markov Chain Monte Carlo
MDL	Minimum Description Length
MEG	Magnetoencephalography

MNI	Montreal Neurological Institute
MR	Magnetic Resonance
MRG	Markov Random Field
MRI	Magnetic Resonance Imaging
MS-JPDE	Multi-Subject Joint Parcellation Detection Estimation
MSE	Mean Square Error
NMR	Nuclear Magnetic Resonance
NP-JPDE	Non-Parametric Joint Parcellation Detection Estimation
NRL	Neural Response Levels
OGI	Oxygen-Glucose Index
OLS	Ordinary Least Squares
OxyHB	Oxygenated Hemoglobin
pdf	Probability Density Function
PET	Positron Emission Tomography
PSF	Point-Spread Function
RF	Radio Frequency
ROI	Region of Interest
SNR	Signal to Noise Ratio
TE	Echo Time
TR	Time of Repetition
TTP	Time to Peak
VEM	Variational Expectation Maximization

List of Figures

List of Tables

List of Algorithms

CHAPTER 1

Introduction

Contents

1.1 Motivation

FMRI is a powerful non-invasive technique to study the relationship between sensory or cognitive tasks and the evoked neural activity by measuring the blood oxygen level dependent (BOLD) signal. Event-related BOLD fMRI relies on two main tasks: 1) detection of the activated brain areas in response to a given stimuli, 2) estimation of the dynamics of the brain which is known as the hemodynamic response function (HRF). These two tasks are dependent and cannot be handled using a two-step procedure. One of the models that account for this interdependency is the joint parcellation detection estimation (JPDE) model. The JPDE model can be used to jointly detect the activation within the brain for a given stimulus, estimate the HRF profiles and to determine a parcellation of the brain into hemodynamic territories or parcels. In order to obtain the brain parcellation, a single HRF shape can be assumed for a given parcel and all the voxels belonging to this parcel have their HRF defined as local stochastic perturbations of a common HRF pattern (HRF profile of the parcel). This HRF variability is motivated by the fact that the HRF may vary between subjects and even between cortical regions in a given subject brain. However, this model still requires to provide a proper initialization for the number of parcels. Relying on the JPDE model, the aim of this thesis is to propose new approaches and algorithms to

overcome the challenge of hemodynamic brain parcellation in fMRI analysis at both subject and group levels. Different procedures and approaches have been developed within the framework of the Pyhrf software using Python as the main programming language and C, C++ for extensions. The proposed approaches and procedures extend the JPDE model to be more flexible and adaptive. They are mainly based on a variational expectation maximization (VEM) algorithm allowing estimators of the unknown variables and parameters to be constructed.

The main contributions of this work are summarized below

(i) Developing a Bayesian model selection procedure based on the computation of the free energy to determine the optimum number of parcels (Albughdadi et al., 2014).

(ii) Developing a non-parametric Bayesian approach to estimate the parcellation without any prior initialization yielding the NP-JPDE model (Albughdadi et al., 2016c).

(iii) Developing a non-parametric diffusion algorithm by injecting the adaptive mean shift algorithm within the VEM framework to estimate the parcellation, yielding the AMS-JPDE model (Albughdadi et al., 2016b).

(iv) Developing a multi-subject joint parcellation detection estimation (MS-JPDE) model to estimate group-level HRF profiles and parcellation for a group of interest (Albughdadi et al., 2016a).

(v) Developing a hyprid multi-subject (HMS-JPDE) model to allow for subject-level and group-level estimation of the parcellations and HRF profiles along with the detection task over individuals.

1.2 Organization of the manuscript

- **Chapter 2: Functional magnetic resonance imaging**
  This chapter provides an introduction to fMRI, its physics, the acquisition methods, the link between magnetic resonance imaging (MRI) and fMRI and the preprocessing techniques. It also introduces the conventional fMRI analysis approaches with its limitations and drawbacks.

- **Chapter 3: Joint parcellation detection estimation and model selection**
  Brain parcellation into a number of hemodynamically homogeneous regions (parcels) is a challenging issue in fMRI analysis. Although the JPDE model performs online parcellation of the region of interest into parcels, it still requires to fix the number of these parcels manually, which limit its usefulness. This number is critical and may influence the performance of the detection and estimation tasks. This motivates the proposition of an extension of the JPDE framework for model selection. This chapter proposes a Bayesian model selection procedure based on free energy calculations for different candidate models characterized by a different numbers of parcels. The model that maximizes the free energy is the best fit for the fMRI data.

- **Chapter 4: Joint Parcellation Detection Estimation Using a Non-parametric Bayesian Model**
  In this chapter, we propose a novel approach for hemodynamic brain parcellation within the framework of the JPDE model to reduce the computational intensity of the free energy calculations. The parcellation is formulated as a clustering issue that is solved by embedding into the JPDE model a Dirichlet process mixture model (DPMM) with a hidden Markov random field (HMRF). The resulting model automatically estimates the number of parcels directly from the data without any prior knowledge about the number of parcels. A variational expectation maximization algorithm is used for the inference. The model is validated on synthetic and real data. A comparison with other models from the literature demonstrates its superiority and its ability to discriminate HRF profiles depending on many criteria such as the time to peak (TTP) and the full width at half maximum (FWHM).

- **Chapter 5: Adaptive mean shift algorithm for hemodynamic brain parcellation**
  In this chapter, we propose a new algorithm for hemodynamic brain parcellation using the well known adaptive mean shift algorithm to overcome the computational complexity of estimating the interaction parameter of the hidden Markov random field in the non-parametric JPDE model. The adaptive mean shift algorithm is a robust computer vision approach that has been widely used for clustering and classifica-

tion. This algorithm estimates the modes of a multivariate distribution underlying the feature space. In our framework, this algorithm is embedded within the variational expectation maximization algorithm of the standard JPDE model where it replaces the maximization of the HRF profiles. This algorithm does not need any initialization and the only parameter that needs to be adjusted is the number of k-nearest neighbours. Results on synthetic data confirms the ability of the proposed approach to estimate accurate HRF estimates and numbers of parcels. It also manages to discriminate between voxels in different parcels especially at the borders between these parcels. In real data experiment, the proposed approach manages to recover HRF estimates close to the canonical shape in the right motor and bilateral occipital cortices.

- **Chapter 6: Multi-subject joint parcellation detection estimation**
  This chapter introduces a group-level analysis within the framework of the JPDE algorithm. fMRI experiments are usually conducted over a population of interest for investigating brain activity across different regions, stimuli and objects. A multi-subject analysis proceeds in two steps: first an intra-subject analysis is performed sequentially on each individual and then a group-level analysis is conducted to report significant results at the population level. In this chapter, we propose a group-level analysis based on the JPDE model. This model allows the estimation of the group-level HRFs and parcellation along with the subject-level detection of activation. Real data experiments show that the HRF estimates could be sensitive to one of the hyperparameters whicch in turn affect the characteristics of the HRF estimates.

- **Chapter 7: Hyprid multi-subject joint parcellation detection estimation**
  In this chapter, we propose an inter and intra subject joint parcellation detection estimation model that allows studying the HRF variability at both the subject and group level. Moreover, this model overcome the limitations of the multi-subject model proposed in the previous chapter. In this model, the detection task is performed individually for each subject. Detailed comparisons are carried out at the subject and group levels to investigate the performance of this model with respect

to the JPDE and the previous multi-subject model.

- **Chapter 8: Conclusion and future work**
  This chapter presents some conclusions related to our work and describes some prospects that deserve to be investigated in the near future.

1.3 Publication

Journal papers

(i) Albughdadi, M., Chaari, L., Forbes, F., Tourneret, J.-Y., Ciuciu, P. "Hemodynamic brain parcellation using a non-parametric Bayesian approach.", Submitted to Medical Image Analysis, Feb.2016.

Conference papers

(i) Albughdadi, M., Chaari, L., Forbes, F., Tourneret, J.-Y., Ciuciu, P., "Model selection for hemodynamic brain parcellation in fMRI". in Proc. EUSIPCO. Lisbon, Portugal, pp. 31–35, Sept. 2014.

(ii) Albughdadi, M., Chaari, L., Forbes, F., Tourneret, J.-Y., Ciuciu, P., "Multi-subject joint parcellation detection estimation in functional MRI". in Proc. 13th IEEE International Symposium on Biomedical Imaging, Prague, Czech Republic, Apr.2016.

(iii) Albughdadi, M., Chaari, L., Tourneret, J.-Y., . "Adaptive mean shift based hemodynamic brain parcellation in fMRI.", Accepted in the 7th Conference on Medical Imaging and Augmented Reality, Bern, Switzerland, Aug.2016.

CHAPTER 2

Functional Magnetic Resonance Imaging

Contents

2.1 Introduction

fMRI is an imaging technique that indirectly measures neural activity through the blood oxygen level-dependent (BOLD) signal (Ogawa et al., 1990a), which captures the variation in blood oxygenation associated with neural activity. fMRI provides neuroscientists and researchers with means to study human brain in *vivo* in response to a certain task (event-related) or when

at rest (resting-state). Thanks to fMRI, new insights into how the brain processes information and its inner workings have been discovered in the last two decades. Although positron emission tomography (PET) methods are used for some applications to measure cerebral blood flow (CBF) changes to map functional activity in the human brain, the majority of human mapping studies are performed with fMRI.
This chapter briefly describes the basics of functional magnetic resonance imaging (fMRI). More precisely, Section 2.2 describes the transition from nuclear magnetic resonance (NMR) to fMRI. Section 2.3 addresses fMRI physiological basics and the link between stimulus and the fMRI signal. fMRI data basics including the acquisition physics of MRI and the different artifacts are highlighted in Section 2.4. The experimental paradigms are described in Section 2.5. fMRI data preprocessing and analysis are addressed in Sections 2.6 and 2.7, respectively. Finally, some conclusions are drawn in Section 2.8.

2.2 FMRI origins

The discovery of the effect of the changes in the metabolic state of the brain on magnetic resonance (MR) signals is one of the important milestones in MRI studies. These changes provide an intrinsic mechanism of contrast for brain activation studies. This effect is originated from the fact that the magnetic state of hemoglobin (HB) depends on its oxygenation. The small changes in the local MR signal caused by the hemoglobin saturation changes is called blood oxygenation level-dependent (BOLD) effect. The discovery of the changes in hemoglobin magnetic state was discovered in 1936 by Pauling and Coryell (Pauling and Coryell, 1936). These changes are caused by the variations in the hemoglobin oxygenation. In 1982, Thulbron et al. (Thulborn et al., 1982) demonstrated that the presence of paramagnetic deoxyhemoglobin causes changes in relaxation rate (T_2) in blood sampled. However, the potential of the oxygenation state of hemoglobin in functional neuroimaging was discovered in the 1990s (Uludag et al., 2006).
The first realization was a physiologic manipulation in which a gradient-echo imaging at high magnetic fields (7 and 8.4 T) was used to image the brains of mice (Ogawa et al., 1990b). It has been shown that when the oxygen in the inspired air was reduced, the veins became darker in the MR images. Moreover, the signal from the tissue surrounding these veins was reduced due to a change in the magnetic susceptibility of the blood. The study suggested that

this phenomenon could be used to monitor regional oxygen use in the brain. It also assumed that during brain activation, the amount of oxygen would decrease and the deoxy-hemoglobin concentration would increase. In fact, this assumption is not correct and the concentration of deoxy-hemoglobin decreases due to the large cerebral blood flow (CBF) change. Using the nuclear magnetic resonance (NMR) effect to measure brain function was the first inspiration of fMRI. The experiments on well-controlled animals motivated the possibility of applying this method to humans performing tasks that alter the oxygen utilization in the brain. In (Kwong et al., 1992), images were acquired for a normal human subject in a visual experiment with a gradient-echo planner imaging (EPI) sequence and an echo time of 40 ms. Differences in the measured signal intensity were observed in temporally resolved images with and without stimulations. This study suggested that the increased signal during simulation was associated with the deoxy-hemoglobin concentration decrement. Many studies were performed confirming the latter suggestion (Ogawa et al., 1992; Frahm et al., 1992; Turner et al., 1991, 1993).

2.3 FMRI physiological basics

The objective of fMRI studies is to map patterns of neural activity in the brain to specific tasks. However, the neural activity cannot be measured. The BOLD signal used for fMRI studies is sensitive to the concentration change of deoxygenated hemoglobin, which depends on the cerebral blood flow (CBF), cerebral blood volume (CBV) and cerebral metabolic rate ($CMRO_2$) of oxygen. Fig. 2.1 links the applied stimulus (for a specific task) to the measured BOLD signal during an event-related fMRI experiment where a flickering checkerboard experimental condition is used to trigger the visual cortex in the brain to elicit neural activity. The CBF, CBV and $CMRO_2$ also increase as a consequence of the evoked neural activity. These changes alter the local deoxy-hemoglobin, which affects the local MR signal. The interpretation of fMRI data is done by understanding the link between the neural activity and the underlying dynamics which is also known as the hemodynamic response function (HRF). The neural activation is always followed by a hemodynamic response. Experiments (Grubb et al., 1974; Fox et al., 1986; Hyder et al., 2002) have roughly proven that the basic pattern for a strong stimulus is that CBF increases dramatically (40%), CMRO2 increases much less (<20%), and CBV increases by a modest amount (15%). These physiological changes can

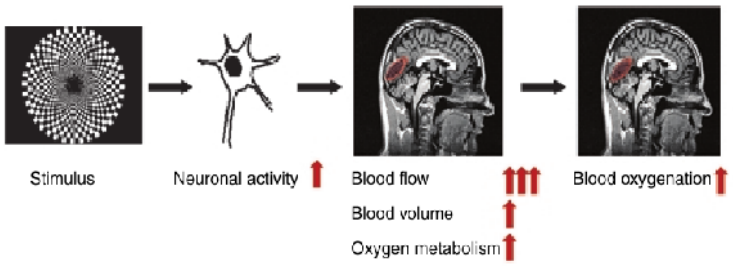

Figure 2.1: The path of changes linking the stimulus to the measured local BOLD signal (Uludag et al., 2006).

be summarized by two key features: the oxygen extraction fraction (E) and the oxygen-glucose index (OGI). It is found that with activation both features decrease. This unexpected pattern has been the focus of a number of recent works.

2.4 FMRI data acquisition

fMRI data consists of 3-D magnetic resonance images (MRIs), each of them consists of a number of uniformly spaced volume elements (voxels). Each voxel has its own intensity value that represents the spatial distribution of the nuclear spin density. This spin density is related to the blood oxygenation and flow in the local area. From a hundred to a thousand 3-D images of the whole brain are acquired during an fMRI experiment. A standard fMRI experiment usually consists of multiple subjects with multiple scanning sessions for each subject. Thus, fMRI data analysis is an example of a big data problem. Moreover, fMRI data show a complicated temporal and spatial noise structure with relatively weak signal to noise ratio (SNR). For these reasons, the statistical analysis of the fMRI data is a difficult task.

2.4.1 The MRI scanner

A standard MRI scanner is used to acquire fMRI data as a series of brain volumes which could serve study the brain dynamics. The main component of this scanner is a superconducting electromagnet with a strong magnetic field $1.5 - 7.0$ Tesla for human brain research. Another component of the

scanner is the radio frequency coils. These coils are placed close to the scanned object and are used to generate and receive energy at the resonance frequency of the volume being imaged. They are turned on and off during the data acquisition. We can also mention the gradient coils as one of the main components. They are electromagnetic coils to create spatial variation in the strength of the magnetic field in a controlled manner. The importance of the gradient coils arises from their ability to spatially encode the information in the signal, which is a key step to form a 2-D image from a 1-D signal.
The same MRI scanner can be used to acquire structural MRI, functional MRI and to perform diffusion tensor imaging (DTI) of white matter tracts. This allows us acquiring several types of images during a scanning session for a specific subject.

2.4.2 MRI physics

The source of the measured MR signal is the net magnetic moment produced by the protons in hydrogen (^{1}H) atoms as they spin around their axis. Hydrogen atoms in the body mainly exist in water and fat. The magnetization of a single proton cannot be measured using an MRI scanner. Therefore, the net magnetization (M) of the ensemble of all nuclei within a chosen volume is measured. The net magnetization can be represented as a vector of two components; a longitudinal component which is parallel to the magnetic field and a transverse component which is orthogonal to the field. A spinning proton generates its own little magnetic field. When an external magnetic field (B_0) is applied, the spinning proton tends to align with its direction. Fig. 2.2 shows how the spinning protons act with and without the application of an external magnetic field. A radio frequency (RF) electromagnetic field pulse is used to disturb the equilibrium of a nuclei to be able to measure its net magnetization within a certain volume. The nuclei absorbs the energy at a specific frequency band and become excited due to the applied RF. The excitation of the nuclei forces the longitudinal magnetization to decrease and establishes a new transversal magnetization. The excitations process is illustrated in Fig. 2.3. When the RF pulse is removed, the nuclei comes back to equilibrium as it emits the absorbed energy. The process of emitting the absorbed energy is known as "relaxation". During the relaxation, the longitudinal magnetization grows backs (longitudinal relaxation) to its original size and the transversal magnetization disappears (transversal relaxation). On one hand, the longitudinal relaxation can be considered as an

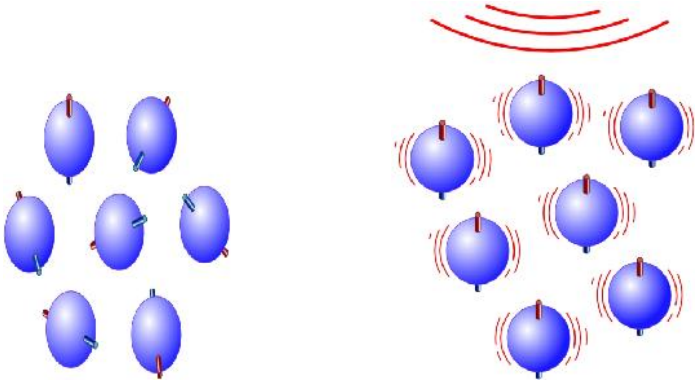

(a) Spinning protons act like little magnets

(b) Spinning protons align with an external field

Figure 2.2: Representation of the status of the spinning protons without and with applied magnetic filed (Berger, 2002).

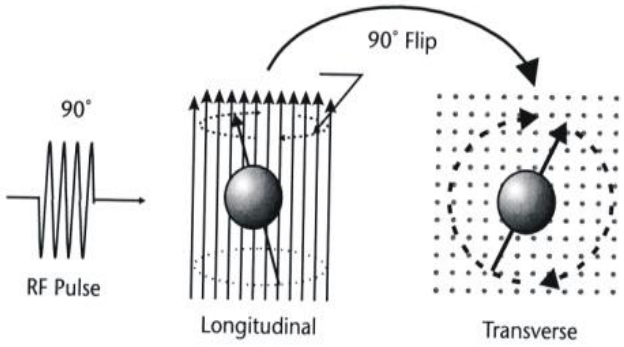

Figure 2.3: The excitation of the nuclei magnetization by applying RF. The absorbed energy by the nuclei flips its alignment away from the direction of the magnetic field (Sprawls, 2000).

exponential recovery in magnetization along the longitudinal direction and it is described by a time constant T_1. On the other hand, the transverse relaxation represents the loss of net magnetization in the transverse plane due to loss of phase coherence. Hence, an exponential decay in magnetization is caused by the de-phase of nuclei after the turning off RF pulse. This decay is described by a time constant T_2. However, the values of T_1 and T_2 depend on the tissue type which allow creating structural MR images to differentiate between tissue types. T_2^*, which is similar to T_2 but it also depends on local inhomogeneity in the magnetic field caused by blood flow and oxygenation changes, provides the basis for fMRI due to its sensitivity to neurovascular changes associated with a psychological and behavioral function. Fig. 2.4 shows examples of different types of images that can be acquired using an MRI scanner.

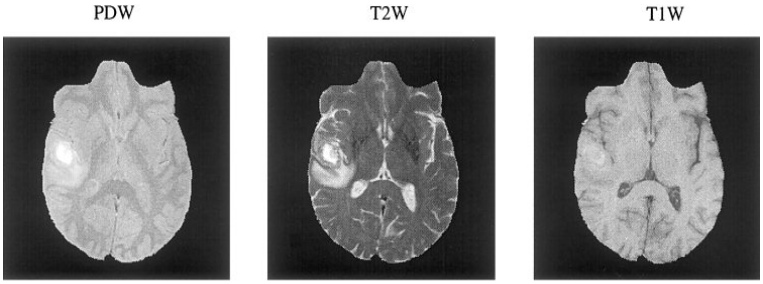

Figure 2.4: Examples of proton density (PDW), T_2 (T_2W) and T_1 (T_1W) weighted images (Witjes et al., 2003).

2.4.3 Image contrast in MRI

Image contrast in MRI is a difference in signal intensity between two adjacent tissues. Assuming that the initial value of magnetization before excitation is M_0, TR is the time of repetition for nuclei excitation and TE the time of data collection after excitation (echo time). By alternating TR and TE, it is possible to control the characteristics of the explored tissue. The measured signal can be approximated by

$$M_0 \left(1 - \exp(-TR/T_1)\right) \exp(\mathrm{TE}/T_2). \qquad [2.1]$$

For further understanding of the effect of these parameters on the acquired image, some scenarios are provided in what follows. The first scenario is when

the TR is long and TE is short, the signal will be approximately equal to M_0 and the proton density image can be produced. Such an image provides maps of the hydrogen distribution across the sample. The second scenario is when TE is short and TR has intermediate length. In this case we will get T_1-weighted images which are used to reveal anatomical structures. The third scenario is when TR is long and TE has an intermediate length. In this case T_2-weighted image is registered registered which is another type of structural images. It is worth noticing that T_2^*-weighted images are generated in a way similar to T_2-weighted images except that the pulse sequence uses the magnetic gradients in a different way. More details are provided in (Brown et al., 2014; Huettel et al., 2004).

2.4.4 The BOLD fMRI signal

Several approaches can be used to perform fMRI experiments. One can mention the Arterial Spin Labeling (ASL) which is an imaging technique that measures tissue perfusion using a freely diffusible intrinsic tracer (Petcharunpaisan et al., 2010). However, the BOLD contrast is the most common technique used for performing fMRI experiments (Kwong et al., 1992; Ogawa et al., 1992). Oxygen and carbon dioxide tension of cortical tissues locally controls the blood flow in the brain. The increase of an activity in a specific cortex region after a given task causes an initial drop in oxygenated hemoglobin (oxyHb) in addition to an increase in the local carbon dioxide and deoxygenated hemoglobin (deoxyHb). A surplus of oxygenated hemoglobin is delivered due to an increase in the cerebral blood flow (CBF) after 2-6 seconds lag. This surplus washes away deoxyhemoglobin. Through BOLD fMRI, we are able to study the hemoynamic response to neural firing. These hemodynamics can be captured by measuring the changes in the MR signal and it is referred to as the hemodynamic response function (HRF). An example of the HRF shape is shown in Fig. 2.5. Neural activity in the brain leads to an increase in the metabolic demands which in turn leads to an increase in the inflow of oxygenated blood to active regions. However, the concentration of deoxygenated hemoglobin decreases since not all the oxygen supplies are consumed. This causes an increase in the signal. This positive increment lasts for 1-2 seconds after the onset of neural activity and peaks 5-8 seconds after peak neural activity. The BOLD signal decreases below its baseline after reaching the peak which lasts for approximately 10 seconds (undershoot). Moreover, it has been proven in some studies (Mechelli et al., 2002; Malonek

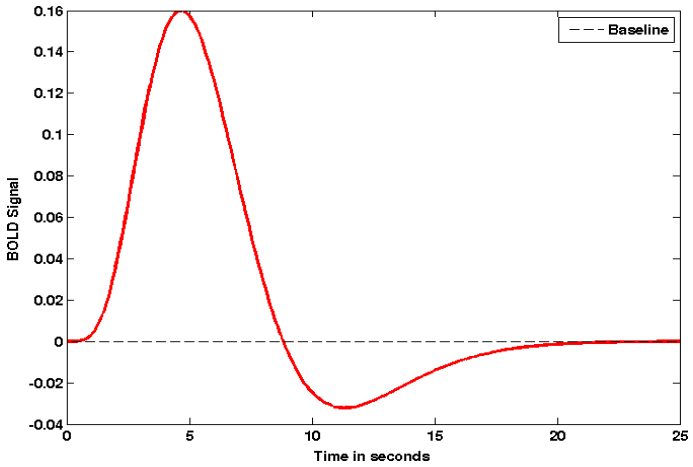

Figure 2.5: The standard canonical HRF shape.

and Grinvald, 1996) that neural activity causes an immediate decrease in oxygenation levels which causes a decrease in the BOLD signal in the first half second following activation.

2.4.5 BOLD fMRI limitations

The BOLD fMRI has shown many advantages in studying the brain metabolism, though it still has some limitations. This part describes these limitations and some possible solutions to avoid them.

(i) **Temporal resolution**
Time of repetition (TR) is the main factor that affects the temporal resolution in fMRI. The used TR usually ranges between 0.5 to 4.0 seconds in fMRI experiments. Oxygenation patterns which take place 5 to 8 seconds after activation are the base of statistical inference for fMRI data. Hence, it is convenient to select the value of TR to be in range of 2 seconds. However, the currently used temporal resolutions do not allow for an efficient modeling of the physiological artifacts in fMRI due to the violation of the Nyquist theory. One can mention the heart rate and respiration. These artifacts cause periodic fluctuations in the BOLD signal. Since the fMRI BOLD signal suffers from a low signal-to-noise ratio (SNR) and the presence of physiological artifacts, many recent studies (Larkman et al., 2001; Lindquist et al., 2008a; Moeller

et al., 2010) have been investigating the possibility of increasing the temporal resolution of fMRI experiments by making TR on the order of hundreds of milliseconds which will solve many of these issues. The medical image reconstruction community has also developed several techniques for accelerating the acquisition process. We can for instance mention parallel MRI proposed in (Pruessmann et al., 1999; Sodickson and Manning, 1997). This parallel imaging technique uses multiple coils with different spatial sensitivities to simultaneously measure k-space. This allows increasing the amount of data acquired in a window time which can be used either to increase the spatial resolution or to decrease the time to sample an image with a specific spatial resolution. Compressed sensing MRI is another technique that can be used to accelerate data acquisition (Lustig et al., 2007).

(ii) **Spatial resolution**
Although fMRI provides better spatial resolution when compared with other functional imaging techniques such as PET, MEG and EEG, it is still difficult to study certain small-scale features due to the its spatial limitations. These limitations include signal strength and the point-spread function (PSF) of BOLD imaging. The PSF decreases as the magnetic field strength increases and it also interacts with the head movement and physiological artifacts. In addition, the spatial smoothing applied to fMRI data before analysis leads to a decrease in the data resolution. Moreover, the registration applied to individuals involved in a group-level study is another type of such limitations since it causes substantial blurring and noise in the group average.
Spatial limitations can be solved by making improvements in the acquisition methods by using pMRI and CS MRI techniques (Pruessmann et al., 1999; Sodickson and Manning, 1997) or preprocessing methods. As regards the preprocessing methods, the use of enhanced spatial inter-subject normalization (Tahmasebi et al., 2009) and improved smoothing techniques can reduce the blurring in the fMRI data.

(iii) **Acquisition artifacts**
Many acquisition artifacts can corrupt the fMRI data such as brain movement and head movement. Moreover, fMRI data contain transient spike artifacts and slow drift components. The latter components can be caused by the magnetic gradient instability, movement

and physiologically induced inhomogeneities in the magnetic field and RF interference. The combination of these artifacts can disturb the underlying assumption for statistical analysis conducted on the data, such as the normality assumption. Examples of some artifacts in fMRI data are shown in Fig. 2.6.

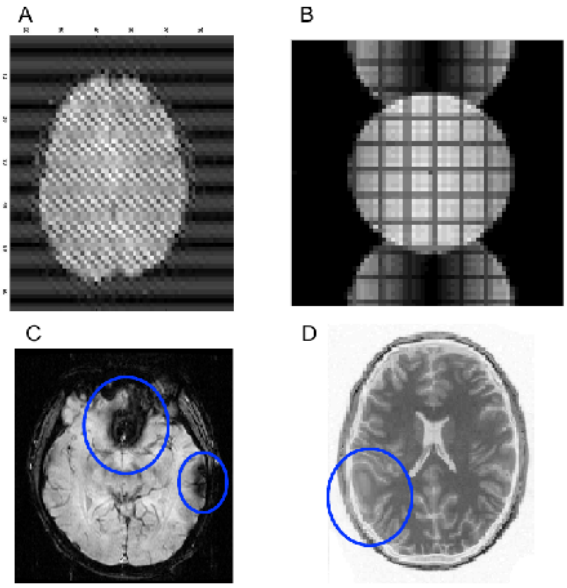

Figure 2.6: Common artifacts example in fMRI data. A): k-space artifact. B) Ghosting in a phantom. C) Susceptibility artifact. D) Normalization artifact (Lindquist and Wager, 2014).

2.5 fMRI paradigms

Three main types of stimulus design are used for fMRI experiments. These types are the blocked, the event-related and the mixed designs. The chosen design type depends on the performed study (Amaro and Barker, 2006). For example, the blocked paradigm can be used at the exploratory stages of a study. Event-elated paradigm is adequate for studies that require sophisticated experiments since it is flexible and allows the stimuli from different experimental conditions to be presented randomly. The mixed design is used to investigate sustained processes and brain responses. The different types

are graphically illustrated in Fig. 2.7. Further details about each type are provided in what follows.

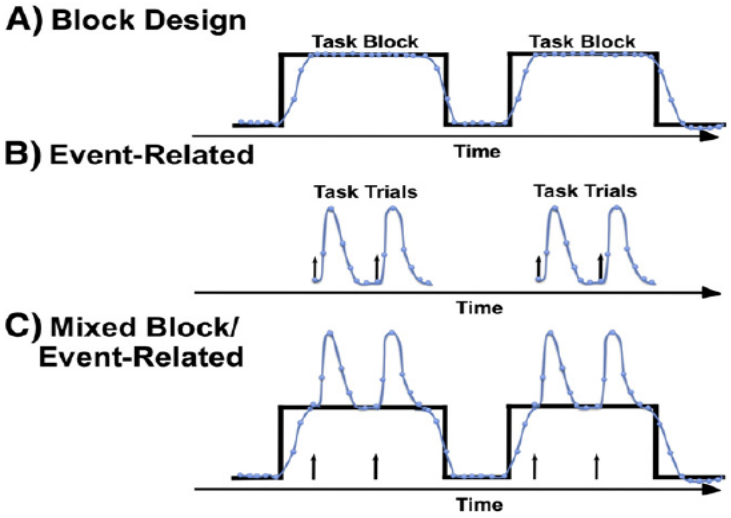

Figure 2.7: A graphical illustration of the different types of fMRI paradigms (Petersen and Dubis, 2012).

(i) **Blocked paradigms**
This type of stimulus design is used to localize functional brain areas and to study the processes of the brain state. It is presented as epochs, *i.e.,* on-off periods. The "on" state refers to stimuli presentation period while the "off" state refers to a rest-state or baseline period. Blocked designs are robust methods to identify the activated voxels during an experiment.

(ii) **Event-related paradigms**
They are used to study the activity in the brain in response to mental tasks (Kao et al., 2009). The occurrences of stimuli are arbitrary in contrast with the blocked paradigms. Using this type of designs allows obtaining temporal information about the underlying neural activity.

(iii) **Mixed designs**
This type of designs is used to study the interaction between processes that work at different time scales (Otten et al., 2002). It is a hyprid design between the blocked and event-related paradigms. It allows to

identify brain regions which exhibit item-related or task-related information processing (Donaldson, 2004).

2.6 FMRI data preprocessing

In this section, we will summarize the preprocessing techniques that the fMRI data undergo a priori to statistical analysis. These techniques aims at eliminating the effects of the physiological and acquisition artifacts on the data in order to validate the prior assumptions of the models used for analysis. To be more specific, one reason to apply these techniques is to achieve a standardization in the locations of brain regions across individuals for group-level analysis. For a specific voxel, it is assumed that each data point in its time series only consists of a signal coming from that particular voxel. However, this assumption is invalid in case of subject's movements between scans. Moreover, the individuals' brain are supposed to be registered to hold true the assumption that each voxel is located at the same anatomical region for all subjects.
The preprocessing can be divided into different steps; starting from the slice time correction, realignment, structural and functional images co-registration, brain normalization to a group template and ending with smoothing. These steps are briefly described in what follows.

(i) **Slice time correction**
In spite of the fact that during the acquisition process different slices from the same volume are acquired sequentially in time, in the data analysis all the voxels in a 3-D image are assumed to be acquired simultaneously. For this reason, the signal intensity has to be estimated in all voxels at a common standardized time point in the acquisition period. The latter can be done by interpolating the signal intensity at the chosen time point for a specific voxel in previous and subsequent acquisitions (Calhoun et al., 2000). However, this can add interpolation errors to data. To avoid these errors, slice time correction can be replaced by two approaches. The first approach is to use more flexible hemodynamic models to account for variations in acquisition time across the brain (Lund et al., 2006). The second one relies on using a rapid acquisition sequence to acquire multiple slices at the same time(Lindquist and Wager, 2014).

(ii) **Realignment**
Motion during the acquisition in fMRI experiment can be a main error source in the fMRI data. It causes contamination of signals from different voxels in the intensity of a specific voxel. Thus, realignment for each individual image is critical in order to compensate for the subject movement. The realignment is done with a reference image that can be the first image or the mean one (Andersson et al., 2001). A rigid body transformation is then applied to the rest of the images in the time series. The parameters of the best match between the target image and the reference one are estimated using an iterative algorithm. Once the match is found, the data is interpolated into the new space. The matching process is done by minimizing the sum of the squared differences between the two images.

(iii) **Co-registration**
It is well known that fMRI data provides little anatomical details due to its low spatial resolution. For this reason, the analysis results of functional data are mapped to high resolution MR images for visualization which is known as co-registration. The co-registration can be done in two ways, either by using an affine or a rigid body transformation. The transformation parameters are estimated by maximizing the mutual information of the two images (Lindquist and Wager, 2014). The co-registration step is also important for the normalization step.

(iv) **Normalization**
Individual brains have differences in their shapes and features. However, non-pathological brains share specific regularities from an anatomical point of view. The normalization step aims at registering each subject's brain anatomy with a standardized atlas space (MNI or Talairach and Tournoux (Dervin, 1990)). Two types of normalization exist in the literature (Woods et al., 1998). The first one is the linear normalization which consists of simple registration of the gross shape of the brain. The second one is the non-linear normalization which consists of warping brain images to match the local features. The importance of the normalization arises in the group-level studies due to the inter-subject registration which is the largest source of error. The normalization of each brain involved in the study has to be assessed in order to eliminate this error in the statistical analysis.

(v) **Smoothing**
A spatial smoothing kernel is usually applied to the functional data tofilter the image intensities in space and reduce the acquisition noise effect. By doing so, the intra-subject differences are eliminated which in turn improves the inter-subject registration. Applying this kernel also involves convolution with a Gaussian kernel. The later is a 3-D normal probability density function (pdf) and it is described by the full width at half maximum of the kernel (FWHM). The FWHM should be 3 times the voxels size (around 9 mm) in order to meet the assumption of the Gaussian Random Field theory (Brett et al., 2004) which states that the variations across space are continuous and normally distributed.

2.7 FMRI data analysis

After increasing the quality of the fMRI data in the preprocessing stages, a statistical analysis is carried out. Task-related fMRI data analysis generally focuses on three main issues: *i)* detecting the activated brain areas in response to a given stimulus, *ii)* estimating the underlying dynamics associated with such an activation through the estimation of the HRF and the *iii)* parcellating of the brain into functionally homogeneous regions (parcels).

(i) **Detection**
So far, many approaches have been proposed to characterize the link between the presented stimuli and the induced BOLD signal through the brain. As a start, one can mention the approach proposed in (Kim et al., 2006) which relies on a non-parametric Bayesian approach where a mixture of experts model combined with a Dirichlet process prior is used to extract and characterize spatial clusters of activation patterns from fMRI data. The most usually used approach is based on a general linear model (GLM) where the link between the stimulus onset and the BOLD effect is modelled through a convolution between the HRF and a binary stimulus sequence. The GLM has been primarily used for detecting task-related brain activity in a massive univariate manner (Friston et al., 1995), considering a constant and fixed canonical HRF shape (Boynton et al., 1996). In the GLM framework, the time course associated with each voxel is modeled as a weighted sum of one or more known predictor variables plus an error term. These predictor

variables could be the onset and offset of an experimental condition (which involves performing a sensory or cognitive task). The contribution of each predictor to the variability in the observed voxel's time series is estimated in the statistical analysis for the data. The simplest version assumes that both the stimulus function and HRF are known where the stimulus is equivalent to the experimental paradigm and the HRF is modeled using a canonical shape (using a gamma function or the difference between two gamma functions (Lindquist et al., 2008b)). Denoting the observed BOLD response at a specific voxel as $\boldsymbol{y}$, the GLM framework considers the following observation model

$$\boldsymbol{y} = \boldsymbol{X}\boldsymbol{\beta} + \boldsymbol{\varepsilon} \qquad [2.2]$$

where $\boldsymbol{y}$ is sampled at n time points. The design matrix is denoted as $\boldsymbol{X}$ and has the size of $n \times p$. This matrix gathers the known predictor variables of $\boldsymbol{y}$ such that $\boldsymbol{X} = \{\boldsymbol{x}_{i,j}, i = 1, \ldots, n\}$ with $\boldsymbol{x}_i = \{x_1, \ldots, x_p\}$ (see Fig. 2.8). The variable $\boldsymbol{\beta}$ is a column vector of size p and it contains the unknown values of the predictor function. Finally $\boldsymbol{\varepsilon}$ is a column vector of size n and containing all the error values. Fig. 2.9 depicts the GLM framework for a single voxel with time series $\boldsymbol{y}$.

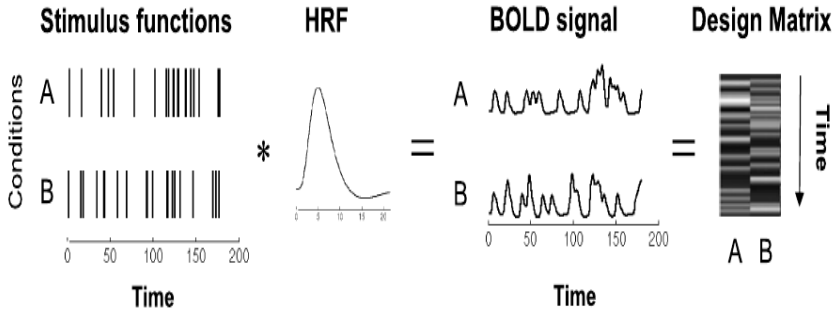

Figure 2.8: A convolution is carried out between a stimuls function with two experimental conidtions and a canonical HRF to obrain two sets of predicted BOLD response. The obtained responses are placed in a design matrix $\boldsymbol{X}$ (Lindquist et al., 2008b).

This model has to be fitted independently for the time course of each voxel. Thus, the spatial covariance between neighbouring voxels is ignored at this stage. The massive univariate approach is motivated

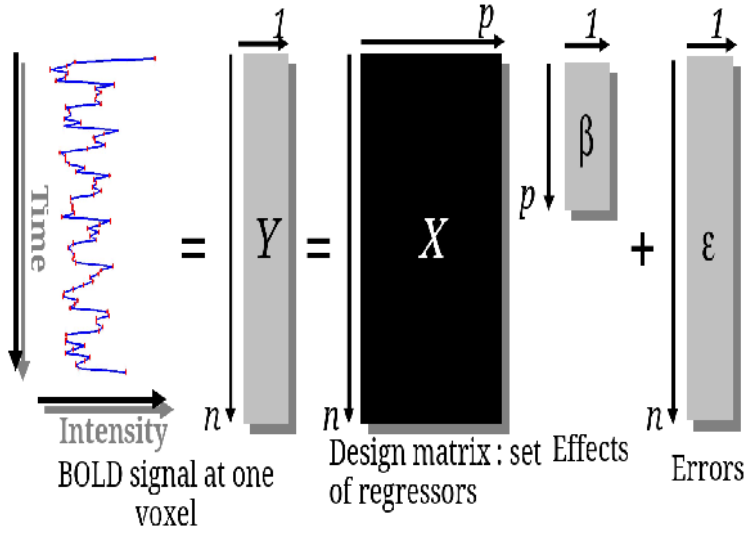

Figure 2.9: Depiction of the GLM for a signle voxel with time series $\boldsymbol{y}$.

by the combination of the presence of more voxels than the observation and the aim of developing topographically specific claims about BOLD activity. However, more studies have investigated multivariate approaches to represent information from specific brain areas (Bowman, 2007; Bowman et al., 2007; Kriegeskorte et al., 2006, 2008). Several approaches have been proposed to estimate the values of $\boldsymbol{\beta}$ such as the ordinary least squares (OLS), the smoothing and sandwich approaches and the generalized least squares (GLS) (more details about these approaches are provided in (Waldorp, 2009)). The estimated values identify the contribution of the predictor in the variance observed in the voxel's time course. Using the OLS approach, the parameters can be estimated by minimizing the sum of the squared residuals $\sum_{i=1}^{n} \left(y_i - x_i\hat{\beta}\right)^2$ yielding the following

$$\hat{\boldsymbol{\beta}} = \left(\boldsymbol{X}^{\mathrm{t}}\boldsymbol{X}\right)^{-1}\boldsymbol{X}^{\mathrm{t}}\boldsymbol{y} \qquad [2.3]$$

and

$$var\left(\hat{\boldsymbol{\beta}}\right) = \sigma^2\left(\boldsymbol{X}^{\mathrm{t}}\boldsymbol{X}\right)^{-1}. \qquad [2.4]$$

The OLS corresponds to the best linear unbiased estimator as stated in the Gauss-Markov theorem. However, the following assumptions regarding the properties of the error term have to be met:

- The errors are independently and identically distributed.
- The independence between the regressors in $\boldsymbol{X}$ and the error.
- No regressor is a linear transformation of one ore more regressors.

The noise variance can be estimated using

$$\hat{\sigma}^2 = \frac{(\boldsymbol{y} - \boldsymbol{X}\hat{\boldsymbol{\beta}})^t(\boldsymbol{y} - \boldsymbol{X}\hat{\boldsymbol{\beta}})}{n}. \quad [2.5]$$

Once the model parameters are estimated, different statistical tests are carried out to define the significance of these estimates. The two widely used tests in the classical approaches are the Student's test (T-test) and Fisher test (F-test). These tests are briefly described below.

T-test

This test is carried out to check whether a univariate linear combination of the estimated $\boldsymbol{\beta}$ is significantly different from a value d. This check can be accomplished using the null and alternative hypotheses which can be summarized as

$$\begin{aligned} \mathcal{H}_0 &: \boldsymbol{c}^{\mathrm{t}}\boldsymbol{\beta} = d \\ \mathcal{H}_1 &: \boldsymbol{c}^{\mathrm{t}}\boldsymbol{\beta} > d \\ &\quad \text{or} \\ &\boldsymbol{c}^{\mathrm{t}}\boldsymbol{\beta} < d, \end{aligned} \quad [2.6]$$

where $\boldsymbol{c}^{\mathrm{t}} = \{c_j, j = 1 : p\}$ is a vector containing the coefficients of the linear combination and $c_j \in \{-1, 0, 1\}$. The T-test can be used for many cases. For example, if one wants to test whether the condition m causes a significant activity at a specific voxel. In this case, $c_j = 1$ for $j = m$ and 0 otherwise and $\boldsymbol{c}^{\mathrm{t}}\boldsymbol{\beta} = \beta^m$. Another example where a T-test is used is to check whether the condition a causes a more significant activity than the condition b. We set $c_a = 1$,$c_b = -1$ and $c_j = 0$ for $j \neq a, b$. In this case, $\boldsymbol{c}^{\mathrm{t}}\boldsymbol{\beta} = \beta^a - \beta^b$.

It is important to know the distribution of $\boldsymbol{\beta}$ in order to define the distribution of the used test. Knowing that $\boldsymbol{y} \sim \mathcal{N}(\boldsymbol{X}\boldsymbol{\beta}, \sigma^2\boldsymbol{I}_n)$ and $\hat{\boldsymbol{\beta}} = (\boldsymbol{X}^{\mathrm{t}}\boldsymbol{X})^{-1}\boldsymbol{X}^{\mathrm{t}}\boldsymbol{y}$, *i.e.*, $\hat{\boldsymbol{\beta}} \sim \mathcal{N}(\boldsymbol{\beta}, \sigma^2(\boldsymbol{X}^{\mathrm{t}}\boldsymbol{X})^{-1})$. Thus $\boldsymbol{c}^{\mathrm{t}}\hat{\boldsymbol{\beta}}$ can be expressed as

$$\boldsymbol{c}^{\mathrm{t}}\hat{\boldsymbol{\beta}} \sim \mathcal{N}(\boldsymbol{c}^{\mathrm{t}}\boldsymbol{\beta}, \sigma^2\boldsymbol{c}^{\mathrm{t}}\left(\boldsymbol{X}^{\mathrm{t}}\boldsymbol{X}\right)^{-1}\boldsymbol{c}). \quad [2.7]$$

As a result, we can use the following statistical test that follows a Student distribution with $n - p$ degrees of freedom

$$T = \frac{\boldsymbol{c}^{\mathrm{t}}\hat{\boldsymbol{\beta}} - \boldsymbol{c}^{\mathrm{t}}\boldsymbol{\beta}}{(\hat{\sigma}^2\boldsymbol{c}^{\mathrm{t}}\left(\boldsymbol{X}^{\mathrm{t}}\boldsymbol{X}\right)^{-1}\boldsymbol{c})^{-1/2}}. \quad [2.8]$$

Under the null hypothesis in [2.6], the previous equation can be written as

$$T = \frac{\boldsymbol{c}^{\mathrm{t}}\hat{\boldsymbol{\beta}} - d}{(\hat{\sigma}^2\boldsymbol{c}^{\mathrm{t}}\left(\boldsymbol{X}^{\mathrm{t}}\boldsymbol{X}\right)^{-1}\boldsymbol{c})^{-1/2}}. \quad [2.9]$$

After completing the statistical test, the significance of each voxel is determined using a threshold value u_α associated with an error risk α that controls the rate of false positive

$$\alpha = p_{\mathcal{H}_0}(T > u_\alpha). \quad [2.10]$$

The null hypothesis is then rejected if $T > u_\alpha$. More details can be found in (Poline and Kherif, 2007).

F-test

This F-test allows checking multiple combinations. In this case $\boldsymbol{c}^{\mathrm{t}}$ has the size of $r \times p$ where r is the number of the tested linear combinations. For example, if there are p experimental conditions in the paradigm and we want to test if at least one of them causes a significant activity at a specific voxel. In this case, one can use the F-test with $c_{j,j'}$ is the entry of matrix $\boldsymbol{c}^{\mathrm{t}}$ and $c_{j,j'} = \delta(m - m')$ where δ is the dirac function that gives zero everywhere except if $j = j'$. This test can be used to compare reduced models (with a specific type of the experimental conditions) to the full models (considering all the experimental conditions) to see which fits the data better. In this case, the statistical test is defined by

$$\mathcal{F} = \frac{(S_{red} - S_f)/(R_red - R_f)}{S_f/(n - R_f)} \quad [2.11]$$

where S_red and S_f are the sums of the quadratic errors of the reduced and full model, respectively. R_red (resp. R_f) is the rank of the reduced model (resp. full model) design matrix. The interested reader can refer to (Poline and Kherif, 2007) for further details.

(ii) **Estimation**

Although the classical GLM is widely used for the statistical analysis

of fMRI data, the assumption that the HRF is fixed limits its usefulness. A single HRF shape is not physiologically appropriate and many studies have reported the variability of the HRF in different levels. In (Miezin et al., 2000; Ciuciu et al., 2003), it has been proven that the HRF varies between regions and sessions within subject. Moreover, it has been shown in (Handwerker et al., 2004; Aguirre et al., 1998) that HRF also varies across subjects. The HRF also varies between groups (infants, patients, etc.) (D'Esposito et al., 1998, 2003). The GLM has been progressively extended to account for the HRF variability using more regressors and hence more flexible design matrices (Glover, 1999; Friston et al., 2000; Henson et al., 2001; Lindquist et al., 2009). Nonetheless, due to the increase of regressors the main difficulty that comes up in this context is the decrease of statistical sensitivity in the subsequent tests, making the detection task less reliable. Besides, other approaches that rely on physiologically-informed non-linear models (e.g., the Balloon model) have been pushed forward for recovering hemodynamics but most often they are deployed in brain regions where evoked activity has already been detected (Buxton and Frank, 1997; Friston et al., 2000; Riera et al., 2004; Deneux and Faugeras, 2006). Their computational cost is actually prohibitive for whole brain analysis and some identifiability issues (different pairs of state variables and parameters give the same goodness-of-fit) arise because of the presence of noise.

(iii) **Joint detection estimation**
The above mentioned approaches mainly address detection of evoked activity and HRF recovery as a two-step procedure whereas both tasks are strongly linked. A precise localization of activations depends on a reliable HRF estimate, while a robust HRF shape is only achievable in brain regions eliciting task-related activity (Kershaw et al., 1999; Ciuciu et al., 2003). Moreover, most of linear and non-linear models are designed for univariate inference whereas it is known that the BOLD signal is spatially smooth and thus the HRF shapes remain similar over a certain spatial distance (Handwerker et al., 2004; Ciuciu et al., 2004; Handwerker et al., 2012; Badillo et al., 2013b). One of the approaches that accounts for this interdependence is the joint detection-estimation (JDE) framework, where both tasks are performed jointly (Makni et al., 2008; Vincent et al., 2010; Chaari et al., 2013). To im-

prove the estimation robustness and account for spatial correlation of the BOLD signal, a single HRF shape model was assumed for a specific group of voxels, also referred to as a *parcel*. Within this JDE formalism, two approaches for posterior inference have been developed, the first one relies on computationally intensive stochastic sampling (Makni et al., 2008; Vincent et al., 2010) and the second one is based on the variational expectation maximization (VEM) algorithm (Chaari et al., 2013) to achieve numerical convergence at lower cost.

The JDE model is a parcel-based model which was firstly proposed in (Makni et al., 2008; Vincent et al., 2010). This model assumes that the brain is divided a priori into $\boldsymbol{\mathcal{P}} = (\mathcal{P})_{\alpha=1:A}$ parcels and each of them consists of J_α voxels. All voxels share similar homogeneous properties. The fMRI time series is denoted as $\boldsymbol{y}_j$ and it is measured at each voxel $j \in \mathcal{P}_\alpha$ at times $(t_n)_{n=1,\dots,N}$, where $t_n = nTR$, TR is the time of repetition and N is the number of scans. M different experimental conditions are considered. A unique BOLD signal model is used for a group of connected voxels (a parcel) in order to link the observed data $\boldsymbol{Y} = \{\boldsymbol{y}_j \in \mathbb{R}^N, j \in \mathcal{P}_\alpha\}$ with the unknown HRF $\boldsymbol{h}_\alpha \in \mathbb{R}^D$ of parcel $\mathcal{P}_\alpha$ and to the unknown response amplitudes $\boldsymbol{A} = \{\boldsymbol{a}^m, m = 1 \dots, M\}$ (where $\boldsymbol{a}^m = \{a_j^m, j \in \mathcal{P}_\alpha\}$ and a_j^m is the magnitude for voxel j at condition m). The following observation model is considered

$$\forall j \in \mathcal{P}_\alpha \quad \boldsymbol{y}_j = \sum_{m=1}^{M} a_j^m \boldsymbol{X}_m \boldsymbol{h}_\alpha + \boldsymbol{P}\boldsymbol{\ell}_j + \boldsymbol{b}_j \qquad [2.12]$$

where $\boldsymbol{X}_m = \{x_m^{n-d\Delta t}, n = 1, \dots, N, d = 0, \dots, D-1\}$ is a $N \times D$ binary matrix which provides information on the stimulus occurrences, $\Delta t < TR$ is the sampling period of the unknown HRF $\boldsymbol{h}_\alpha = \{h_{d\Delta t}, d = 0, \dots, D-1\}$. The weights a_j^m's are scalars associated with the magnitude of the response and they are referred to as Neural Response Levels (NRL). The NRL a_j^m's follow spatial Gaussian mixtures defined by a set of parameters $\boldsymbol{\theta}_a$ and governed by binary Markov fields. To be more specific, each NRL is assigned to one of the activation classes encoded by the variables $\boldsymbol{Q} = \{\boldsymbol{q}^m, m = 1, \dots, M\}$ where $\boldsymbol{q}^m = q_j^m, j \in \mathcal{P}_\alpha$. Akin to (Vincent et al., 2010), two activation classes are considered (activated and non-activated voxels). The matrix $\boldsymbol{P}$ corresponds to the physiological artifacts. These artifacts are accounted for by consider-

ing a low frequency orthonormal function basis of size $N \times O$. Each voxel j is associated with a vector of low frequency drifts $\boldsymbol{\ell}_j \in \mathbb{R}^O$. The observation noise coefficients $\boldsymbol{b}_j$'s are assumed to be independent with $\boldsymbol{b}_j \sim \mathcal{N}(0, \Gamma_j^{-1})$ where Γ_j is the precision matrix and the set of all unknown precision matrices is denoted as $\Gamma = \{\Gamma_j, j \in \mathcal{P}_\alpha\}$. The observation model in [2.12] is a general form of the GLM framework. It relies on the classical assumption of a linear and time invariant system of the GLM. In the JDE model, the response magnitudes a_j^m's correspond to the effects associated with stimulus-induced while the drift coefficients $\boldsymbol{\ell}_j$'s correspond to the low frequency basis regressors. However, the JDE model generalizes the GLM one since it considers the hemdodynamic response as an unknown variable. The graphical model in Fig. 2.10 illustrates the dependencies between the latent and observed variables in the JDE model. Two inference strategies were adopted to compute

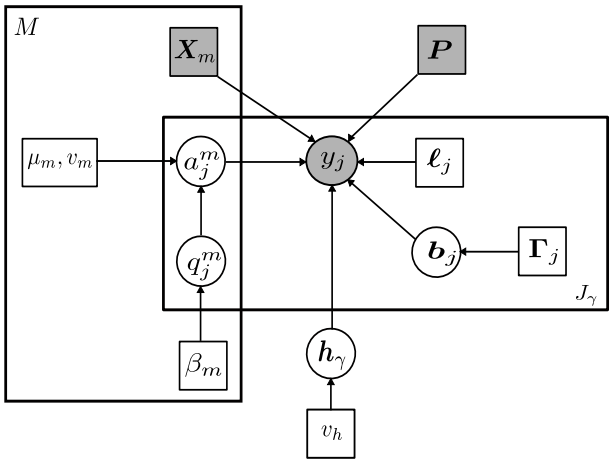

Figure 2.10: Graphical model describing dependencies between latent and observed variables involved in the JDE generative model for a given parcel $\boldsymbol{\mathcal{P}}$ with J voxels.

the posterior distribution associated with the NRL, activation classes and HRF estimate. The first strategy consists of sampling the posterior distribution using the intensive Markov Chain Monte Carlo (MCMC) and building estimators using the generated samples (Vincent et al., 2010). The other one which is less computationally intensive relies on the variational expectation maximization (VEM) algorithm to approximate the posterior as a product of the pdf of the unknown variables (Chaari et al., 2013). This algorithm alternates maximization of the

following free energy with respect to q and $\boldsymbol{\Theta}$

$$\mathcal{F}(q, \boldsymbol{\Theta}) \quad = \quad \mathrm{E}_q\big[\log p(\boldsymbol{Y}, \boldsymbol{A}, \boldsymbol{h}_\gamma, \boldsymbol{Q} \,|\, \boldsymbol{\Theta})\big] + \mathcal{G}(q), \qquad [2.13]$$

where $q \in \mathcal{D}$, $\mathcal{D}$ ois the set of all probability distributions on the probability spaces associated with the unknown variables $\boldsymbol{A}, \boldsymbol{h}_\gamma$ and $\boldsymbol{Q}$.

(iv) **Parcellation**
Whatever the numerical algorithm deployed, the JDE formalism requires a prior parcellation of the brain into functionally homogeneous regions. These parcels should achieve a fair compromise between *homogeneity* and *reliability* (Thirion et al., 2014). Homogeneity means that the parcels should be small enough to meet the assumption of HRF shape invariance within each parcel, whereas reliability should guarantee that parcels are large enough to ensure reliable HRF estimation and detection performance. This issue has motivated a number of recent developments that try to cope with the identification of relevant parcellation of the brain (Flandin et al., 2002; Thirion et al., 2006; Golland et al., 2007; Lashkari et al., 2010, 2012; Eickhoff et al., 2011). One of the popular methods that are used for this purpose is the K-means algorithm. It is a widely used clustering technique for vector data (Thirion et al., 2014). The feature data used for brain parcellation using this algorithm is of dimension $S \times F$ (no. of subjects $\times$ no. of contrasts). Principle Component Analysis (PCA) is then used to reduce the feature data to 100 components prior to clustering. However, the spatial structure is not explicitly considered when parcellating the brain using the K-means and spatial smoothing has to be applied prior to clustering for spatial regularization. One can also mention Ward's algorithm (Ward and Joe, 1963). This algorithm uses the variance minimizing approach such that two clusters are merged if the resulting cluster minimizes the sum squared differences of fMRI signal within all clusters. The spectral clustering proposed in (Shi and Malik, 2000; Ng et al., 2002) is also used for brain parcellation and it consists of applying the K-means algorithm on a representation of the data. This representation preservers the spatial structure and represents the functional features' similarity. Fig. 2.11 shows an axial slice of the parcellation obtained using the three mentioned parcellation techniques with 500 parcels (Thirion et al., 2014).

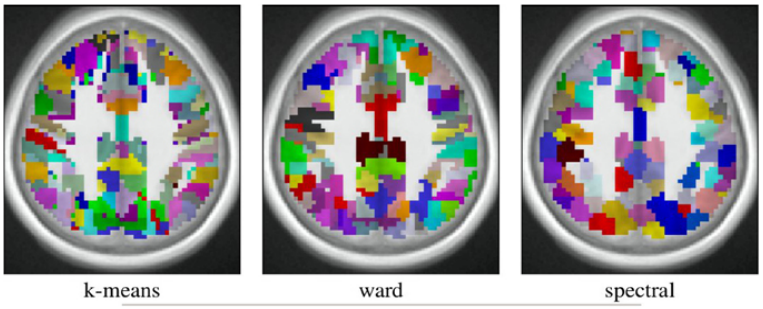

Figure 2.11: Example of the parcellation obtained using the K-means, ward and spectral clustering techniques with 500 parcels (Thirion et al., 2014).

(v) **Joint parcellation detection estimation**
Among the above mentioned fMRI analysis techniques, none allows to uncover functional regions that appear homogeneous with respect to their hemodynamic profile. This issue has been specifically addressed in (Badillo et al., 2013a) using random parcellation and consensus clustering. Another approach relying on a multivariate Gaussian probabilistic modelling has been proposed in (Fouque et al., 2009). One can also mention the joint parcellation within the JDE framework (Chaari et al., 2012, 2015; Frau-Pascual et al., 2014), giving rise to the joint parcellation detection estimation (JPDE) approach (which will be illustrated in chapter 3). This strategy performs parcellation during the detection estimation steps through the selection of hemodynamic territories, *i.e.*, sets of voxels that share the same HRF pattern.
Although an automated inference of parcellation is performed in the JPDE methodology, the algorithm still requires the manual setting of the number of parcels. This thesis mainly investigates the automatic hemodynamic parcellation of the brain and the estimation of the associated HRF profiles of the parcels in both the subject and group levels.

2.8 Conclusion

This chapter presented a brief illustration of fMRI basics and principles, and how fMRI was motivated by NMR. It also addressed the acquisition of fMRI using an MRI scanner. The constructed fMRI data has to be preprocessed

in order to eliminate physiological and acquisition artifacts. Different approaches can be used to analyze the preprocessed data in order to detect the activity and estimate the dynamics in the brain. The simplest approach is the GLM which was shortly described. This model aims at localizing the brain activity by assuming a fixed HRF shape. Many extensions have been proposed to the GLM in order to allow the estimation of the HRF where an activation has already been detected. However, the detection and estimation are linked and have to be dealt with simultaneously. The JDE model comes to solve the latter issue but it still requires a prior parcellation of the brain. A parcellation step has been added in the JPDE model to divide the brain into hemodynamic territories according to the voxel-dependent HRFs. However, the JPDE still requires the number of parcels to be fixed which can be complicated when no prior information exists about the optimal number of parcels which motivates the proposed methods at the subject-level in this thesis. The objective is to provide techniques that allow the automatic parcellation of the brain at the subject-level. To the best of our knowledge, non of the approaches in the literature deals with the heomdynamic parcellation of the brain at the group-level. Thus, we propose two approaches for a group-level fMRI data analysis that estimate the group-level parcellation and dynamics.

CHAPTER 3

Joint Parcellation Detection Estimation and Model Selection

Contents

3.1 Introduction

In subject-level fMRI data analysis, two tasks are usually performed separately; detection of brain activity in response to a given stimulus and estimation of the hemodynamic response. However, these tasks are strongly linked and should be considered simultaneously as discussed in the first chapter. Moreover, the estimation of the brain dynamics relies on the hemodynamic parcellation, which is a problematic issue especially if no previous knowledge about the number of these parcels and their shapes is available. In this chapter, we propose a model selection procedure based on the free energy calculation of the joint parcellation detection estimation (JPDE) model. As

a first step, we recall the JPDE model in Section 3.2. This model extends the region-based JDE model to a whole brain area. It jointly detects the activity evoked by a stimulus, estimates the underlying dynamics for a given brain area and performs online parcellation along with the detection and estimation tasks. However, this model still needs the number of parcels to be fixed a priori. Hence, we introduce a variational model selection procedure based on the free energy calculation in Section 3.3 which allows this number of parcels to be estimated.

3.2 The joint parcellation detection estimation model

This section is devoted to the presentation of the JPDE model proposed in (Chaari et al., 2012, 2015). This model is the extension of the parcel-based JDE model developed in (Makni et al., 2008; Vincent et al., 2010; Chaari et al., 2013) to a whole-brain or a wide brain area.

3.2.1 Observed and missing variables

Let $\boldsymbol{\mathcal{P}}$ be the set of voxels of interest belonging to the whole brain or wide brain area. At voxel j, the fMRI time series $\boldsymbol{y}_j$ is measured at times $\{t_n, n = 1, ..., N\}$, where $t_n = nTR$, N being the number of scans and TR the time of repetition. The number of different stimulus types or experimental conditions is M. At each voxel j, a voxel dependent HRF $\boldsymbol{h}_j \in \mathbb{R}^D$ is assumed where D is the voxel-dependent HRF size and $\boldsymbol{H} = \{\boldsymbol{h}_j, j \in \boldsymbol{\mathcal{P}}\}$ is the set of all possible HRF shapes. Each $\boldsymbol{h}_j$ is associated with an HRF group among K possible groups. These groups or HRF classes are specified by a set of hidden labels $\boldsymbol{z} = \{z_j, j \in \boldsymbol{\mathcal{P}}\}$ where $z_j \in \{1, ..., K\}$ and $z_j = k$ means that the voxel j belongs to the k-th group. An estimation of $\boldsymbol{z}$ corresponds to a partition of the domain into K hemodynamic territories whose connected components define a parcellation of the whole brain or of the considered region of interest (ROI). The link to the observed BOLD data is specified via the following forward model

$$\boldsymbol{y}_j = \sum_{m=1}^{M} a_j^m \boldsymbol{X}_m \boldsymbol{h}_j + \boldsymbol{P}\boldsymbol{\ell}_j + \boldsymbol{b}_j \qquad [3.1]$$

where $\boldsymbol{X}_m = \{x_m^{n-d\Delta t}, n = 1, \ldots, N, d = 0, \ldots, D-1\}$ is a known binary matrix which provides information on the stimulus occurrences for the m-th experimental condition, $N \times D$ is the dimension of this matrix, and $\Delta t \leq TR$ is the sampling period of the unknown HRFs. The scalar weights a_j^m's are the unknown response amplitudes. They are generally referred to as neural response levels (NRL). Denote as $\boldsymbol{A} = \{\boldsymbol{a}^m, m = 1, \ldots, M\}$ with $\boldsymbol{a}^m = \left\{a_j^m, j \in \boldsymbol{\mathcal{P}}\right\}$, a_j^m being the amplitude at voxel j for the m-th experimental condition. Similarly to the HRF, each NRL is assumed to be in one of I groups specified by activation class assignment variables $\boldsymbol{Q} = \{\boldsymbol{q}^m, m = 1, \ldots, M\}$ where $\boldsymbol{q}^m = \left\{q_j^m, j \in \boldsymbol{\mathcal{P}}\right\}$ and $q_j^m \in \{1, ..., I\}$ represents the activation class at voxel j for the m-th experimental condition. Two classes are considered here ($I = 2$) where $i = 0$ and $i = 1$ refer to non-activated and activated voxels, respectively. Finally, the rest of the signal is made of the vector $\boldsymbol{P}\boldsymbol{\ell}_j$, which corresponds to low frequency drifts where $\boldsymbol{P}$ is an $N \times O$ matrix, $\boldsymbol{\ell}_j \in \mathbb{R}^O$ is a vector to be estimated and $\boldsymbol{L} = \{\boldsymbol{\ell}_j, j \in \boldsymbol{\mathcal{P}}\}$. Regarding the observation noise, the $\boldsymbol{b}_j$'s are assumed to be independent, zero-mean Gaussian vectors with covariance matrix $\boldsymbol{\Gamma}_j^{-1}$, *i.e*, $\boldsymbol{b}_j \sim \mathcal{N}(0, \boldsymbol{\Gamma}_j^{-1})$. The set of all unknown precision matrices is denoted by $\boldsymbol{\Gamma} = \{\boldsymbol{\Gamma}_j, j \in \boldsymbol{\mathcal{P}}\}$. All the notations for variables and parameters used in the JPDE model are summarized in Tab. 3.1.

3.2.2 Hierarchical model

Adopting a Bayesian formulation for the JPDE model, the joint distribution of $\boldsymbol{Y}, \boldsymbol{A}, \boldsymbol{H}, \boldsymbol{Q}, \boldsymbol{z}$ is defined as follows

$$\begin{aligned} p(\boldsymbol{Y}, \boldsymbol{A}, \boldsymbol{H}, \boldsymbol{Q}, \boldsymbol{z}; \boldsymbol{\Theta}) &= p(\boldsymbol{Y} \mid \boldsymbol{A}, \boldsymbol{H}; \boldsymbol{\Theta})\, p(\boldsymbol{A} \mid \boldsymbol{Q}; \boldsymbol{\Theta})\, p(\boldsymbol{Q}; \boldsymbol{\Theta}) \\ &\times p(\boldsymbol{H} \mid \boldsymbol{z}; \boldsymbol{\Theta})\, p(\boldsymbol{z}; \boldsymbol{\Theta}) \end{aligned} \quad [3.2]$$

where $\boldsymbol{\Theta}$ is the set of all parameters which will be defined later. More details about the right-hand side term of [3.2] are provided below.

(i) **Likelihood**

To account for serial correlation in fMRI time series, an autoregressive (AR) noise model has been adopted (Makni et al., 2008; Woolrich et al., 2001; Chaari et al., 2011, 2012). It follows that the noise covariance matrix for voxel $\#j$ can be defined as $\boldsymbol{\Gamma}_j = \sigma_j^{-2}\boldsymbol{\Lambda}_j$ where $\boldsymbol{\Lambda}_j$ is a tridiagonal symmetric matrix whose components depend on the AR(1) parameter ρ_j (Makni et al., 2008): $(\boldsymbol{\Lambda}_j)_{1,1} = (\boldsymbol{\Lambda}_j)_{N,N} = 1$, $(\boldsymbol{\Lambda}_j)_{n,n} =$

Table 3.1: Notations for variables and parameters used in the JPDE model.

	Notation	Definition	Dimension
Variables	$\boldsymbol{y}_j \in \mathbb{R}^N$	Observed BOLD signal at voxel j	N
	$\boldsymbol{b}_j \in \mathbb{R}^N$	Acquisition noise vector at voxel j	N
	$\boldsymbol{h}_j = \{h_{d\Delta t}, d = 0, \ldots, D-1\} \in \mathbb{R}^D$	HRF sampled at Δt	D
	$a_j^m \in \mathbb{R}$	NRL at voxel j for condition m	1
	$\boldsymbol{a}^m = \{a_j^m, j \in \mathcal{P}\} \in \mathbb{R}^J$	NRLs for condition m	J
	$q_j^m \in \{0, 1\}$	Activation class for voxel j and condition m	1
	$\boldsymbol{q}^m = \{q_j^m, j \in \mathcal{P}\} \in \{0, 1\}^J$	Activation classes for condition m	J
	$z_j \in \{0, \ldots, K\}$	HRF group for voxel j	1
Unknown Parameters	$\boldsymbol{\ell}_j \in \mathbb{R}^O$	Low frequency drifts for voxel j	O
	$\boldsymbol{\Gamma}_j \in \mathbb{R}^{N \times N}$	Noise precision matrix for voxel j	$N \times N$
	$\boldsymbol{\mu}_m = \{\mu_{m0}, \mu_{m1}\} \in \mathbb{R}^2$	Mixture model means for NRLs in condition m	2
	$\boldsymbol{v}_m = \{v_{m0}, v_{m1}\} \in \mathbb{R}_+^2$	Mixture model variances for NRLs in condition m	2
	$\beta_m \in \mathbb{R}_+$	Potts regularization parameter for condition m	1
	$\theta_m = \{\boldsymbol{\mu}_m, \boldsymbol{v}_m, \boldsymbol{\beta}_m\}$	Parameters of the condition m	1
	$\beta_z \in \mathbb{R}_+$	Potts regularization parameter for HRF groups	1
	$\bar{\boldsymbol{h}} = \{\bar{\boldsymbol{h}}_k, k = 0, \ldots, K\} \in \mathbb{R}^{D \times K}$	HRF patterns	$D \times K$
	$\bar{\boldsymbol{\Sigma}} = \{\bar{\boldsymbol{\Sigma}}_k, k = 0, \ldots, K\}$	HRF covariance matrices	D
Fixed	$\boldsymbol{X}_m \in \{0, 1\}^{N \times D}$	Binary stimulus occurrence matrix for condition m	$N \times D$
	$\boldsymbol{P} \in \mathbb{R}^{N \times O}$	Low frequency orthonormal function basis	$N \times O$

$1+\rho_j^2$ for $n=2,\ldots,N-1$ and $(\boldsymbol{\Lambda}_j)_{n+1,n}=(\boldsymbol{\Lambda}_j)_{n,n+1}=-\rho_j$ for $n=1,\ldots,N-1$. Using the notation $\boldsymbol{\theta}_0=(\sigma_j^2,\rho_j)_{1\leq j\leq J}$ and $\overline{\boldsymbol{y}}_j=\boldsymbol{y}_j-\boldsymbol{P}\boldsymbol{\ell}_j-\boldsymbol{S}_j\boldsymbol{h}_j$ with $\boldsymbol{S}_j=\sum_{m=1}^{M}a_j^m\boldsymbol{X}_m$, the likelihood can be factorized over voxels as follows

$$p(\boldsymbol{Y}\,|\,\boldsymbol{A},\boldsymbol{H};\boldsymbol{\theta}_0)\propto\prod_{j=1}^{J}\left[\frac{\sqrt{\det\boldsymbol{\Lambda}_j}}{\sigma_j^N}\right]\exp\left(-\frac{\overline{\boldsymbol{y}}_j^{\mathrm{t}}\boldsymbol{\Lambda}_j\overline{\boldsymbol{y}}_j}{2\sigma_j^2}\right). \qquad [3.3]$$

(ii) **Neuronal response levels**

The NRLs are assumed to be statistically independent across conditions, *i.e*,

$$p(\boldsymbol{A};\boldsymbol{\theta}_{\boldsymbol{a}})=\prod_{m=1}^{M}p(\boldsymbol{a}^m;\boldsymbol{\theta}_m) \qquad [3.4]$$

where $\boldsymbol{\theta}_{\boldsymbol{a}}=\{\boldsymbol{\theta}_m,m=1,\ldots,M\}$ and $\boldsymbol{\theta}_m$ gathers the parameters for the m-th condition. A mixture model is then adopted by using the allocation variables q_j^m to segregate non-activated voxels ($q_j^m=0$) from activated ones ($q_j^m=1$). For the m-th condition, and conditionally to the assignment variables $\boldsymbol{q}^m$, the NRLs are assumed to be independent, *i.e*,

$$p(\boldsymbol{a}^m\,|\,\boldsymbol{q}^m;\boldsymbol{\theta}_m)=\prod_{j\in\boldsymbol{\mathcal{P}}}p(a_j^m\,|\,q_j^m;\boldsymbol{\mu}_m,\boldsymbol{v}_m) \qquad [3.5]$$

with $p(a_j^m\,|\,q_j^m=i;\boldsymbol{\theta}_m)\sim\mathcal{N}(\mu_{mi},v_{mi})$. All the means and variances of the response amplitudes are gathered in the two unknown vectors $\boldsymbol{\mu}=\{\boldsymbol{\mu}_{mi},m=1,\ldots,M,i=0,1\}$ and $\boldsymbol{v}=\{\boldsymbol{v}_{mi},m=1,\ldots,M,\ \ i=0,1\}$, respectively. Note that for non-activated voxels ($i=0$), $\mu_{m1}=0$ for all $m=1,\ldots,M$.

(iii) **Activation classes**

As in (Vincent et al., 2010), the M experimental conditions are assumed to be independent a priori regarding the activation class assignments, *i.e*, $p(\boldsymbol{Q})=\prod_{m=1}^{M}p(\boldsymbol{q}^m;\beta_m)$ where $p(\boldsymbol{q}^m;\beta_m)$ is a Markov random field prior, namely a Potts model with interaction parameter β_m defined as

$$p(\boldsymbol{q}^m;\beta_m)=W(\beta_m)^{-1}\exp\bigl(\beta_m U(\boldsymbol{q}^m)\bigr) \qquad [3.6]$$

with $U(\boldsymbol{q}^m) = \sum_{j\sim l} I(q_j^m = q_l^m)$, $W(\beta_m)$ is a normalizing constant and I is an indicator function such that $I(a = b) = 1$ if $a = b$ and 0 otherwise. The notation $j \sim l$ means that the summation covers all neighbouring voxels. The neighbouring system is covering a 3D scheme through the brain volume. In what follows, we will consider a 6-connexity 3D neighboring system as shown in Fig. 3.1.

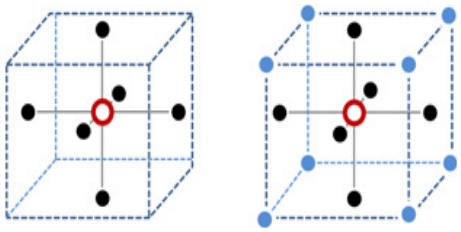

Figure 3.1: 6-connexity 3D neighbouring system used in the Markov random field prior for activation classes in the JPDE model.

(iv) **HRF patterns**

A unique HRF shape was considered for the whole parcel in (Makni et al., 2008; Vincent et al., 2010; Chaari et al., 2011). The JPDE model considered in this thesis assumes that the HRF is voxel-dependent and that the distribution of $\boldsymbol{h}_j$ is expressed, for each voxel j, conditionally to the HRF group variable z_j

$$p(\boldsymbol{H}|\boldsymbol{z}) = \prod_{j\in\mathcal{P}} p(\boldsymbol{h}_j \mid z_j) \qquad [3.7]$$

with

$$p(\boldsymbol{h}_j \mid z_j = k) \sim \mathcal{N}(\bar{\boldsymbol{h}}_k, \bar{\boldsymbol{\Sigma}}_k) \qquad [3.8]$$

where $\bar{\boldsymbol{h}}_k$ denotes the mean HRF pattern of group $\#k$, while $\bar{\boldsymbol{\Sigma}}_k = \nu_k \boldsymbol{I}_{D+1}$ adjusts the stochastic perturbations around $\bar{\boldsymbol{h}}_k$ via the value of the hyperparameter ν_k. The smoothness of the HRF pattern is ensured by assigning the prior distribution $\bar{\boldsymbol{h}}_k \sim \mathcal{N}(\boldsymbol{0}, \sigma_h^2 \boldsymbol{R})$, with $\boldsymbol{R} = (\Delta t)^4 \, (\boldsymbol{D}_2^{\mathrm{t}} \boldsymbol{D}_2)^{-1}$, where $\boldsymbol{D}_2$ is the second-order finite difference matrix and σ_h^2 is a parameter to be estimated or fixed. Moreover, $\bar{\boldsymbol{h}}_{k0} = \bar{\boldsymbol{h}}_{kD\Delta t} = 0$ as in (Makni et al., 2008; Vincent et al., 2010; Chaari et al., 2011). Hence, $\bar{\boldsymbol{h}}_k \in \mathbb{R}^{D-1}$.

(v) **HRF groups**
A spatial K-class Potts model with interaction parameter β_z is used to promote parcellation connexity

$$p(\boldsymbol{z};\beta_z) = W(\beta_z)^{-1}\exp\big(\beta_z U(\boldsymbol{z})\big) \quad \text{with} \quad U(\boldsymbol{z}) = \sum_{j\sim l} I(z_j = z_l) \quad [3.9]$$

where $W(\beta_z)$ is a normalizing constant. Using this kind of prior forces the neighbouring voxels to belong to the same HRF group and thus to share the same HRF pattern.

The set of all parameters will be denoted by $\boldsymbol{\Theta} = \big\{\boldsymbol{\Gamma}, \boldsymbol{L}, \boldsymbol{\theta}_a, \beta_z, \sigma_h^2, (\bar{\boldsymbol{h}}_k, \nu_k)_{1\leq k\leq K}\big\}$. The graphical model in Fig. 3.2 illustrates the dependencies between the latent and observed variables in the JPDE model.

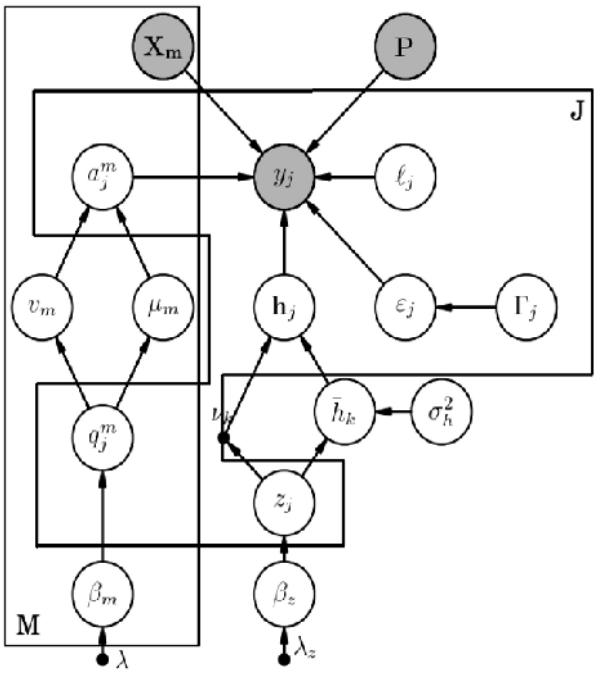

Figure 3.2: Graphical model describing dependencies between latent and observed variables involved in the JPDE generative model for a given parcel $\boldsymbol{\mathcal{P}}$ with J voxels.

3.2.3 Variational expectation maximization estimation

Computing closed form expressions of the Bayesian estimators associated with the posterior distribution $p(\ \boldsymbol{A}, \boldsymbol{H}, \boldsymbol{Q}, \boldsymbol{z}\ \mid\ \boldsymbol{Y}; \boldsymbol{\Theta})$ is difficult and intractable for the JPDE model. In this case, different approaches can be investigated for estimating the unknown parameters $\boldsymbol{A}, \boldsymbol{H}, \boldsymbol{Q}, \boldsymbol{z}$ and the vector $\boldsymbol{\Theta}$ from its posterior distribution. The first approach consists of sampling the posterior distribution using Markov Chain Monte Carlo (MCMC) methods and building estimators using the generated samples. Another approach is based on the variational expectation maximization (VEM) principle that is less computationally intensive. A VEM algorithm was studied in (Chaari et al., 2012, 2015) to estimate the missing variables $\boldsymbol{A}$,$\boldsymbol{Q}$,$\boldsymbol{H}$, and $\boldsymbol{z}$. Approximate posterior distributions were computed for these missing variables by using an iterative algorithm which alternates maximization of the following free energy with respect to q and $\boldsymbol{\Theta}$

$$\mathcal{F}(q, \boldsymbol{\Theta}) \quad = \quad \mathrm{E}_q\big[\log p(\boldsymbol{Y}, \boldsymbol{A}, \boldsymbol{H}, \boldsymbol{Q}, \boldsymbol{z} \,|\, \boldsymbol{\Theta})\big] + \mathcal{G}(q) \qquad [3.10]$$

where $q \in \mathcal{D}$, $\mathcal{D}$ is the set of all probability distributions on $\mathcal{A} \times \mathcal{H} \times \mathcal{Q} \times \mathcal{Z}$ where $\mathcal{A}, \mathcal{H}, \mathcal{Q}, \mathcal{Z}$ are the probability spaces associated with $\boldsymbol{A}, \boldsymbol{H}, \boldsymbol{Q}, \boldsymbol{z}$ respectively and $\mathcal{G}(q) = -\mathrm{E}_q\big[\log q(\boldsymbol{A}, \boldsymbol{H}, \boldsymbol{Q}, \boldsymbol{z})\big]$ is the entropy of q. At the r-th iteration, the current value of the unknown parameters is denoted by $\boldsymbol{\Theta}^{(r-1)}$. The alternating procedure proceeds as follows

$$\textbf{E-step: } p^{(r)}_{A,H,Q,z} = \arg\max_{p \in \mathcal{D}} \ \mathcal{F}(p, \boldsymbol{\Theta}^{(r-1)}) \qquad [3.11]$$

$$\textbf{M-step: } \boldsymbol{\Theta}^{(r)} = \arg\max_{\Theta \in \underline{\boldsymbol{\Theta}}} \ \mathcal{F}(p^{(r)}_{A,H,Q,z}, \boldsymbol{\Theta}). \qquad [3.12]$$

As previously mentioned in (Chaari et al., 2013), this optimization procedure leads to an intractable posterior which is $p^{(r)}_{A,H,Q,z} = p(\boldsymbol{A}, \boldsymbol{H}, \boldsymbol{Q}, \boldsymbol{z} \,|\, \boldsymbol{Y}; \boldsymbol{\Theta}^{(r-1)})$. A variational approximation is therefore used in order to alternatively optimize the free energy with respect to p_H, p_A, p_Q and p_z while fixing the other distributions. The posterior distribution $p^{(r)}_{A,H,Q,z}$ is then approximated by the product of the distributions $\widetilde{p}^{(r)}_A(\boldsymbol{A}), \widetilde{p}^{(r)}_H(\boldsymbol{H}), \widetilde{p}^{(r)}_Q(\boldsymbol{Q})$ and $\widetilde{p}^{(r)}_z(\boldsymbol{z})$. The

resulting four E-steps can be written as follows

$$\textbf{VE-H:}\ \widetilde{p}_H^{(r)}(\boldsymbol{H}) \propto \exp\left(\mathrm{E}_{\widetilde{p}_A^{(r-1)}\widetilde{p}_z^{(r-1)}}\left[\log p(\boldsymbol{H}\,|\,\boldsymbol{Y},\boldsymbol{A},\boldsymbol{z};\boldsymbol{\Theta}^{(r-1)}\right]\right) \quad [3.13]$$

$$\textbf{VE-A:}\ \widetilde{p}_A^{(r)}(\boldsymbol{A}) \propto \exp\left(\mathrm{E}_{\widetilde{p}_H^{(r)}\widetilde{p}_Q^{(r-1)}}\left[\log p(\boldsymbol{A}\,|\,\boldsymbol{Y},\boldsymbol{H},\boldsymbol{Q};\boldsymbol{\Theta}^{(r-1)})\right]\right) \quad [3.14]$$

$$\textbf{VE-Q:}\ \widetilde{p}_Q^{(r)}(\boldsymbol{Q}) \propto \exp\left(\mathrm{E}_{\widetilde{p}_A^{(r)}}\left[\log p(\boldsymbol{Q}\,|\,\boldsymbol{Y},\boldsymbol{A};\boldsymbol{\Theta}^{(r-1)})\right]\right) \quad [3.15]$$

$$\textbf{VE-Z:}\ \widetilde{p}_z^{(r)}(\boldsymbol{z}) \propto \exp\left(\mathrm{E}_{\widetilde{p}_H^{(r)}}\left[\log p(\boldsymbol{z}\,|\,\boldsymbol{Y},\boldsymbol{H};\boldsymbol{\Theta}^{(r-1)})\right]\right)\ . \quad [3.16]$$

On the other hand, the M-step of the algorithm can be written as follows

$$\textbf{M:}\ \boldsymbol{\Theta}^{(r)} = \arg\max_{\boldsymbol{\Theta}}\ \mathrm{E}_{\widetilde{p}_A^{(r)}\widetilde{p}_H^{(r)}\widetilde{p}_Q^{(r)}\widetilde{p}_z^{(r)}}\left[\log p(\boldsymbol{Y},\boldsymbol{A},\boldsymbol{H},\boldsymbol{Q},\boldsymbol{z};\boldsymbol{\Theta})\right]\ . \quad [3.17]$$

Straightforward computations of [3.13]-[3.16] lead to the following results

(i) **VE-H** step:

This step is different from the one in the JDE model since it considers the voxel-dependent HRFs. Using [3.13] and standard algebra, $\widetilde{p}_{H_j}^{(r)}$ is shown to be a Gaussian distribution, *i.e*, $\widetilde{p}_{H_j}^{(r)} \sim \mathcal{N}(\boldsymbol{m}_{H_j}^{(r)}, \boldsymbol{\Sigma}_{H_j}^{(r)})$, where $\boldsymbol{\Sigma}_{H_j}^{(r)} = (\boldsymbol{V}_{1j} + \boldsymbol{V}_{2j})^{-1}$ and $\boldsymbol{m}_{H_j}^{(r)} = \boldsymbol{\Sigma}_{H_j}^{(r)}(\boldsymbol{m}_{1j} + \boldsymbol{m}_{2j})$ are defined for voxel $j = \{1, \ldots, J\}$ with

$$\begin{aligned}
\boldsymbol{V}_{1j} &= \sum_{m,m'} \upsilon_{A_j^m A_j^{m'}}^{(r-1)} \boldsymbol{X}_m^{\mathrm{t}} \boldsymbol{\Gamma}_j^{(r-1)} \boldsymbol{X}_{m'} + \widetilde{\boldsymbol{S}}_j^{\mathrm{t}} \boldsymbol{\Gamma}_j^{(r-1)} \widetilde{\boldsymbol{S}}_j, \\
\boldsymbol{V}_{2j} &= \sum_{k=1}^{K} \widetilde{p}_{z_j}(k)^{(r-1)} \bar{\boldsymbol{\Sigma}}_k^{(r-1)-1}, \\
\boldsymbol{m}_{1j} &= \widetilde{\boldsymbol{S}}_j^{\mathrm{t}} \boldsymbol{\Gamma}_j^{(r-1)} (\boldsymbol{y}_j - \boldsymbol{P}\boldsymbol{\ell}_j^{(r-1)}), \\
\boldsymbol{m}_{2j} &= \sum_{k=1}^{K} \bar{\boldsymbol{\Sigma}}_k^{(r-1)-1} \widetilde{p}_{z_j}(k)^{(r-1)} \bar{\boldsymbol{h}}_k^{(r-1)}
\end{aligned} \quad [3.18]$$

where $\widetilde{\boldsymbol{S}}_j = \sum_{m=1}^{M} m_{A_j^m}^{(r-1)} \boldsymbol{X}_m$. Note that $m_{A_j^m}^{(r-1)}$, $\upsilon_{A_j^m A_j^{m'}}^{(r-1)}$ denote the m and (m, m') entries of $\boldsymbol{m}_{A_j}^{(r-1)}$ and $\boldsymbol{\Sigma}_{A_j}^{(r-1)}$, respectively.

(ii) **VE-A** step : This step is similar to the VE-A step of (Chaari et al., 2013), except that it accounts for the fact that the HRF is voxel-dependent. Standard algebra is used to identify a Gaussian distribution in [3.14], (*i.e*, $\widetilde{p}_{A_j}^{(r)} \sim \mathcal{N}(\boldsymbol{m}_{A_j}^{(r)}, \boldsymbol{\Sigma}_{A_j}^{(r)})$, where

$$\begin{aligned}
\boldsymbol{\Sigma}_{A_j}^{(r)} &= \left(\sum_{i=1}^{I} \boldsymbol{\Delta}_{ij} + \widetilde{\boldsymbol{H}_j} \right)^{-1}, \\
\boldsymbol{m}_{A_j}^{(r)} &= \boldsymbol{\Sigma}_{A_j}^{(r)} \left(\sum_{i=1}^{I} \boldsymbol{\Delta}_{ij} \boldsymbol{\mu}_i^{(r-1)} + \widetilde{\boldsymbol{G}}^{\mathrm{t}} \boldsymbol{\Gamma}_j^{(r-1)} \big(\boldsymbol{y}_j - \boldsymbol{P} \boldsymbol{\ell}_j^{(r-1)} \big) \right). \qquad [3.19]
\end{aligned}$$

The computation of $\boldsymbol{\Sigma}_{A_j}^{(r)}$ and $\boldsymbol{m}_{A_j}^{(r)}$ in [3.19] requires to define a number of intermediate quantities. Denote as, $\boldsymbol{\mu}_i^{(r-1)} = \left[\mu_{i1}^{(r-1)}, \ldots, \mu_{iM}^{(r-1)} \right]^{\mathrm{t}}$ and $\widetilde{\boldsymbol{G}} = \mathrm{E}_{\widetilde{p}_H^{(r)}} \left[\boldsymbol{G} \right]$ where $\boldsymbol{G}$ is the matrix $\boldsymbol{G} = [\boldsymbol{g}_1 \,|\, \ldots \,|\, \boldsymbol{g}_M]$ whose columns are $\boldsymbol{g}_m = \boldsymbol{X}_m \boldsymbol{h}_j$. The m-th column of $\widetilde{\boldsymbol{G}}$ is denoted as $\widetilde{\boldsymbol{g}}_m = \boldsymbol{X}_m \boldsymbol{m}_{H_j}^{(r)} \in \mathbb{R}^N$. Then, $\boldsymbol{\Delta}_{ij} = \mathrm{diag}_M \left[\widetilde{p}_{Q_j^m}^{(r-1)}(i) / v_{im}^{(r-1)} \right]$ and $\widetilde{\boldsymbol{H}_j} = \mathrm{E}_{\widetilde{p}_{H_j}^{(r)}} \left[\boldsymbol{G}^{\mathrm{t}} \boldsymbol{\Gamma}_j^{(r-1)} \boldsymbol{G} \right]$ is an $M \times M$ matrix whose (m, m') element is

$$\begin{aligned}
\mathrm{E}_{\widetilde{p}_{H_j}^{(r)}} \left[\boldsymbol{g}_m^{\mathrm{t}} \boldsymbol{\Gamma}_j^{(r-1)} \boldsymbol{g}_{m'} \right] &= \mathrm{E}_{\widetilde{p}_{H_j}^{(r)}} \left[\boldsymbol{g}_m \right]^{\mathrm{t}} \boldsymbol{\Gamma}_j^{(r-1)} \mathrm{E}_{\widetilde{p}_{H_j}^{(r)}} \left[\boldsymbol{g}_{m'} \right] \\
&\quad + \mathrm{trace} \big(\boldsymbol{\Gamma}_j^{(r-1)} cov_{\widetilde{p}_{H_j}^{(r)}} (\boldsymbol{g}_m, \boldsymbol{g}_{m'}) \big) \\
&= \widetilde{\boldsymbol{g}}_m^{\mathrm{t}} \boldsymbol{\Gamma}_j^{(r-1)} \widetilde{\boldsymbol{g}}_{m'} + \mathrm{trace} \big(\boldsymbol{\Gamma}_j^{(r-1)} \boldsymbol{X}_m \boldsymbol{\Sigma}_{H_j}^{(r)} \boldsymbol{X}_{m'}^{\mathrm{t}} \big). \qquad [3.20]
\end{aligned}$$

(iii) **VE-Q** step: A product approximation is assumed such that $\widetilde{p}_Q(\boldsymbol{Q}) = \prod_{j=1}^{J} \widetilde{p}_{Q_j}(\boldsymbol{q}_j)$ with $\widetilde{p}_{Q_j}(\boldsymbol{q}_j) = \prod_{m=1}^{M} \widetilde{p}_{Q_j^m}(q_j^m)$. This step includes $M \times J$ sub-steps. Using [3.15], for $m = 1, \ldots, M$ and $j = 1, \ldots, J$, the following result is obtained

$$\widetilde{p}_{q_j^m}^{(r)}(q_j^m) \propto \exp \left(\mathrm{E}_{\widetilde{p}_A^{(r)} \widetilde{p}_{q^{\setminus m}}^{(r)} \widetilde{p}_{q_{\setminus j}^m}^{(r)}} \left[\log p \left(q_j^m \mid \boldsymbol{Y}, \boldsymbol{A}, \boldsymbol{q}_{\setminus j}^m, \boldsymbol{q}^{\setminus m}; \boldsymbol{\Theta}^{(r-1)} \right) \right] \right) \qquad [3.21]$$

where $\boldsymbol{q}^m_{\setminus j} = \{q^m_{j'}, j' \neq j\}$ and $\boldsymbol{q}^{\setminus m} = \{\boldsymbol{q}^{m'}, m' \neq m\}$. If we remove the terms which do not depend on q^m_j, [3.21] can be rewritten as

$$\widetilde{p}_{q^m_j}\left(q^m_j\right) \propto \exp\left(\mathrm{E}_{\widetilde{p}^{(r)}_{a^m_j}}\left[\log p(a^m_j \mid q^m_j; \mu^{(r-1)}_m, v^{(r-1)}_m)\right] + \mathrm{E}_{\widetilde{p}^{(r-1)}_{\boldsymbol{q}^m_{\setminus j}}}\left[\log p(q^m_j \mid \boldsymbol{q}^m_{\setminus j}; \beta^{(r-1)}_m)\right]\right) \quad [3.22]$$

With straightforward calculations, [3.22] can be rewritten as follows

$$\widetilde{p}_{q^m_j}\left(q^m_j\right) \propto \exp\left(-\frac{1}{2}\log v^{(r-1)}_{mq^m_j} - \frac{1}{2}\frac{\left(\boldsymbol{m}^{(r)}_{a^m_j} - \mu^{(r-1)}_{mq^m_j}\right)^2 + \boldsymbol{\Sigma}^{(r)}_{a^{(m,m)}_j}}{v^{(r-1)}_{mq^m_j}}\right) \times \exp\left(\beta^{(r-1)}_m \sum_{j' \in \boldsymbol{\mathcal{P}}, j' \sim j} \widetilde{p}^{(r-1)}_{q^m_{j'}}(q^m_j)\right). \quad [3.23]$$

Knowing that $q^m_j = i$, [3.23] reads

$$\widetilde{p}_{q^m_j}(i) \propto \mathcal{N}(\boldsymbol{m}^{(r)}_{a^m_j}; \mu^{(r-1)}_{mi}, v^{(r-1)}_{mi}) \times \exp\left(-\frac{1}{2}\frac{\boldsymbol{\Sigma}^{(r-1)}_{a^{(m,m)}_j}}{v^{(r-1)}_{mi}} + \beta^{(r-1)}_m \sum_{j' \in \boldsymbol{\mathcal{P}}, j' \sim j} \widetilde{p}^{(r-1)}_{q^m_{j'}}(i)\right). \quad [3.24]$$

(iv) **VE-Z** step: As in the VE-Q step, we also assume a product approximation $\tilde{p}_z(\boldsymbol{z}) = \prod_{j=1}^{J} \tilde{p}_{z_j}(z_j)$. This step includes J sub steps. Using [7.13], and for $j = 1, \ldots, J$ the following result is obtained

$$\tilde{p}_{z_j}(z_j) \propto \exp\left(\mathrm{E}_{\widetilde{p}^{(r)}_H \widetilde{p}^{(r-1)}_{\boldsymbol{z}_{\setminus j}}}\left[\log p\left(z_j \mid \boldsymbol{Y}, \boldsymbol{A}, \boldsymbol{z}_{\setminus j}, \boldsymbol{H}; \Theta^{(r-1)}\right)\right]\right). \quad [3.25]$$

After simplifying the right side of [3.25], we obtain

$$\tilde{p}_{z_j}(z_j) \propto \exp\left(\underbrace{\mathrm{E}_{\widetilde{p}_{H_j}}\left[\log p(h_j \mid z_j)\right]}_{A} + \underbrace{\mathrm{E}_{\widetilde{p}_{\boldsymbol{z}_{\setminus j}}}\left[\log p(\boldsymbol{z} \mid \beta_z)\right]}_{B}\right) \quad [3.26]$$

with

$$\begin{aligned} & \mathrm{E}_{\tilde{p}_{H_j}}\left[\log p(h_j \mid z_j)\right] = -\tfrac{D+1}{2}\log 2\pi - \tfrac{D+1}{2}\log \bar{\boldsymbol{\Sigma}}_k \\ - \; & \tfrac{1}{2\bar{\boldsymbol{\Sigma}}_k}\left[(m_{H_j} - \bar{\boldsymbol{h}}_k)^T(m_{H_j} - \bar{\boldsymbol{h}}_k) + \mathrm{trace}(\boldsymbol{\Sigma}_{H_j})\right] \end{aligned} \tag{3.27}$$

and

$$\mathrm{E}_{\tilde{p}_{\boldsymbol{z}_{\setminus j}}}\left[\log p(\boldsymbol{z} \mid \beta_z)\right] = \beta_z \sum_{l\sim j}\sum_{k=1}^{K} I(z_j = k)\tilde{p}_{z_l}(k) + C_3' \tag{3.28}$$

where $C_3' = \mathrm{E}_{\tilde{p}_{\boldsymbol{z}_{\setminus j}}}\left[C_3\right]$ and $C_3 = \log Z(\beta_z)^{-1} + \log p(\boldsymbol{z}_{\setminus j} \mid \beta_z)$. For $k = 1:K$, [3.25] can be written as

$$\begin{aligned} & \tilde{p}_{z_j}^{(r)}(z_j) \propto \mathcal{N}(\boldsymbol{m}_{H_j}; \bar{\boldsymbol{h}}_k^{(r-1)}, \bar{\boldsymbol{\Sigma}}_k^{(r-1)})\times \\ & \exp\left(-\frac{1}{2}\mathrm{trace}(\boldsymbol{\Sigma}_{H_j}^{(r)}\bar{\boldsymbol{\Sigma}}_k^{(r-1)-1}) + \beta_z^{(r-1)}\sum_{j'\sim j}\tilde{p}_{z_{j'}}^{(r-1)}(k)\right). \end{aligned} \tag{3.29}$$

(v) **VM** step: The M-steps involved in this VM step are associated with $(\boldsymbol{\mu}, \boldsymbol{v})$, $\boldsymbol{\beta}$, β_z, $\left(\bar{\boldsymbol{h}}, \nu\right)$, σ_h^2 and $(\boldsymbol{L}, \boldsymbol{\Gamma})$ as detailed below

(a) M-$(\boldsymbol{\mu}, \boldsymbol{v})$: Maximizing [3.17] w.r.t $(\boldsymbol{\mu}, \boldsymbol{v})$ yields

$$\left(\boldsymbol{\mu}^{(r)}, \boldsymbol{v}^{(r)}\right) = \arg\max_{(\boldsymbol{\mu},\boldsymbol{v})} \mathrm{E}_{\tilde{p}_A^{(r)}\tilde{p}_Q^{(r)}}\left[\log p(\boldsymbol{A} \mid \boldsymbol{Q}; \boldsymbol{\mu}, \boldsymbol{v})\right] \tag{3.30}$$

For $i \in \{0, 1\}$ and $m \in \{1, \ldots, M\}$ the following result is obtained

$$\begin{aligned} \mu_{mi} &= \sum_{j\in\mathcal{P}_\gamma} \tilde{p}_{q_j^m}^{(r)}(i) m_{a_j^m} / \tilde{p}_{mi}^{(r)}, \\ v_{mi}^{(r)} &= \sum_{j\in\mathcal{P}_\gamma} \tilde{p}_{q_j^m}^{(r)}(i)\left(\left(m_{a_j^m}^{(r)} - \mu_{mi}^{(r)}\right)^2 + v_{a_j^m a_j^m}\right) / \tilde{p}_{mi}^{(r)} \end{aligned} \tag{3.31}$$

where $\tilde{p}_{mi}^{(r)} = \sum_{j\in\mathcal{P}_\gamma} \tilde{p}_{q_j^m}^{(r)}(i)$.

(b) M-$\boldsymbol{\beta}$: Maximizing with respect to $\boldsymbol{\beta}$, [3.17] reads

$$\boldsymbol{\beta}^{(r)} = \arg\max_{\boldsymbol{\beta}} \mathrm{E}_{\tilde{p}_Q^{(r)}}\left[\log p(\boldsymbol{Q}; \boldsymbol{\beta})\right]. \tag{3.32}$$

Using the mean-field approximation (Celeux et al., 2003) leads to a function that can be optimized using a gradient algorithm. To avoid overestimation of $\boldsymbol{\beta}$, an exponential prior with mean λ_{β_m} can be used to penalize each β_m. The expression used to optimize for the m-th component of $\boldsymbol{\beta}$ denoted as β_m is

$$\begin{aligned}\beta_m^{(r)} &= \arg\max_{\beta_m} \mathrm{E}_{\tilde{p}_Q^{(r)}}\left[\log p(\boldsymbol{q}^m;\beta_m)p(\beta_m;\lambda_{\beta_m})\right], \\ &= \arg\max_{\beta_m}\Bigg(-\log Z(\beta_m) + \\ &\beta_m\Big(\sum_{j\sim k}\mathrm{E}_{\tilde{p}_{Q^{m(r)}}}\left[I\left(q_j^m = q_k^m\right)\right] - \lambda_{\beta_m}\Big)\Bigg). \end{aligned} \quad [3.33]$$

(c) M-$(\boldsymbol{L},\boldsymbol{\Gamma})$: Maximizing with respect to $(\boldsymbol{L},\boldsymbol{\Gamma})$ and factorizing over voxels $j\in\mathcal{P}$, the following expression needs to be computed

$$\left(\boldsymbol{\ell}_j^{(r)},\boldsymbol{\Gamma}_j^{(r)}\right) = \arg\max_{(\boldsymbol{\ell}_j,\boldsymbol{\Gamma}_j)} \mathrm{E}_{\tilde{p}_{H_\gamma}\tilde{p}_{A_j}}\left[\log p(\boldsymbol{y}_j \mid \boldsymbol{a}_j,\boldsymbol{h}_\gamma;\boldsymbol{\ell}_j,\boldsymbol{\Gamma}_j)\right], \quad [3.34]$$

where $\boldsymbol{a}_j = \{a_j^m, m=1,\ldots,M\}$. Maximizing w.r.t $\boldsymbol{\ell}_j$ leads to the following result

$$\boldsymbol{\ell}_j^{(r)} = \arg\max_{\boldsymbol{\ell}_j}\left(2\left(\tilde{\boldsymbol{G}}\boldsymbol{m}_{A_j}^{(r)} - \boldsymbol{y}_j\right)^{\mathrm{t}}\boldsymbol{\Gamma}_j^{(r)}\boldsymbol{P}\boldsymbol{\ell}_j + \boldsymbol{\ell}_j^{\mathrm{t}}\boldsymbol{P}^{\mathrm{t}}\boldsymbol{\Gamma}_j^{(r)}\boldsymbol{P}\boldsymbol{\ell}_j\right) \quad [3.35]$$

where the term $\tilde{\boldsymbol{G}}$ has been defined in the VE-A step. Computing the derivative w.r.t $\boldsymbol{\ell}_j$ yields the following expression $\boldsymbol{\ell}_j = \left(\boldsymbol{P}^{\mathrm{t}}\boldsymbol{\Lambda}_j^{(r)}\boldsymbol{P}\right)\boldsymbol{P}^{\mathrm{t}}\boldsymbol{\Gamma}_j^{(r)}\left(\boldsymbol{y}_j - \tilde{\boldsymbol{G}}\boldsymbol{m}_{A_j}^{(r)}\right)$, with $\boldsymbol{\Gamma}_j = \sigma_j^{-2}\boldsymbol{\Lambda}_j$. In the case of an AR(1) noise

$$\boldsymbol{\ell}_j^{(r)} = \left(\boldsymbol{P}^{\mathrm{t}}\boldsymbol{\Lambda}_j^{(r)}\boldsymbol{P}\right)^{-1}\boldsymbol{P}^{\mathrm{t}}\boldsymbol{\Lambda}_j^{(r)}\left(\boldsymbol{y}_j - \tilde{\boldsymbol{S}}_j\boldsymbol{m}_{H_\gamma}^{(r)}\right) = F_1(\rho_j^{(r)}). \quad [3.36]$$

In the above expression, F_1 is a function linking the estimates $\boldsymbol{\ell}_j^{(r)}$ and $\rho_j^{(r)}$. Denoting $\boldsymbol{y}_j^{(r)} = \boldsymbol{y}_j - \boldsymbol{P}\boldsymbol{\ell}_j^{(r)}$ and considering the maximization w.r.t σ_j^2, we obtain

$$\sigma_j^{2(r)} = \frac{1}{N}\left(\mathrm{E}_{\widetilde{p}_{A_j}^{(r)}}\left[\boldsymbol{a}_j^{\mathrm{t}}\tilde{\boldsymbol{\Lambda}}_j^{(r)}\boldsymbol{a}_j\right] - 2\boldsymbol{m}_{A_j}^{(r)^{\mathrm{t}}}\tilde{\boldsymbol{G}}\boldsymbol{\Lambda}_j^{(r)}\boldsymbol{y}_j^{(r)} + \boldsymbol{y}_j^{(r)^{\mathrm{t}}}\boldsymbol{\Lambda}_j^{(r)}\boldsymbol{y}_j^{(r)}\right),$$
$$= F_2\left(\rho_j^{(r)}, \boldsymbol{\ell}_j^{(r)}\right) \quad [3.37]$$

where F_2 is a function linking the estimates $\sigma_j^{2(r)}$ with $\boldsymbol{\ell}_j^{(r)}$ and $\rho_j^{(r)}$. The Matrix $\tilde{\boldsymbol{\Lambda}}_j = \mathrm{E}_{\widetilde{p}_{H_\gamma}}\left[\boldsymbol{G}^{\mathrm{t}}\boldsymbol{\Lambda}_j^{(r)}\boldsymbol{G}\right]$ is an $M \times M$ matrix similar to the matrix $\widetilde{\boldsymbol{H}}_j$ in the VE-A step. The (m, m') entry of this matrix is given by $\widetilde{\boldsymbol{g}}_m^{\mathrm{t}}\boldsymbol{\lambda}_j^{(r)}\widetilde{\boldsymbol{g}}_{m'} + \mathrm{trace}(\boldsymbol{\Lambda}_j^{(r)}\boldsymbol{X}_m\boldsymbol{\Sigma}_{H_\gamma}^{(r)}\boldsymbol{X}_m'^{\,\mathrm{t}})$.
The maximization w.r.t ρ_j yields

$$\rho_j^{(r)} = \arg\max_{\rho_j}\{\left(\mathrm{trace}\left(\boldsymbol{U}_1\widetilde{\Lambda}_j\right) + \mathrm{trace}\left(\boldsymbol{U}_2\Lambda_j\right)\right)/\sigma_j^{2(r)} + \log|\Lambda_j|\} \quad [3.38]$$

with $|\Lambda_j| = 1 - \rho_j^2$ and $\widetilde{\Lambda}_j$ has the same expression as for $\widetilde{\boldsymbol{\Lambda}}_j^{(r)}$. The matrix $\boldsymbol{U}_1 = \Sigma_{A_j}^{(r)} + \boldsymbol{m}_{A_j}^{(r)}\boldsymbol{m}_{A_j}^{(r)^{\mathrm{t}}}$ is of size $M \times M$ while $\boldsymbol{U}_2 = \boldsymbol{y}_j^{(r)}\left(\boldsymbol{y}_j^{(r)} + 2\widetilde{\boldsymbol{G}}\boldsymbol{m}_{A_j}^{(r)}\right)^{\mathrm{t}}$ is of size $N \times N$. The derivative of the matrix Λ_j can be written as $\Lambda_j' = 2\rho_j\boldsymbol{B} + \boldsymbol{C}$, where all entries of $\boldsymbol{B}$ and $\boldsymbol{C}$ are zeros except $(\boldsymbol{B})_{n,n} = 1$ for $n = 2, \ldots, N-1$ and $(\boldsymbol{C})_{n,n+1} = (\boldsymbol{C})_{n+1,n} = -1$ for $n = 1, \ldots, N-1$. The matrix $\widetilde{\Lambda}_j'$ can be written as $\widetilde{\Lambda}_j' = 2\rho_j\widetilde{\boldsymbol{B}} + \widetilde{\boldsymbol{C}}$ where $\widetilde{\boldsymbol{B}}$ and $\widetilde{\boldsymbol{C}}$ are $M \times M$ matrices whose entries (m, m') are respectively
$(\widetilde{\boldsymbol{B}})_{m,m'} = \mathrm{trace}\left(\left(\boldsymbol{X}_m\boldsymbol{\Sigma}_{H_\gamma}^{(r)}\boldsymbol{X}_m^{\,\mathrm{t}} + \widetilde{\boldsymbol{g}}_{m'}\widetilde{\boldsymbol{g}}_m^{\mathrm{t}}\right)\boldsymbol{B}\right)$ and
$(\widetilde{\boldsymbol{C}})_{m,m'} = \mathrm{trace}\left(\left(\boldsymbol{X}_m\boldsymbol{\Sigma}_{H_\gamma}^{(r)}\boldsymbol{X}_m^{\,\mathrm{t}} + \widetilde{\boldsymbol{g}}_{m'}\widetilde{\boldsymbol{g}}_m^{\mathrm{t}}\right)\boldsymbol{C}\right)$. The derivative w.r.t ρ_j leads to
$\rho_j^{(r)} = \frac{1-\rho_j^{(r)}}{\sigma_j^{2(r)}}\left(2\rho_j^{(r)}\left(\mathrm{trace}\left(\boldsymbol{U}_1\widetilde{\boldsymbol{B}}\right) + \mathrm{trace}\left(\boldsymbol{U}_2\boldsymbol{B}\right)\right) + \mathrm{trace}\left(\boldsymbol{U}_1\widetilde{\boldsymbol{C}}\right)\right.$
$\left. + \mathrm{trace}\left(\boldsymbol{U}_2\boldsymbol{C}\right)\right) = F_3\left(\rho_j^{(r)}, \sigma_j^{2(r)}\right)$, which is the following fixed-point equation $\rho_j^{(r)} = F_3\left(\rho_j^{(r)}, F_2\left(\rho_j^{(r)}, F_1(\rho_j^{(r)})\right)\right)$.

(d) M-β_z: Maximizing [3.17] with respect to β_z yields

$$\beta_z^{(r)} = \arg\max_{\beta_z} \mathrm{E}_{\widetilde{p}_z^{(r)}}\left[\log p\left(\boldsymbol{z}; \beta_z\right)\right]. \quad [3.39]$$

In order to avoid high values of β_z that can lead to over-spatial regularization, β_z is assigned a priori to an exponential distribution, yielding

$$\beta_z^{(r)} = \arg\max_{\beta_z} \mathrm{E}_{\widetilde{p}_z^{(r)}}\left[\log p\left(\boldsymbol{z};\beta_z\right)\right] + \log p\left(\beta_z;\lambda_z\right) \qquad [3.40]$$

where λ_{β_z} is the parameter of the exponential prior. An iterative procedure can be used to reach the optimal value of β_z by approximating the gradient as

$$\nabla_{\beta_z} \approx \sum_{(j,j')\in\boldsymbol{\mathcal{V}}^2, j\ j'} \sum_{k=1:K} \left(\widetilde{p}_{z_j}^{(r)}(k)\widetilde{p}_{z_{j'}}^{(r)}(k) - p_{z_j}^{MF}(k;\beta_z)p_{z_{j'}}^{MF}(k;\beta_z)\right) - \lambda_{\beta_z}, \qquad [3.41]$$

$$p_{z_j}^{MF}\left(z_j = k;\beta_z\right) = \frac{\exp\left(\beta_z \sum\limits_{j'\in\boldsymbol{\mathcal{V}}, j'\ j} \widetilde{p}_{z_{j'}}^{(r)}(k)\right)}{\sum\limits_{l=1:K} \exp\left(\beta_z \sum\limits_{j'\in\boldsymbol{\mathcal{V}}, j'\ j} \widetilde{p}_{z_{j'}}^{(r)}(k)\right)}. \qquad [3.42]$$

(e) M-$\left(\sigma_h^2, \bar{\boldsymbol{h}}, \boldsymbol{\nu}\right)$:

$$\left(\sigma_h^{2(r)}, \bar{\boldsymbol{h}}^{(r)}, \boldsymbol{\nu}^{(r)}\right) = \arg\max_{\sigma_h^2, \bar{\boldsymbol{h}}, \boldsymbol{\nu}} \mathrm{E}_{\widetilde{p}_H^{(r)}\widetilde{p}_z^{(r)}}\left[\log p\left(\boldsymbol{H} \mid \boldsymbol{z}; \bar{\boldsymbol{h}}, \boldsymbol{\nu}\right)\right] + \log p\left(\bar{\boldsymbol{h}}; \sigma_h^2\right). \qquad [3.43]$$

Maximizing w.r.t $\boldsymbol{\nu}_k$ for a given k yields

$$\boldsymbol{\nu}_k = \frac{\sum\limits_{j\in\boldsymbol{\mathcal{V}}} \widetilde{p}_{z_j}^{(r)}(k)\left(\mathrm{trace}\left(\boldsymbol{\Sigma}_{H_j}^{(r)}\right) + \left(\boldsymbol{m}_{H_j}^{(r)} - \bar{\boldsymbol{h}}_k\right)^{\mathrm{t}}\left(\boldsymbol{m}_{H_j}^{(r)} - \bar{\boldsymbol{h}}_k\right)\right)}{(D+1)\sum\limits_{j\in\boldsymbol{\mathcal{V}}} \widetilde{p}_{z_j}^{(r)}(k)}. \qquad [3.44]$$

Maximizing w.r.t $\bar{\boldsymbol{h}}_k$ for a given k yields

$$\bar{\boldsymbol{h}}_k = \left(\boldsymbol{I}_{D+1} + \frac{\nu_k \boldsymbol{R}^{-1}/\sigma_h^2}{\sum\limits_{j\in\boldsymbol{\mathcal{V}}} \widetilde{p}_{z_j}^{(r)}(k)}\right)^{-1} \left(\frac{\sum\limits_{j\in\boldsymbol{\mathcal{V}}} \widetilde{p}_{z_j}^{(r)}(k)\boldsymbol{m}_{H_j}^{(r)}}{\sum\limits_{j\in\boldsymbol{\mathcal{V}}} \widetilde{p}_{z_j}^{(r)}(k)}\right). \qquad [3.45]$$

The updated values of $\boldsymbol{\nu}_k^{(r)}$ and $\bar{\boldsymbol{h}}_k^{(r)}$ can be finally used to update the value of σ_h^2

$$\sigma_h^{2(r)} = \frac{\sum_{k=1}^{K} \bar{\boldsymbol{h}}_k^{(r)^{\mathrm{t}}} \boldsymbol{R}^{-1} \bar{\boldsymbol{h}}_k^{(r)}}{K}. \qquad [3.46]$$

3.3 Variational model selection procedure for the JPDE model

3.3.1 JPDE model selection

As stated in Section 3.1, selecting the number of parcels (K) is a challenging issue when analyzing fMRI data using the JPDE model. We propose here an automatic model selection procedure that allows the estimation of the number of useful parcels based on the calculated free energy ($\mathcal{F}$). It has been clearly stated in (Attias, 2000) that, when data is large enough, the free energy corresponds precisely to the Bayesian information criterion (BIC) and the minimum description length criterion (MDL) (Chickering and Heckerman, 1997). Calculating the free energy allows therefore model selection according to these popular criteria. This section details this technique proposed in (Albughdadi et al., 2014), which is the first contribution of this PhD thesis. If we consider Ω different candidate models, the number of parcels associated with these models will be denoted by K^ω where $\omega \in \{1, ..., \Omega\}$. In this section, we use different notations for the parameters $\boldsymbol{\Psi}$ and the hyperparameters $\boldsymbol{\Phi}$ where $\Psi = \{\bar{\boldsymbol{h}}, \beta_z, \boldsymbol{\beta}\}$ and $\boldsymbol{\Phi} = \{\boldsymbol{L}, \boldsymbol{\Gamma}, \boldsymbol{\mu}, \boldsymbol{\upsilon}, \boldsymbol{\nu}, \boldsymbol{\gamma}, \gamma_z, \sigma_h^2\}$. After running the adopted VEM algorithm, for each model order we obtain estimated posteriors denoted as $\tilde{p}_A^{(\infty)}, \tilde{p}_H^{(\infty)}, \tilde{p}_Q^{(\infty)}, \tilde{p}_z^{(\infty)}$ and point estimates $\boldsymbol{\Psi}^{(\infty)}$, $\boldsymbol{\Phi}^{(\infty)}$.

Following (Albughdadi et al., 2014), we refer to the model ω by writing p_x^ω instead of $\tilde{p}_x^{(\infty)}$ for $x \in \{\boldsymbol{A}, \boldsymbol{H}, \boldsymbol{Q}, \boldsymbol{z}\}$. The free energy in [3.10] can then be defined as

$$\mathcal{F}(p^\omega, \boldsymbol{\Psi}^\omega, \boldsymbol{\Phi}^\omega) = \mathrm{E}_{p^\omega}\left[\log p(\boldsymbol{Y}, \boldsymbol{A}, \boldsymbol{Q}, \boldsymbol{H}, \boldsymbol{z}, \boldsymbol{\Psi}^\omega; \boldsymbol{\Phi}^\omega)\right] + \mathcal{G}(p^\omega) \qquad [3.47]$$

where p^ω is the factorized posterior approximation

$$p^\omega(\boldsymbol{A}, \boldsymbol{Q}, \boldsymbol{H}, \boldsymbol{z}) = p_A^\omega(\boldsymbol{A}) p_Q^\omega(\boldsymbol{Q})\ p_H^\omega(\boldsymbol{H})\ p_z^\omega(\boldsymbol{z}). \qquad [3.48]$$

The free energy in [3.47] can therefore be rewritten as

$$\begin{aligned}\mathcal{F}(p^{\omega}, \boldsymbol{\Psi}^{\omega}, \boldsymbol{\Phi}^{\omega}) = & \mathrm{E}_{p_A^{\omega} p_H^{\omega}}\left[\log p(\boldsymbol{Y} \mid \boldsymbol{A}, \boldsymbol{H}; \boldsymbol{\Phi}^{\omega})\right] + \mathrm{E}_{p_A^{\omega} p_Q^{\omega}}\left[\log p(\boldsymbol{A} \mid \boldsymbol{Q}; \boldsymbol{\Phi}^{\omega})\right] \\ & + \mathrm{E}_{p_Q^{\omega}}\left[\log p(\boldsymbol{Q} | \boldsymbol{\beta}^{\omega})\right] + \mathrm{E}_{p_H^{\omega} p_z^{\omega}}\left[\log p(\boldsymbol{H} \mid \boldsymbol{z}, \bar{\boldsymbol{h}}^{\omega}; \boldsymbol{\Phi}^{\omega})\right] \\ & + \mathrm{E}_{p_z^{\omega}}\left[\log p(\boldsymbol{z} | \beta_z^{\omega})\right] + \log p(\bar{\boldsymbol{h}}^{\omega}; \boldsymbol{\Phi}^{\omega}) + \log p(\boldsymbol{\beta}^{\omega}; \boldsymbol{\Phi}^{\omega}) \\ & + \log p(\beta_z^{\omega}; \boldsymbol{\Phi}^{\omega}) + \mathcal{G}(p_A^{\omega}) + \mathcal{G}(p_Q^{\omega}) + \mathcal{G}(p_H^{\omega}) + \mathcal{G}(p_z^{\omega}). \end{aligned} \quad [3.49]$$

Each of the above terms can be calculated from the outputs of the VEM algorithm based on the estimated posteriors and hyperparameters. [1] In what follows, detailed computations of the free energy terms in [3.49] are provided. These terms are computed after convergence of the JPDE VEM model.

(i) $\mathrm{E}_{p_A^{\omega} p_H^{\omega}}\left[\log p(\boldsymbol{Y} \mid \boldsymbol{A}, \boldsymbol{H}; \boldsymbol{\Phi}^{\omega})\right]$
This term corresponds to $E_{p_A^{\omega} p_H^{\omega}}\left[\log p(\boldsymbol{Y} \mid \boldsymbol{A}, \boldsymbol{H}; \boldsymbol{L}^{\omega}, \boldsymbol{\Gamma}^{\omega})\right]$ and can be computed as follows

$$\begin{aligned} & E_{p_A^{\omega} p_H^{\omega}}\left[\log p(\boldsymbol{Y} \mid \boldsymbol{A}, \boldsymbol{H}; \boldsymbol{L}^{\omega}, \boldsymbol{\Gamma}^{\omega})\right] = -\frac{NJ}{2}\log 2\pi + \frac{J}{2}\log|\boldsymbol{\Lambda}_j| - N\sum_{j=1}^{J}\log\sigma_j \\ & + \sum_{j}^{J} \boldsymbol{m}_{H_j}^{\mathrm{t}}\Big(\sum_{m=1}^{M} m_{A_j^m} \boldsymbol{X}^{m\mathrm{t}} \boldsymbol{\Gamma}_j^{\omega}(\boldsymbol{y}_j - \boldsymbol{P}\boldsymbol{\ell}_j)\Big) - \frac{1}{2}\sum_{j=1}^{J}(\boldsymbol{y}_j - \boldsymbol{P}\boldsymbol{\ell}_j)^{\mathrm{t}}\boldsymbol{\Gamma}_j^{\omega}(\boldsymbol{y}_j - \boldsymbol{P}\boldsymbol{\ell}_j) \\ & - \frac{1}{2}\sum_{j=1}^{J}\sum_{m,m'}\Big\{\Big(m_{A_j^m} m_{A_j^{m'}} + \upsilon_{A_j^m A_j^{m'}}\Big) \\ & \times \Big[\boldsymbol{m}_{H_j}^{\mathrm{t}} \boldsymbol{X}^{m\mathrm{t}} \boldsymbol{\Gamma}_j^{\omega} \boldsymbol{X}^{m'} \boldsymbol{m}_{H_j} + trace\left(\boldsymbol{\Sigma}_{H_j} \boldsymbol{X}^{m\mathrm{t}} \boldsymbol{\Gamma}_j^{\omega} \boldsymbol{X}^{m'}\right)\Big]\Big\} \end{aligned} \quad [3.50]$$

(ii) $\mathrm{E}_{p_A^{\omega} p_Q^{\omega}}\left[\log p(\boldsymbol{A} \mid \boldsymbol{Q}; \boldsymbol{\Phi}^{\omega})\right]$
This term is equivalent to $E_{p_A^{\omega} p_Q^{\omega}}\left[\log p(\boldsymbol{A} \mid \boldsymbol{Q}, \boldsymbol{\mu}^{\omega}, \boldsymbol{v}^{\omega})\right]$. Straightforward calculations lead to the following equation

[1] This free energy has to be calculated once the convergence of the VEM algorithm has been reached for each model. The best model is therefore the one associated with the highest free energy value.

$$E_{p_A^\omega p_Q^\omega}\left[\log p(\boldsymbol{A}\,|\,\boldsymbol{Q},\boldsymbol{\mu},\boldsymbol{v})\right]$$
$$= \sum_{m=1}^{M}\sum_{j=1}^{J}\left\{\left[1-p_{q_j^m}^\omega(1)\right]\left[\log\frac{1}{\sqrt{2\pi v_{m0}^\omega}} - \frac{(m_{A_j^m}-\mu_{m0}^\omega)^2 + v_{A_j^m A_j^{m'}}}{2v_{m0}^\omega}\right]\right.$$
$$\left. + p_{q_j^m}^\omega(1)\left[\log\frac{1}{\sqrt{2\pi v_{m1}^\omega}} - \frac{(m_{A_j^m}-\mu_{m1}^\omega)^2 + v_{A_j^m A_j^{m'}}}{2v_{m1}^\omega}\right]\right\} \quad [3.51]$$

(iii) $\mathrm{E}_{p_Q^\omega}\left[\log p(\boldsymbol{Q}|\boldsymbol{\beta}^\omega)\right]$
Using straightforward calculations we obtain

$$E_{p_Q^\omega}\left[\log p(\boldsymbol{Q}\,|\,\boldsymbol{\beta}^\omega)\right] = \sum_{m=1}^{M}\left\{-\log W(\beta_m^\omega) + \beta_m^\omega E_{p_{\boldsymbol{q}^m}}\left[U(\boldsymbol{q}^m)\right]\right\} \quad [3.52]$$

with

$$E_{p_{Q^m}}[U(\boldsymbol{q}^m)] = \frac{1}{2}\sum_{j=1}^{J}\sum_{l\sim j}E_{p_{Q_j^m}p_{Q_l^m}}\left[I(q_j^m = q_l^m)\right],$$
$$= \frac{1}{2}\sum_{j}\sum_{l\sim j}\sum_{i=0}^{1}p_{Q_j^m}^\omega(i)p_{Q_l^m}^\omega(i). \quad [3.53]$$

- **Computing $W(\beta_m^\omega)$:** Using a mean field approximation, we obtain

$$W(\beta_m^\omega) \simeq W_{mf}(\beta_m^\omega)\exp\left(\beta_m^\omega E_{p_{mf}}\left[U(\boldsymbol{q}^m) - U_{mf}(\boldsymbol{q}^m)\right]\right), \quad [3.54]$$

where $U_{mf}(\boldsymbol{q}^m)$,$W_{mf}(\beta_m^\omega)$ and p_{mf} have been derived in (Bakhous, 2013)

$$W(\beta_m^\omega) \simeq \prod_{j=1}^{J}\sum_{i=0}^{1}\exp\left(\beta_m^\omega\sum_{l\sim j}p_{Q_l^m}^\omega(i)\right)$$
$$\times\exp\left(\beta_m^\omega\sum_{j}\sum_{l\sim j}\sum_{i=0}^{1}\left[p_{mfj}(i)\left(\frac{p_{mfl}(i)}{2} - p_{Q_l^m}^\omega(i)\right)\right]\right) \quad [3.55]$$

with $P_{mfj}(i) = \dfrac{\exp\left(\beta_m^\omega\sum\limits_{l\sim j}p_{Q_l^m}^\omega(i)\right)}{\sum\limits_{i\in\{0,1\}}\exp\left(\beta_m^\omega\sum\limits_{l\sim j}p_{Q_l^m}^\omega(i)\right)}$.

(iv) $\mathrm{E}_{p_H^\omega p_z^\omega}\left[\log p(\boldsymbol{H} \mid \boldsymbol{z}, \bar{\boldsymbol{h}}^\omega; \boldsymbol{\Phi}^\omega)\right]$
This term is equivalent to $\mathrm{E}_{p_H^\omega p_z^\omega}\left[\log p(\boldsymbol{H} \mid \boldsymbol{z}, \bar{\boldsymbol{h}}^\omega; \boldsymbol{\nu}^\omega)\right]$ and can be computed as follows

$$
\begin{aligned}
&\mathrm{E}_{p_H^\omega p_z^\omega}\left[\log p(\boldsymbol{H} \mid \boldsymbol{z}, \bar{\boldsymbol{h}}^\omega; \boldsymbol{\nu}^\omega)\right] \\
&= \sum_{j=1}^{J}\sum_{k=1}^{K} p_{z_j}^\omega(k)\left(-\frac{D+1}{2}\log 2\pi - \frac{D+1}{2}\log \nu_k^\omega\right) \\
&- \sum_{j=1}^{J}\sum_{k=1}^{K} p_{z_j}^\omega(k)\left(\frac{1}{2\nu_k^\omega} E_{p_{H_j}}[(H_j - \bar{\boldsymbol{h}}_k^\omega)^T(H_j - \bar{\boldsymbol{h}}_k^\omega)]\right), \\
&= \sum_{j=1}^{J}\sum_{k=1}^{K} p_{z_j}^\omega(k)\left(-\frac{D+1}{2}\log 2\pi - \frac{D+1}{2}\log \nu_k^\omega\right) \\
&- \sum_{j=1}^{J}\sum_{k=1}^{K} p_{z_j}^\omega(k)\left(\frac{1}{2\nu_k^\omega}[(m_{H_j} - \bar{\boldsymbol{h}}_k^\omega)^T(m_{H_j} - \bar{\boldsymbol{h}}_k^\omega) + \mathrm{trace}(\boldsymbol{\Sigma}_{H_j})\right).
\end{aligned}
\tag{3.56}
$$

(v) $\mathrm{E}_{p_z^\omega}\left[\log p(\boldsymbol{z}|\beta_z^\omega)\right]$

$$
E_{p_z^\omega}\left[\log p(\boldsymbol{z} \mid \beta_z^\omega)\right] = -\log W^z(\beta_z^\omega) + \beta_z^\omega E_{p_z}\left[U(\boldsymbol{z})\right] \tag{3.57}
$$

with

$$
E_{p_z^\omega}[U(\boldsymbol{z})] = \frac{1}{2}\sum_{j=1}^{J}\sum_{l\sim j} E_{p_{z_j}p_{z_l}}[I(z_j = z_l)] = \frac{1}{2}\sum_{j=1}^{J}\sum_{l\sim j}\sum_{i=1}^{K} p_{z_j}^\omega(i) p_{z_l}^\omega(i).
$$

- **Computing $W^z(\beta_z^\omega)$:** Using a mean field approximation yields

$$
W^z(\beta_z^\omega) \simeq W_{mf}^z(\beta_z^\omega)\exp\left(\beta_z^\omega E_{p_{mf}}\left[U(\boldsymbol{z}) - U_{mf}(\boldsymbol{z})\right]\right) \tag{3.58}
$$

where $U_{mf}(\boldsymbol{z})$, $W_{mf}^z(\beta_z^\omega)$ and p_{mf} have been derived in (Bakhous, 2013)

$$W^z(\beta_z^\omega) \simeq \prod_{j=1}^{J}\sum_{i=1}^{K}\exp\left(\beta_z^\omega \sum_{l\sim j} p_{z_l}^\omega(i)\right) \times \exp\left(\beta_z^\omega \sum_{j=1}^{J}\sum_{l\sim j}\sum_{i=1}^{K}\left[p_{mfj}(i)\left(\frac{p_{mfl}(i)}{2} - p_{z_l}^\omega(i)\right)\right]\right) \quad [3.59]$$

with $P_{mfj}(i) = \dfrac{\exp\left(\beta_z^\omega \sum\limits_{l\sim j} p_{z_l}^\omega(i)\right)}{\sum\limits_{i\in\{1,\ldots,K\}} \exp\left(\beta_z^\omega \sum\limits_{l\sim j} q_{z_l}(i)\right)}$.

(vi) $\log p(\bar{\boldsymbol{h}}^\omega; \boldsymbol{\Phi}^\omega)$
This term corresponds to $\log p(\bar{\boldsymbol{h}}^\omega; \sigma_h^{2(\omega)})$ whose computation is summarized below

$$\log p(\bar{\boldsymbol{h}}^\omega; \sigma_h^{2(\omega)}) = \sum_{k=1}^{K} \log p(\bar{\boldsymbol{h}}_k^\omega; \sigma_h^{2(\omega)}) \quad [3.60]$$

where $p(\bar{\boldsymbol{h}}_k^\omega; \sigma_h^{2(\omega)})$ is a zero mean Gaussian distribution with covariance matrix $\sigma_h^{2(\omega)}\boldsymbol{R}$ and

$$\log p(\bar{\boldsymbol{h}}^\omega; \sigma_h^2) = \sum_{k=1}^{K} \log \mathcal{N}(\bar{\boldsymbol{h}}_k^\omega; 0, \sigma_h^2 \boldsymbol{R}). \quad [3.61]$$

(vii) $\log p(\boldsymbol{\beta}^\omega; \boldsymbol{\Phi}^\omega)$
This term is equivalent to $\log p(\boldsymbol{\beta}^\omega; \lambda^\omega)$, which is an exponential distribution with parameter λ^ω

$$\log p(\boldsymbol{\beta}^\omega; \lambda^\omega) = \lambda^\omega \exp(-\lambda^\omega \boldsymbol{\beta}^\omega), \quad [3.62]$$

where $\boldsymbol{\beta}^\omega \geqslant 0$.

(viii) $\log p(\beta_z^\omega; \boldsymbol{\Phi}^\omega)$
Following the same steps as above, this term is equivalent to $\log p(\beta_z^\omega; \lambda^\omega)$, which is also an exponential distribution with parameter λ_z^ω

$$\log p(\hat{\beta}_z; \lambda_z^\omega) = \lambda_z^\omega \exp(-\lambda_z^\omega \beta_z^\omega), \quad [3.63]$$

where $\beta_z^\omega \geqslant 0$.

(ix) $\mathcal{G}(p_A^\omega) = \sum_{j=1}^{J} \sum_{m=1}^{M} \mathcal{G}(p_{A_j^m}^\omega)$
To calculate this term, we use the expression of the Gaussian entropy yielding

$$\mathcal{G}(p_A^\omega) = \sum_{j=1}^{J} \sum_{m=1}^{M} \mathcal{G}(p_{a_j^m}^\omega) = \frac{1}{2} \sum_{j=1}^{J} \sum_{m=1}^{M} \log \left(\left| \Sigma_{a_j^m} \right| (2\pi e)^D \right). \quad [3.64]$$

(x) $\mathcal{G}(p_H^\omega) = \sum_{j=1}^{J} \mathcal{G}(p_{H_j}^\omega)$
The Gaussian entropy is used as well to calculate this term leading to

$$\mathcal{G}(p_H^\omega) = \sum_{j=1}^{J} \mathcal{G}(p_{H_j}^\omega) = \frac{1}{2} \sum_{j=1}^{J} \log \left(\left| \Sigma_{H_j} \right| (2\pi e)^D \right). \quad [3.65]$$

(xi) $\mathcal{G}(p_Q^\omega) = \sum_{j=1}^{J} \sum_{m=1}^{M} \mathcal{G}(p_{Q_j^m}^\omega)$
Using the definition of the entropy for a discrete random variable, the following results is obtained

$$\mathcal{G}(p_Q^\omega) = -\sum_{j=1}^{J} \sum_{m=1}^{M} p_{Q_j^m}^\omega \log_2 \left(p_{Q_j^m}^\omega \right). \quad [3.66]$$

(xii) $\mathcal{G}(p_z^\omega) = \sum_{j=1}^{J} \mathcal{G}(p_{z_j}^\omega)$
As for $\mathcal{G}(p_Q^\omega)$, we obtain

$$\mathcal{G}(p_z^\omega) = -\sum_{j} p_{z_j}^\omega \log_2 \left(p_{z_j}^\omega \right). \quad [3.67]$$

The resulting model selection procedure with the JPDE model is summarized in Algorithm 3.1.

3.3.2 Experimental validation

To validate the free energy model selection procedure, we performed numerical experiments for both synthetic and real data.

Algorithm 3.1 The model selection procedure for the JPDE model. The subscript (r) refers to the current iteration.

for the candidate model ω in $\boldsymbol{\Omega}$ **do**
  Initialization:
    $\tilde{p}_z^{(0)}(\boldsymbol{z})$ from the initial parcellation.
    $\tilde{p}_Q^{(0)}(\boldsymbol{Q})$ such that $\tilde{p}_{Q_j}^{(0)}(q_j^m) \in \{0, 1\}$.
    for all j **do**
      - $\boldsymbol{m}_{H_j}^{(0)}$ is initialized from the canonical HRF.
      - $\boldsymbol{m}_{A_j}^{(0)}$ is initialized with zeros.
    end for
    Initialize with some $\boldsymbol{\Theta}^{(0)}$.
  $r = 1$
  repeat
    Expectation step:
      Compute $\tilde{p}_H^{(r)}(\boldsymbol{H})$ according to [3.18].
      Compute $\tilde{p}_A^{(r)}(\boldsymbol{A})$ according to [3.19].
      Compute $\tilde{p}_Q^{(r)}(\boldsymbol{Q})$ according to [3.24]
      Compute $\tilde{p}_z^{(r)}(\boldsymbol{z})$ according to [3.26]-[3.28].
    Maximization step:
      Compute $\boldsymbol{\Theta}^{(r)}$ according to [3.30]-[3.46].
    set $r \leftarrow r + 1$
  until convergence
  Compute the free energy value using [3.49].
end for

(i) **Synthetic fMRI time series:**
Three experiments were conducted to validate the proposed model selection procedure. These experiments were denoted as Exp. 1, Exp. 2 and Exp. 3. For each experiment a different parcellation mask is considered with two, three and four parcels as shown in Fig. 3.3[top row]. Different HRF groups were considered each with $k^{\omega} = \omega + 1$ where $\omega \in$

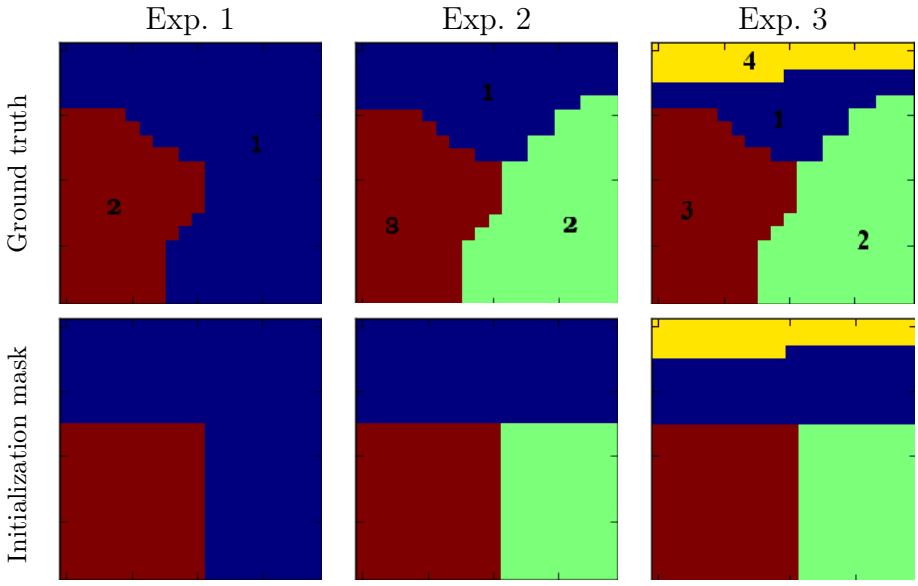

Figure 3.3: Ground truth parcellations used for the 3 experiments and corresponding initialization masks (grid size = 20×20).

$\{1, \ldots, 3\}$ and $\omega \in \Omega$. The HRFs associated with these groups were selected from the ground truth HRFs $\left(\bar{\boldsymbol{h}}_k\right)_{1<k\leq K}$ as shown in Fig. 3.4. Based on these reference parcellation, a BOLD signal was generated according to the observation model in [3.1] for each experiment (using the pyhrf software). Two experimental conditions ($M = 2$) were considered with 30 trials for each condition. The reference binary activation maps are of size 20×20 and are shown in Fig. 3.5. Given these labels, the NRLs were simulated from their prior conditionally to the activation labels $\boldsymbol{Q}$ as shown in Fig. 3.6. For $m = 0, 1 : a_j^m \mid q_j^m = 0 \sim \mathcal{N}(0, 0.5)$ and $a_j^m \mid q_j^m = 1 \sim \mathcal{N}(3.2, 0.5)$. The inter stimuli interval and variance used to generate the onsets of the trials were 3 s and 5 s, respectively. The other parameters were $TR = 1$ s and $\Delta t = 0.5$ s. Data resulting

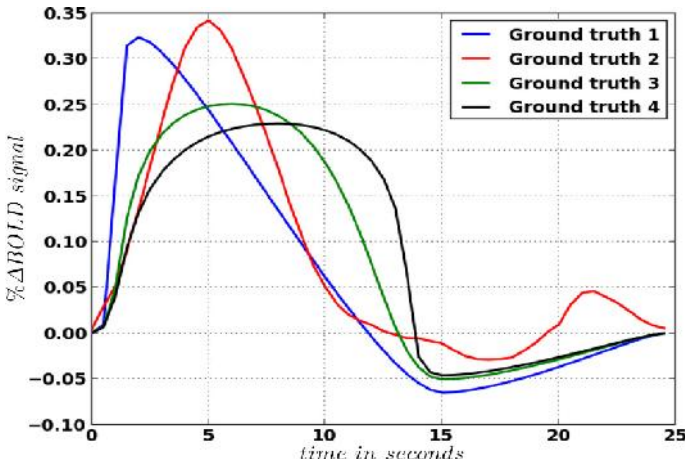

Figure 3.4: Ground truth HRF shapes ($\bar{h}_k, k = 1, \ldots, K^\omega$ with $\omega = \{1, \ldots, 3\}$) used for generating synthetic fMRI time series.

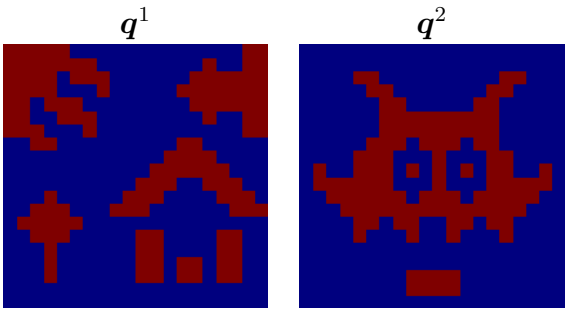

Figure 3.5: Reference activation labels for the two experimental conditions (grid size = 20×20).

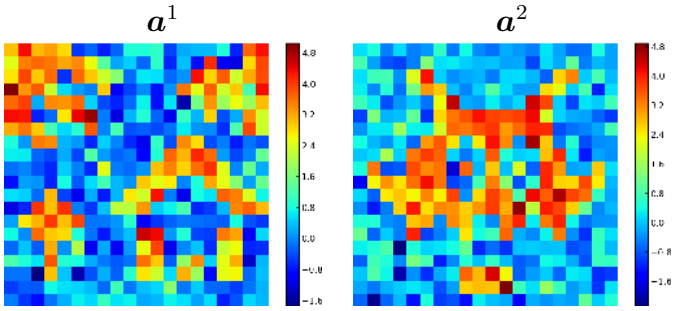

Figure 3.6: Reference NRLs for the two experimental conditions (grid size = 20×20).

for the three experiments were processed by the JPDE algorithm while performing model selection based on the proposed free energy. For each experiment, a set of $\Omega = 1, \ldots, 3$ models was investigated. The initial parcellation masks are shown in Fig. 3.3[bottom row]. After evaluating the free energies for all models, it turns out that the retained models were $\omega = 1$, $\omega = 2$ and $\omega = 3$ for Exp. 1, 2 and 3, respectively. The corresponding values of the free energy are provided in Tab. 3.2, where the highest value for each experiment appears in bold font. The parcellation estimates for the three experiments are shown in Fig. 3.7. This figure shows accurate parcellation estimates from a visual point of view. The estimated parcellation error probability for the selected model in each experiment is shown in Tab. 3.3.

Table 3.2: Evaluated free energy values for the three experiments and the three competing models. Bold values indicate the highest free energy.

Competing model	Exp.1	Exp.2	Exp.3
$\omega = 1$ (2 parcels)	**78614.04**	59459.32	6185.50
$\omega = 2$ (3 parcels)	77126.72	**86584.94**	83424.95
$\omega = 3$ (4 parcels)	78365.17	86492.43	**89146.02**

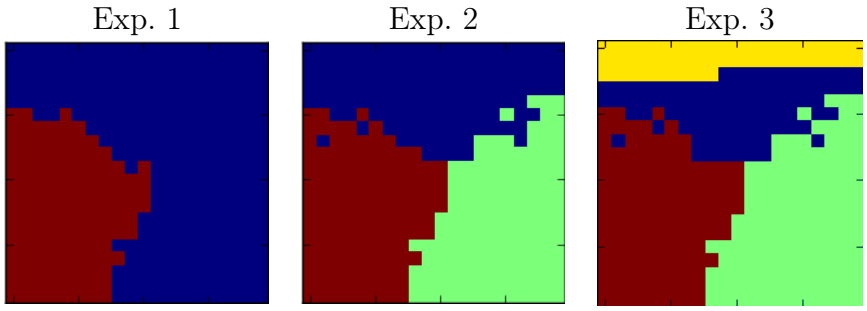

Figure 3.7: Parcellation estimates for the three experiments using the standard JPDE model with the variational model selection procedure (grid size = 20×20).

Quantitatively speaking, mean square error (MSE) values for NRL and activation labels estimates are reported in Tab. 3.4. The reported results shows a robust detection accuracy.

Fig. 3.8 shows the curve of the calculated free energy at each iteration for the three experiments. We can notice that the free energy is strictly

Table 3.3: The estimated error probabilities for the parcellation estimates using the standard JPDE model.

	Exp. 1	Exp. 2	Exp. 3
Error probability	1.5%	2.75%	3.25%

Table 3.4: Mean square error of NRLs and activation maps. The reported values correspond to the retained model in the three experiments.

		Exp.1	Exp.2	Exp.3
NRLs	$m = 1$	0.016	0.017	0.017
	$m = 2$	0.012	0.012	0.012
Labels	$m = 1$	0.0034	0.011	0.011
	$m = 2$	0.0026	0.0026	0.0027

monotonic and that it can be used as a stopping criteria for the VEM algorithm when the difference between the free energy values in the current and previous iterations is less than a predefined threshold.

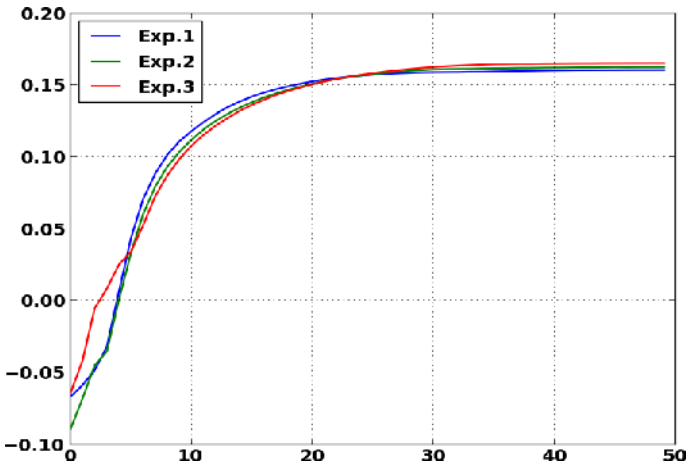

Figure 3.8: The curve of the normalized free energy calculated through the VEM iterations in the three synthetic experiments.

(ii) **Real data:**
A gradient-echo EPI (echo planar imaging) sequence (Echo Time=30ms / Repetition Time=2.4s / slice thickness = 3mm / Field Of View=192mm^2) was used to acquire the real fMRI data at 3T during a localizer experiment (Pinel et al., 2007). This paradigm involved sixty auditory, visual and motor stimuli, defined in ten experimental conditions ($M = 10$). During the used paradigm, 128 scans were acquired at a $2 \times 2 \times 3$mm^3 3D spatial resolution. Akin to the experiment conducted in (Chaari et al., 2012), we focus on the auditory condition that generates activations in the temporal lobe. Specifically, we focus on two bilateral temporal regions of interest (ROI) presented in Fig. 3.9 denoted as ROI 1 (left ROI) and ROI 2 (right ROI). $\Omega = 5$ different models were tested with $K^1 = 1$, $K^2 = 2$, $K^3 = 3$, $K^4 = 5$ and $K^5 = 8$. For each model, the initial parcellation was obtained by merging neighboring parcels obtained by applying the method of (Thirion et al., 2006). After running all the models separately and calculating the final free energies (see Tab. 3.5), it turns out that $\omega = 2$ (2 parcels) is the best model that fits the fMRI data. The initialization and estimated masks with the selected model are illustrated in Fig. 3.10[left column] and 3.10[right column], respectively. This figure shows the two estimated parcels. Fig. 3.11 also shows the estimated NRLs with the same model. These results are consistent with those obtained in (Chaari et al., 2012) where three parcels have been identified, two of them being very similar. In our results, these two parcels have been successfully merged in a two-parcel model.

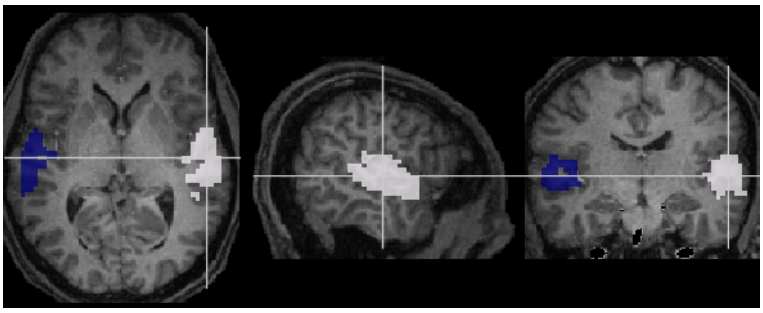

Figure 3.9: Anatomical localization of the bilateral temporal regions of interest.

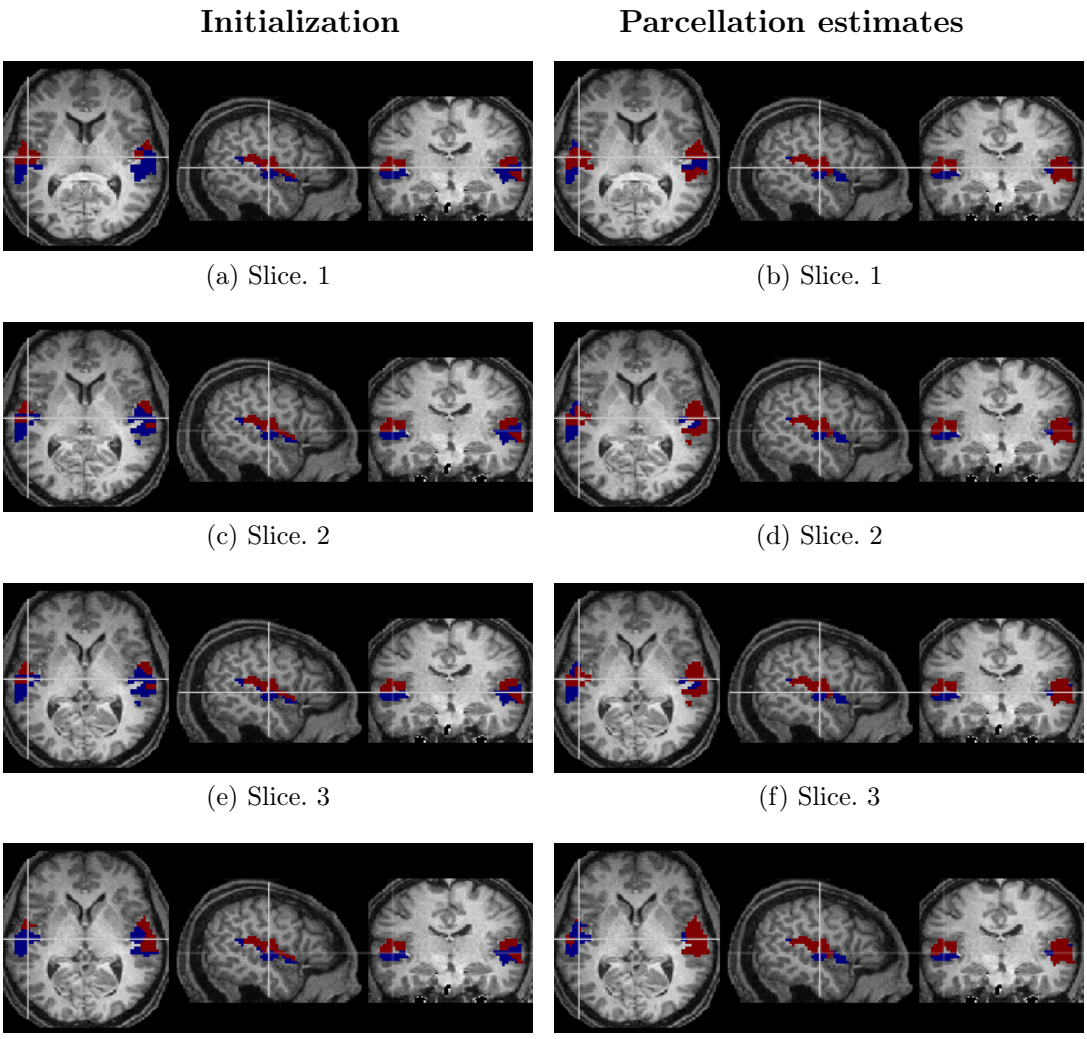

(a) Slice. 1 (b) Slice. 1

(c) Slice. 2 (d) Slice. 2

(e) Slice. 3 (f) Slice. 3

(g) Slice. 4 (h) Slice. 4

Figure 3.10: Consecutive slices of the initial parcellation (left column) and estimated parcellation (right column) for the two-parcels model selected by the variational model selection procedure.

Table 3.5: Evaluated free energy values for the 5 models tested on real data using the variational model selection procedure .

Competing model	ROI. 1	ROI. 2
$\omega = 1$ (1 par.)	-307292	-226216
$\omega = 2$ (2 par.)	**-306941**	**-224608**
$\omega = 3$ (3 par.)	-309810	-226127
$\omega = 4$ (5 par.)	-309580	-227406
$\omega = 5$ (8 par.)	-310089	-226571

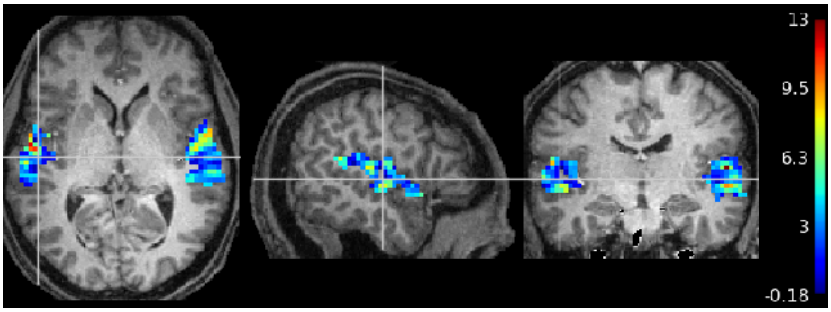

(a) Auditory experimental condition

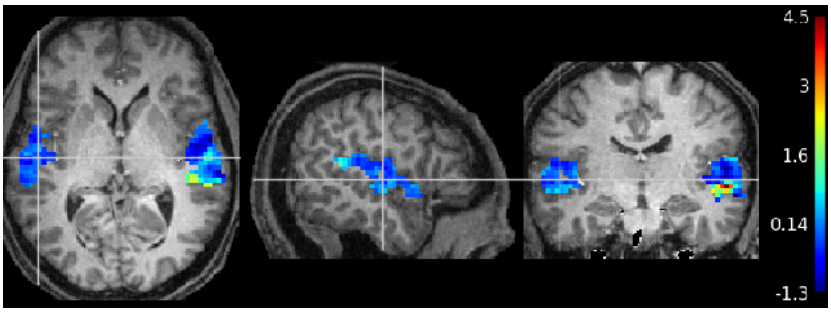

(b) Visual experimental condition

Figure 3.11: NRL estimates for the auditory and visual experimental conditions for the two-parcels model selected by the variational model selection procedure.

3.4 Conclusion

In this chapter, we introduced the JPDE model which is an extension of the parcel-based JDE model. This model assumes that a single unknown HRF shape is driving hemodynamic responses in a given parcel. Activated voxels within the parcel are then localized by inferring a spatially regularized bilinear model. One major limitation of the JDE model that it requires the parcellation to be fixed a priori by, *e.g.*, using clustering algorithms. The JPDE model solves this problem by avoiding the pre-defined parcellation. This model allows the grouping of the regions that share a similar HRF pattern and relaxing the hard constraint of a single HRF profile over a given parcel to cope with possible parcellation errors. These concerns were addressed by introducing HRF patterns represented by Gaussian distributions and assigned to representative voxels using latent variables. These latent variables are governed by a hidden Markov random field, namely a Potts model that enforces spatial correlation between neighbouring voxels. However, the number of the hemodynamic territories (parcels) has to be specified a priori for the JPDE model. This number has a huge influence of the detection and estimation tasks and its adjustment is generally a non-trivial task. In this context, we proposed a variational model selection procedure based on the free energy calculation. This procedure was added as an extension to the JPDE model where the free energy was calculated for different candidate models after convergence. Each of these models is characterized by a given number of parcels and the model maximizing the free energy is the best fit for the fMRI data. In other words, if we have Ω different models then we have to run the JPDE model with the model selection procedure Ω times and compute the value of the free energy each time. The proposed extension was validated using synthetic and real data experiments. For synthetic data, the proposed procedure managed to estimate the correct number of parcels (when compared to the ground truth) for all the experiments. As regards real data, the region of interest was the temporal lobes and the model with two parcels was selected as the best data fit. These results are coherent with those obtained by the JPDE model in (Chaari et al., 2012) where two similar HRF profiles were estimated in the left component and one HRF profile was estimated in the right component.
The main limitation of model selection based on the free energy calculations is that it requires to run the algorithm for each candidate model, which can

be time consuming especially if no approximate idea about the number of parcels is available. To avoid such a limitation, in chapter 4 we propose a non-parametric Bayesian model to estimate the number of parcels directly from the data in addition to the parcels themselves.

CHAPTER 4

Joint Parcellation Detection Estimation Using a Non-parametric Bayesian Model

Contents

4.1 Introduction

One of the most challenging issues in task-related fMRI data analysis consists of obtaining a meaningful functional brain parcellation. The joint parcellation detection estimation (JPDE) model addresses this issue through an automatic inference of the parcels directly from fMRI data. However, for doing so, the number of parcels needs to be fixed a priori and an appropriate initialization for the parcellation mask must be provided too. Hence, this

difficult task generally depends on the subject. In this chapter, an automatic model selection approach is proposed to overcome this limitation at the subject-level. This approach relies on a non-parametric Bayesian approach that estimates the number of parcels online using a Dirichlet process mixture model combined with a hidden Markov random field. The inference of the different model parameters is carried out using a variational expectation maximization strategy. As compared to a variational model selection procedure in the standard JPDE framework, this non-parametric extension appears more efficient in terms of computational time and does not require a precise initialization. This method is the second contribution of this thesis. It is first validated on synthetic data to demonstrate its robustness in selecting the right model order and providing accurate estimates for the parcellation, the hemodynamic response function (HRF) shapes and the activation maps. As regards the computational cost of the non-parametric Bayesian algorithm, it is reduced when compared to the free energy calculations of many candidate models. The method is then validated on real fMRI data in two regions of interest (ROIs): the right motor ROI and the bilateral occipital ROI. The results illustrated in this chapter show the ability of the proposed method to aggregate parcels with similar behaviour from a hemodynamic point of view, while discriminating them from other parcels having different hemodynamic properties. The HRF estimates of the different hemodynamic territories obtained with our approach are close to the canonical HRF shape in both the right motor and the bilateral occipital cortices. The discrimination power of the proposed approach is increased compared to its ancestors (Chaari et al., 2013, 2015) where the results on real data show its ability to discriminate HRF profiles with different Full Width at Half Maximum (FWHM). The robust detection of the elicited task-related activity is confirmed by comparing the neural response level estimates obtained using our approach with those obtained using the joint detection estimation (JDE) model.
This chapter is organized as follows; Section 4.2 introduces the Dirichlet processes that will be embedded in the JPDE model, the resulting non-parametric Bayesian model and its variational inference. The proposed NP-JPDE model is validated on synthetic and real data experiments in Section 4.3. Some conclusions and discussions are finally drawn in Section 4.4.

4.2 Non-parametric Bayesian model selection for hemodynamic brain parcellation

One important issue for fitting the JPDE model to fMRI data is to determine the number of parcels within the brain or the region of interest. Even though the algorithm presented in (Chaari et al., 2012, 2015) automatically estimates the parcels from the data in parallel to the joint detection-estimation task, it still requires to manually set the number of parcels which limits its usefulness. Determining the optimal number of parcels K, which yields the best fit to the data is a model selection problem. In this case, the likelihood cannot be used directly as a model score since it does not account for the model complexity. Some alternatives investigated in the literature are based on a penalized likelihood such as the Bayesian information criterion (BIC) and the minimum description length (MDL) criterion (Chickering and Heckerman, 1997). Although the model selection procedure proposed in (Albughdadi et al., 2014) and introduced in Chapter 3 automatically estimates the number of parcels, it can be time consuming since it requires to be run for each candidate model.

We present here a novel approach to perform model selection (Albughdadi et al., 2016c). This approach relies on a non-parametric model to estimate the number of parcels from the data. In this approach, the above mentioned JPDE model is reformulated to incorporate a non-parametric model selection using Dirichlet processes combined with a hidden Markov random field prior. This section first recalls the basic principles of Dirichlet processes. In a second step, we show how Dirichlet processes can be included in the JPDE framework. The resulting VEM inference scheme is finally presented in detail.

4.2.1 Dirichlet processes

Dirichlet processes were first proposed in (Ferguson, 1973) as distributions placed over distributions. A Dirichlet process (DP), denoted by $DP(G_0, \alpha)$, is characterized by a base distribution G_0 and a positive scaling parameter α. More precisely, a random distribution G is distributed according to a Dirichlet Process (Ferguson, 1973) with scaling parameter α and base distribution G_0, if for all natural numbers k and for all k-partitions $\{B_1, ..., B_k\}$

$$(G(B_1), G(B_2), ..., G(B_k)) \sim Dir(\alpha G_0(B_1), \alpha G_0(B_2), ..., \alpha G_0(B_k)) \quad [4.1]$$

where $Dir\left(\alpha G_0\left(B_1\right), \alpha G_0\left(B_2\right), ..., \alpha G_0\left(B_k\right)\right)$ is the Dirichlet distribution with parameter $\left(\alpha G_0\left(B_1\right), \ldots, \alpha G_0\left(B_k\right)\right)$.
A Dirichlet process mixture model (DPMM) uses the DP as a non-parametric prior in a hierarchical Bayesian model. Let us consider a mixture model where η_n is the parameter associated with the n-th data point x_n, η_n is not observed and the DP is used to induce a prior on the η_n's. If G is a measure generated according to a DP, G is discrete with probability one. As a consequence, the following hierarchical representation can be seen as a countably infinite mixture model

$$\begin{aligned} x_n \mid \eta_n &\sim p(x_n \mid \eta_n) \\ \eta_n \mid G &\sim G \\ G \mid \{\alpha, G_0\} &\sim DP(\alpha, G_0) \end{aligned} \tag{4.2}$$

where $n = 1, \ldots, N$. Among the values of the parameter η_n generated according to G, a number of them are equal. These unique values can be used to partition the samples $x_1, \ldots, x_N$ into clusters. Thus, the DP mixture is a flexible mixture model with a random number of clusters which grows with new observed data. An explicit DP characterization, which will be useful hereafter, is provided in terms of a stick-breaking construction (Blei et al., 2006). Consider two infinite collections of independent random variables $\boldsymbol{\tau}_i \sim Be(1, \alpha)$,where $Be(1, \alpha)$ is a beta distribution with parameters 1 and α, and $\eta_i^* \sim G_0$, for $i = 1, 2, \ldots$. With $\boldsymbol{\tau} = \tau_1, \tau_2, \ldots$, the stick-breaking representation of G is

$$\begin{aligned} \pi_i(\boldsymbol{\tau}) =& \tau_i \prod_{j=1}^{i-1}(1 - \tau_j) \\ G =& \sum_{i=1}^{\infty} \pi_i(\boldsymbol{\tau}) \delta_{\eta_i^*}. \end{aligned} \tag{4.3}$$

It is clear that G is a discrete distribution whose mixing proportions $\pi_i(\boldsymbol{\tau})$ are given by successively breaking a unit length stick into an infinite number of pieces. The size of each successive piece is proportional to the rest of the stick and is given by an independent draw from a beta distribution $Be(1, \alpha)$. Let z_n be the cluster assignment variable for the n-th data point. The hierarchical model of a Dirichlet process mixture model can be represented as follows

(i) $\tau_i \mid \alpha \sim Be(1, \alpha), i = 1, 2, ...$

(ii) $\eta_i^* \mid G_0 \sim G_0, i = 1, 2, ...$

(iii) for the n-th data point

(a) $z_n \mid \boldsymbol{\tau}$ is distributed according to a multinomial distribution, *i.e*, $z_n \mid \boldsymbol{\tau} \sim Mult(\pi(\boldsymbol{\tau}))$ with $\boldsymbol{\tau} = \tau_1, \tau_2, \ldots$

(b) $x_n \mid z_n \sim p(x_n \mid \eta_{z_n}^*)$

4.2.2 Non-parametric Bayesian JPDE model

Following the line of DPMM, we address the issue of automatically selecting the number of parcels by considering a countable infinite number of parcels. This requires the extension of the standard finite state space Potts model to a countable infinite number of states in which we use a DPM prior on the $\boldsymbol{z}$ variable in the JPDE formulation. Our proposal differs from that in (Chatzis and Tsechpenakis, 2010) in that it is not a mean field approximation using a set of independent variables but a direct generalization of the Potts model that uses a stick breaking representation. The stick breaking representation is used here to consider an infinite number of states. For such a generalization, we can consider the Potts model with an external field defined over $\boldsymbol{z} = \{z_1, \ldots, z_J\}$ as

$$p(\boldsymbol{z}; \beta_z, \boldsymbol{\alpha}) \propto \exp\left(\sum_{j=1}^{J} \alpha_{z_j} + \beta_z \sum_{i \sim j} I(z_i = z_j)\right) , \qquad [4.4]$$

for all $j = 1, \ldots, J$, $z_j \in \{1, \ldots, K\}$, where β_z is an interaction parameter and $\boldsymbol{\alpha}$ is a parameter vector such that $\boldsymbol{\alpha} = \{\alpha_1, \ldots, \alpha_K\}$ is an additional external field where each α_k is scalar. Such a Potts model is defined up to a multiplicative constant depending on $\boldsymbol{\alpha}$, meaning that the distribution (4.4) can be also obtained when adding the same constant value to all the α_k's. To avoid such an identifiability issue, it is common to consider additional constraints on the α_k's. One way to make the parameter vector $\boldsymbol{\alpha}$ unique is to asssume $\alpha_k = \log \pi_k$ with $\sum_{k=1}^{K} \pi_k = 1$. The Potts model in (4.4) can

then be defined by the following joint probability

$$p(\boldsymbol{z};\beta_z,\boldsymbol{\pi}) \propto \exp\left(\sum_{j=1}^{J}\log\pi_{z_j}+\beta_z\sum_{i\sim j}I(z_i=z_j)\right)$$
$$\propto \left(\prod_{j=1}^{J}\pi_{z_j}\right)\exp\left(\beta_z\sum_{i\sim j}I(z_i=z_j)\right). \qquad [4.5]$$

Define $V(\boldsymbol{z};\boldsymbol{\pi},\beta_z)=\sum_{j=1}^{J}\log\pi_{z_j}+\beta_z\sum_{i\sim j}I(z_i=z_j)$, which is called the energy function, where the first and the second sum respectively represents the first and the second order potentials. In the finite state space case, such a representation is equivalent, via the Hammersley-Clifford theorem (Besag, 1974), to assume that the distribution in (4.4) is a Markov random field.

Using the stick breaking construction, we can then consider a countable infinite number of probabilities π_k that sum to 1, *i.e*, $\sum_{k=1}^{\infty}\pi_k=1$. From this, we can define the same energy function V as before but consider it over an infinite countable set (homogeneous to the set of positive integers),

$$V(\boldsymbol{z};\boldsymbol{\pi},\beta_z)=\sum_{j=1}^{J}\log\pi_{z_j}+\beta_z\sum_{i\sim j}I(z_i=z_j)$$

for $z_j\in\{1,2,\ldots\}$. Next, using the Gibbs representation $p(\boldsymbol{z})\propto\exp(V(\boldsymbol{z};\boldsymbol{\pi},\beta_z))$, the Hammersley-Clifford theorem still holds if $\sum_{\boldsymbol{z}}\exp(V(\boldsymbol{z};\boldsymbol{\pi},\beta_z))<\infty$. Our choice of $\boldsymbol{\pi}$ ensures this property. Indeed,

$$\sum_{\boldsymbol{z}}\exp(V(\boldsymbol{z};\boldsymbol{\pi},\beta_z))=\sum_{\boldsymbol{z}}\left(\prod_{j=1}^{J}\pi_{z_j}\right)\exp\left(\beta_z\sum_{i\sim j}I(z_i=z_j)\right)$$
$$<\exp\left(\beta_z J(J-1)\right)\sum_{\boldsymbol{z}}\prod_{j=1}^{J}\pi_{z_j}$$
$$<\exp\left(\beta_z J(J-1)\right)<\infty$$

where $J(J-1)$ is the maximum number of neighbors among J sites. We also used that for all $j=1,\ldots,J$, $\sum_{z_j}\pi_{z_j}=\sum_{k=1}^{\infty}\pi_k=1$. It follows that $p(\boldsymbol{z};\boldsymbol{\pi},\beta_z)$, in the infinite state space case, is still a valid probability distribution and is a Markov field by the Hammersley-Clifford theorem. Note that such a generalization of the Potts model is possible because of the presence

of the external field parameters π_k that satisfy $\sum_{k=1}^{\infty} \pi_k = 1$. A Potts model with equal external field parameters cannot be as simply extended to an infinite countable state space. For a Potts model with no external field, such an extension is not possible because in the K-state case this Potts model is equivalent to $\pi_k = 1/K$ for all k where their sum does not tend to 1 when K tends to infinity.

In the stick breaking setting, we then consider $\pi_k(\boldsymbol{\tau}) = \tau_k \prod_{l=1}^{k-1}(1-\tau_l)$ and

$$p(\boldsymbol{z}; \beta_z, \boldsymbol{\tau}) \propto \left(\prod_{j=1}^{J} \pi_{z_j}(\boldsymbol{\tau}) \right) \exp\left(\beta_z \sum_{i \sim j} I(z_i = z_j) \right) . \qquad [4.6]$$

Such a construction is valid for any set of parameters $\boldsymbol{\tau} = \{\tau_k\}_{k=1}^{\infty}$ with each $\tau_k \in [0,1]$. However we would be left with an infinite number of parameters τ_k to estimate. The Bayesian point of view solves this problem by assuming that all τ_k's are i.i.d. variables having the same $Be(1,\alpha)$ distribution so that the number of parameters to estimate reduces to a single parameter α.
To reformulate the JPDE model in a non-parametric Bayesian framework coupled with HMRF, the original model of (Chaari et al., 2012, 2015) is kept except for the HRF groups $\boldsymbol{z}$. The extension of JPDE to an infinite number of parcels therefore consists of augmenting the original JPDE formulation with additional variables $\{\tau_k\}_{k=1}^{\infty}$ and of considering the following hierarchical construction which we call the NP-JPDE model

(i) $\tau_k \mid \alpha \sim Be(1,\alpha), k = 1, 2, ...$

(ii) $(\Theta_k^* = (\bar{\boldsymbol{h}}_k, \bar{\boldsymbol{\Sigma}}_k) \mid G_0) \sim G_0, k = 1, 2, ...$ where $G_0 = \mathcal{N}(0, \sigma_h^2 \boldsymbol{R}) \otimes \delta_{\nu \boldsymbol{I}}$

(iii) $p(\boldsymbol{z}|\boldsymbol{\tau}; \beta_z) \propto (\prod_{j=1}^{J} \pi_{z_j}(\boldsymbol{\tau}))\ \exp(\beta_z \sum_{i \sim j} I(z_i = z_j))$

(iv) $\boldsymbol{h}_j \mid z_j \sim p(\boldsymbol{h}_j | \Theta_{z_j}^*)$, where $p(\boldsymbol{h}_j | \Theta_k^*) = \mathcal{N}(\boldsymbol{h}_j; \bar{\boldsymbol{h}}_k, \bar{\boldsymbol{\Sigma}}_k)$ is a Gaussian distribution whose parameters $\bar{\boldsymbol{h}}_k, \bar{\boldsymbol{\Sigma}}_k$ are associated with the k-th parcel[1].

The directed acyclic graph in Fig. 4.1 illustrates the new hierarchical model, which differs from the model of (Chaari et al., 2012, 2015) by the green

[1]The other distributions defining the model remain the same as in the standard JPDE model. Note that in the extended version above we assume $\nu_k = \nu$ for all k to define G_0.

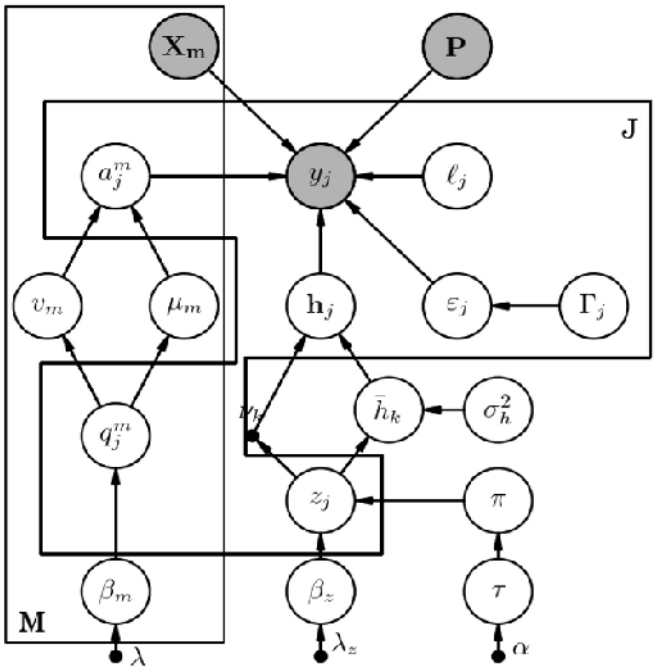

Figure 4.1: Graphical model describing dependencies between observed and missing variables involved in the non-parametric JPDE generative model for a given parcel $\boldsymbol{\mathcal{P}}$ with J voxels.

circled variables required for model selection. The resulting joint distribution of $\boldsymbol{Y}, \boldsymbol{A}, \boldsymbol{H}, \boldsymbol{Q}, \boldsymbol{z}$ and the additional variable $\boldsymbol{\tau}$ reads

$$\begin{aligned} p(\boldsymbol{Y}, \boldsymbol{A}, \boldsymbol{H}, \boldsymbol{Q}, \boldsymbol{z}, \boldsymbol{\tau}; \boldsymbol{\Theta}) =& p(\boldsymbol{Y} \mid \boldsymbol{A}, \boldsymbol{H}; \boldsymbol{\Theta})\, p(\boldsymbol{A} \mid \boldsymbol{Q}; \boldsymbol{\Theta})\, p(\boldsymbol{Q}; \boldsymbol{\Theta}) \\ & \times p(\boldsymbol{H} \mid \boldsymbol{z}; \boldsymbol{\Theta})\, p(\boldsymbol{z}|\boldsymbol{\tau}; \boldsymbol{\Theta})\, p(\boldsymbol{\tau}; \boldsymbol{\Theta}) \end{aligned} \quad [4.7]$$

where $\boldsymbol{\Theta} = \left\{\boldsymbol{\Gamma}, \boldsymbol{L}, \boldsymbol{\theta}_a, \beta_z, \sigma_h^2, (\bar{\boldsymbol{h}}_k)_{1\leq k\leq K}, \nu, \alpha\right\}$ and $p(\boldsymbol{\tau}) = \prod_{k=1}^{\infty} p(\tau_k)$, $p(\boldsymbol{z}|\boldsymbol{\tau})$ are defined in steps (i) and (iii), respectively.

4.2.3 Variational expectation maximization estimation

Different inference strategies can be used to estimate the missing variables $\boldsymbol{A}, \boldsymbol{H}, \boldsymbol{Q}, \boldsymbol{z}, \boldsymbol{\tau}$ and the parameters $\boldsymbol{\Theta}$ from the posterior distribution $p(\boldsymbol{A}, \boldsymbol{H}, \boldsymbol{Q}, \boldsymbol{z}, \boldsymbol{\tau} \mid \boldsymbol{Y}; \boldsymbol{\Theta})$ associated with [4.7]. Due to the computational complexity of MCMC methods, we propose to use a VEM algorithm to derive

an approximation of the true posterior distribution $p(\boldsymbol{A}, \boldsymbol{H}, \boldsymbol{Q}, \boldsymbol{z}, \boldsymbol{\tau} \mid \boldsymbol{Y}; \boldsymbol{\Theta})$ of the form

$$\widetilde{p}(\boldsymbol{A}, \boldsymbol{H}, \boldsymbol{Q}, \boldsymbol{z}, \boldsymbol{\tau}; \boldsymbol{\Theta}) = \widetilde{p}_A(\boldsymbol{A})\, \widetilde{p}_H(\boldsymbol{H}) \prod_{j=1}^{J} \widetilde{p}_{Q_j}(Q_j) \prod_{j=1}^{J} \widetilde{p}_{z_j}(z_j)\, \widetilde{p}_\tau(\boldsymbol{\tau}). \quad [4.8]$$

In the variational distribution above, the approximations $\prod_{j=1}^{J} \widetilde{p}_{Q_j}(Q_j)$ and $\prod_{j=1}^{J} \widetilde{p}_{z_j}(z_j)$ are sought in a form that factorizes over voxels (mean field) to handle intractability due to the spatial neighborhood. The infinite state space for $\boldsymbol{z}$ is dealt with by considering a truncation to a number K which consists of assuming that the variational distribution satisfies $\widetilde{p}_{z_j}(k) = 0$ for $k > K$ and $\widetilde{p}_\tau(\boldsymbol{\tau}) = \prod_{k=1}^{K-1} \widetilde{p}_{\tau_k}(\tau_k)$. This amounts to setting $\tau_k = 1$ for $k \geq K$ or $\widetilde{p}_{\tau_k}(\tau_k) = \delta_1(\tau_k)$.

The VEM approach requires five steps associated with five expectations referred to as: VE-A, VE-H, VE-Q, VE-Z and VE-$\boldsymbol{\tau}$. Compared to the standard JPDE, the new steps are the VE-Z and VE-$\boldsymbol{\tau}$ steps which are detailed below. (See (Chaari et al., 2012, 2015) for more details about the other expectation steps.) In what follows, we recall all the expectation steps

$$\textbf{VE-H:}\ \widetilde{p}_H^{(r)}(\boldsymbol{H}) \propto \exp\left(\mathrm{E}_{\widetilde{p}_A^{(r-1)}\widetilde{p}_z^{(r-1)}}\left[\log p(\boldsymbol{H} \mid \boldsymbol{Y}, \boldsymbol{A}, \boldsymbol{z}; \boldsymbol{\Theta}^{(r-1)}\right]\right) \quad [4.9]$$

$$\textbf{VE-A:}\ \widetilde{p}_A^{(r)}(\boldsymbol{A}) \propto \exp\left(\mathrm{E}_{\widetilde{p}_H^{(r)}\widetilde{p}_Q^{(r-1)}}\left[\log p(\boldsymbol{A} \mid \boldsymbol{Y}, \boldsymbol{H}, \boldsymbol{Q}; \boldsymbol{\Theta}^{(r-1)})\right]\right) \quad [4.10]$$

$$\textbf{VE-Q:}\ \widetilde{p}_Q^{(r)}(\boldsymbol{Q}) \propto \exp\left(\mathrm{E}_{\widetilde{p}_A^{(r)}}\left[\log p(\boldsymbol{Q} \mid \boldsymbol{Y}, \boldsymbol{A}; \boldsymbol{\Theta}^{(r-1)})\right]\right) \quad [4.11]$$

$$\textbf{VE-}\boldsymbol{\tau}\textbf{:}\ \widetilde{p}_z^{(r)}(\boldsymbol{\tau}) \propto \exp\left(\mathrm{E}_{\widetilde{p}_z^{(r)}}\left[\log p(\boldsymbol{\tau} \mid \boldsymbol{Y}, \boldsymbol{z}; \boldsymbol{\Theta}^{(r-1)})\right]\right) \quad [4.12]$$

$$\textbf{VE-Z:}\ \widetilde{p}_z^{(r)}(\boldsymbol{z}) \propto \exp\left(\mathrm{E}_{\widetilde{p}_H^{(r)}\widetilde{p}_\tau^{(r)}}\left[\log p(\boldsymbol{z} \mid \boldsymbol{Y}, \boldsymbol{H}, \boldsymbol{\tau}; \boldsymbol{\Theta}^{(r-1)})\right]\right). \quad [4.13]$$

In the following part, further details are provided for the two new steps, namely the VE-$\boldsymbol{\tau}$ and VE-$\boldsymbol{Z}$ steps. The interested reader can refer to Subsection 3.2.3 for more details on the other steps.

(i) **VE-$\boldsymbol{\tau}$** step: The VE-$\boldsymbol{\tau}$ step results straightforwardly from results on variational approximation in the exponential family. Given [4.3] and

for $k = 1, \ldots, K-1$,

$$\widetilde{p}_{\tau_k}(\tau_k) \propto p(\tau_k) \ \exp\left(\sum_{j=1}^{J} \mathrm{E}_{\widetilde{p}_{z_j}\widetilde{p}_{\tau\setminus\{k\}}}\left[\log \pi_{z_j}(\boldsymbol{\tau})\right]\right) \tag{4.14}$$

$$\propto p(\tau_k) \exp\left(\sum_{j=1}^{J}\sum_{l=k+1}^{K} \widetilde{p}_{z_j}(l)\log(1-\tau_k) + \sum_{j=1}^{J}\widetilde{p}_{z_j}(k)\log(\tau_k)\right) \tag{4.15}$$

$$\propto Be(\gamma_{k,1}, \gamma_{k,2}) \tag{4.16}$$

with

$$\gamma_{k,1} = 1 + \sum_{j=1}^{J} \widetilde{p}_{z_j}(k) \tag{4.17}$$

$$\gamma_{k,2} = \alpha + \sum_{j=1}^{J}\sum_{l=k+1}^{K} \widetilde{p}_{z_j}(l). \tag{4.18}$$

A gamma prior is placed over the scaling parameter α following (Escobar and West, 1995) with parameters $(\hat{s}_1, \hat{s}_2)$. The gamma distribution is conjugate to the stick lengths and the parameters $\hat{s}_1$ and $\hat{s}_2$ are given by

$$\hat{s}_1 = s_1 + K - 1 \tag{4.19}$$

$$\hat{s}_2 = s_2 - \sum_{k=1}^{K-1} \mathrm{E}_{\widetilde{p}_{\tau_k}}\left[\log(1-\tau_k)\right]. \tag{4.20}$$

After computing these parameters, we replace α in [4.18] with its expectation $\mathrm{E}_q[\alpha] = \frac{\hat{s}_1}{\hat{s}_2}$.

(ii) **VE-Z** step: The VE-Z step is divided into J VE-Z_j steps. Since we assume $\widetilde{p}_{z_j}(z_j) = 0$ for $z_j > K$, we only need to compute the distributions for $z_j \leq K$,

$$\widetilde{p}_{z_j}(z_j) \propto \exp\left(\mathrm{E}_{\widetilde{p}_{H_j}}\left[\log p(\boldsymbol{h}_j|z_j)\right] + \mathrm{E}_{\widetilde{p}_\tau}\left[\log \pi_{z_j}(\boldsymbol{\tau})\right] + \beta_z \sum_{i\sim j} \widetilde{p}_{z_i}(z_j)\right) \tag{4.21}$$

where

$$\mathrm{E}_{\widetilde{p}_\tau}\left[\log \pi_k(\boldsymbol{\tau})\right] = \mathrm{E}_{\widetilde{p}_{\tau_k}}\left[\log \tau_k\right] + \sum_{l=1}^{k-1} \mathrm{E}_{\widetilde{p}_{\tau_l}}\left[\log(1-\tau_l)\right]. \tag{4.22}$$

The previous expectations can be computed using the fact that $\widetilde{p}_{\tau_k}$ is a beta distribution, *i.e.*, $Be(\gamma_{k,1}, \gamma_{k,2})$ defined by (4.17) and (4.18)

$$\mathrm{E}_{\widetilde{p}_{\tau_k}}\big[\log(\tau_k)\big] = \Psi(\gamma_{k,1}) - \Psi(\gamma_{k,1}+\gamma_{k,2}) \quad [4.23]$$

$$\mathrm{E}_{\widetilde{p}_{\tau_k}}\big[\log(1-\tau_k)\big] = \Psi(\gamma_{k,2}) - \Psi(\gamma_{k,1}+\gamma_{k,2}) \quad [4.24]$$

where $\Psi(.)$ is the digamma function defined by

$$\Psi(z) = \tfrac{d}{dz}\log\Gamma(z) = \tfrac{\Gamma'(z)}{\Gamma(z)}.$$

The term $\mathrm{E}_{\widetilde{p}_{H_j}}\big[\log p(H_j|z_j)\big]$ is computed as in the JPDE model as shown in the VE-H step of (Chaari et al., 2015).

(iii) **VM** step: The maximization step in this extended JPDE is the same as in (Chaari et al., 2015). As a consequence, it can be rewritten as

$$\begin{aligned}\boldsymbol{\Theta}^{(r)} = \arg\max_{\boldsymbol{\Theta}}\{ & \mathrm{E}_{\widetilde{p}_A^{(r)}\widetilde{p}_H^{(r)}}\big[\log p(\boldsymbol{Y}\,|\,\boldsymbol{A},\boldsymbol{h};\boldsymbol{L},\boldsymbol{\Gamma})\big] + \mathrm{E}_{\widetilde{p}_A^{(r)}\widetilde{p}_Q^{(r)}}\big[\log p(\boldsymbol{A}\,|\,\boldsymbol{Q};\boldsymbol{\mu},\boldsymbol{v})\big] \\ & + \mathrm{E}_{\widetilde{p}_H^{(r)}\widetilde{p}_z^{(r)}}\big[\log p(\boldsymbol{h}|\boldsymbol{z};\{\bar{\boldsymbol{h}}_k,\bar{\boldsymbol{\Sigma}}_k\}_{k=1:K}\big] + \mathrm{E}_{\widetilde{p}_Q^{(r)}}\big[\log p(\boldsymbol{Q};\boldsymbol{\beta})\big] \\ & + \mathrm{E}_{\widetilde{p}_z^{(r)}\widetilde{p}_\tau^{(r)}}\big[\log p(\boldsymbol{z}\,|\,\boldsymbol{\tau};\beta_z)\big]\}. \end{aligned} \quad [4.25]$$

The only step that differs from the original JPDE model is the maximization of [4.25] with respect to β_z which leads to

$$\beta_z^{(r)} = \arg\max_{\beta_z} \mathrm{E}_{\widetilde{p}_z^{(r)}\widetilde{p}_\tau^{(r)}}\big[\log p(\boldsymbol{z}|\boldsymbol{\tau};\beta_z)\big]. \quad [4.26]$$

This step does not admit an explicit closed-form expression but can be solved numerically using gradient ascent schemes. It is straightforward to show that the maximization of (4.26) with respect to β_z admits a unique solution. Indeed, it is equivalent to solve

$$\beta_z^{(r)} = \arg\max_{\beta_z} \mathrm{E}_{\widetilde{p}_z^{(r)}\widetilde{p}_\tau^{(r)}}\big[V(\boldsymbol{z};\boldsymbol{\tau},\beta_z)\big] - \mathrm{E}_{\widetilde{p}_\tau^{(r)}}\big[\log\mathcal{K}(\beta_z,\boldsymbol{\tau})\big] \quad [4.27]$$

where $\mathcal{K}$ denotes the normalizing constant that depends on $\boldsymbol{\tau}$ and β_z. Denoting the gradient vector and Hessian matrix respectively by ∇_{β_z} and $\nabla^2_{\beta_z}$, it comes

$$\begin{aligned}&\nabla_{\beta_z}\mathrm{E}_{\widetilde{p}_z^{(r)}\widetilde{p}_\tau^{(r)}}\big[\log p(\boldsymbol{z}|\boldsymbol{\tau};\beta_z)\big] \\ &= \mathrm{E}_{\widetilde{p}_z^{(r)}\widetilde{p}_\tau^{(r)}}\big[\nabla_{\beta_z}V(\boldsymbol{z};\boldsymbol{\tau},\beta_z)\big] - \mathrm{E}_{p(\boldsymbol{z};\boldsymbol{\tau},\beta_z)\widetilde{p}_\tau^{(r)}}\big[\nabla_{\beta_z}V(\boldsymbol{z};\boldsymbol{\tau},\beta_z)\big] \end{aligned} \quad [4.28]$$

$$\nabla^2_{\beta_z} \mathrm{E}_{\widetilde{p}_z^{(r)}\widetilde{p}_\tau^{(r)}}\left[\log p(\boldsymbol{z}|\boldsymbol{\tau};\beta_z)\right]$$
$$= \mathrm{E}_{\widetilde{p}_z^{(r)}\widetilde{p}_\tau^{(r)}}\left[\nabla^2_{\beta_z} V(\boldsymbol{z};\boldsymbol{\tau},\beta_z)\right] - \mathrm{E}_{p(\boldsymbol{z};\boldsymbol{\tau},\beta_z)\widetilde{p}_\tau^{(r)}}\left[\nabla^2_{\beta_z} V(\boldsymbol{z};\boldsymbol{\tau},\beta_z)\right]$$
$$- \mathrm{E}_{\widetilde{p}_\tau^{(r)}}\left[\mathrm{var}_{p(\boldsymbol{z};\boldsymbol{\tau},\beta_z)}[\nabla_{\beta_z} V(\boldsymbol{z};\boldsymbol{\tau},\beta_z)]\right] . \qquad [4.29]$$

The last expectations in (4.28) and (4.29) are taken over the Potts prior (4.6). It follows that whenever $V(\boldsymbol{z};\boldsymbol{\tau},\beta_z)$ is linear in β_z, $\nabla^2_{\beta_z} V(\boldsymbol{z};\boldsymbol{\tau},\beta_z)$ is zero, the Hessian matrix is a semi-definite negative matrix and the function to optimize is concave. Unfortunately, due to the intractable normalizing constant $\mathcal{K}$, expressions (4.28) and (4.29) are not directly available. It is necessary to approximate the terms involving the true MRF prior $p(\boldsymbol{z};\boldsymbol{\tau},\beta_z)$ using an approximation. A natural approach is to use

$$\widetilde{p}_z^{prior}(\boldsymbol{z};\boldsymbol{\tau},\beta_z) = \prod_{j=1}^{J} \widetilde{p}_{z_j}^{prior}(z_j;\boldsymbol{\tau},\beta_z) \qquad [4.30]$$

with $\widetilde{p}_{z_j}^{prior}(z_j;\boldsymbol{\tau},\beta_z)$ defined by

$$\widetilde{p}_{z_j}^{prior}(z_j = k;\boldsymbol{\tau},\beta_z) = \frac{\exp(\log \pi_k + \beta_z \sum_{i\sim j} \widetilde{p}_{z_i}^{(r-1)}(k))}{\sum_{l=1}^{K} \exp(\log \pi_l + \beta_z \sum_{i\sim j} \widetilde{p}_{z_i}^{(r-1)}(l))} . \qquad [4.31]$$

This MRF prior approximation induced by the posterior variational approximation has been proposed in (Celeux et al., 2003) and also exploited in (Chaari et al., 2013). Similarly, we obtain

$$\mathrm{E}_{\widetilde{p}_z^{(r)}\widetilde{p}_\tau^{(r)}}\left[\nabla_{\beta_z} V(\boldsymbol{z};\boldsymbol{\tau},\beta_z)\right] \simeq \textstyle\sum_{k=1}^{K} \sum_{i\sim j} \widetilde{p}_{z_j}(k)\widetilde{p}_{z_i}(k) \qquad [4.32]$$

$$\mathrm{E}_{p(\boldsymbol{z};\boldsymbol{\tau},\beta_z)\widetilde{p}_\tau^{(r)}}\left[\nabla_{\beta_z} V(\boldsymbol{z};\boldsymbol{\tau},\beta_z)\right] \simeq \sum_{k=1}^{K} \sum_{i\sim j} \mathrm{E}_{\widetilde{p}_\tau^{(r)}}\left[\widetilde{p}_{z_j}^{prior}(k;\boldsymbol{\tau},\beta_z)\widetilde{p}_{z_i}^{prior}(k;\boldsymbol{\tau},\beta_z)\right]. \qquad [4.33]$$

The additional difficulty is that we have to compute an additional expectation with regards to $\widetilde{p}_\tau^{(r)}$. The last expectation with respect to $\widetilde{p}_\tau^{(r)}$ can be approximated using Monte Carlo sums. Since $\widetilde{p}_\tau^{(r)}$ is the product of $K-1$ independent beta distributions defined in [4.17] and [4.18], it is straightforward to draw T realizations of $(\tau_1,\ldots,\tau_{K-1})$. Denoting

these realizations as $\boldsymbol{\tau}^{(t)}$ for $t = 1, \ldots, T$, the following approximation is obtained

$$\begin{aligned} &\mathrm{E}_{\widetilde{p}_{\tau}^{(r)}}\left[\sum_{k=1}^{K}\sum_{i\sim j}\widetilde{p}_{z_j}^{prior}(k;\boldsymbol{\tau},\beta_z)\widetilde{p}_{z_i}^{prior}(k;\boldsymbol{\tau},\beta_z)\right] \\ &\simeq \frac{1}{T}\sum_{t=1}^{T}\left[\sum_{k=1}^{K}\sum_{i\sim j}\widetilde{p}_{z_j}^{prior}(k;\boldsymbol{\tau}^{(t)},\beta_z)\widetilde{p}_{z_i}^{prior}(k;\boldsymbol{\tau}^{(t)},\beta_z)\right]. \end{aligned}$$

An approximation of the gradient in [4.28] can then be computed. Setting this approximate gradient to zero leads to an equation that can be solved to provide β_z. This solution is computationally expensive. For this reason, the experiments considered hereafter have been conducted with a fixed value of β_z.

The proposed NP-JPDE model is summarized in Algorithm 4.1.

Algorithm 4.1 The NP-JPDE model algorithm. The subscript (r) refers to the current iteration.

Initialization:

set the truncation level for the number of parcels T.

$\tilde{p}_z^{(0)}(\boldsymbol{z})$ initialized randomly for a uniform distribution.

$\tilde{p}_Q^{(0)}(\boldsymbol{Q})$ such that $\tilde{p}_{Q_j}^{(0)}(q_j^m) \in \{0, 1\}$.

for all j **do**

- $\boldsymbol{m}_{H_j}^{(0)}$ is initialized from the canonical HRF.
- $\boldsymbol{m}_{A_j}^{(0)}$ is initialized with zeros.

end for

Initialize with some $\boldsymbol{\Theta}^{(0)}$.

$r = 1$

repeat

Expectation step:

Compute $\tilde{p}_H^{(r)}(\boldsymbol{H})$ according to [3.18].

Compute $\tilde{p}_A^{(r)}(\boldsymbol{A})$ according to [3.19].

Compute $\tilde{p}_Q^{(r)}(\boldsymbol{Q})$ according to [3.24].

Compute $\boldsymbol{\gamma}_1^{(r)}$ and $\boldsymbol{\gamma}_2^{(r)}$ according to [4.17] and [4.18], respectively.

Compute $\tilde{p}_z^{(r)}(\boldsymbol{z})$ according to [4.21]-[4.24].

Maximization step:

Compute $\boldsymbol{\Theta}^{(r)}$ according to [4.25].

set $r \leftarrow r + 1$

until convergence

4.3 Experimental validation

To validate the NP-JPDE model, we performed numerical experiments on both synthetic and real data[2]. In the synthetic data experiments, the proposed non-parametric Bayesian algorithm is compared with the strategy adopted in (Albughdadi et al., 2014) and studied in Section 3.3 which consists of selecting the model that provides the highest free energy. Note that the free energy calculations have to be done for all the candidate models which can be time consuming specially when no prior information is available about the optimum number of parcels. In a second step, we perform numerical experiments on real data using the NP-JPDE model and compare the results to those obtained with the JDE model.

4.3.1 Synthetic fMRI time series

To validate the NP-JPDE model, three different synthetic experiments referred to as Exps. 1-3 have been conducted. Different parcellation masks have been used in each experiment to generate BOLD signal according to [3.1]. Two experimental conditions ($M = 2$) have been considered with 30 trials for each of them. The reference activation labels are shown in Fig. 4.2.

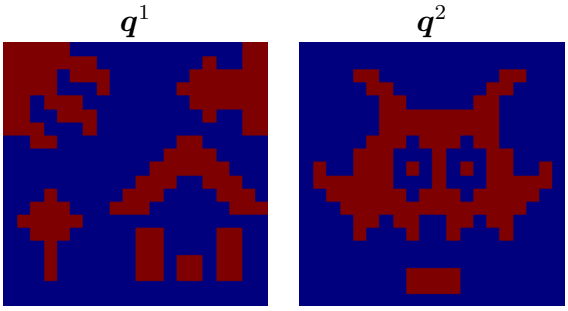

Figure 4.2: Reference activation labels for the two experimental conditions (grid size = 20×20).

Using Pyhrf, the NRLs were drawn according to their prior distribution conditionally to the activation labels $\boldsymbol{Q}$ of Fig. 4.2. Given these 20×20 binary labels, the NRLs were simulated as follows, for $m = 0, 1$: $a_j^m \,|\, q_j^m = 0 \sim$

[2]These experiments were implemented in Python within the framework offered by the Pyhrf software (Vincent et al., 2014), see also `http://pyhrf.org`.

$\mathcal{N}(0, 0.5)$ and $a_j^m \,|\, q_j^m = 1 \sim \mathcal{N}(3.2, 0.5)$. The representative NRLs are displayed in Fig. 4.3. The onsets of these trials were randomly generated with a mean inter stimuli interval of 3 s and a variance of 5 s. The fMRI time series $\boldsymbol{y}_j$ were then generated according to [3.1] using $\Delta t = 0.5$ and $TR = 1$ s.

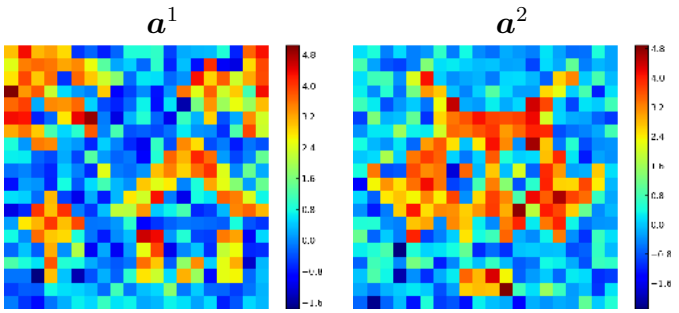

Figure 4.3: Reference NRLs for the two experimental conditions (grid size $= 20 \times 20$).

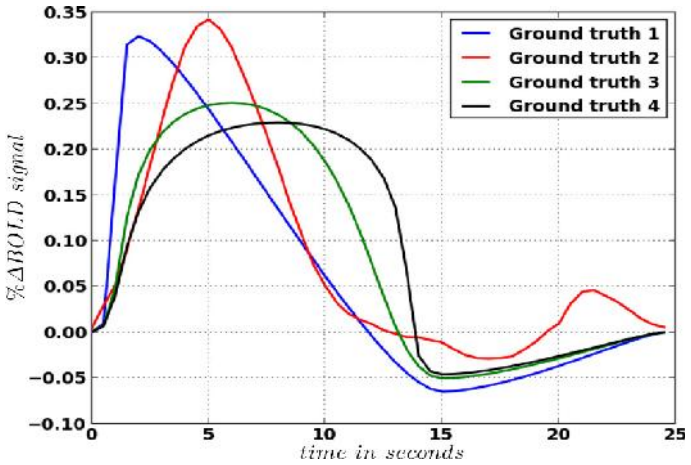

Figure 4.4: Ground truth HRF shapes ($\bar{h}_k, k = 1, \ldots, K^\omega$ with $\omega = \{1, \ldots, 3\}$) used for generating synthetic fMRI time series.

As a ground truth for the parcellation, different HRFs groups were considered, each with $K^\omega = \omega + 1$ parcels where $\omega \in \{1, \ldots, 3\}$. The HRFs associated with these groups were selected from the ground truth HRFs $(\bar{\boldsymbol{h}}_k)_{k=1}^{K^\omega}$ shown in Fig. 4.4. Reference parcellations for the three experiments are displayed in Fig. 4.5[top row]. These reference parcellations were chosen with different

cardinalities and such that they overlap with activation areas. This strategy was considered in order to investigate the robustness of the NP-JPDE model to the total amount of evoked activity in each parcel. Indeed, from a statistical point of view, the estimation of parcels involving a large amount of activated voxels should be more accurate than the estimation of parcels overlapping only a few activated voxels. Importantly, to mimic a real scenario in all experiments, we set the percentage of the activated voxels to be approximately 53% of the total number of voxels (this percentage was calculated by performing a bitwise OR between the reference activation binary labels of the two experimental conditions Fig. 4.2). Tab. 4.1 reports for each experiment the percentage of activated voxels in each parcel of the ground truth.

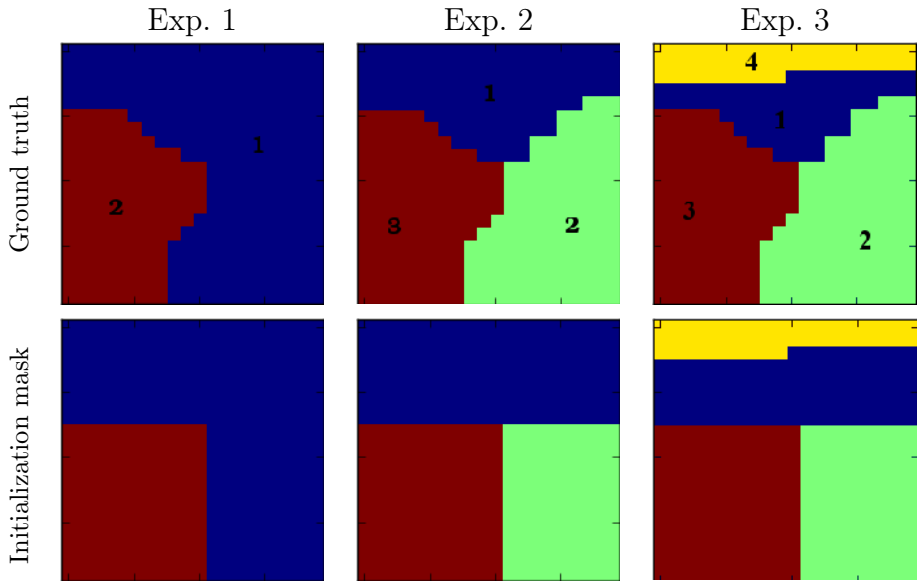

Figure 4.5: Ground truth parcellations used for the 3 experiments and corresponding initialization masks (only used for the original version of the JPDE approach) (grid size = 20×20).

These synthetic fMRI time series were then processed by the JPDE and NP-JPDE models. Results obtained with the two models were compared especially in terms of model selection. When using the original JPDE, three competing models $K^{\omega} = \omega + 1$ where $\omega \in \{1, \ldots, 3\}$ were run and their corresponding free energy was computed according to [3.47]. As regards the

Table 4.1: Percentage of activated voxels in each parcel of the ground truth parcellations for the three experiments. The parcels indexes are shown in Fig. 4.5

Experiment	# Parcel	% of activated voxels
Exp. 1	1	66.7%
	2	33.3%
Exp. 2	1	22.2%
	2	44.5%
	3	33.3%
Exp. 3	1	19.5%
	2	44.5%
	3	33.3%
	4	2.7%

NP-JPDE, it is worth noting that we do not need to specify any specific initialization. Hence, the latter was done randomly in contrast to the shown initializations for the original JPDE reported in Fig. 4.5[bottom]. The NP-JPDE model only requires to set the maximum number of parcels K (truncation level) for the variational approximation. This number was set to $K = 20$ for the three experiments, while the Potts parameter β_z was fixed to 1.2 for the spatial regularity of the parcellation[3]. The parameter β_m for activation classes which corresponds to the m-th experimental condition was estimated in the maximization step as in (Chaari et al., 2013, 2015). The prior values over the scaling parameter α of the DPMM were set to $\hat{s}_1 = 20, \hat{s}_2 = 5$. The estimated parcellations obtained by the two JPDE versions are shown in Fig. 4.6. This figure shows accurate parcellation estimates from a visual point of view. A comparison with the ground truth allows one to conclude that the proposed NP-JPDE algorithm estimates the different parcels more accurately than the JPDE algorithm especially for activated parcels. A quantitative evaluation of the parcellation estimates is provided in Tab. 4.2 where the error rate with respect to the ground truth is given. First, one can notice the small error probabilities for both models in all experiments. Furthermore, the NP-JPDE outperforms the standard JPDE as seen in the errors reported for Exps. 2-3. This remark corroborates the better visual performance of the

[3]This value of β_z was adjusted by cross validation.

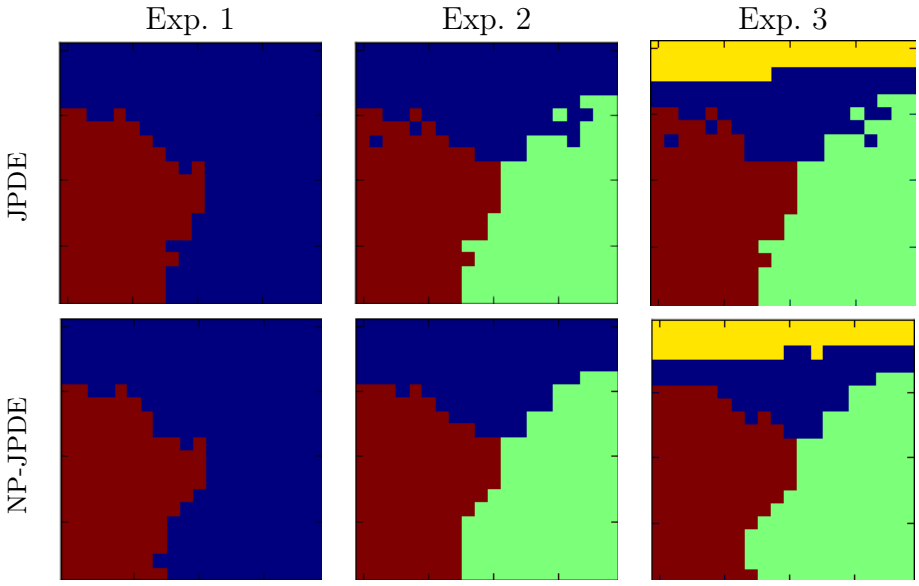

Figure 4.6: Parcellation estimates for the three experiments using the original JPDE and NP-JPDE (grid size = 20×20).

proposed NP-JPDE model.

Table 4.2: Error probabilities on the parcellation estimates using the original JPDE and the NP-JPDE algorithms.

Model	Exp. 1	Exp. 2	Exp. 3
NP-JPDE	1.5%	**0.25**%	**1.5**%
JPDE	1.5%	2.75%	3.25%

To investigate more deeply the robustness of the parcellation estimation using the NP-JPDE model, the confusion matrix for each of the three experiments was computed and shown in Tables. 4.3-4.5. We observed that the proposed NP-JPDE is highly accurate regarding the parcellation estimation step as the overlap between the reference and estimate for each parcel is larger than 95% in all experiments.
In order to further investigate the robustness of the proposed model, Tab. 4.6 provides the mean square errors (MSEs) for the NRLs and activation labels associated with the JPDE and NP-JPDE models. These results corroborate

the fact that the NP-JPDE model ensures precise estimation of the NRLs for both experimental conditions and outperforms the classical JPDE version. The construction of the parcellation for the NP-JPDE model has therefore very little impact on the NRL estimates and the detection task. Next, we investigated the accuracy of the estimation task by looking at the HRF estimates using the NP-JPDE model as reported in Fig. 4.7. A comparison between the reference and estimated HRF shapes shows that the NP-JPDE model is able to recover precise hemodynamics profiles and they are close to the HRF estimates of the original JPDE version (shown in the same figure).

Table 4.3: Confusion matrix for Exp. 1. (NP-JPDE model). RP and EP refer to the reference and the estimated parcellations, respectively.

EP \ RP	Parcel. 1	Parcel. 2
Parcel. 1	**1.0**	0.046
Parcel. 2	0.0	**0.954**

Table 4.4: Confusion matrix for Exp. 2. (NP-JPDE model). RP and EP refer to the reference and the estimated parcellations, respectively.

EP \ RP	Parcel. 1	Parcel. 2	Parcel. 3
Parcel. 1	**1.0**	0.0	0.008
Parcel. 2	0.0	**1.0**	0.0
Parcel. 3	0.0	0.0	**0.992**

Table 4.5: Confusion matrix for Exp. 3. (NP-JPDE model). RP and EP refer to the reference and the estimated parcellations, respectively.

EP \ RP	Parcel. 1	Parcel. 2	Parcel. 3	Parcel. 4
Parcel. 1	**1.0**	0.013	0.0	0.0
Parcel. 2	0.00	**0.961**	0.0	0.0
Parcel. 3	0.0	0.0	**1.0**	0.023
Parcel. 4	0.0	0.026	0.0	**0.977**

Exp. 1

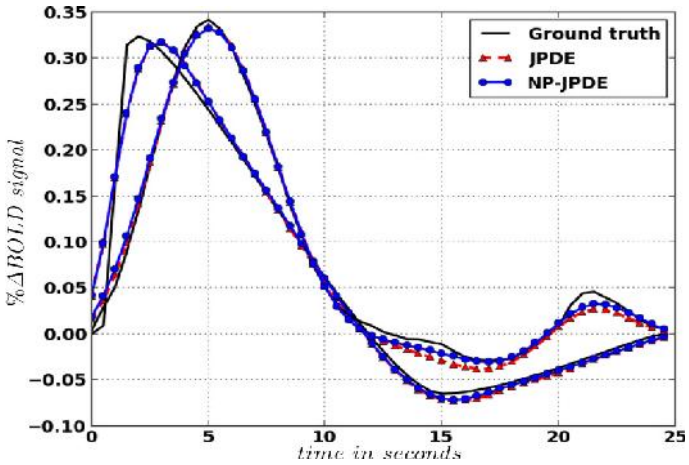

Exp. 2

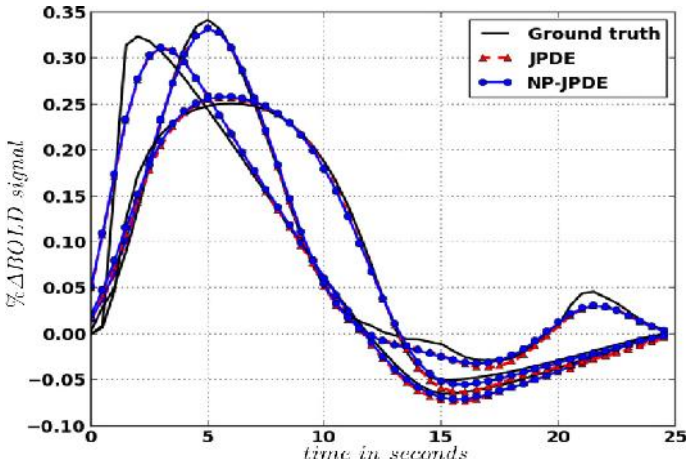

Exp. 3

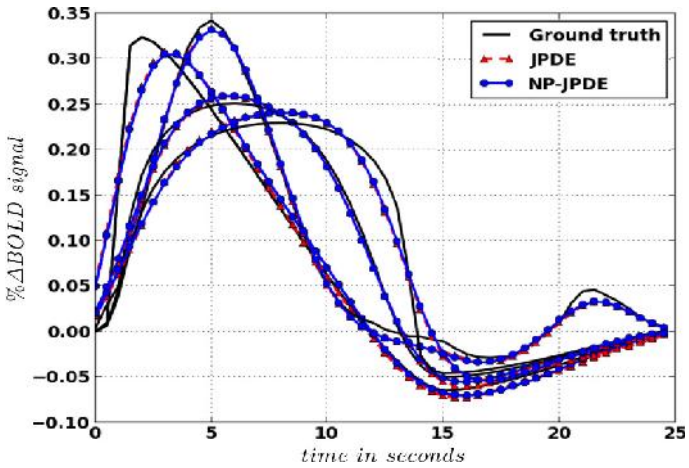

Figure 4.7: HRF estimates for the three experiments using JPDE and NP-JPDE models.

Table 4.6: MSEs of NRL estimates and activation labels for the JPDE and NP-JPDE models.

		Exp. 1		Exp. 2		Exp. 3	
		JPDE	NP-JPDE	JPDE	NP-JPDE	JPDE	NP-JPDE
NRLs	$m = 1$	0.016	**0.007**	0.017	**0.008**	0.017	**0.008**
	$m = 2$	0.012	**0.006**	0.012	**0.006**	0.012	**0.006**
Labels	$m = 1$	**0.003**	0.004	0.011	**0.003**	0.011	**0.003**
	$m = 2$	0.003	0.003	0.003	**0.002**	0.003	0.003

Last, we studied the convergence of the estimated number of parcels over iterations within the NP-JPDE. To this end, we present in Fig. 4.8 the parcellation estimate for Exp. 2 along different iterations until convergence. Starting with a random initialization, this figure shows that after about 7 iterations all the main parcels are well established. Furthermore, for the same experiment, fifty runs of the VEM algorithm using different random initializations were performed and the subsequent box plot graph was drawn to investigate the sensitivity of the NP-JPDE model to this setting. Fig. 4.9 shows the evolution of the estimated number of parcels over iterations for the fifty runs. It appears first that all the parcels were present after the first few iterations. Second, this number decreased through the iterations. Finally, we investigated the computational load. For doing so, we computed the running time for the standard JPDE framework by accumlating all elapsed times required for assessing the free energy associated with each candidate model, as done in (Albughdadi et al., 2014). Using a machine with 8 cores, each corresponding to an Intel® Xeon(R) CPU E3-1240 v3 chipset clocking at 3.40GHz processor and 16 GB of RAM, the four investigated models in the classical JPDE framework run in about 35 mins whereas for the NP-JPDE model it takes less than 9 mins. Thus, the computational cost of the NP-JPDE model is reduced when compared to free energy calculations of many candidate models.

4.3.2 Real data

Two experiments were conducted on real fMRI data to validate the proposed NP-JPDE model. The two experiments differ by the regions of interest (ROI) under consideration. Exp. 1 and Exp. 2 focused on the right motor and bilateral occipital ROIs, respectively. These ROIs are shown

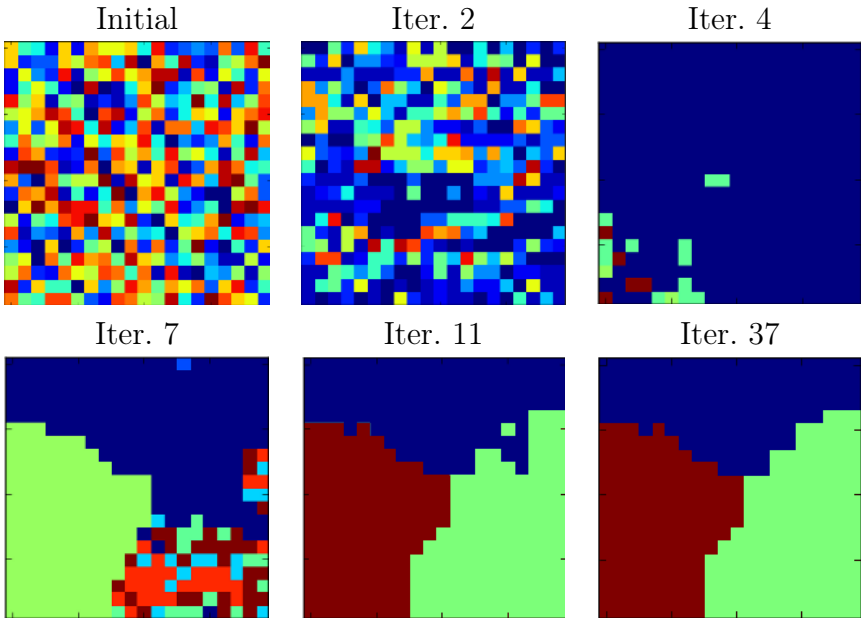

Figure 4.8: Parcellation estimates for Exp. 2 using the NP-JPDE model along successive iterations (grid size = 20×20).

in Fig. 4.10 and have been defined from the statistical results of a standard subject-level GLM analysis of fMRI data. More precisely, Student$-t$ maps associated with the two contrasts of interest, namely `(Left Click - Right Click)` and `(Visual stimuli - Auditory stimuli)`, have been thresholded at $p = 0.05$, corrected for multiple comparisons according to the FWER criterion, see (Badillo et al., 2013b; Chaari et al., 2014) for details. The fMRI data were collected using a gradient-echo EPI sequence (TE = 30 ms/TR = 2.4s/thickness = 3 mm/FOV = 192×192 mm^2, matrix size: 96×96) at a 3 Tesla during a localizer experiment (Pinel et al., 2007). Sixty auditory, visual and motor stimuli were involved in the paradigm and defined in ten experimental conditions ($M = 10$) (see (Badillo et al., 2013b; Chaari et al., 2014) for details). During this paradigm, $N = 128$ scans were acquired. For both experiments, we considered the truncation level $K = 20$, the parameter of the HMRF β_z was empirically set to 1.8 and the parameters of the gamma prior for the scaling parameter α were set to $\hat{s}_1 = 20$, $\hat{s}_2 = 5$.[4] In Exp. 1, two parcels were estimated in the right motor cortex. Different

[4]These parameters were determined empirically by cross validation.

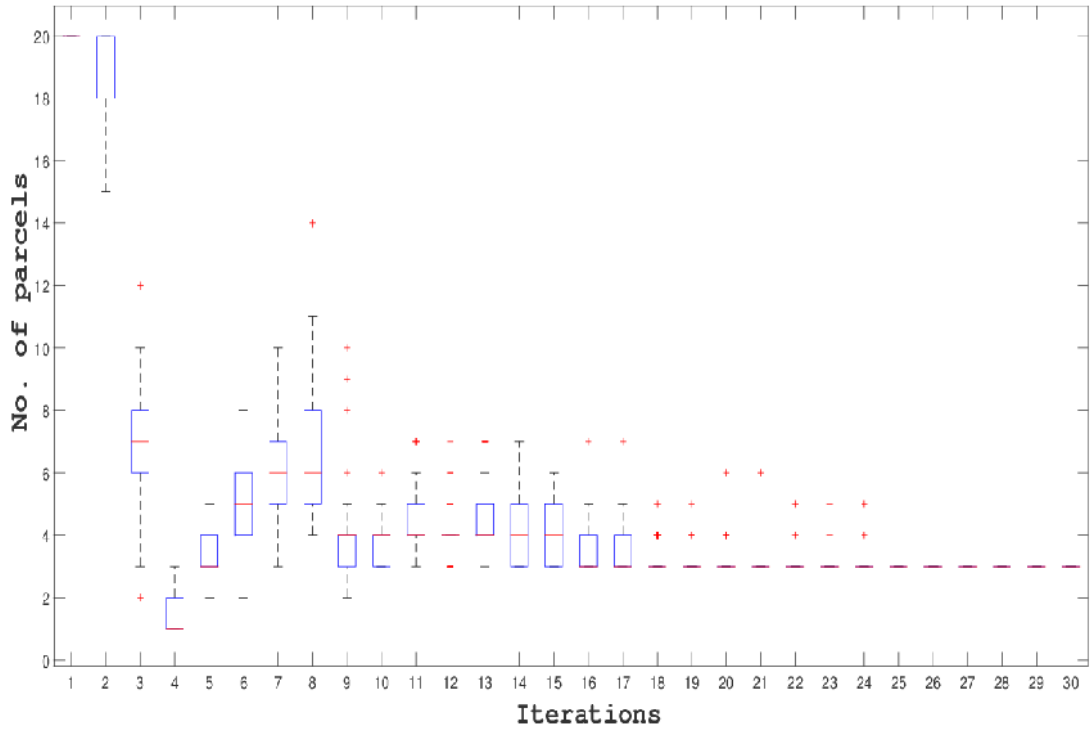

Figure 4.9: Boxplot for fifty different runs of Exp. 2 using the NP-JPDE model showing the convergence of the parcellation up to 30 iterations. The convergence is achieved from iteration 16.

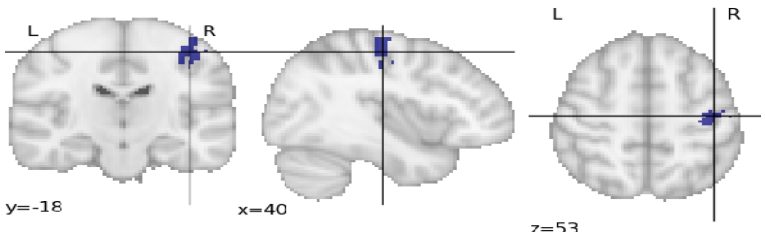

(a) Right motor ROI

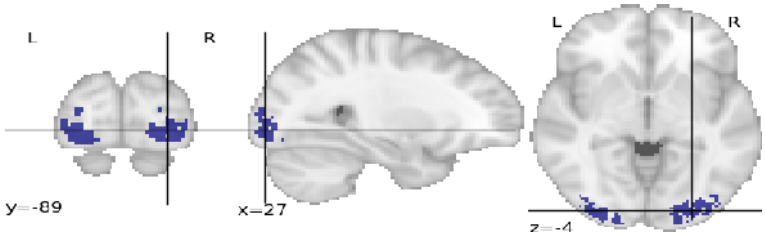

(b) Bilateral occipital ROI

Figure 4.10: Anatomical localization of brain regions. On top, the ROI is located in the right motor cortex and consists of a single connected component. At the bottom, the ROI is located in the primary visual cortex and made up of two connected components, one in each hemisphere.

slices of the estimated parcellation are shown in Fig. 4.11. The HRF shape estimates are shown in Fig. 4.12 along with the canonical HRF and the HRF estimated with the JDE model. These HRF estimates have the same value of the time to peak (TTP) and the full width at half maximum (FWHM): TTP = 4.8 s and FWHM = 4.2 s. As regards the HRF obtained with JDE, the TTP and FWHM values are 4.8 s and 3.6 s, respectively. We notice that both models recover the same TTP whereas the JDE yields a slightly narrower HRF (lower FWHM). The Euclidean distances were calculated between the HRF estimates and the canonical HRF. These values are reported in Tab. 4.7 in addition to the distance between the individual NP-JPDE HRF estimates. The reported distances indicate that the NP-JPDE model provides closer HRF estimates to the canonical one (average Euclidean distance of 0.4) compared to the JDE model (average Euclidean distance of 0.43). In this sense, the NP-JPDE model provides more coherent results than the JDE one in terms of closeness of the HRF estimates to the canonical shape in the motor cortex as it has already been shown in the literature (Badillo et al., 2013b).

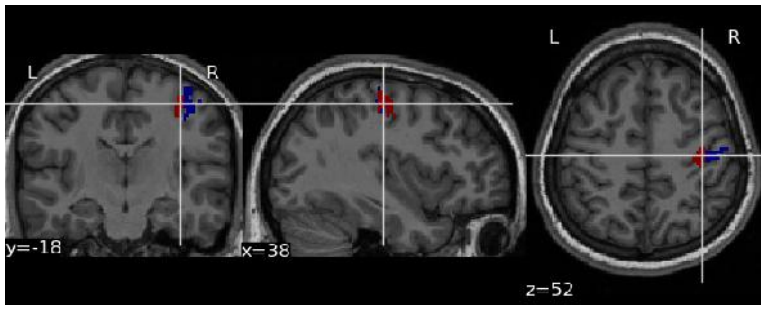

(a) Slice. 1

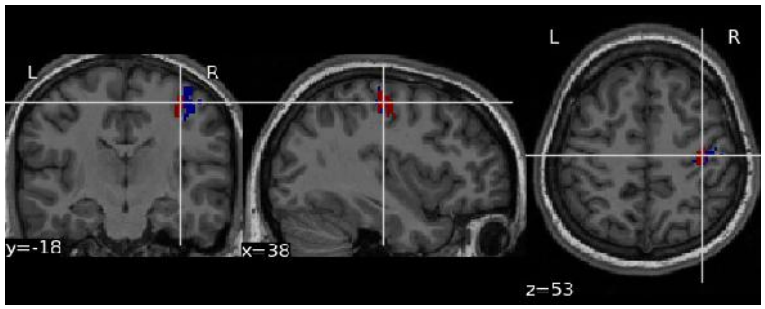

(b) Slice. 2

Figure 4.11: Consecutive slices of the estimated parcellation located in the right motor cortex.

As regards the NRL estimates, we focused on the left and right click visual and auditory experimental conditions which are expected to elicit evoked activity in the right motor cortex. Figs. 4.13 and 4.14 show the NRL estimates using the NP-JPDE and JDE models (with respect to the left and right auditory experimental conditions) and the computed contrast (auditory left click-auditory right click). Figs. 4.15 and 4.16 show the NRL estimates for both models with respect to the left and right click visual experimental conditions and the computed contrast (visual left click-visual right click). These results confirm the coherence between the NRL estimates obtained with the JDE and NP-JPDE models, especially in terms of maximum activation location and amplitude values.
The NP-JPDE was also run for Exp. 2 on the bilateral occipital cortex. Four parcels were detected as shown in Fig. 4.17. The corresponding HRF shape estimates for these parcels are shown in Fig. 4.18. These HRF estimates are displayed along with the canonical HRF and the one estimated using the

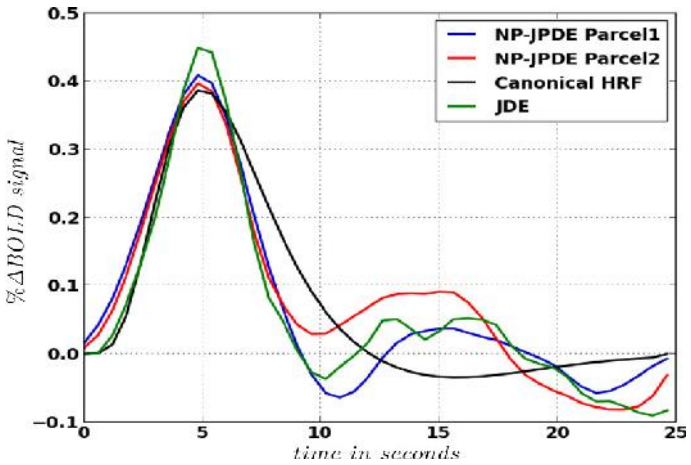

Figure 4.12: HRF shape estimates using the NP-JPDE and JDE models in the right motor cortex and the canonical HRF.

Table 4.7: Euclidean distance between the HRF estimates in the right motor cortex and the canonical HRF. Distance between the individual NP-JPDE HRF estimates are also provided.

	HRF. 1	HRF. 2	JDE
Canonical HRF	0.37	0.43	0.43
HRF. 2	0.30	–	–

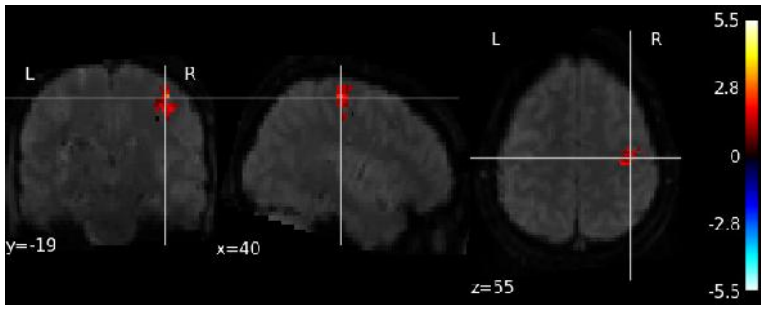

(a) Auditory left click (NP-JPDE)

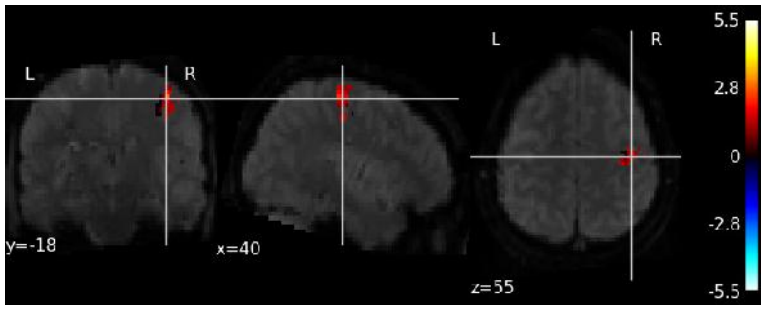

(b) Auditory right click (NP-JPDE)

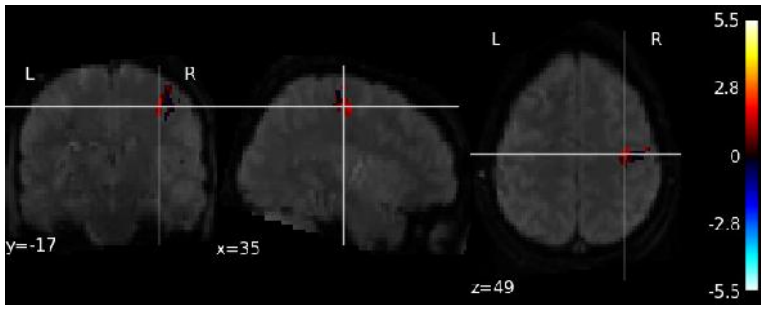

(c) Left click-Right click contrast (NP-JPDE)

Figure 4.13: NRL estimates for the auditory left and right click experimental conditions and their computed contrast (left click-right click) using the NP-JPDE model.

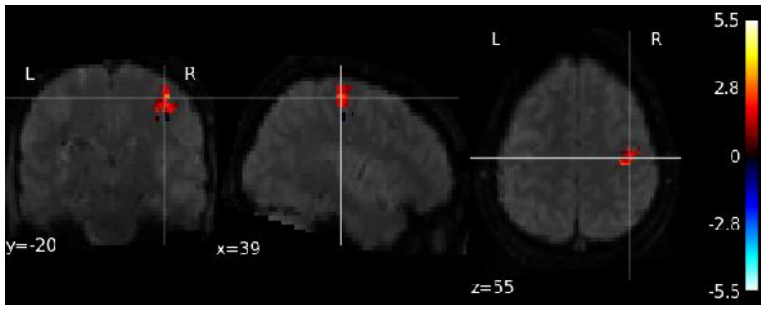

(a) Auditory left click (JDE)

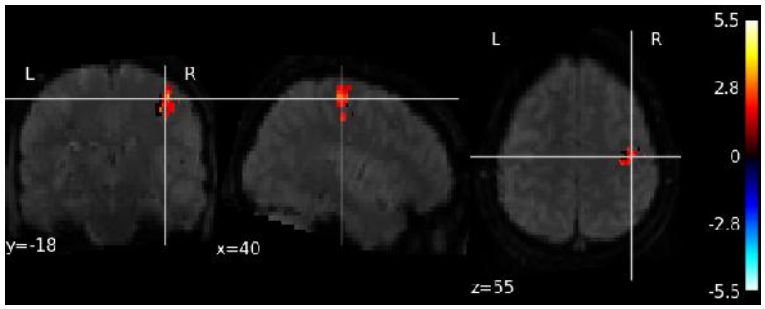

(b) Auditory right click (JDE)

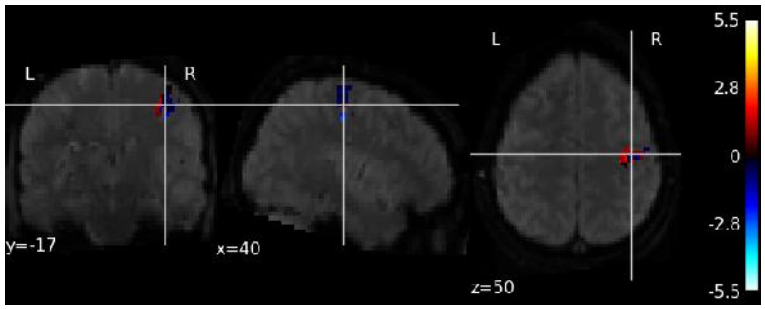

(c) Left click-Right click contrast (JDE)

Figure 4.14: NRL estimates for the auditory left and right click experimental conditions and their computed contrast (left click-right click) using the JDE model.

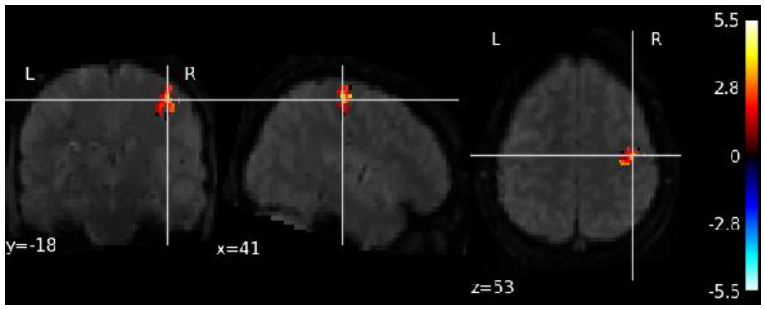

(a) Visual left click (NP-JPDE)

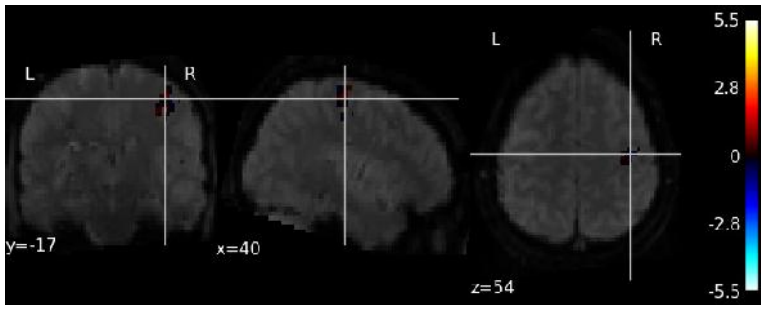

(b) Visual right click (NP-JPDE)

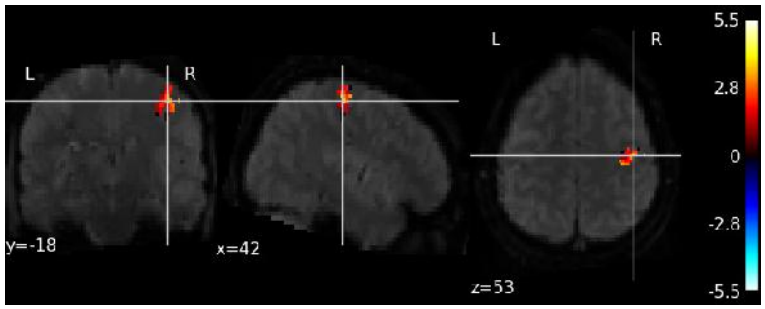

(c) Left click-Right click contrast (NP-JPDE)

Figure 4.15: NRL estimates for the visual left and right click experimental conditions and their computed contrast (left click-right click) using the NP-JPDE model.

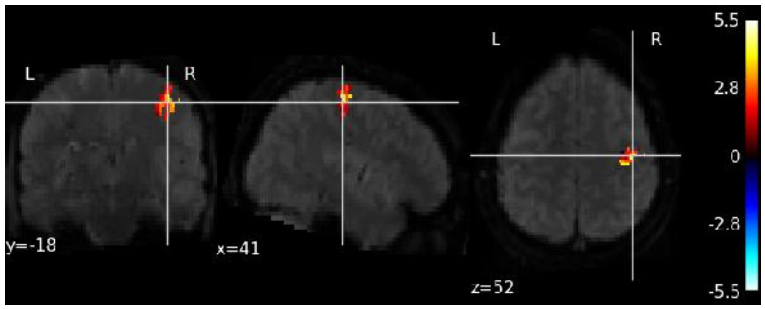

(a) Visual left click (JDE)

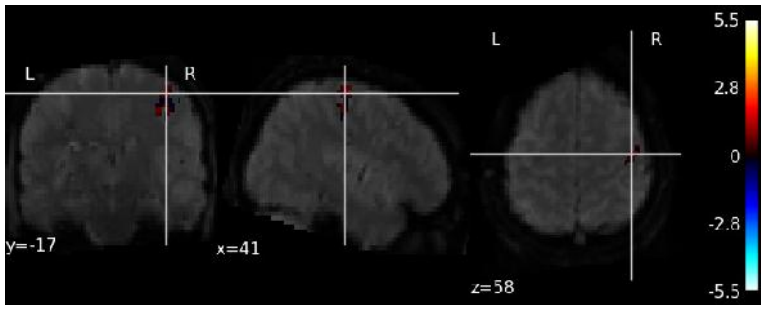

(b) Visual right click (JDE)

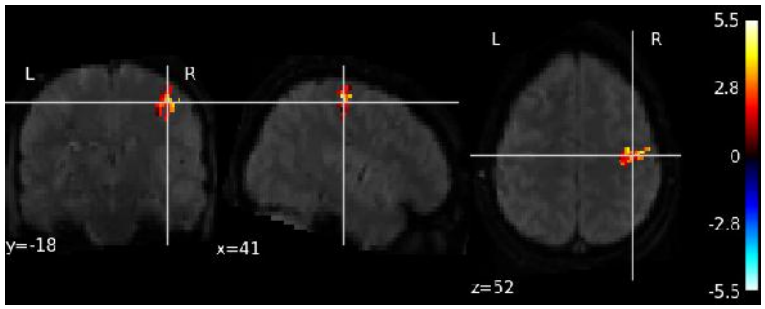

(c) Left click-Right click contrast (JDE)

Figure 4.16: NRL estimates for the visual left and right click experimental conditions and their computed contrast (left click-right click) using the JDE model.

JDE model. The computed TTP for the HRF profiles of parcels 1, 2 and 4 is TTP = 5.4 s, while for parcel 3 we have TTP = 6.0 s. The FWHM was also computed and is equal to 4.2 s for parcels 1 and 4, and to 4.8 s for parcels 2 and 3. As regards the HRF estimated using the JDE model, we have TTP = 5.4 s and FWHM = 4.2 s. Moreover, Tab. 4.8 reports the computed Euclidean distances between the different HRF estimates and the canonical HRF. It also reports the same distance between the individual NP-JPDE HRF estimates. The reported distances indicate that the NP-JPDE model provides closer HRF estimates to the canonical shape with average Euclidean distance of 0.42. More interestingly, it is clear that the NP-JPDE model is able to discriminate between parcels that have very close HRFs in terms of Euclidean distance, namely those of parcels 1 and 2. Indeed, these two parcels have similar TTPs, but different FWHM values. They are therefore detected as different parcels by the NP-JPDE model. Figs. 4.19 and 4.20 show the NRL estimates for some of the experimental conditions which are supposed to induce evoked activity in the bilateral occipital cortex (namely, video calculations, video sentences, horizontal checkerboard and vertical checkerboard). The obtained NRL estimates with the NP-JPDE and the JDE are similar in terms of amplitude values and the location of the highest activation.

Table 4.8: Euclidean distance between the HRF estimates in the bilateral occipital cortex and the canonical HRF. Dinstance between the individual NP-JPDE HRF estimates are also provided.

	HRF. 1	HRF. 2	HRF. 3	HRF. 4	JDE
Canonical HRF	0.42	0.41	0.43	0.41	0.47
HRF. 2	0.06	–	0.22	0.20	–
HRF. 3	0.17	–	–	0.35	–
HRF. 4	0.23	–	–	–	–

(a) Slice.1

(b) Slice.2

Figure 4.17: Consecutive slices of the estimated parcellation located in the occipital cortex.

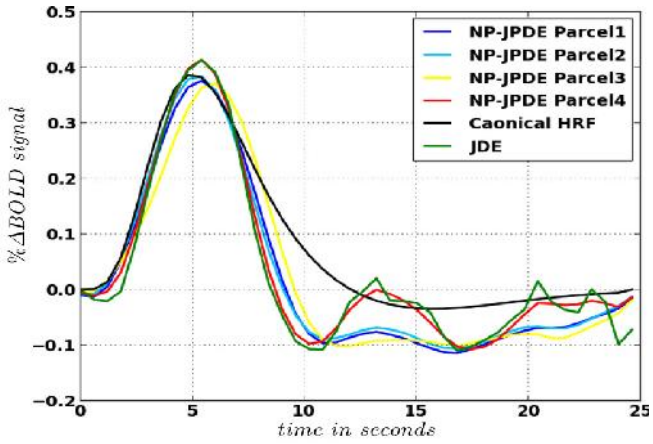

Figure 4.18: HRF shape estimates using the NP-JPDE and JDE models in the bilateral occipital cortex and the canonical HRF shape.

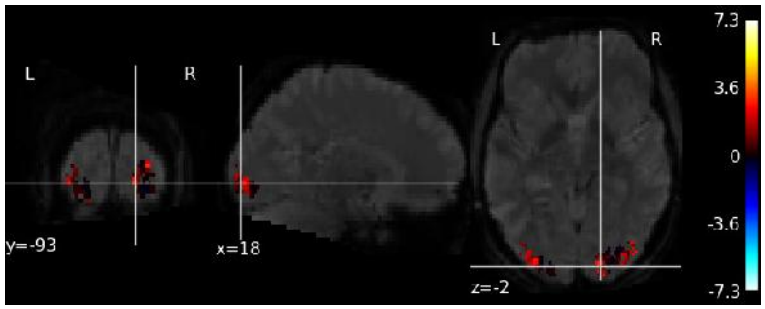

(a) Video calculations (NP-JPDE)

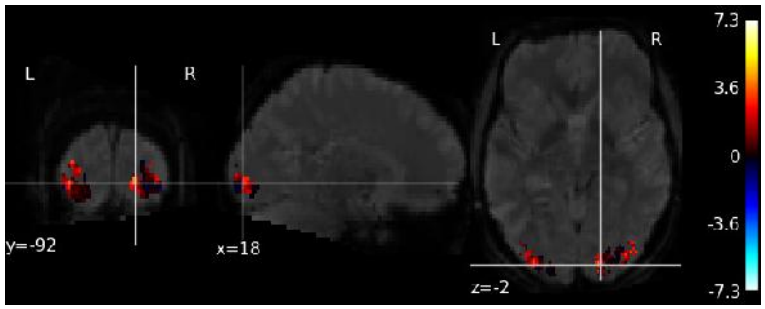

(b) Video sentences (NP-JPDE)

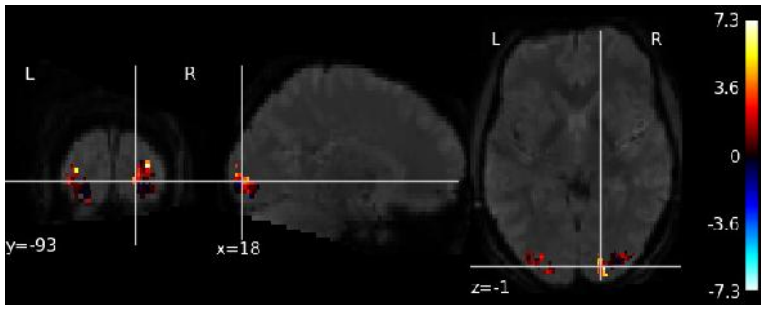

(c) Horizontal checkerboard (NP-JPDE)

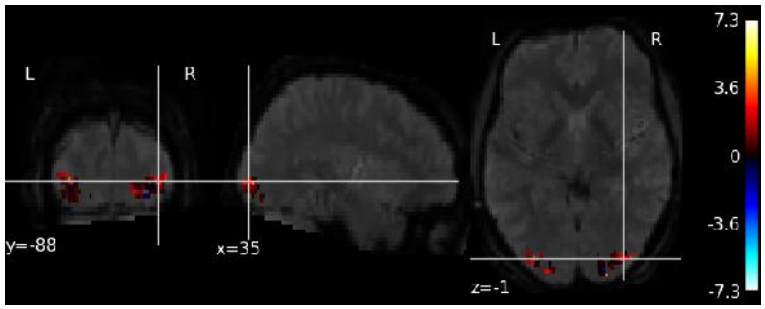

(d) Vertical checkerboard (NP-JPDE)

Figure 4.19: NRL estimates for the video calculations, video sentences horizontal and vertical checkerboard experimental conditions using NP-JPDE model.

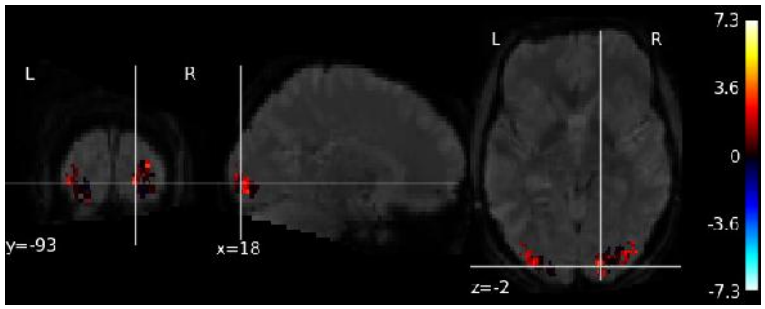

(a) Video calculations (JDE)

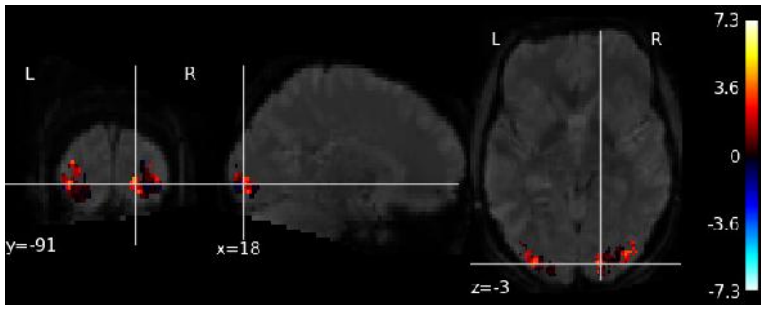

(b) Video sentences (JDE)

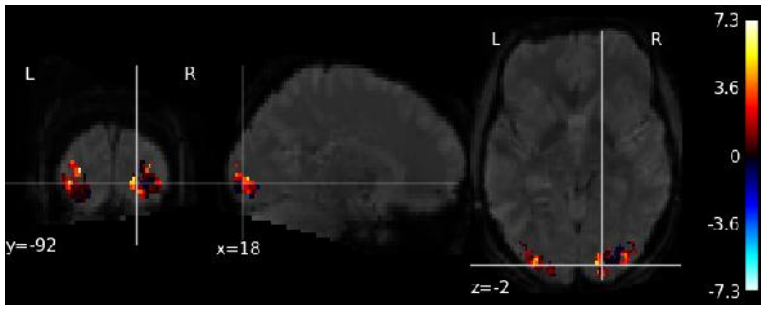

(c) Horizontal checkerboard (JDE)

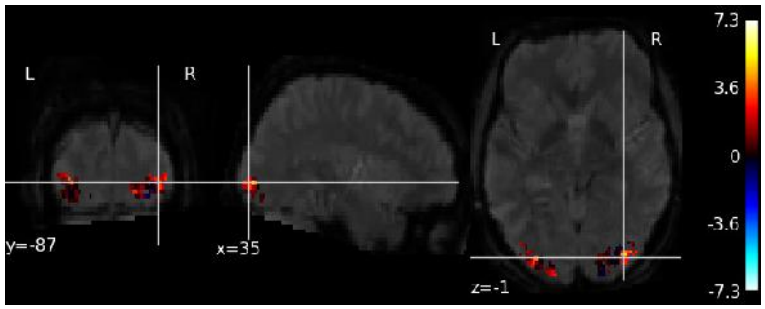

(d) Vertical checkerboard (JDE)

Figure 4.20: NRL estimates for the video calculations, video sentences horizontal and vertical checkerboard experimental conditions using JDE model.

4.4 Conclusion

This chapter proposed a new approach to estimate the number of hemodynamic parcels in fMRI data where model selection was formulated as a clustering issue. This approach was based on a Dirichlet process mixture model combined with a hidden Markov random field. A direct generalization of the Potts model that uses a stick breaking representation allowed an infinite number of states to be considered. The advantage of the non-parametric framework was to allow an automatic estimation of the number of parcels from the fMRI data. The use of a hidden Markov random field accounted for the spatial constraints on the connexity of the estimated parcels. The JPDE model proposed in (Chaari et al., 2012, 2015) was extended using this non-parametric Bayesian formulation yielding the so called NP-JPDE model. Following its ancestor (the JPDE), the NP-JPDE relied on the VEM as an inference strategy. However, the new layers in the hierarchy of the NP-JPDE model resulted in two new expectations steps (namely, VE$-Z$ and VE$-\boldsymbol{\tau}$ steps) while the others remained the same as in the classical JPDE model. The maximization of the interaction parameter of the Potts model (β_z) over the parcellation labels was not straightforward and was changed to account for the dependency of the parcellation label variable $\boldsymbol{z}$ on the stick breaking length $\boldsymbol{\tau}$ of the DPMM. The proposed model was also extended by injecting a new prior on the concentration parameter α of the DPMM which allowed for its automatic estimation through the VEM iterations.

Synthetic and real data experiments were used to validate the proposed approach. Using synthetic data experiments, we studied the performance of our approach in estimating an accurate parcellation and HRFs and detecting the task-related activity. Experiments with different scenarios were conducted using synthetic data generated for a different number of parcels. Our results were consistent with the classical JPDE model that relies on the model selection procedure in (Albughdadi et al., 2014) in terms of HRF recovery and evoked activation detection. However, the proposed NP-JPDE extension outperformed the original JPDE formulation in terms of parcellation inference. We also investigated the performance of the NP-JPDE in terms of convergence speed and computational time, and we showed again its superiority over its ancestor. As regards the NRL estimates, the NP-JPDE managed to preserve the robust performance of the classical JPDE in detecting the task-related activity. On real fMRI data, we used two ROIs

to validate the proposed approach, the right motor cortex and the bilateral occipital area embodying the primary visual cortices. In the right motor cortex, two different parcels were estimated with HRF estimates close to the canonical HRF. These results came consistent with the HRF estimate of the JDE model and with the conclusion in (Badillo et al., 2013b). In the bilateral occipital cortex, the left and the right parcels showed similar hemodynamic territories. The HRF estimates with the NP-JPDE were close to the canonical HRF especially in terms of time to peak and they were better recovered than using the JDE model. For both experiments, the NRL estimates using the NP-JPDE model were coherent with those obtained by analysing the same fMRI data using the JDE model. Due to the deep hierarchy of the NP-JPDE model, the output results could be sensitive to the value of the interaction parameter of the Potts model. To eliminate the effect of this parameter on the estimation task and reduce the computational cost resulting from the BNP, an adaptive mean shift-based approach for hemodynamic brain parcellation will be introduced in Chapter 5 to alleviate this sensitivity problem.

CHAPTER 5

Adaptive Mean Shift Algorithm for Hemodynamic Brain Parcellation

Contents

5.1 Introduction

This chapter is devoted to the application of the mean shift algorithm for fMRI data analysis where we use the mean shift algorithm to solve the

problem of the hemodynamic brain parcellation. Although an automatic parcellation approach was introduced in the previous chapter in a Bayesian non-parametric framework, the deep hierarchy of the NP-JPDE model could make the output results sensitive to some parameters such as the interaction parameter β_z of the Potts model. The mean shift is a very powerful algorithm that is widely used in machine learning for image segmentation. In this chapter, we first introduce a specific type of the mean shift algorithm which is known as the adaptive mean shift (AMS) in Section 5.2. In a second step, we illustrate the embedding of the AMS algorithm within the VEM framework of the standard JPDE algorithm yielding the AMS-JPDE model (Section 5.3). The experimental validation of the AMS-JPDE model is conducted in Section 5.4. Finally, some conclusions and discussions are drawn in Section 5.5.

5.2 Adaptive Mean Shift algorithm

In computer vision, low level tasks are a challenging difficulty. The dependency on a correct guessing of tuning parameters leads easily to incorrect results. To improve the performance of low level tasks in computer vision, their execution has to be task driven. To achieve the later, a reliable representation of the data at the low stage can be investigated. Another strategy is to limit the number of tuning parameters that control the feature extraction process. These techniques can be applied by relying on feature space-based analysis to map the input obtained through the processing of the data in small subsets at a time. After the entire input is processed, significant features correspond to the denser regions in the feature space. However, extracting features from the data has advantages and disadvantages. On one hand, excellent tolerance to a noise level is provided due to the pooling of a significant feature. On the other hand, features that have smaller support in the feature space may not be detected in spite of being salient for the task to be executed. The latter disadvantage can be solved by applying robust post-processing of the input domain guided by the feature space analysis or by imposing spatial parameters on the input domain.

Mean shift is a feature space analysis algorithm which is widely used for computer vision tasks. Feature space analysis is used to reduce the data to a few significant features which is also known as clustering or classification. This algorithm is a robust clustering technique which does not require set-

ting the number of clusters. It is an iterative algorithm that estimates the modes of a multivariate distribution underlying the feature space and the number of clusters is obtained automatically by estimating centers of these clusters (Comaniciu and Meer, 2002). Dense regions presented in the feature space correspond to a mode (local maxima) of the probability density function (see Fig. 5.1). Each data point is associated with the nearby peak of the probability density function. The mean shift defines a window (kernel) around each data point and then computes its mean. The center of the window is shifted to the mean in an iterative procedure until convergence. The mean shift algorithm relies on kernel density estimation which is a non-parametric approach to estimate the density function of a random variable.

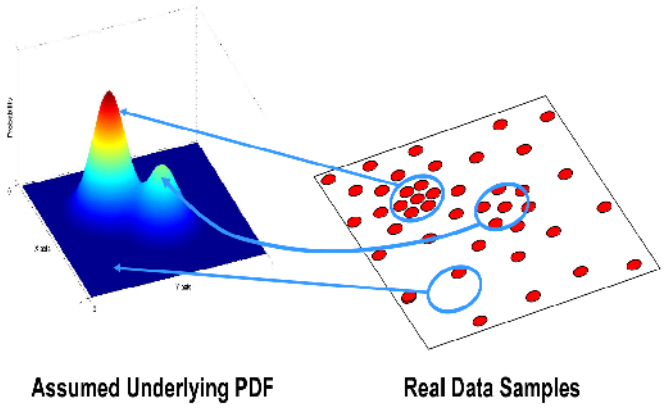

Figure 5.1: Modes correspond to dense regions in the mean shift algorithm (Yaron and Bernard, 2004).

5.2.1 The adaptive mean shift procedure

One of the most popular density estimation methods is the kernel density estimation which is also known as the Parzen window technique (Duda et al., 1973) in pattern recognition literature. Assuming n data points $\mathbf{x}_i, \quad i = 1, \ldots, n$ in the d-dimensional space $\mathbb{R}^d$, the multivariate kernel density estimator with kernel $K(\mathbf{x})$ and a symmetric positive definite $d \times d$

bandwidth matrix $\boldsymbol{H}$ is defined by

$$\hat{f}(\mathbf{x}) = \frac{1}{n}\sum_{i=1}^{n} K_{\boldsymbol{H}}(\mathbf{x} - \mathbf{x}_i) \qquad [5.1]$$

where $K_{\boldsymbol{H}}(\mathbf{x}) = |\boldsymbol{H}|^{-1/2} K(\boldsymbol{H}^{-1/2}\mathbf{x})$ is the d-variate kernel, *i.e.,* a bounded function with compact support satisfying

$$\begin{aligned} &\int_{R^d} K(\mathbf{x})d\mathbf{x} = 1, \quad \lim_{\|\mathbf{x}\|\to\infty} \|\mathbf{x}\|^d K(\mathbf{x}) = 0 \\ &\int_{R^d} \mathbf{x}K(\mathbf{x})d\mathbf{x} = 0, \quad \int_{R^d} \mathbf{x}\mathbf{x}^{\mathrm{t}} K(\mathbf{x})d\mathbf{x} = c_K \boldsymbol{I}. \end{aligned} \qquad [5.2]$$

In [5.2], c_K is a constant. A symmetric univariate kernel $K_1(x)$, where $x \in \mathbb{R}^d$, can be used to generate a multivariate kernel in two different ways:

$$K^P(\mathbf{x}) = \prod_{i=1}^{d} K_1(x_i) \quad K^S(\mathbf{x}) = a_{k,d} K_1(\|\mathbf{x}\|) \qquad [5.3]$$

where the product of the univariate kernels yields $K^P(\mathbf{x})$ and $K^S(\mathbf{x})$ is radially symmetric and obtained by rotating $K_1(\mathbf{x})$ in $\mathbb{R}^d$. Note that $a_{k,d}$ is a constant which ensures that $K^S(\mathbf{x})$ integrates to one, *i.e.*,

$$a_{k,d}^{-1} = \int_{\mathbb{R}^d} K_1 \|\mathbf{x}\| d\mathbf{x}. \qquad [5.4]$$

In the context of hemodynamic brain parcellation using the adaptive mean shift algorithm, we are only interested in the radially symmetric kernels satisfying

$$K(\mathbf{x}) = c_{k,d} k(\|\mathbf{x}\|^2) > 0 \quad \|\mathbf{x}\| \leq 1 \qquad [5.5]$$

where $k(x)$ ($0 \leq x \leq 1$) is called the profile of the kernel. Assuming that each data point is associated with a bandwidth value $h_i > 0$ that defines the radius of the kernel, the sample point estimator can be defined as

$$\hat{f}_K(\mathbf{x}) = \frac{1}{n}\sum_{i=1}^{n} \frac{1}{h_i^d} k\left(\left\|\frac{\mathbf{x} - \mathbf{x}_i}{h_i}\right\|^2\right). \qquad [5.6]$$

To proceed in the feature space analysis, we need first to find the modes of the underlying density $f(\mathbf{x})$. These modes are located among the zeros of the gradient of $f(\mathbf{x})$, *i.e.*, $\nabla f(\mathbf{x}) = 0$. The adaptive mean shift allows these zeros to be located without estimating the underlying density.

5.2.2 Density gradient estimation

The gradient density estimator can be obtained using [5.6]:

$$\hat{\nabla} f_K(\mathbf{x}) \equiv \nabla \hat{f}_K(\mathbf{x}) = \frac{2c_{k,d}}{n} \sum_{i=1}^{n} \frac{1}{h_i^d} (\mathbf{x} - \mathbf{x}_i) k' \left(\left\| \frac{\mathbf{x} - \mathbf{x}_i}{h_i} \right\|^2 \right). \quad [5.7]$$

Defining a function $g(x) = -k'(x)$ that exists when the derivative of the kernel profile $k(x)$ exists and using it as a profile, the kernel $G(\mathbf{x})$ is defined as $G(\mathbf{x}) = c_{g,d} g(\|\mathbf{x}\|^2)$ where $c_{g,d}$ is the normalization constant. Using $g(x)$ as a substitute for $k'(x)$ in [5.7], we get

$$\begin{aligned} \hat{\nabla} f_K(\mathbf{x}) &= \frac{2c_{k,d}}{n} \sum_{i=1}^{n} \frac{1}{h_i^d} (\mathbf{x} - \mathbf{x}_i) g \left(\left\| \frac{\mathbf{x} - \mathbf{x}_i}{h_i} \right\|^2 \right) \\ &= \frac{2c_{k,d}}{n} \sum_{i=1}^{n} \left[g \left(\left\| \frac{\mathbf{x} - \mathbf{x}_i}{h_i} \right\|^2 \right) \right] \left[\frac{\sum_{i=1}^{n} \frac{1}{h_i^d} \mathbf{x}_i g \left(\left\| \frac{\mathbf{x} - \mathbf{x}_i}{h_i} \right\|^2 \right)}{\sum_{i=1}^{n} \frac{1}{h_i^d} g \left(\left\| \frac{\mathbf{x} - \mathbf{x}_i}{h_i} \right\|^2 \right)} - \mathbf{x} \right]. \end{aligned} \quad [5.8]$$

In [5.8], the first term of the product is proportional to the density estimate at point $\mathbf{x}$ with kernel G

$$\hat{f}_G(\mathbf{x}) = \frac{1}{n} \sum_{i=1}^{n} \frac{1}{h_i^d} g \left(\left\| \frac{\mathbf{x} - \mathbf{x}_i}{h_i} \right\|^2 \right) \quad [5.9]$$

while the second term is the mean shift

$$\boldsymbol{m}_G(\mathbf{x}) = \frac{\sum_{i=1}^{n} \frac{1}{h_i^{d+2}} \mathbf{x}_i g \left(\left\| \frac{\mathbf{x} - \mathbf{x}_i}{h_i} \right\|^2 \right)}{\sum_{i=1}^{n} \frac{1}{h_i^{d+2}} g \left(\left\| \frac{\mathbf{x} - \mathbf{x}_i}{h_i} \right\|^2 \right)} - \mathbf{x}. \quad [5.10]$$

5.2.3 Convergence condition

The sequence of successive locations of the kernel G is denoted as $\{\mathbf{y}_j\}_{j=1,2,\ldots}$. The following iterative procedure

$$\mathbf{y}_{j+1} = \frac{\sum_{i=1}^{n} \frac{\mathbf{x}_i}{h_i^{d+2}} g\left(\left\|\frac{\mathbf{y}_j - \mathbf{x}_i}{h_i}\right\|^2\right)}{\sum_{i=1}^{n} \frac{1}{h_i^{d+2}} g\left(\left\|\frac{\mathbf{y}_j - \mathbf{x}_i}{h_i}\right\|^2\right)} \quad j = 1, 2, \ldots \qquad [5.11]$$

is a hill climbing technique to the nearest stationary point of the density until the density gradient vanishes. The points of convergence of this iterative procedure are the local maxima (modes) of the density (Georgescu et al., 2003).

5.2.4 Adaptive mean shift mode detection and bandwidth estimation

Let $\mathbf{y}_c$ and $\hat{f}_K = \hat{f}_K(\mathbf{y}_c)$ be the convergence points of $\{\mathbf{y}_j\}_{j=1,2,\ldots}$ and $\{\hat{f}_K(\mathbf{y}_j)\}_{j=1,2,\ldots}$, respectively. The j-th mean shift vector can be written as

$$\boldsymbol{m}_G(\mathbf{y}_j) = \mathbf{y}_{j+1} - \mathbf{y}_j, \qquad [5.12]$$

and the gradient at $\mathbf{y}_c$ is zero, *i.e*,

$$\nabla \hat{f}_K(\mathbf{y}_c) = 0. \qquad [5.13]$$

The bandwidth values associated with the data points can be estimated using different methods in the literature. Most of these methods use a pilot density estimate and the simplest one uses nearest neighbours (Georgescu et al., 2003). More precisely, defining $\mathbf{x}_{i,k}$ as the k-nearest neighbour of $\mathbf{x}_i$, the bandwidth h_i associated with $\mathbf{x}_i$ can be computed using the ℓ_1 norm as follows

$$h_i = \|\mathbf{x}_i - \mathbf{x}_{i,k}\|_1. \qquad [5.14]$$

The number of nearest neighbours should be large enough to ensure that there is an increase in density within the support of most kernels having the bandwidth h_i.
A practical algorithm for mode detection can be summarized as in (Comaniciu and Meer, 2002):

- Run the adaptive mean shift to find the stationary points of $\hat{f}_K$;
- Prune these points by keeping only the local maxima.

An intuitive description of the mean shift algorithm is described in Fig. 5.2. This figure shows the movement of the center of mass $\mathbf{y}_j$ to the mode in an iterative procedure until convergence.

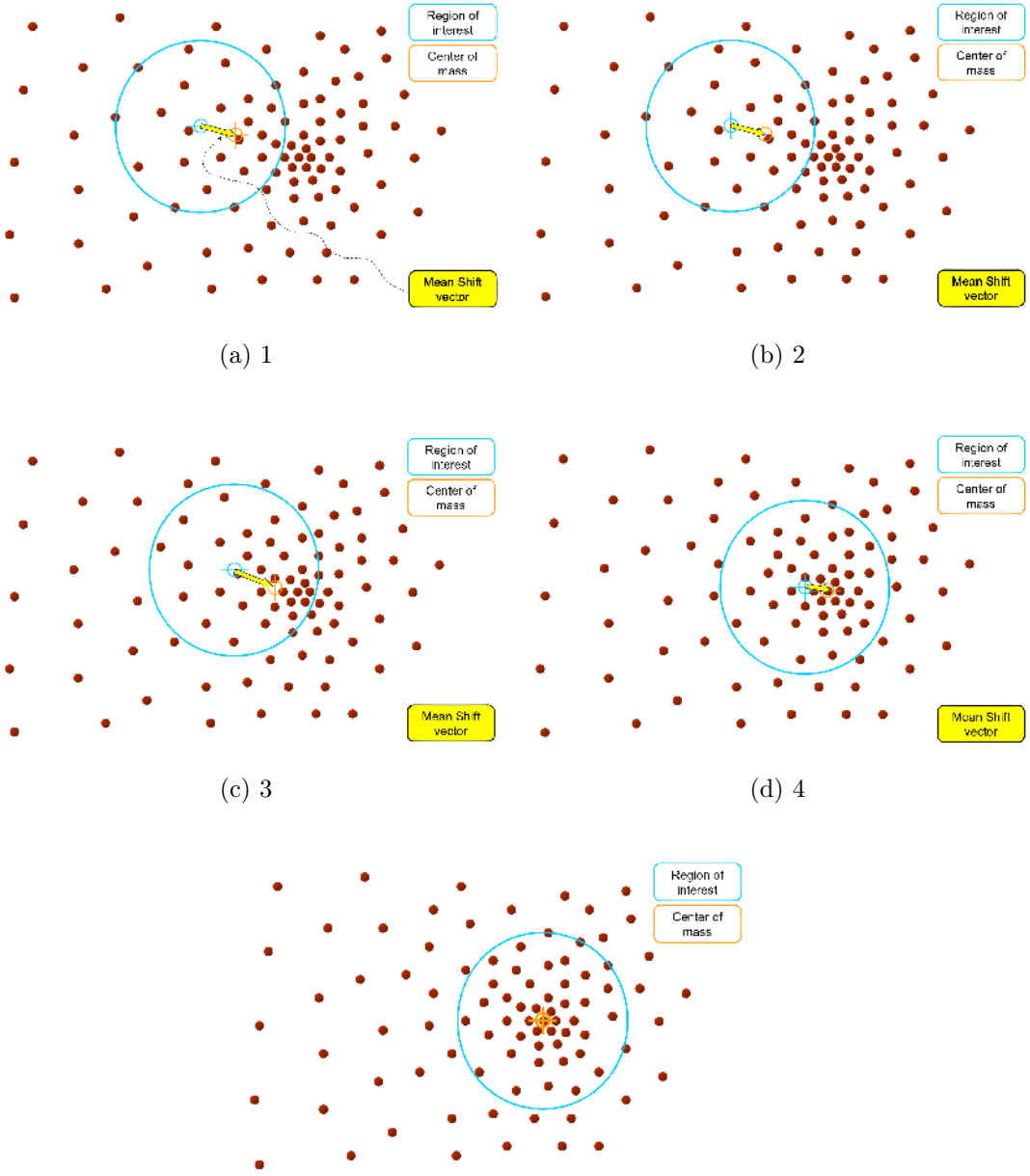

(a) 1 (b) 2

(c) 3 (d) 4

(e) 5

Figure 5.2: Intuitive description of the mean shift algorithm (Yaron and Bernard, 2004).

5.3 AMS within the VEM framework of the JPDE model

The AMS-JPDE model relies on the VEM algorithm for inference as in the standard JPDE model. However, modifications were carried out to embed the AMS algorithm within the VEM framework. We updated the hierarchy of the JPDE model in a way such that no spatial prior is imposed over the HRF groups assignment variable $\boldsymbol{z}$. The hierarchy of the AMS-JPDE model is shown in Fig. 5.3 where the dependencies between observed and latent variables are illustrated. The difference between Fig. 5.3 and Fig. 3.2 is that in the first one there is no prior over the variable of the parcellation labels $\boldsymbol{z}$. The posterior distribution of the AMS-JPDE is the same as in the standard model, *i.e.*, $p^{(r)}(\boldsymbol{A}, \boldsymbol{H}, \boldsymbol{Q}, \boldsymbol{z}; \boldsymbol{Y}, \boldsymbol{\Theta})$ is approximated as a product of the distributions $\tilde{p}_A^{(r)}(\boldsymbol{A})$, $\tilde{p}_H^{(r)}(\boldsymbol{H})$, $\tilde{p}_Q^{(r)}(\boldsymbol{Q})$ and $\tilde{p}_z^{(r)}(\boldsymbol{z})$. Using the VEM algorithm for inference, we have four different expectation steps (VE-A, VE-H, VE-Z and VE-Q), one for each of the missing variables. However, in the AMS-JPDE the expectation over $\boldsymbol{z}$ is different compared to the standard JPDE model while the other expectation steps (VE-A, VE-Q and VE-H) are the same (see (Chaari et al., 2012, 2015) and Subsection 3.2.3).

- **VE-A step:** This step is exactly the same as in the standard JPDE model((Chaari et al., 2012, 2015)). It reads as follows

$$\widetilde{p}_A^{(r)}(\boldsymbol{A}) \propto \exp\left(\mathrm{E}_{\widetilde{p}_H^{(r)}\widetilde{p}_Q^{(r-1)}}\left[\log p(\boldsymbol{A} \,|\, \boldsymbol{Y}, \boldsymbol{H}, \boldsymbol{Q}; \boldsymbol{\Theta}^{(r-1)})\right]\right). \qquad [5.15]$$

- **VE-Q step:** It corresponds to the VE-Q step of the standard JPDE model((Chaari et al., 2012, 2015))

$$\widetilde{p}_Q^{(r)}(\boldsymbol{Q}) \propto \exp\left(\mathrm{E}_{\widetilde{p}_A^{(r)}}\left[\log p(\boldsymbol{Q} \,|\, \boldsymbol{Y}, \boldsymbol{A}; \boldsymbol{\Theta}^{(r-1)})\right]\right). \qquad [5.16]$$

- **VE-H step:** As in the standard JPDE model, the VE-H step is

$$\widetilde{p}_H^{(r)}(\boldsymbol{H}) \propto \exp\left(\mathrm{E}_{\widetilde{p}_A^{(r-1)}\widetilde{p}_z^{(r-1)}}\left[\log p(\boldsymbol{H} \,|\, \boldsymbol{Y}, \boldsymbol{A}, \boldsymbol{z}; \boldsymbol{\Theta}^{(r-1)}\right]\right). \qquad [5.17]$$

- **VE-Z step:** This step is similar to the VE-Z step in the standard JPDE model (Chaari et al., 2012, 2015). Neglecting the term that

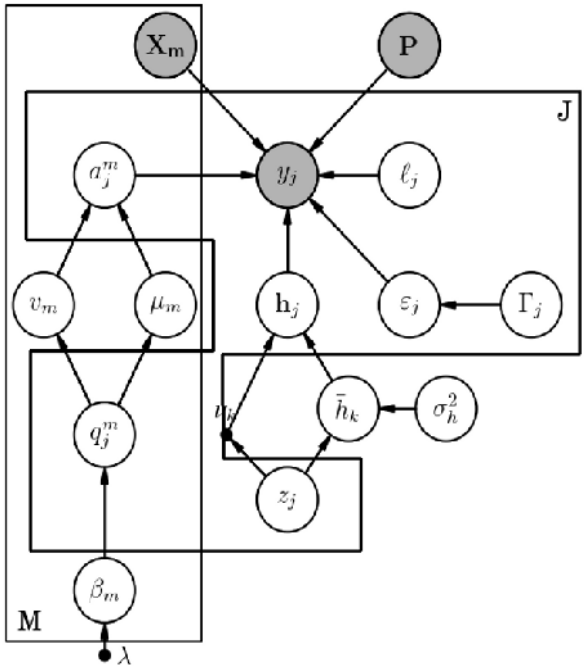

Figure 5.3: Graphical model describing the hierarchy of the AMS-JPDE model.

comes from the spatial prior over the labels $\boldsymbol{z}$, $\widetilde{p}_{z_j}$ can be rewritten as follows

$$\begin{aligned}\widetilde{p}_{z_j}^{(r)}(k) &\propto \mathcal{N}\left(\boldsymbol{m}_{H_j}^{(r)}; \bar{\boldsymbol{h}}_k^{(r-1)}, \bar{\boldsymbol{\Sigma}}_k^{(r-1)}\right), \\ &\propto \exp\left(-\left(\boldsymbol{m}_{H_j}^{(r)} - \bar{\boldsymbol{h}}_k^{(r-1)}\right)^T \bar{\boldsymbol{\Sigma}}_k^{-1}\left(\boldsymbol{m}_{H_j}^{(r)} - \bar{\boldsymbol{h}}_k^{(r-1)}\right)\right) \end{aligned} \quad [5.18]$$

where $\bar{\boldsymbol{h}} = \left(\bar{\boldsymbol{h}}_k\right)_{1\leq k\leq K}$ are the modes of the parcels (HRF patterns) obtained by the AMS algorithm in the maximization step at iteration $(r-1)$.

- **M-Step:** In the maximization step, the HRF profiles $\bar{\boldsymbol{h}} = \left(\bar{\boldsymbol{h}}_k\right)_{1\leq k\leq K}$ corresponding to the estimated parcels are obtained using the AMS algorithm while the maximization of the rest of the parameters remains the same as in the standard JPDE model. The corresponding M-step for the AMS-JPDE model reads

$$\boldsymbol{\Theta}^{(r)} = \arg\max_{\boldsymbol{\Theta}} \left[\mathrm{E}_{\tilde{p}_A^{(r)}\tilde{p}_H^{(r)}\tilde{p}_Q^{(r)}\tilde{p}_z^{(r)}}\left[\log p\left(\boldsymbol{Y}, \boldsymbol{A}, \boldsymbol{H}, \boldsymbol{Q}, \boldsymbol{z}; \boldsymbol{\Theta}\right)\right]\right]. \quad [5.19]$$

Eq. [5.19] can be rewritten as

$$\begin{aligned}\boldsymbol{\Theta}^{(r)} = \; & \arg\max_{\boldsymbol{\Theta}} \Big[\mathrm{E}_{\tilde{p}_A^{(r)}\tilde{p}_H^{(r)}}\left[\log p(\boldsymbol{Y} \mid \boldsymbol{A}, \boldsymbol{H}; \boldsymbol{L}, \boldsymbol{\Gamma})\right] \\ & + \mathrm{E}_{\tilde{p}_A^{(r)}\tilde{p}_Q^{(r)}}\left[\log p(\boldsymbol{A} \mid \boldsymbol{Q}; \boldsymbol{\mu}, \boldsymbol{v})\right] + \mathrm{E}_{\tilde{p}_Q^{(r)}}\left[\log p(\boldsymbol{Q}; \boldsymbol{\beta})\right] \\ & + \mathrm{E}_{\tilde{p}_H^{(r)}\tilde{p}_z^{(r)}}\left[\log p(\boldsymbol{H} \mid \boldsymbol{z}; \bar{\boldsymbol{h}}, \boldsymbol{\nu})\right]\Big]. \end{aligned} \quad [5.20]$$

The term $\mathrm{E}_{\tilde{p}_H^{(r)}\tilde{p}_z^{(r)}}\left[\log p(\boldsymbol{H} \mid \boldsymbol{z}; \bar{\boldsymbol{h}}, \boldsymbol{\nu})\right]$ is associated with the maximization of $\bar{\boldsymbol{h}}$ and is replaced by the modes obtained using the AMS algorithm (see Section 5.2 for more details).

5.3.1 HRF profile smoothing

One of the remaining issues in this model is to control the smoothness of the HRF profiles. In the standard JPDE model, the smoothness of $\left(\bar{\boldsymbol{h}}_k\right)_{1\leq k\leq K}$ is favoured by controlling their second order derivatives with the following prior: $\bar{\boldsymbol{h}}_k \sim \mathcal{N}\left(0, \sigma_h^2 \boldsymbol{R}\right)$. In the AMS-JPDE model, we rely on a weighted least squares regularization technique for smoothness. The idea of this technique is to obtain a smooth signal from the noisy one. The energy of the second

order derivative of a signal can be used as a measure of its smoothness, *i.e*, the smoother the signal, the smaller the energy of its derivative. Let $\mathbf{x}$ be the smooth signal that we are looking for and defined as

$$\begin{bmatrix} x_1 \\ x_2 \\ \vdots \\ x_N \end{bmatrix}$$

,

and $\mathbf{y} = \mathbf{x} + \mathbf{n}$ is the corresponding noisy signal. Let $\boldsymbol{D}_2$ be a matrix defined as

$$\begin{bmatrix} 1 & -2 & 1 & \dots & \dots \\ \dots & 1 & -2 & 1 & \dots \\ \dots & \dots & \ddots & \ddots & \dots \\ \dots & \dots & 1 & -2 & 1 \end{bmatrix}$$

Then we can define $\boldsymbol{D}\mathbf{x}_2$ as a second order difference of the signal $\mathbf{x}$. It follows that if $\mathbf{x}$ is smooth then $\|\boldsymbol{D}\mathbf{x}\|_2^2$ has a small value. If $\mathbf{y} = \mathbf{x} + \mathbf{n}$ is a noisy signal, the signal $\mathbf{x}$ can be recovered by solving the following problem

$$\min_{\mathbf{x}} \|\mathbf{y} - \mathbf{x}\|_2^2 + \lambda_h \|\boldsymbol{D}\mathbf{x}_2\|_2^2. \qquad [5.21]$$

On one hand minimizing $\min_{\mathbf{x}} \|\mathbf{y}-\mathbf{x}\|_2^2$ forces the smooth signal $\mathbf{x}$ to be close to the noisy one $\mathbf{y}$. On the other hand, minimizing the term $\|\boldsymbol{D}\mathbf{x}\|_2^2$ favours the smoothness of $\mathbf{x}$. The parameter λ_h balances the solution between the first (data fidelity) and the second (penalization) terms and is fixed by the user. Straightforward computations lead to the following $\mathbf{x}$ that minimizes the expression in [5.21]

$$\hat{\mathbf{x}} = \left(\boldsymbol{I}_D + \lambda_h \boldsymbol{D}_2^{\mathrm{t}} \boldsymbol{D}_2\right)^{-1} \mathbf{y}. \qquad [5.22]$$

Assuming that the output of the AMS algorithm is the noisy signal $\mathbf{y}$ denoted as $\bar{\boldsymbol{h}}_k^0$ and the signal we are seeking $\mathbf{x}$ is the smooth HRF profile denoted as $\bar{\boldsymbol{h}}_k$, [5.22] leads to

$$\bar{\boldsymbol{h}}_k = \left(\boldsymbol{I}_D + \lambda_h \boldsymbol{D}_2^{\mathrm{t}} \boldsymbol{D}_2\right)^{-1} \bar{\boldsymbol{h}}_k^0. \qquad [5.23]$$

Note that such a regularization is equivalent to fixing a Gaussian prior on $\bar{\boldsymbol{h}}_k$ in the hierarchical Bayesian model of the standard JPDE model.
The different steps in the AMS-JPDE are summarized in Algorithm 5.1

Algorithm 5.1 The AMS-JPDE model algorithm. The subscript (r) refers to the current iteration.

Initialization:

set the truncation level for the number of parcels T.
$\tilde{p}_z^{(0)}(\boldsymbol{z})$ initialized randomly for a uniform distribution.
$\tilde{p}_Q^{(0)}(\boldsymbol{Q})$ such that $\tilde{p}_{Q_j}^{(0)}(q_j^m) \in \{0, 1\}$.
for all j
- $\boldsymbol{m}_{H_j}^{(0)}$ is initialized from the canonical HRF.
- $\boldsymbol{m}_{A_j}^{(0)}$ is initialized with zeros.

end for
Initialize with some $\boldsymbol{\Theta}^{(0)}$.

$r = 1$
repeat
Expectation step:
Compute $\tilde{p}_H^{(r)}(\boldsymbol{H})$ according to [3.18].
Compute $\tilde{p}_A^{(r)}(\boldsymbol{A})$ according to [3.19].
Compute $\tilde{p}_Q^{(r)}(\boldsymbol{Q})$ according to [3.24].
Compute $\tilde{p}_z^{(r)}(\boldsymbol{z})$ according to [5.18]
Maximization step:
Compute $\boldsymbol{\Theta}^{(r)}$ according to [5.20].
Compute $\bar{\boldsymbol{h}}$ using the AMS algorithm
Input: The mean of the voxel-dependent HRFs $\boldsymbol{m}_H$.
Output: The HRF profiles $\bar{\boldsymbol{h}}$.
for all j **do**
- Compute the gradient for $\boldsymbol{m}_{H_j}$ using [5.8] and [5.14] to estimate the bandwidth associated with the neighbours of $\boldsymbol{m}_{H_j}$.
- Compute the mean shift victor using [5.10].
- Compute the convergence condition using [5.11].

end for
for all k **do**
Obtain the smooth HRF using [5.23].
end for
set $r \leftarrow r + 1$
until convergence

5.4 Experimental validation

To validate the AMS based parcellation with the JPDE model, we performed numerical experiments on both synthetic and real data[1].

5.4.1 Synthetic fMRI time series

The proposed model was validated using four different experiments. Different parcellation masks (see Fig. 5.4) were used to generate the BOLD signal according to [3.1]. We considered two experimental conditions, *i.e.*, $M = 2$ with 30 trials for each. The reference binary labels used for these experiments are shown in Fig. 5.5.

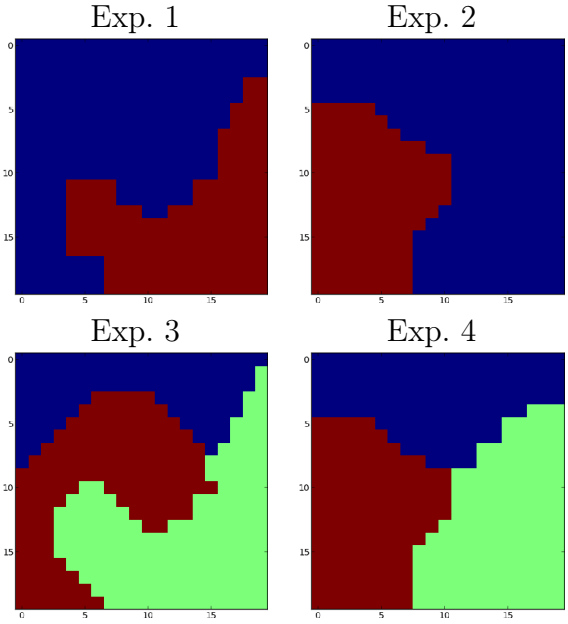

Figure 5.4: Reference parcellations (RP) used for the 4 experiments (grid size = 20×20).

The NRLs were simulated from their prior conditionally to the activation labels $\boldsymbol{Q}$ (shown in Fig. 5.5). More precisely, given the 20×20 binary labels of Fig. 5.5, the NRLs were simulated as follows: for $m = 0, 1$, $a_j^m \,|\, q_j^m =$

[1]These experiments were implemented in Python within the framework offered by the Pyhrf software (Vincent et al., 2014), see also `http://pyhrf.org`.

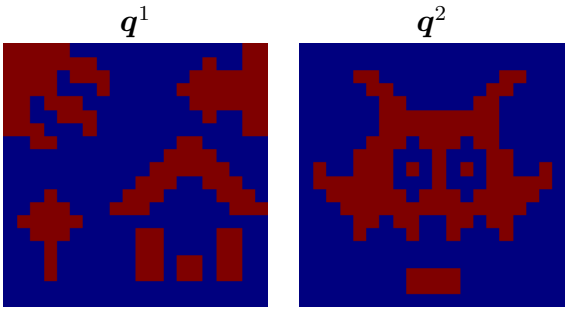

Figure 5.5: Reference activation labels for the two experimental conditions (grid size = 20×20).

$0 \sim \mathcal{N}(0, 0.5)$ and $a_j^m \,|\, q_j^m = 1 \sim \mathcal{N}(3.2, 0.5)$.The inter-stimuli interval and variance used to generate the onsets of the trials were 3 s and 5 s, respectively. Finally, the fMRI time series $\boldsymbol{y}_j$ were generated according to [3.1] with $\Delta t = 0.5$ and $TR = 1$ s. As a ground truth for the parcellation, different HRF groups were considered. We analysed the generated fMRI time series for the four experiments using the AMS-JPDE model. The parcellation estimate for each experiment is shown in Fig. 5.7. It is worth noticing that for the AMS-JPDE, no prior initialization for the parcellation or truncation level for the maximum number of parcels is needed. The number of K-nearest neighbours (K_{NN}) is the only parameter that needs to be manually set. For the synthetic data experiments, we empirically set $K_{NN} = 50$[2]. The computed parcellation errors between the reference and the estimated

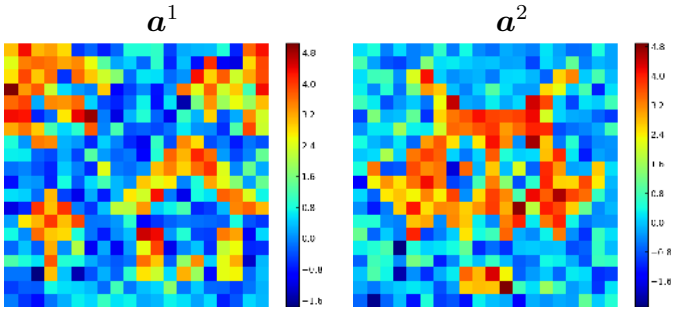

Figure 5.6: Reference NRLs for the two experimental conditions (grid size = 20×20).

parcellation were $2.25\%, 3.25\%, 4.5\%$ and 4.75% for Exp. 1 to 4, respectively.

[2]The parameter K_{NN} is adjusted using cross validation.

These results show a good ability of the AMS-JPDE to recover the hemodynamic territories with low error probability. Moreover, for each experiment, we computed the confusion matrix between the reference and the estimated parcellation. The results displayed in Tables. 5.1 and 5.2 show a major intersection between them. Although some voxels were misclassified (since no spatial constraints are imposed over the parcellation step), the AMS-JPDE model managed to establish a good parcellation especially for those voxels located on the borders between parcels. The results of the AMS-JPDE model were coherent with the results of the model selection procedure in (Albughdadi et al., 2014) that calculates the free energy of different competing models each with k^{ω} parcels and $K^{\omega} = \omega + 1$, $\omega \in \{1, \ldots, 3\}$. The models maximizing the free energy are the best fit for the data. These optimal

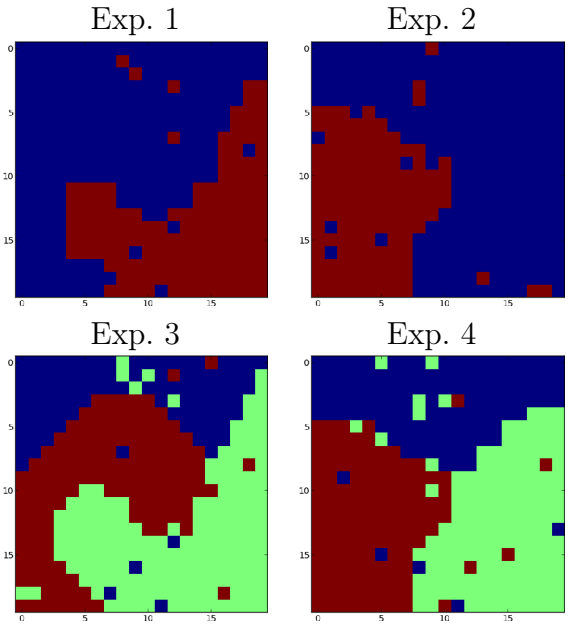

Figure 5.7: Estimated parcellations (EP) used for the 4 experiments (grid size = 20×20).

models lead to two parcels for Exp. 1 and 2 and three parcels for Exp. 3 and 4. Fig. 5.8 shows a 3-D representation of the parcellation result for each experiment where each point corresponds to a projection of a given vector on the three main principal components computed using a principal component analysis (PCA). For each experiment in Fig. 5.8, each color represents one of the estimated parcels such that all the voxels that have similar HRF charac-

teristics have the same color. Regarding the running time of the algorithm and considering Exp. 4 as an example, using the model selection procedure in (Albughdadi et al., 2014) the accumulated time required to run the 3 competing models is around 35 mins. On the other hand, the AMS-JPDE model takes around 11 mins while it takes around 9 mins to run the same experiment using the NP-JPDE model. Thus, the computational time of the AMS-JPDE is reduced compared to free energy calculations of the competing models and is still reasonable when compared to the computational time of the NP-JPDE model. We also explored the ability of the AMS-JPDE model to estimate the HRF profiles for the estimated parcels, as shown in Fig. 5.9. The modes of the parcels are the outputs of the mean shift algorithm which represent the HRF estimate for each parcel. Note that the estimates are close to the corresponding ground truths. The AMS-JPDE also managed to obtain a good performance in detecting the activation as in the JPDE and NP-JPDE models. The mean square error (MSE) was computed for each experimental condition in the four experiments. These results are reported in Tab. 5.3

Table 5.1: Confusion matrices for Exp. 1 and 2. RP and EP refer to the reference and the estimated parcellations, respectively.

RP \ EP	Parcel. 1		Parcel. 2	
	Exp. 1	Exp. 2	Exp. 1	Exp. 2
Parcel. 1	**0.98**	**0.98**	0.03	0.05
Parcel. 2	0.02	0.02	**0.97**	**0.95**

Table 5.2: Confusion matrices for Exp. 3 and 4. RP and EP refer to the reference and the estimated parcellations, respectively.

RP \ EP	Parcel. 1		Parcel. 2		Parcel. 3	
	Exp. 3	Exp. 4	Exp. 3	Exp. 4	Exp. 3	Exp. 4
Parcel. 1	**0.93**	**0.94**	0.02	0.01	0.01	0.02
Parcel. 2	0.05	0.01	**0.96**	**0.96**	0.02	0.02
Parcel. 3	0.02	0.05	0.02	0.03	**0.97**	**0.96**

We were able to prove numerically the convergence of the AMS-JPDE algorithm by calculating the free energy for 100 iterations, which is supposed to be strictly monotonic. The calculated free energy at each iteration is

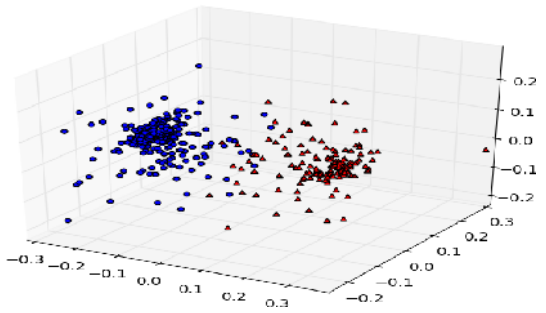

(a) Exp. 1

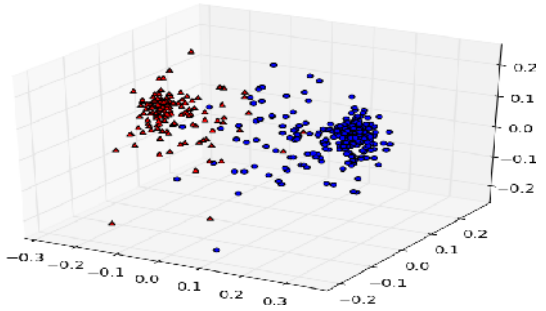

(b) Exp. 2

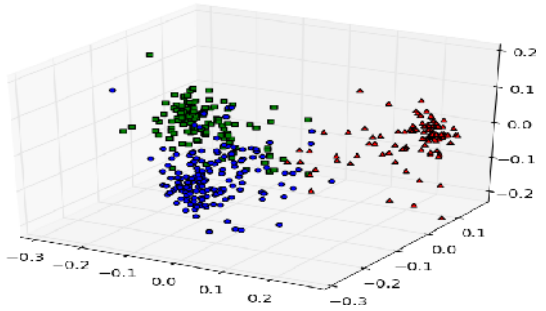

(c) Exp. 3

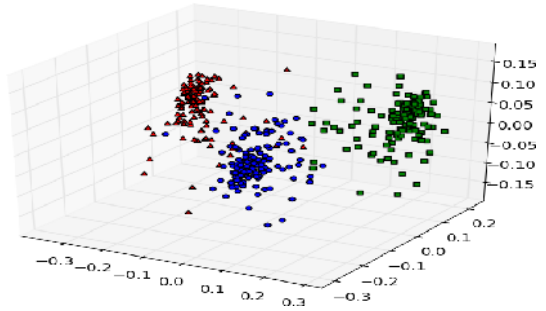

(d) Exp. 4

Figure 5.8: Transformed voxel-dependent HRFs in 3-D representation using PCA with HRF groups labels.

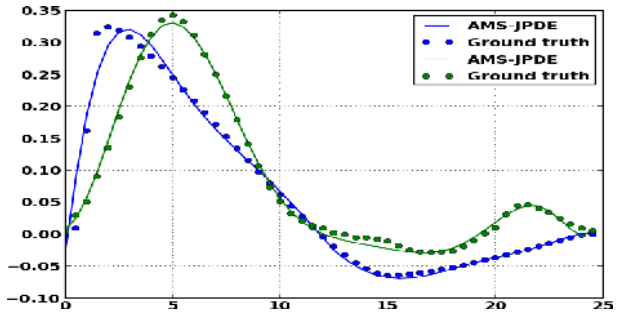

(a) Exp. 1

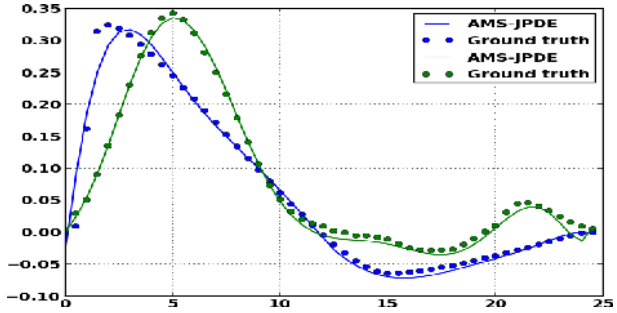

(b) Exp. 2

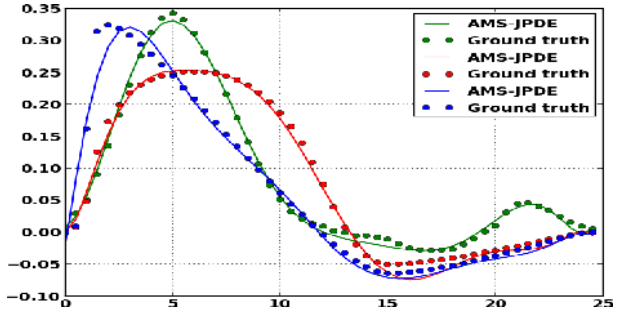

(c) Exp. 3

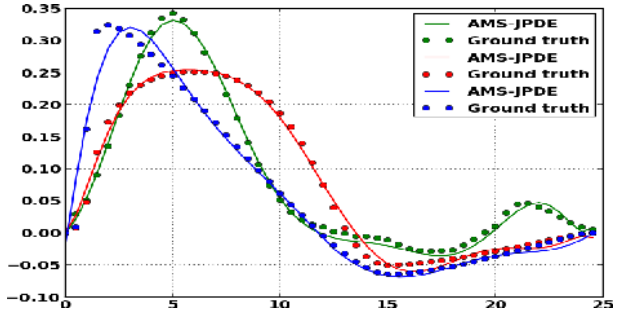

(d) Exp. 4

Figure 5.9: HRF estimates for the synthetic data experiments.

Table 5.3: MSEs of NRLs and activation labels estimates using the AMS-JPDE model.

		Exp. 1	Exp. 2	Exp. 3	Exp. 4
NRLs	$m = 1$	0.008	0.008	0.009	0.007
	$m = 2$	0.005	0.006	0.004	0.005
Labels	$m = 1$	0.003	0.003	0.002	0.003
	$m = 2$	0.001	0.008	0.006	0.006

shown in Fig. 5.10. Thus, using an approximate E-$\boldsymbol{Z}$ step does not have a noticeable effect on the convergence of the algorithm. However, this issue needs to be proven numerically by deriving a lower bound of the posterior distribution over $\boldsymbol{z}$, which will be one of the perspectives of a future work.

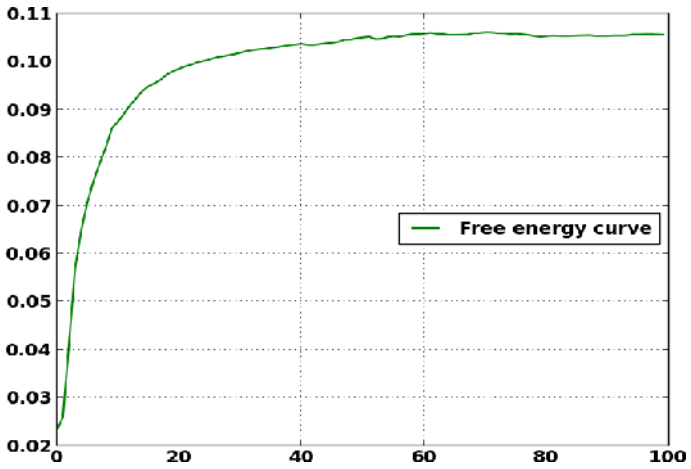

Figure 5.10: The calculated free energy of the AMS-JPDE algorithm at 100 iterations.

5.4.2 Real data

Two experiments were conducted on real fMRI data to validate the AMS-JPDE model. The considered regions of interest (ROI) were the right motor cortex and the bilateral occipital cortex (see Subsection. 4.3.2 for more information about the ROIs). The fMRI data were collected using a gradient-echo EPI sequence (TE = 30 ms/TR = 2.4 s /thickness = 3 mm/ FOV = 192×192 mm^2, matrix size: 96×96) with a 3 Tesla magnetic field during a localizer

experiment. Sixty auditory, visual and motor stimuli were involved in the paradigm and defined in ten experimental conditions ($M = 10$). During the experiment, $N = 128$ scans were acquired and $\Delta t = 0.6$ s. The number of K-nearest neighbours was set to $K_{NN} = 50$[3]. Analyzing the fMRI data of the two experiments using the AMS-JPDE model, one parcel was estimated in the right motor cortex as shown in Fig. 5.11. The corresponding HRF

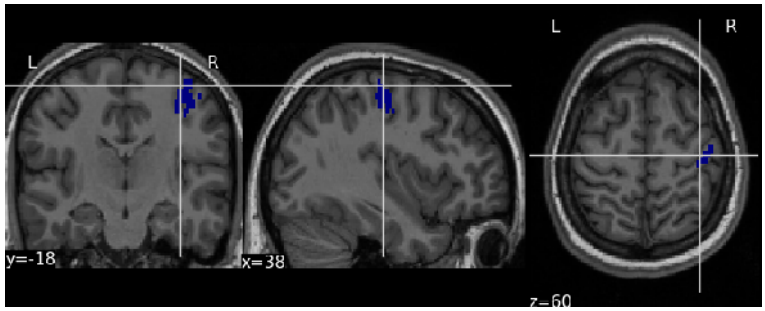

Figure 5.11: The estimated parcellation in the right motor cortex.

estimate of the detected parcel is shown in Fig. 5.12 along with the canonical HRF shape. The computed time to peak for the estimated HRF is TTP = 4.8 s and the full width at half maximum is FWHM = 4.8 s too. We can notice that the HRF estimate is close to the canonical HRF as demonstrated in (Badillo et al., 2013b; Albughdadi et al., 2016c). To further investigate the closeness of the HRF estimate to the canonical HRF, we computed the Euclidean distance between both of them and it was 0.45. This result is similar to the computed Euclidean distance between the HRF profile estimated by the NP-JPDE JDE models and the canonical HRF. As regards the NRL estimates, Fig. 5.13 and 5.14 show these estimates with respect to specific experimental conditions, as we expected activation in the right motor cortex in response to motor tasks (left and right video click- left and right audio click). These results are similar to those obtained by the NP-JPDE and JDE models (see Figs. 4.13,4.14,4.15 and 4.16).

Running the second experiment using the AMS-JPDE model, 3 parcels were estimated as shown in Fig. 5.15. The corresponding HRF shape estimates are shown in Fig. 5.16. The computed time to peak (TTP) for the HRF estimates was 5.4 s for all of them while the full width at half maximum (FWHM) was 4.2 s for parcels 1 and 3 and 4.8 s for parcel 2.

[3]The parameter K_{NN} was adjusted using cross validation.

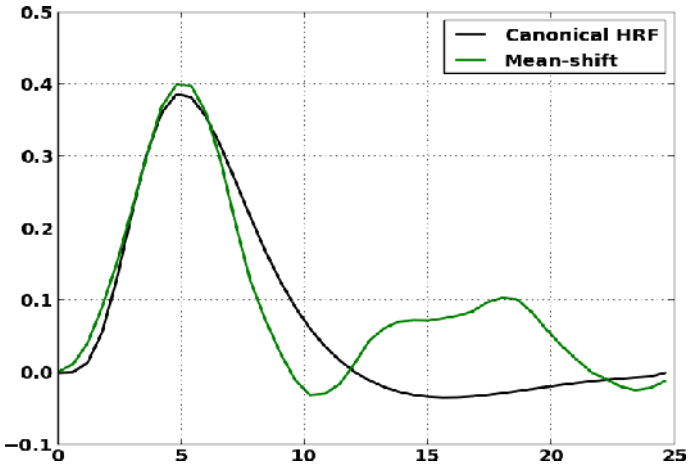

Figure 5.12: HRF shape estimates using the AMS-JPDE model in the bilateral occipital cortex and the canonical HRF.

The obtained results are coherent with the conclusion that the HRF estimates in the bilateral occipital cortex should be consistent with the canonical shape (Badillo et al., 2013b; Albughdadi et al., 2016c). We also computed the Euclidean distance between the HRF Estimate and the canonical HRF. The results are reported in Tab. 5.4. The NRLs estimated with the AMS-JPDE model are shown in Fig. 5.17. These results are also coherent with the outputs of the JDE and the NP-JPDE models (see Figs. 4.19 and 4.20).

Table 5.4: The Euclidean distance between the HRF estimates in the bilateral occipital cortex and the canonical HRF. Distance between the individual AMS-JPDE HRF estimates are also provided.

	HRF. 1	HRF. 2	HRF. 3
Canonical HRF	0.31	0.40	0.41
HRF. 2	0.28	–	0.06
HRF. 3	0.30	–	–

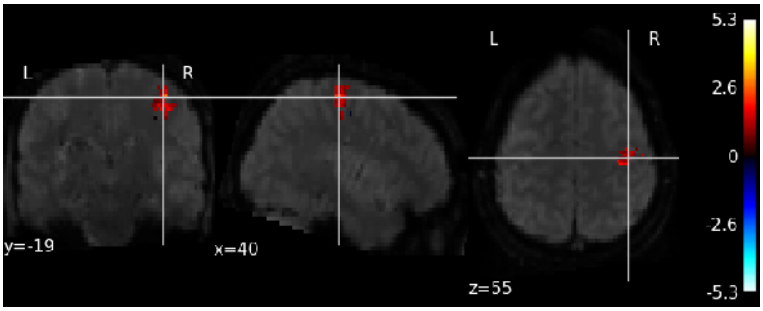

(a) Auditory left click

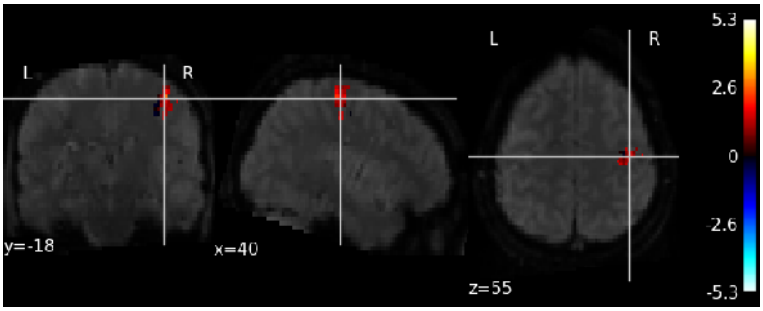

(b) Auditory right click

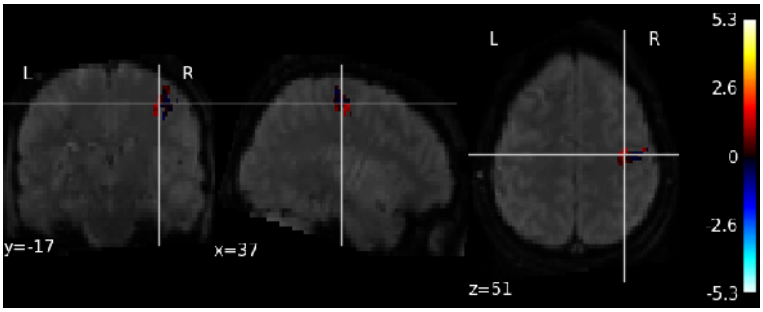

(c) Left click-Right click auditory contrast

Figure 5.13: NRL estimates for the visual left and right click experimental conditions and their computed contrast (left click-right click) using the AMS-JPDE model.

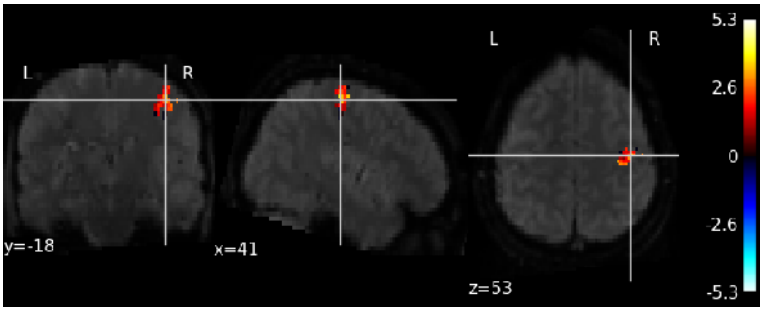

(a) Visual left click

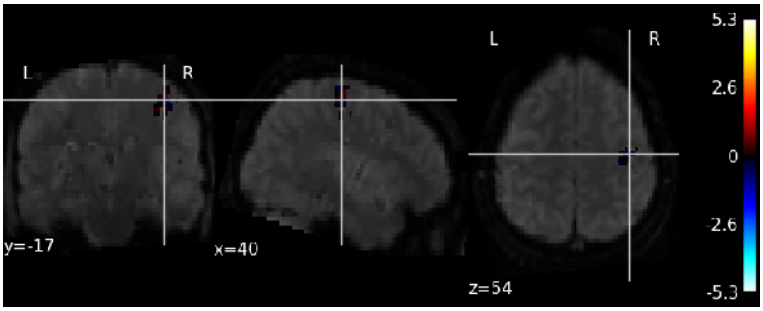

(b) Visual right click

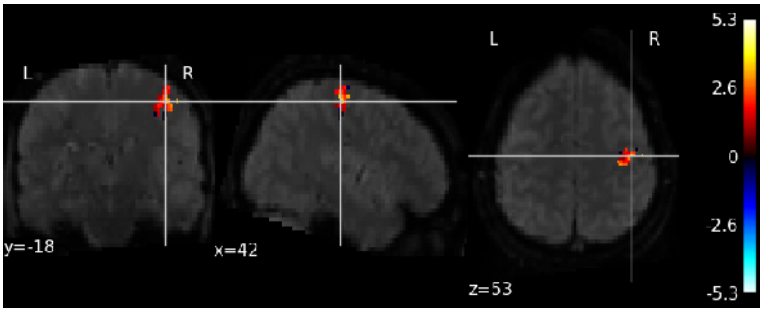

(c) Left click-Right click visual contrast

Figure 5.14: NRL estimates for the auditory left and right click experimental conditions and their computed contrast (left click-right click) using the AMS-JPDE model.

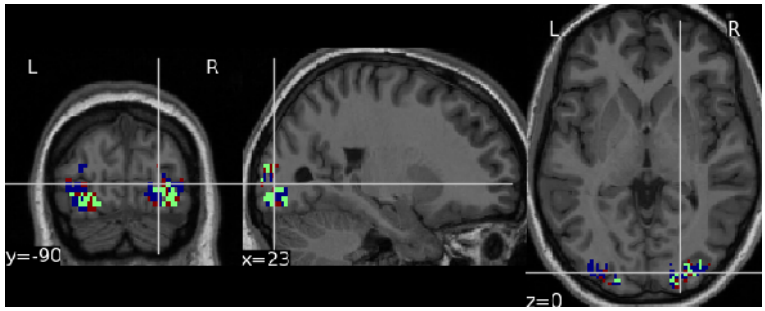

Figure 5.15: The estimated parcellation in the bilateral occipital cortex.

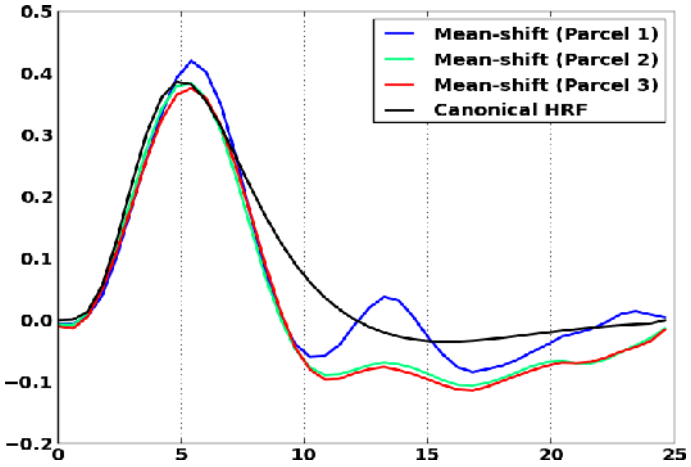

Figure 5.16: HRF shape estimates using the AMS-JPDE model in the bilateral occipital cortex and the canonical HRF.

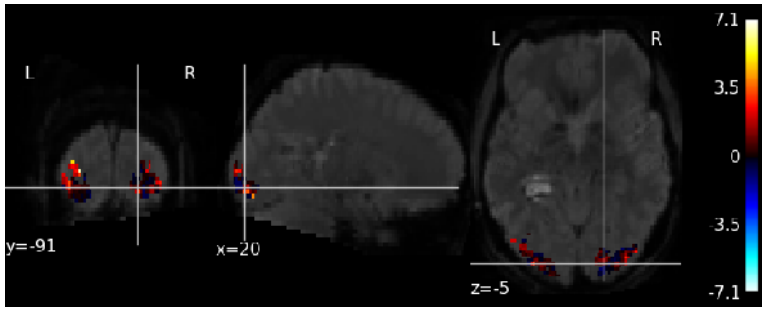

(a) Vertical checkerboard

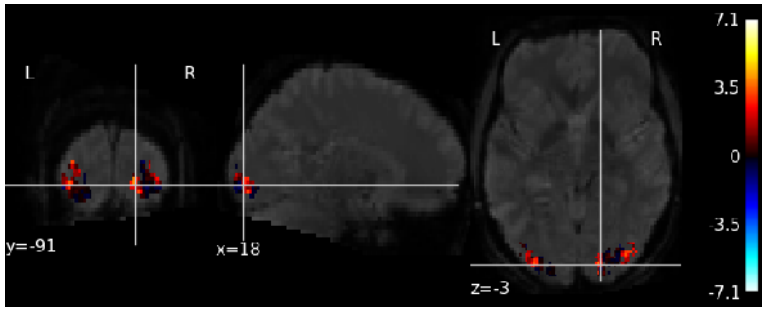

(b) Video sentences

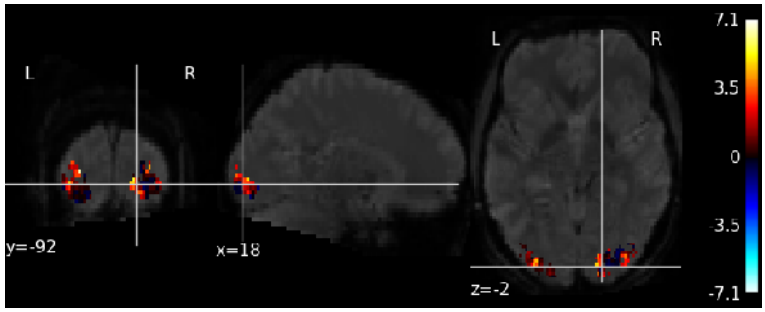

(c) Horizontal checkerboard

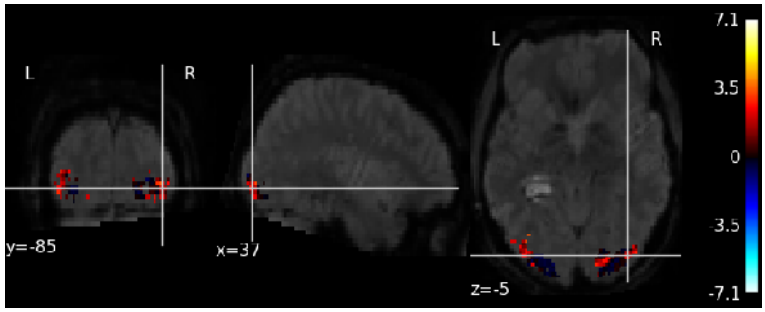

(d) Video calculations

Figure 5.17: NRL estimates for the visual sentences and calculations, horizontal and vertical checkerboards experimental conditions using the AMS-JPDE model.

5.5 Conclusion

In this chapter, we proposed a new non-parametric approach to automatically estimate the hemodynamic parcellation in fMRI analysis. This automatic parcellation was performed along with the detection and estimation task by making use of the well known adaptive mean shift algorithm. This algorithm was embedded within the VEM framework of the standard JPDE model yielding the AMS-JPDE model. More precisely, it was used in the maximization step to estimate the HRF profiles. Moreover, the expectation over the HRF group labels $\boldsymbol{z}$ was replaced by an approximation step which is the same as in the JPDE model but with omitting the term that comes from the Potts model. The standard JPDE model hierarchy was modified by removing the Potts model prior over the parcellation labels $\boldsymbol{z}$. The combination of the adaptive mean shift and the JPDE model was motivated by the fact that the deep hierarchy of the NP-JPDE model could make the analysis results sensitive to some parameters that are manually adjusted such as the interaction parameter β_z of the Potts model. This model was validated using synthetic and real data. In synthetic data experiments, the AMS-JPDE managed to estimate the correct number of parcels and accurate parcellation estimates with low error probabilities. The corresponding HRF profiles were close to the reference ones. In the real data experiments, the two ROIs that had been used to validate the NP-JPDE were analyzed with the AMS-JPDE model. The results obtained with the AMS-JPDE are similar to those obtained by the NP-JPDE and JDE models in the right motor and bilateral occipital cortices. The AMS-JPDE model also managed to preserve a good performance in the detection of the activation as in its ancestors. The main advantage of the AMS-JPDE model is that it does not require many parameters to be tuned. Indeed, the only parameter that needs to be tuned is the number of k-nearest neighbours required in the mean shift algorithm. This model would require further investigation regarding the presence of outliers in the parcellation. This can be solved by a robust post-processing or by imposing spatial priors over the data.
The proposed methods presented in the previous chapters tackled the parcellation challenge at the subject-level. However, few approaches have been proposed to tackle the parcellation and estimation tasks at the group-level, which will be investigated thoroughly in the two last chapters of this manuscript.

CHAPTER 6

Multi-Subject Joint Parcellation Detection Estimation

Contents

6.1 Introduction

Recent fMRI studies focus on the multi-subject designs to study a specific population or disease (Badillo et al., 2014, 2013b; Degras and Lindquist, 2014; Zhang et al., 2013). The variability of the hemodynamics in group-level fMRI studies is usually assessed by estimating subject-level HRF profiles and then averaging them over the subjects to derive a group-level HRF (Badillo et al., 2014). However, averaging the HRF profiles over subjects can be sensitive to the presence of outliers. Other sophisticated approaches have been proposed to estimate the group-level HRF profiles from the fMRI data of different subjects. One can mention the approach proposed in (Degras and Lindquist, 2014) in which a linear combination of B-spline functions is used to model the HRFs. This approach is based on the assumption that the

subject-level HRFs are random draws from a population-level distribution and that the population average response for a given voxel varies only in scale across stimuli. In (Badillo et al., 2014), the joint detection estimation (JDE) model is used in a multi-subject analysis where the parcellation is fixed a priori. In this model, an additional layer of hierarchy is added to the hierarchical Bayesian model of JDE to describe the link between the single subject and the group-level HRFs. However, this model does not consider the multi-subject parcellation and it relies on a prior functional parcellation of fMRI data. This parcellation is generated according to the Ward's clustering algorithm by pulling all individual normalized fMRI datasets (Thirion et al., 2006). Another approach was proposed in (Zhang et al., 2013) based on a semi-parametric framework with the general linear model. This approach assumes that for a fixed voxel and a given stimulus, the HRFs share the same unknown functional form across subjects but with different characteristics such as the time to peak, height and width. This common functional form is then estimated using a non-parametric spline-smoothing method. However, none of the approaches proposed in literature allows parcellating the brain into regions that show homogeneity in their hemodynamic profiles at the group-level.

In this chapter, a model for multi-subject analysis is proposed, namely the multi-subject joint parcellation detection estimation (MS-JPDE) model (Albughdadi et al., 2016a). The motivation for this model is to obtain estimates of group-level hemodynamic territories in order to address the variability of the hemodynamic response function at the group-level in different brain regions. The MS-JPDE accomplishes the latter objective by allowing the estimation of the group-level parcellation and HRF profiles along with the activation detection for each individual. In the MS-JPDE model, the analysis is done for all the parcels contained in a region of interest contrary to the model proposed in (Badillo et al., 2014) where the analysis is done for a specific parcel.

The rest of the chapter is organized as follows. Section 6.2 introduces the observation model used in the proposed model. Section 6.3 illustrates the Bayesian hierarchy of the MS-JPDE model. The variational inference strategy used to approximate the posterior as the product of simple distributions is studied in Section 6.4. An experimental validation is carried out in Section 6.5 on synthetic and real data. Finally, some conclusions are drawn in Section 6.6.

6.2 Multi-subject observation model

The proposed model is based on the standard JPDE model studied in (Chaari et al., 2012, 2015) (refer to Chapter 3, Section 3.2 for further details). The MS-JPDE model studied in this chapter handles fMRI data related to S subjects involved in a group study where the set of voxels is the same for all the subjects. This is ensured by performing prior registration of the fMRI data in a unique space associated with these subjects. The set of voxels of interest belonging to the whole brain or wide brain area is denoted as $\boldsymbol{\mathcal{P}}$. The fMRI time series at voxel j for subject s is denoted as $\boldsymbol{y}_j^s$. This time series is measured at time instants $\{t_n, n = 1, ..., N\}$ where $t_n = nTR$, N being the number of scans and TR the time of repetition. The number of different stimulus types or experimental conditions is denoted as M. All individuals are involved in the same fMRI experiment (using the same experimental paradigm). At each voxel j of subject s, a voxel dependent HRF $\boldsymbol{h}_j^s \in \mathbb{R}^D$ is considered leading to $\boldsymbol{H}^s = \left\{\boldsymbol{h}_j^s, j \in \boldsymbol{\mathcal{P}}\right\}$ the set of all possible HRF shapes for subject s. Each HRF $\boldsymbol{h}_j^s$ is associated with a group-level HRF class among K^G possible groups. These groups or HRF classes are specified by a set of hidden labels $\boldsymbol{z}^G = \left\{z_j^G, j \in \boldsymbol{\mathcal{P}}\right\}$ where $z_j^G \in \left\{1, ..., K^G\right\}$ and the group-level HRF class labels $\boldsymbol{z}^G$ is a priori assigned a Markov random field, namely a Potts model. The resulting observation model is defined as follows

$$\forall s, \forall j \quad \boldsymbol{y}_j^s = \sum_{m=1}^{M} a_j^{m,s} \boldsymbol{X}_m \boldsymbol{h}_j^s + \boldsymbol{P}\boldsymbol{\ell}_j^s + \boldsymbol{b}_j^s, \tag{6.1}$$

where the matrix $\boldsymbol{X}_m$ is the same for all the subjects, $a_j^{m,s}$ is amplitude of the neural response level (NRL) for subject s, voxel j and the m-th experimental condition . Denote as $\boldsymbol{A}^s = \{\boldsymbol{a}^{m,s}, m = 1, \ldots, M\}$ with $\boldsymbol{a}^{m,s} = \left\{a_j^{m,s}, j \in \boldsymbol{\mathcal{P}}\right\}$. The NRLs are assumed to belong to one of the I groups. These groups are specified by activation class assignment variable $\boldsymbol{Q}^s = \{\boldsymbol{q}^{m,s}, m = 1, \ldots, M\}$ where $\boldsymbol{q}^{m,s} = \left\{q_j^{m,s}, j \in \boldsymbol{\mathcal{P}}\right\}$ and $q_j^{m,s} \in \{0, ..., I-1\}$ represents the activation class at voxel j for the m-th experimental condition. In this model, two classes are considered ($I = 2$) such that $i = 0$ refers to non-activated voxels and $i = 1$ the activated ones. The rest of the signal consists of low frequency drifts which are denoted as $\boldsymbol{P}\boldsymbol{\ell}_j^s$ where $\boldsymbol{P}$ is an $N \times O$ matrix, $\boldsymbol{\ell}_j^s \in \mathbb{R}^O$ is a vector to be estimated and $\boldsymbol{L}^s = \{\boldsymbol{\ell}_j^s, j \in \boldsymbol{\mathcal{P}}\}$. The observation noise is denoted as $\boldsymbol{b}_j^s$ and is assumed to be a zero-mean Gaussian vector with covariance matrix $\boldsymbol{\Gamma}_j^{s\,-1}$, *i.e.*, $\boldsymbol{b}_j^s \sim \mathcal{N}(0, \boldsymbol{\Gamma}_j^{s\,-1})$. The set of

all unknown precision matrices is denoted by $\boldsymbol{\Gamma}^s = \left\{\boldsymbol{\Gamma}_j^s, j \in \boldsymbol{\mathcal{P}}\right\}$. The noises associated with different subjects and different voxels of the same subject are assumed to be independent.

6.3 Hierarchical Bayesian model

This section introduces the Bayesian hierarchy associated with the MS-JPDE model. More precisely, we proposed to extend the model presented in Section 3.2 to the multi-subject case according to the description of the previous section.

(i) **Likelihood**

Following (Makni et al., 2008; Woolrich et al., 2001; Chaari et al., 2011, 2012), an AR noise model is adopted to account for serial correlation in fMRI time series. Following this model, the covariance matrix at voxel $\#j$ is denoted as $\boldsymbol{\Gamma}_j^s = {\sigma_j^s}^{-2}\boldsymbol{\Lambda}_j^s$ where $\boldsymbol{\Lambda}_j^s$ is a tridiagonal symmetric matrix whose components depend on the AR(1) parameter ρ_j^s (Makni et al., 2008):

$$\begin{aligned}
&(\boldsymbol{\Lambda}_j^s)_{1,1} = (\boldsymbol{\Lambda}_j^s)_{N_s,N_s} = 1, (\boldsymbol{\Lambda}_j^s)_{n_s,n_s} = 1 + {\rho_j^s}^2 \quad \text{for} \quad n_s = 2, \ldots, N_s - 1, \\
&(\boldsymbol{\Lambda}_j^s)_{n_s+1,n_s} = (\boldsymbol{\Lambda}_j^s)_{n_s,n_s+1} = -\rho_j^s \quad \text{for} \quad n_s = 1, \ldots, N_s - 1.
\end{aligned} \tag{6.2}$$

Using the notation $\boldsymbol{\theta}_0^s = ({\sigma_j^s}^2, \rho_j^s)_{1 \leq j \leq J}$ and $\overline{\boldsymbol{y}}_j^s = \boldsymbol{y}_j^s - \boldsymbol{P}\boldsymbol{\ell}_j^s - \boldsymbol{S}_j^s\boldsymbol{h}_j^s$ with $\boldsymbol{S}_j^s = \sum_{m=1}^{M} a_j^{m,s}\boldsymbol{X}_m$, the likelihood can be factorized over voxels as follows

$$p(\boldsymbol{Y}^s \mid \boldsymbol{A}^s, \boldsymbol{H}^s; \boldsymbol{\theta}_0^s) \propto \prod_{j=1}^{J} \left[\frac{\sqrt{\det \boldsymbol{\Lambda}_j^s}}{{\sigma_j^s}^{N_s}}\right] \exp\left(-\frac{\overline{\boldsymbol{y}}_j^{s\mathrm{t}}\boldsymbol{\Lambda}_j^s\overline{\boldsymbol{y}}_j^s}{2{\sigma_j^s}^2}\right). \tag{6.3}$$

The joint likelihood over the S subject can then be defined as

$$\prod_{s=1}^{S} p(\boldsymbol{Y}^s \mid \boldsymbol{A}^s, \boldsymbol{H}^s; \boldsymbol{\theta}_0^s) \propto \prod_{s=1}^{S}\prod_{j=1}^{J} \left[\frac{\sqrt{\det \boldsymbol{\Lambda}_j^s}}{{\sigma_j^s}^{N_s}}\right] \exp\left(-\frac{\overline{\boldsymbol{y}}_j^{s\mathrm{t}}\boldsymbol{\Lambda}_j^s\overline{\boldsymbol{y}}_j^s}{2{\sigma_j^s}^2}\right). \tag{6.4}$$

(ii) **Neural response levels**

NRLs are assumed to be statistically independent across subjects and

experimental conditions:

$$p(\boldsymbol{A}^1,\ldots,\boldsymbol{A}^S;\boldsymbol{\theta}^1_{\{1:M\}},\ldots,\boldsymbol{\theta}^S_{\{1:M\}}) = \prod_{s=1}^{S}\prod_{m=1}^{M} p(\boldsymbol{a}^{m,s};\boldsymbol{\theta}^s_m), \qquad [6.5]$$

and all the parameters of the m-th experimental condition are gathered in $\boldsymbol{\theta}^s_m$. A mixture model is used to discriminate between activated and non-activated voxels such that $q_j^{m,s} = 1$ if voxel j is activated and $q_j^{m,s} = 0$ if not for the m-th experimental condition. Based on this mixture model, we obtain

$$p(\boldsymbol{a}^{m,s} \mid \boldsymbol{q}^{m,s};\boldsymbol{\theta}^s_m) = \prod_{j\in\mathcal{P}} p(a_j^{m,s} \mid q_j^{m,s};\boldsymbol{\mu}^s_m,\boldsymbol{v}^s_m), \qquad [6.6]$$

where the unknown response means and variances are gathered in $\boldsymbol{\mu}^s_m$ and $\boldsymbol{v}^s_m$, respectively.

(iii) **Activation classes**

The activation class assignments are assumed to be independent across S subjects and the M experimental conditions following (Vincent et al., 2010), *i.e.*

$$\prod_{s=1}^{S} p(\boldsymbol{Q}^s) = \prod_{s=1}^{S}\prod_{m=1}^{M} p(\boldsymbol{q}^{m,s};\beta^s_m). \qquad [6.7]$$

A Potts model $p(\boldsymbol{q}^{m,s};\beta^s_m)$ with interaction parameter β_m is used as a prior leading to

$$p(\boldsymbol{q}^{m,s};\beta^s_m) = W(\beta^s_m)^{-1}\exp\big(\beta^s_m U(\boldsymbol{q}^{m,s})\big), \qquad [6.8]$$

where $W(\beta_m)$ is the normalizing constant and $U(\boldsymbol{q}^{m,s}) = \sum_{j\sim l} I(q_j^{m,s} = q_l^{m,s})$. I is an indicator function as defined in Section 3.2(iii). The prior distribution of the NRLs across the subjects can then be written as

$$\prod_{s=1}^{S}\prod_{m=1}^{M} p(\boldsymbol{q}^{m,s};\beta^s_m) = \prod_{s=1}^{S}\prod_{m=1}^{M} W(\beta^s_m)^{-1}\exp\big(\beta^s_m U(\boldsymbol{q}^{m,s})\big). \qquad [6.9]$$

Remark. The previous terms associated with the hierarchy of the MS-JPDE model (the likelihood, NRLs and activation classes in [6.4], [6.5] and [6.9], respectively) are identical to those in the JPDE model in [3.3], [3.4] and [3.6] if they factorize over the subjects S. In what follows, the new hierarchical terms associated with the group-level parcellation and HRF estimates are further discussed.

(iv) **Group-level HRF patterns**
The voxel-wise HRFs of the individual subjects are expressed conditionally to their group-level HRF group k^G, where $k^G = 1, \ldots, K^G$:

$$\prod_{s=1}^{S} p(\boldsymbol{H}^s \mid \boldsymbol{z}^G) = \prod_{s=1}^{S} \prod_{j=1}^{J} p(\boldsymbol{h}_j^s \mid z_j^G) \qquad [6.10]$$

and

$$p(\boldsymbol{h}_j^s \mid z_j^G = k^G) \sim \mathcal{N}(\bar{\boldsymbol{h}}_k^G, \nu_k^G I_D) \qquad [6.11]$$

where $z_j^G \in \{1, \ldots, K^G\}$ is the group parcellation label, $\bar{\boldsymbol{h}}_k^G$ and $\nu_k^G I_D$ are the HRF pattern and covariance matrix for class k^G, respectively. Note that all the voxels of different subjects of group k^G are stochastic perturbations of the same HRF pattern $\bar{\boldsymbol{h}}_k^G$. The parameter $\bar{\boldsymbol{h}}_k^G \in \mathbb{R}^{D-1}$ is assigned a Gaussian distribution such that $\bar{\boldsymbol{h}}_k^G \sim \mathcal{N}(0, (\sigma_h^G)^2 \boldsymbol{R})$ where $(\sigma_h^G)^2$ is a parameter to be fixed or estimated, $\boldsymbol{R} = (\Delta t)^4 (\boldsymbol{D}_2^{\mathrm{t}} \boldsymbol{D}_2)^{-1}$ and $\boldsymbol{D}_2$ is the second order finite difference matrix controlling the smoothness of the HRF patterns. Finally, $\bar{\boldsymbol{h}}_{k0}^G = 0$.

Remark. The voxel-wise HRFs in the MS-JPDE model are expressed conditionally to the group-level HRF classes [6.11] contrary to the JPDE model where they are expressed conditionally to the subject-level HRF classes(see [3.8]).

(v) **Group-level HRF classes**
The group-level parcellation connexity is promoted by using a K^G-class Potts model with spatial interaction parameter β_z^G

$$p(\boldsymbol{z}^G; \beta_z^G) = W(\beta_z^G)^{-1} \exp(\beta_z^G U(\boldsymbol{z}^G)), \qquad [6.12]$$

where $W(\beta_z^G)$ is a normalization constant and $U(\boldsymbol{z}^G) = \sum_{j \sim l} I(z_j^G = z_l^G)$. As for the standard JPDE and NP-JPDE models, the parameter β_z^G ensures a level of spatial regularity of the parcellation variable $\boldsymbol{z}^G$.

Remark. The spatial Potts model prior used in [6.12] is inspired from the Potts model used as a prior over the subject-level parcellation label variable $\boldsymbol{z}$ in the JPDE model in [3.9].

In the MS-JPDE model, we distinguish the parameters of the individual subject $\boldsymbol{\Theta}^s = \{\boldsymbol{\Gamma}^s, \boldsymbol{L}^s, \boldsymbol{\mu}^s, \boldsymbol{v}^s, \boldsymbol{\beta}^s\}$ from the parameters of the group-level

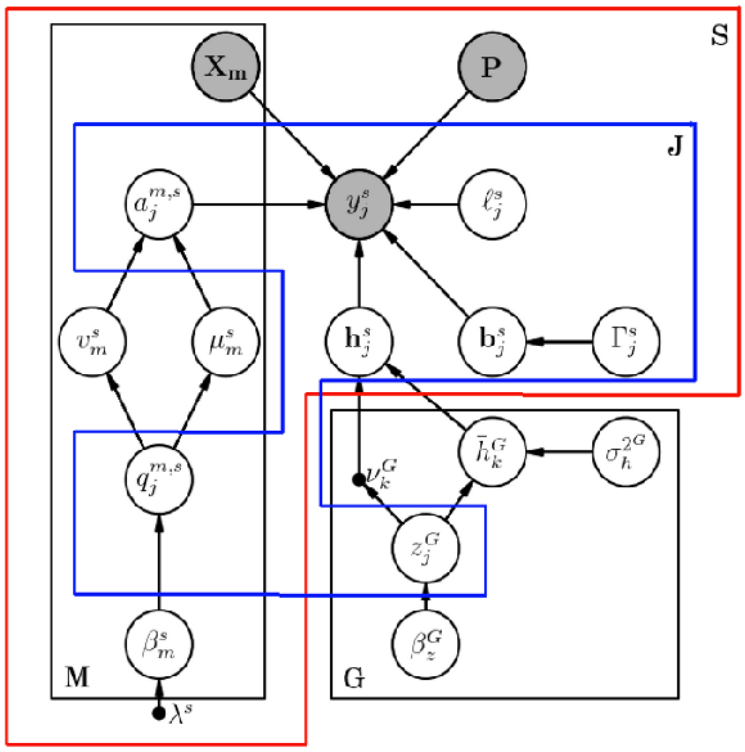

Figure 6.1: Graphical model describing the hierarchy of the MS-JPDE model.

HRF classes (that are denoted as $\boldsymbol{\omega} = \{\beta_z^G, (\sigma_h^G)^2, (\bar{\boldsymbol{h}}_k^G, \nu_k^G)_{k^G=1,\ldots,K^G}\}$) and $\boldsymbol{\Phi}$ gathers all the parameters of the model such that $\boldsymbol{\Phi} = \{\{\boldsymbol{\Theta}^s\}^{1:S}, \boldsymbol{\omega}\}$. The graphical model depicted in Fig. 6.1 illustrates the dependencies between the observed and unknown variables in the MS-JPDE model. Comparing this graphical model to the one in Fig. 3.2 of JPDE, it is clear that for voxel $\#j$ the variable $\boldsymbol{z}_j^G$ and the parameters ν_k^G and $\bar{\boldsymbol{h}}_k^G$ are at the group-level, which is denoted as block G in the figure, and they are shared by all the subjects. All the other variables are at the subject-level and gathered in a block denoted as S.
The next section handles the inference scheme that we have adopted for the MS-JPDE model.

6.4 Variational expectation maximization

We denote the BOLD time series and the unknown variables ($\boldsymbol{H}$, $\boldsymbol{A}$ and $\boldsymbol{Q}$) for all the individuals involved in the fMRI experiment as $\mathbb{Y} = \{\boldsymbol{Y}^s\}^{s=1:S}$, $\mathbb{H} = \{\boldsymbol{H}^s\}^{s=1:S}$, $\mathbb{A} = \{\boldsymbol{A}^s\}^{s=1:S}$ and $\mathbb{Q} = \{\boldsymbol{Q}^s\}^{s=1:S}$, respectively. The resulting joint distribution of the MS-JPDE model can be written as

$$p(\mathbb{Y}, \mathbb{A}, \mathbb{H}, \mathbb{Q}, \boldsymbol{z}^G) \propto \prod_{s=1}^{S} p(\boldsymbol{Y}^s \mid \boldsymbol{A}^s, \boldsymbol{H}^s) p(\boldsymbol{A}^s \mid \boldsymbol{Q}^s) p(\boldsymbol{Q}^s) p(\boldsymbol{H}^s \mid \boldsymbol{z}^G) p(\boldsymbol{z}^G). \quad [6.13]$$

To compute the posterior distribution of the MS-JPDE model, we also rely on the VEM strategy. The target posterior distribution can then be approximated as

$$\tilde{p}(\mathbb{A}, \mathbb{H}, \mathbb{Q}, \boldsymbol{z}^G \mid \mathbb{Y}) = \tilde{p}_A(\mathbb{A}) \tilde{p}_H(\mathbb{H}) \tilde{p}_Q(\mathbb{Q}) \tilde{p}_{z^G}(\boldsymbol{z}^G). \quad [6.14]$$

These variables are computed by alternating maximization of the following free energy with respect to $\tilde{p}$ and $\boldsymbol{\Phi}$

$$\mathcal{F}(\tilde{p}, \boldsymbol{\Phi}) \;=\; \mathrm{E}_{\tilde{p}}\big[\log p(\mathbb{Y}, \mathbb{A}, \mathbb{H}, \mathbb{Q}, \boldsymbol{z}^G \mid \boldsymbol{\Phi})\big] + \mathcal{G}(\tilde{p}) \quad [6.15]$$

where $\tilde{p} \in \mathcal{D}$ and $\mathcal{D}$ is the set of all probability distributions of the probability spaces $\mathcal{A} \times \mathcal{H} \times \mathcal{Q} \times z^G$ associated with $\mathbb{A}, \mathbb{H}, \mathbb{Q}$ and $\boldsymbol{z}^G$ respectively. The entropy of $\tilde{p}$ is denoted as $\mathcal{G}(\tilde{p}) = -\mathrm{E}_{\tilde{p}}\big[\log \tilde{p}(\mathbb{A}, \mathbb{H}, \mathbb{Q}, \boldsymbol{z}^G)\big]$. At the r-th iteration, the current value of the unknown parameters is denoted by $\boldsymbol{\Phi}^{(r-1)}$. The alternating procedure proceeds as follows

$$\textbf{E-step: } \tilde{p}^{(r)}_{\mathbb{A},\mathbb{H},\mathbb{Q},\boldsymbol{z}^G} = \underset{\tilde{p} \in \mathcal{D}}{\arg\max}\ \mathcal{F}(\tilde{p}, \boldsymbol{\Phi}^{(r-1)}) \quad [6.16]$$

$$\textbf{M-step: } \boldsymbol{\Phi}^{(r)} = \underset{\Phi \in \underline{\boldsymbol{\Phi}}}{\arg\max}\ \mathcal{F}(\tilde{p}^{(r)}_{\mathbb{A},\mathbb{H},\mathbb{Q},\boldsymbol{z}^G}, \boldsymbol{\Phi}). \quad [6.17]$$

The posterior distribution $\tilde{p}^{(r)}_{\mathbb{A},\mathbb{H},\mathbb{Q},\boldsymbol{z}^G}$ is approximated as a product of the distributions $\widetilde{p}^{(r)}_{\mathbb{A}}(\mathbb{A}), \widetilde{p}^{(r)}_{\mathbb{H}}(\mathbb{H}), \widetilde{p}^{(r)}_{\mathbb{Q}}(\mathbb{Q})$ and $\widetilde{p}^{(r)}_{\boldsymbol{z}^G}(\boldsymbol{z}^G)$ resulting in four E-steps, namely E-$\mathbb{A}$, E-$\mathbb{H}$, E-$\mathbb{Q}$ and E-$\boldsymbol{z}^G$. The first three steps consist of S sub-steps, one

for each subject. The resulting four E-steps can be written as follows

$$\textbf{VE-}\mathbb{H}\textbf{:}\quad \widetilde{p}^{(r)}_{\mathbb{H}}(\mathbb{H}) \propto \exp\left(\mathrm{E}_{\widetilde{p}^{(r-1)}_{\mathbb{A}}\widetilde{p}^{(r-1)}_{\boldsymbol{z}^G}}\left[\log p(\mathbb{H}\,|\,\mathbb{Y},\mathbb{A},\boldsymbol{z}^G;\boldsymbol{\Phi}^{(r-1)}\right]\right), \quad [6.18]$$

$$\textbf{VE-}\mathbb{A}\textbf{:}\quad \widetilde{p}^{(r)}_{\mathbb{A}}(\mathbb{A}) \propto \exp\left(\mathrm{E}_{\widetilde{p}^{(r)}_{\mathbb{H}}\widetilde{p}^{(r-1)}_{\mathbb{Q}}}\left[\log p(\mathbb{A}\,|\,\mathbb{Y},\mathbb{H},\mathbb{Q};\boldsymbol{\Phi}^{(r-1)})\right]\right), \quad [6.19]$$

$$\textbf{VE-}\mathbb{Q}\textbf{:}\quad \widetilde{p}^{(r)}_{\mathbb{Q}}(\mathbb{Q}) \propto \exp\left(\mathrm{E}_{\widetilde{p}^{(r)}_{\mathbb{A}}}\left[\log p(\mathbb{Q}\,|\,\mathbb{Y},\mathbb{A};\boldsymbol{\Phi}^{(r-1)})\right]\right), \quad [6.20]$$

$$\textbf{VE-}\boldsymbol{z}^G\textbf{:}\ \widetilde{p}^{(r)}_{\boldsymbol{z}^G}(\boldsymbol{z}^G) \propto \exp\left(\mathrm{E}_{\widetilde{p}^{(r)}_{\boldsymbol{z}^G}}\left[\log p(\boldsymbol{z}^G\,|\,\mathbb{Y},\mathbb{H};\boldsymbol{\Phi}^{(r-1)})\right]\right). \quad [6.21]$$

The VE-$\mathbb{A}$ and VE-$\mathbb{Q}$ steps remain the same as in the standard JPDE model (Chaari et al., 2012, 2015) (see Subsection 3.2.3 [3.18]-[3.25] for more details) and they proceed by iterating over individuals. The VE-$\mathbb{H}$ and VE-Z^G steps are detailed below. Note that these new steps take into account the group-level parcellation.

(i) **VE**-$\mathbb{H}$ step
This step consists of S steps, one for each subject. The corresponding E-H^s sub-step for subject s consists of estimating

$$\tilde{p}^{(r)}_{H^s}(\boldsymbol{H}^s) \propto \exp\left(\mathrm{E}_{\tilde{p}^{(r-1)}_{A^s}\tilde{p}^{(r-1)}_{z^G}}\left[\log p(\boldsymbol{H}^s \mid \boldsymbol{Y}^s,\boldsymbol{A}^s,\boldsymbol{z}^G;\boldsymbol{\Theta}^{s(r-1)},\boldsymbol{\omega}^{(r-1)})\right]\right). \quad [6.22]$$

This step is different from the one in the standard JPDE model (Subsection 3.2.3(i)) since it considers the group-level parcellation through the variable $\boldsymbol{z}^G$. Using [6.22] and standard algebra rules, $\widetilde{p}^{(r)}_{H^s}$ is shown to be a Gaussian distribution, *.i.e*, $\widetilde{p}^{(r)}_{H^s} \sim \mathcal{N}(\boldsymbol{m}^{(r)}_{H^s}, \boldsymbol{\Sigma}^{(r)}_{H^s})$, where $\boldsymbol{\Sigma}^{(r)}_{H^s_j} = (\boldsymbol{V}^s_{1j} + \boldsymbol{V}^s_{2j})^{-1}$ and $\boldsymbol{m}^{(r)}_{H^s_j} = \boldsymbol{\Sigma}^{(r)}_{H^s_j}(\boldsymbol{m}^s_{1j} + \boldsymbol{m}^s_{2j})$ are defined for voxel

$j = \{1, \ldots, J\}$ in subject s with

$$\begin{aligned}
\boldsymbol{V}_{1j}^{s} &= \sum_{m,m'} {\upsilon^{s}_{A_j^m A_j^{m'}}}^{(r-1)} \boldsymbol{X}_m^{\mathrm{t}} \boldsymbol{\Gamma}_j^{s(r-1)} \boldsymbol{X}_{m'} + \widetilde{\boldsymbol{S}}_j^{s\mathrm{t}} \boldsymbol{\Gamma}_j^{s(r-1)} \widetilde{\boldsymbol{S}}_j^{s}, \\
\boldsymbol{V}_{2j}^{s} &= \sum_{k=1}^{K} \widetilde{p}_{z_j^G}(k)^{(r-1)} \bar{\boldsymbol{\Sigma}}_k^{G^{(r-1)-1}}, \\
\boldsymbol{m}_{1j}^{s} &= \widetilde{\boldsymbol{S}}_j^{s\mathrm{t}} \boldsymbol{\Gamma}_j^{s(r-1)} (\boldsymbol{y}_j^{s} - \boldsymbol{P}^{s} \boldsymbol{\ell}_j^{s^{(r-1)}}), \\
\boldsymbol{m}_{2j}^{s} &= \sum_{k=1}^{K} \bar{\boldsymbol{\Sigma}}_k^{G^{(r-1)-1}} \widetilde{p}_{z_j^G}(k)^{(r-1)} \bar{\boldsymbol{h}}_k^{G^{(r-1)}},
\end{aligned} \tag{6.23}$$

and where $\widetilde{\boldsymbol{S}}_j^{s} = \sum_{m=1}^{M} m_{A_j^m}^{(r-1)} \boldsymbol{X}_m$. Note that $m_{A_j^m}^{s^{(r-1)}}$, $\upsilon_{A_j^m A_j^{m'}}^{s^{(r-1)}}$ denote the m and (m, m') entries of $\boldsymbol{m}_{A_j}^{s^{(r-1)}}$ and $\boldsymbol{\Sigma}_{A_j}^{s^{(r-1)}}$, respectively. By comparing the terms in the previous equation with the terms in [3.18], we can conclude that $\boldsymbol{V}_{1j}^{s}$ and $\boldsymbol{m}_{1j}^{s}$ are identical to those in [3.18]. On the other hand, the terms $\boldsymbol{V}_{2j}^{s}$ and $\boldsymbol{m}_{2j}^{s}$ are different since they consider $\bar{\boldsymbol{\Sigma}}_k^{G}$ and $\bar{\boldsymbol{h}}_k^{G}$, respectively which are the parameters of the group-level parcel $\#k^G$.

(ii) **VE-$\mathbf{z}^G$** step:
The E-z^G step consists of estimating

$$\tilde{p}_{z^G}^{(r)}(\boldsymbol{z}^G) \propto \exp\left(\mathrm{E}_{\tilde{p}_{\mathbb{H}}^{(r)}} \left[\log p(\boldsymbol{z}^G \mid \mathbb{Y}, \mathbb{H}; \boldsymbol{\Phi}^{(r-1)}) \right] \right). \tag{6.24}$$

This step can be split into J sub-steps by assuming a product approximation over the voxels such that $\tilde{p}_{z^G}(\boldsymbol{z}^G) = \prod_{j=1}^{J} \tilde{p}_{z_j^G}(z_j^G)$. Each E-$\mathrm{z}_j^G$ step therefore consists of estimating

$$\tilde{p}_{z_j^G}^{(r)}(z_j^G) \propto \exp\left(\sum_{s=1}^{S} \mathrm{E}_{\tilde{p}_{h_j^s}} \left[\log p(\boldsymbol{h}_j^{s} \mid z_j^G) \right] + \mathrm{E}_{\tilde{p}_{z_{\setminus j}^G}} \left[p(\boldsymbol{z}^G \mid \beta_z^G) \right] \right) \tag{6.25}$$

where $z_{\setminus j}^G = \{z_{j'}^G, j' \neq j\}$. The previous equation is similar to [3.26] except that its first term sums over all the subjects involved in the analysis and $\boldsymbol{h}_j^{s}$ is expressed conditionally to the group-level parcellation label z_j^G contrary to the JPDE model where it is expressed conditionally to

the subject-level parcellation label z_j^s. Straightforward computations of [6.25] lead to

$$\tilde{p}^{(r)}_{z_j^G}(z_j^G) \propto \prod_{s=1}^{S} \mathcal{N}(\boldsymbol{m}^s_{H_j}; \bar{\boldsymbol{h}}_k^{G(r-1)}, \bar{\boldsymbol{\Sigma}}_k^{G(r-1)}) \times \quad [6.26]$$
$$\exp\left(-\frac{1}{2}\sum_{s=1}^{S} \text{trace}(\boldsymbol{\Sigma}^{s(r)}_{H_j}(\bar{\boldsymbol{\Sigma}}_k^{G(r-1)})^{-1}) + \beta_z^{G(r-1)} \sum_{j' \sim j} \tilde{p}^{(r-1)}_{z_{j'}}(k)\right),$$

for $k = 1, \ldots, K$. The computation of $\tilde{p}^{(r)}_{z_j^G}$ in the previous equation is similar to the computation of $\tilde{p}^{(r)}_{z_j^G}$ in [3.29] except that it considers the voxel-dependent HRFs coming from all the subjects, *i.e.,* the factorization over the subjects for the Gaussian distribution and the summation for the trace function.

On the other hand, the M-step of the algorithm can be written as follows

$$\textbf{VM:} \quad \boldsymbol{\Phi}^{(r)} = \arg\max_{\Phi \in \underline{\boldsymbol{\Phi}}} \; \mathrm{E}_{\tilde{p}^{(r)}_{\mathbb{A}} \tilde{p}^{(r)}_{\mathbb{H}} \tilde{p}^{(r)}_{\mathbb{Q}} \tilde{p}^{(r)}_{\boldsymbol{z}^G}} \left[\log p(\mathbb{Y}, \mathbb{A}, \mathbb{H}, \mathbb{Q}, \boldsymbol{z}^G; \boldsymbol{\Phi})\right], \quad [6.27]$$

or equivalently

$$\begin{aligned} \boldsymbol{\Phi}^{(r)} = \; & \arg\max_{\Phi \in \underline{\boldsymbol{\Phi}}} \left[\mathrm{E}_{\tilde{p}_{\mathbb{A}} \tilde{p}_{\mathbb{H}}}\left[\log p(\mathbb{Y} \mid \mathbb{A}, \mathbb{H}; \boldsymbol{\Phi})\right] + \mathrm{E}_{\tilde{p}_{\mathbb{A}} \tilde{p}_{\mathbb{Q}}}\left[\log p(\mathbb{A} \mid \mathbb{Q}; \boldsymbol{\Phi})\right]\right. \\ & \left. + \mathrm{E}_{\tilde{p}_{\mathbb{H}} \tilde{p}_{\boldsymbol{z}^G}}\left[\log p(\mathbb{H} \mid \boldsymbol{z}^G; \boldsymbol{\Phi})\right] + \mathrm{E}_{\tilde{p}_{\boldsymbol{z}^G}}\left[\log p(\boldsymbol{z}^G; \boldsymbol{\Phi})\right] + \log p(\bar{\boldsymbol{h}}^G; \boldsymbol{\Phi})\right]. \end{aligned} \quad [6.28]$$

The group-level parcellation results in a new maximization step for $\bar{\boldsymbol{h}}^G$ taking into account the data coming from all the individuals.

(i) **VM-$\bar{\boldsymbol{h}}^G$ step**
The maximization of $\bar{\boldsymbol{h}}_k^G$ can be obtained by solving

$$\begin{aligned} \bar{\boldsymbol{h}}_k^{G(r)} = \arg\max_{\bar{\boldsymbol{h}}_k^G} & \left[\sum_{s=1}^{S} \mathrm{E}_{\tilde{p}^{(r)}_{\boldsymbol{H}^s} \tilde{p}^{(r)}_{z^G}} \log p(\boldsymbol{H}^s \mid \boldsymbol{z}^G; \bar{\boldsymbol{h}}_k^G, \boldsymbol{\nu}_k^G)\right] \\ & + \log p(\bar{\boldsymbol{h}}_k^G; (\sigma_h^G)^2). \end{aligned} \quad [6.29]$$

When the previous equation is compared to [3.43], it is clear that in [6.29], HRFs coming from all the subjects are considered, *i.e.*, the summation over the subjects in the first term. Differentiating [6.29] with

respect to $\bar{\boldsymbol{h}}_k^G$ leads to the following result

$$\bar{\boldsymbol{h}}_k^{G^{(r)}} = \left(S \times I_{D+1} + \frac{\nu_k^G \boldsymbol{R}^{-1}/(\sigma_h^G)^2}{S \sum\limits_{j \in \boldsymbol{\mathcal{P}}} \tilde{p}_{z_j}^{(r)}(k)} \right)^{-1} \frac{\sum\limits_{s=1}^{S} \sum\limits_{j \in \boldsymbol{\mathcal{P}}} \tilde{p}_{z_j}^{(r)}(k) \left(\boldsymbol{m}_{H_j}^s \right)^{(r)}}{S \sum\limits_{j \in \boldsymbol{\mathcal{P}}} \tilde{p}_{z_j}^{(r)}(k)}. \quad [6.30]$$

The reader can refer to Subsection 3.2.3 (v)(a),(v)(b) and (v)(c) for further details on the maximization with respect to the other parameters in the MS-JPDE model. The iterative procedure of the MS-JPDE model is illustrated in Algorithm 6.1.

Algorithm 6.1 The MS-JPDE algorithm. The subscript (r) refers to the current iteration.

Initialization:
  $\tilde{p}^{(0)}_{z^G}(\boldsymbol{z}^G)$ is initialized from the initial parcellation.
  for all s **do**
    $\tilde{p}^{(0)}_{Q^s}(\boldsymbol{Q}^s)$ such that $\tilde{p}^{(0)}_{Q^s_j}(q_j^{m,s}) \in \{0,1\}$.
    for all j **do**
      - $\boldsymbol{m}^{(0)}_{H^s_j}$ is initialized as the canonical HRF.
      - $\boldsymbol{m}^{(0)}_{A^s_j}$ is initialized with zeros.
    end for
  end for
  Initialize with some $\boldsymbol{\Phi}^{(0)}$.
$r = 1$
repeat
  Expectation step:
    for all s **do**
      - Compute $\tilde{p}^{(r)}_{H^s}(\boldsymbol{H}^s)$ according to [6.23].
      - Compute $\tilde{p}^{(r)}_{A^s}(\boldsymbol{A}^s)$ according to [3.19].
      - Compute $\tilde{p}^{(r)}_{Q^s}(\boldsymbol{Q}^s)$ according to [3.24].
    end for
    - Compute $\tilde{p}^{(r)}_{z^G}(\boldsymbol{z}^G)$ according to [6.26].
  Maximization step:
    Compute $\boldsymbol{\Phi}^{(r)}$ according to [6.28].
  set $r \leftarrow r + 1$
until convergence

6.5 Experimental validation

Numerical experiments on both synthetic and real data were carried out to validate the proposed model. These experiments are presented in this section.

6.5.1 Synthetic fMRI time series

FMRI synthetic data were generated for four subjects according to the generative model [6.1]. A group parcellation mask was first considered as a mean parcellation mask over the four subjects. This group-level mask, as well as its individual instances are depicted in Fig. 6.2(a-e). All masks involve four different parcels.

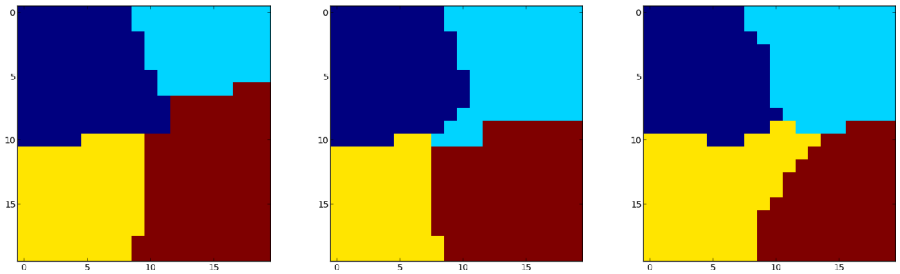

(a) Subject 1 (b) Subject 2 (c) Subject 3

(d) Subject 4 (e) Group mask (f) Initial mask

Figure 6.2: Individual and group-level reference parcellations and the used initial mask in the synthetic data experiment.

The ground truth HRF patterns used for these four parcels are shown in Fig. 6.3 (continuous lines). Two experimental conditions ($M = 2$) were used for all the subjects with 30 trials each. The reference activation labels are illustrated in Fig. 6.4. The corresponding NRLs (Fig. 6.5) were drawn

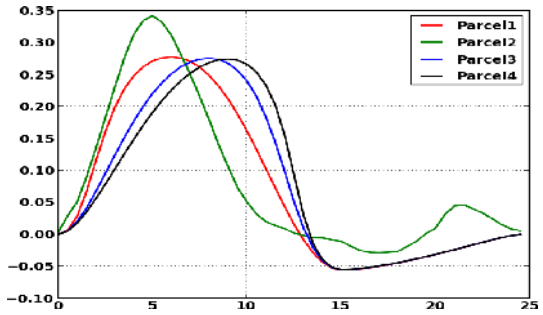

Figure 6.3: Ground truth group-level HRF profiles of the synthetic data experiment.

according to their prior distribution so that $a_j^{m,s} \mid q_j^{m,s} = 0 \sim \mathcal{N}(0, 0.5)$ and $a_j^{m,s} \mid q_j^{m,s} = 1 \sim \mathcal{N}(3.2, 0.5)$. The time of repetition used in this experiment was $TR = 1$ second. The initial parcellation used in this experiment is shown in Fig. 6.2(f).

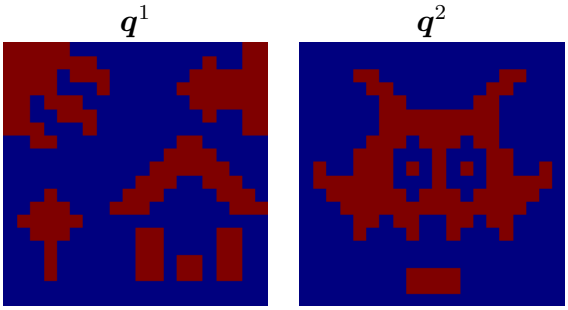

Figure 6.4: Reference activation labels for the two experimental conditions (grid size = 20×20).

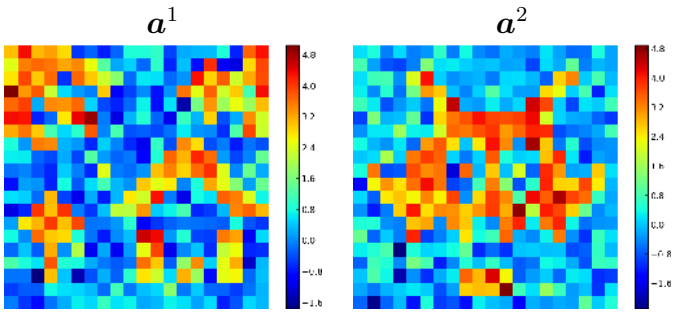

Figure 6.5: Reference NRLs for the two experimental conditions (grid size = 20×20).

These generated BOLD time series signals were analyzed using the MS-JPDE model. Fig. 6.6 shows the estimated group-level parcellation using the MS-JPDE model. The computed parcellation error between this mask and its ground truth shown in Fig. 6.6 is 4.25%. This result shows the ability of the MS-JPDE model to obtain an accurate estimate of the group-level parcellation. Moreover, the confusion matrix between the group-level reference and estimated parcellation was computed and reported in Tab. 6.1. These results demonstrate the accuracy of the MS-JPDE model in estimating the different parcels where we can notice large intersections between the estimated parcels and their counterparts in the reference parcellation Fig. 6.2(e)

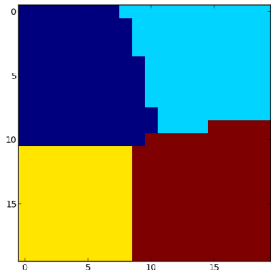

Figure 6.6: Group-level parcellation estimate using the MS-JPDE model.

Table 6.1: Confusion matrix between reference (RP) and estimated (EP) group-level parcellation obtained using the MS-JPDE model.

EP \ RP	Parcel 1	Parcel 2	Parcel 3	Parcel 4
Parcel 1	**0.92**	0.0	0.02	0.0
Parcel 2	0.06	**0.99**	0.0	0.0
Parcel 3	0.0	0.0	**0.92**	0.0
Parcel 4	0.02	0.01	0.06	**1.0**

The HRF profiles that correspond to the four estimated parcels are shown in Fig. 6.7. The MSE values between the ground truth HRF and the group-level HRF estimates are provided in Tab. 6.2. These results are relatively small, which demonstrate the robustness in the estimation task. Tab. 6.3 reports the computed MSEs for the estimated activation labels and NRLs using the MS-JPDE model. Although the MSEs of the NRL estimates were slightly

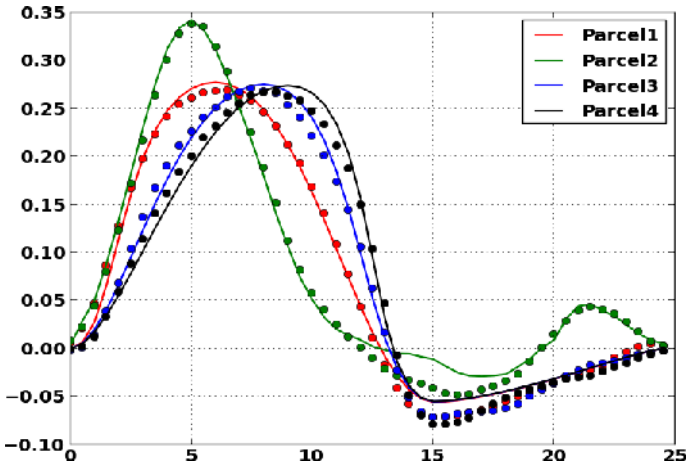

Figure 6.7: Ground truth (contnious lines) and estimated (dotted lines) group-level HRF profiles using the MS-JPDE model).

affected when compared to those of the JPDE model in Tab. 6.4, they are still relatively small which demonstrate the capability of the MS-JPDE model in detecting the activity.

Table 6.2: MSEs between reference and estimated HRF profiles using the MS-JPDE model.

HRF	MS-JPDE
HRF. 1	8.90×10^{-5}
HRF. 2	1.52×10^{-4}
HRF. 3	1.06×10^{-4}
HRF. 4	1.40×10^{-4}

Table 6.3: MSEs between reference and estimated NRLs and activation labels of the four subjects using the MS-JPDE model.

		Subject 1	Subject 2	Subject 3	Subject 4
NRLs	$m = 1$	0.062	0.063	0.065	0.062
	$m = 2$	0.047	0.047	0.046	0.046
Labels	$m = 1$	0.0018	0.0016	0.0019	0.0021
	$m = 2$	0.0024	0.0023	0.0017	0.0015

Table 6.4: MSEs between reference and estimated NRLs and activation labels of the four subjects using the JPDE model.

		Subject 1	Subject 2	Subject 3	Subject 4
NRLs	$m = 1$	0.014	0.016	0.016	0.017
	$m = 2$	0.012	0.012	0.012	0.014
Labels	$m = 1$	0.003	0.011	0.002	0.003
	$m = 2$	0.004	0.004	0.003	0.003

6.5.2 Real data

The proposed model was also validated using real fMRI data. The ROI under consideration is the right motor cortex as shown in Fig. 6.8. The statistical results of a standard subject-level GLM analysis were used to define this ROI. More precisely, Student$-t$ maps associated with the two contrasts of interest, namely `(Left Click - Right Click)` and `(Visual stimuli - Auditory stimuli)`, were thresholded at $p = 0.05$, corrected for multiple comparisons according to the FWER criterion, see (Badillo et al., 2013b; Chaari et al., 2014) for details. The fMRI data were collected using a gradient-echo EPI sequence (TE = 30 ms/TR = 2.4s/thickness = 3 mm/FOV = 192×192 mm^2, matrix size: 96×96) with a 3 Tesla imaging system during a localizer experiment (Pinel et al., 2007). Sixty auditory, visual and motor stimuli were involved in the paradigm and defined in ten experimental conditions ($M = 10$) (see (Badillo et al., 2013b; Chaari et al., 2014) for details). During this paradigm, $N = 128$ scans were acquired. Ten subjects were involved in the experiment and their fMRI were registered a priori. The same initial parcellation was applied to all subjects with 4 parcels as shown in Fig. 6.9. This number was chosen by calculating the free energy for different candidate models (Albughdadi et al., 2014). We empirically set $\beta_z = 0.9$ and $(\sigma_h^G)^2 = 0.1$ after a cross validation procedure. Starting with the estimated group-level parcellation, Fig. 6.10 shows different slices of the parcellation estimates obtained using the MS-JPDE model. The corresponding group-level HRF estimates are shown in Fig. 6.11 along with the canonical HRF. These estimates should be close in shape to the canonical HRF (Badillo et al., 2013b) which is clear from a visual point of view. The Euclidean distances in Tab. 6.5 between the HRF estimates and the canonical HRF confirm the previous observation. We further investigated the HRF estimates by computing their TTP and FWHM in Tab. 6.6. These results indicate that the

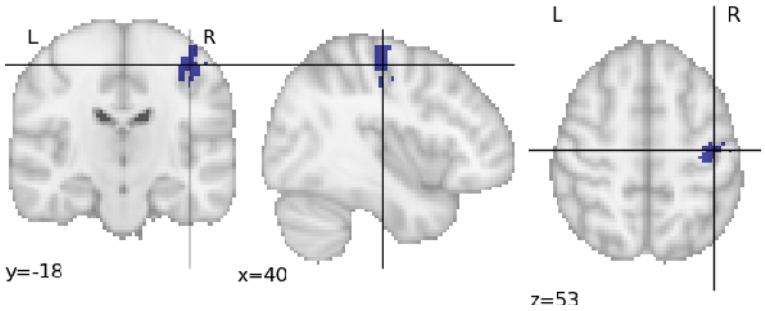

Figure 6.8: Anatomical localization of the right motor cortex that consists of a single connected component.

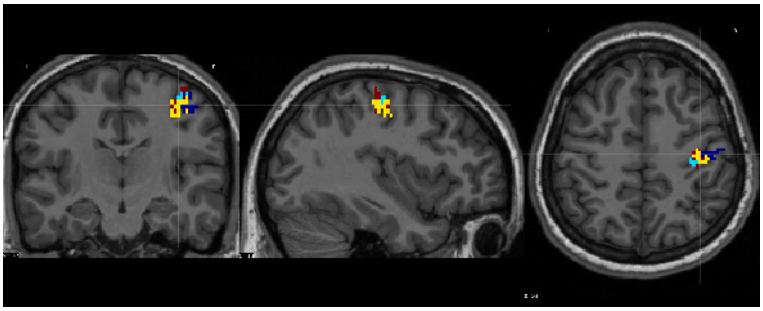

Figure 6.9: Initial parcellation consisting of 4 parcels applied to all the individuals involved in the validation of the MS-JPDE model.

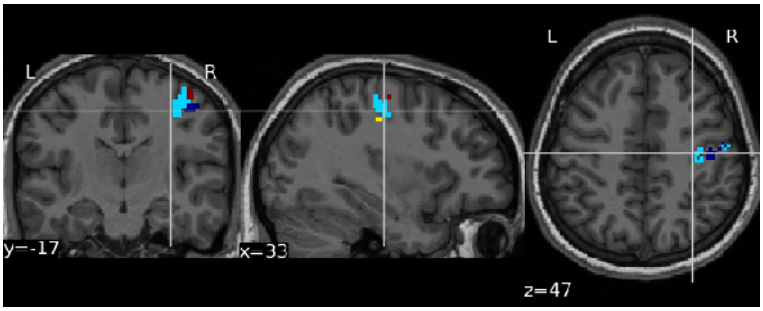

(a) Slice 1

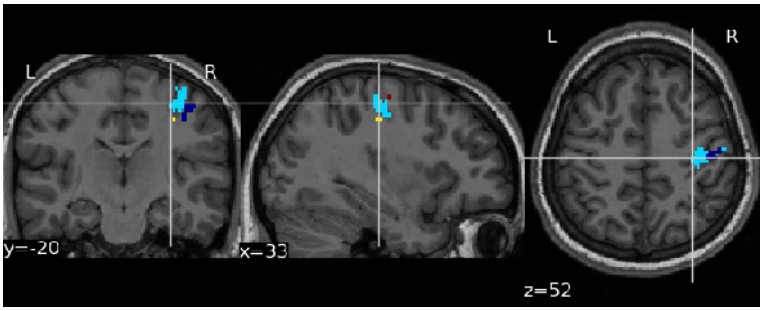

(b) Slice 2

Figure 6.10: Two different slices of the estimated parcellation using MS-JPDE model in the right motor cortex.

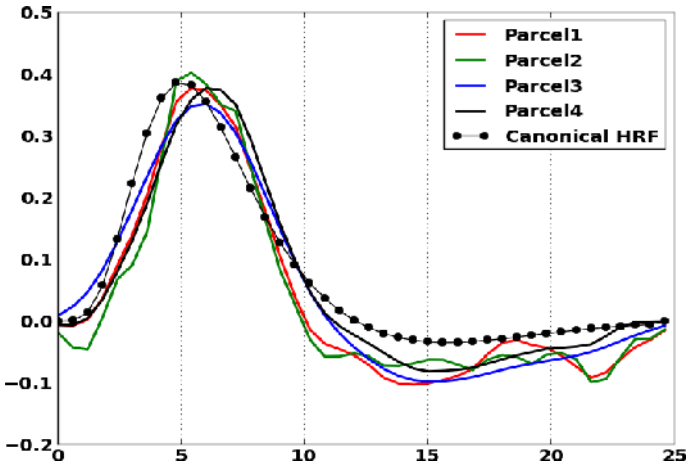

Figure 6.11: HRF shape estimates using the MS-JPDE model in the right motor cortex and the canonical HRF.

HRF profiles of parcels 1 and 2 (respectively 3 and 4) have the same TTP value, therefore they have similar HRF characteristics and could be merged into a single parcel.

Table 6.5: Euclidean distances between the estimated HRFs using the MS-JPDE model and the canonical HRF.

	Euclidean distance
HRF 1	0.31
HRF 2	0.33
HRF 3	0.29
HRF 4	0.30

Table 6.6: The estimated TTP and FWHM for the HRF estimates obtained using the MS-JPDE model.

	TTP	FWHM
HRF 1	5.4	4.8
HRF 2	5.4	4.2
HRF 3	6.0	6.0
HRF 4	6.0	5.4

It is worth noticing that the setting of the hyperparameter $(\sigma_h^G)^2$ was not

arbitrary since it has a significant effect on the smoothness of the group-level HRF profiles which in turn can affect the characteristics of these profiles. When the same experiment was repeated using $(\sigma_h^G)^2 \in \{0.2, 0.5\}$, the smoothness of the HRFs was drastically affected as shown in Fig. 6.12. It is worth noticing that the TTP of the HRF profile is mainly affected by the HRF smoothness. The reported TTP values in Tab. 6.7 for $(\sigma_h^G)^2 \in \{0.2, 0.5\}$ confirm our observation where the TTP of most of the HRF profiles changes with different values of $(\sigma_h^G)^2$.

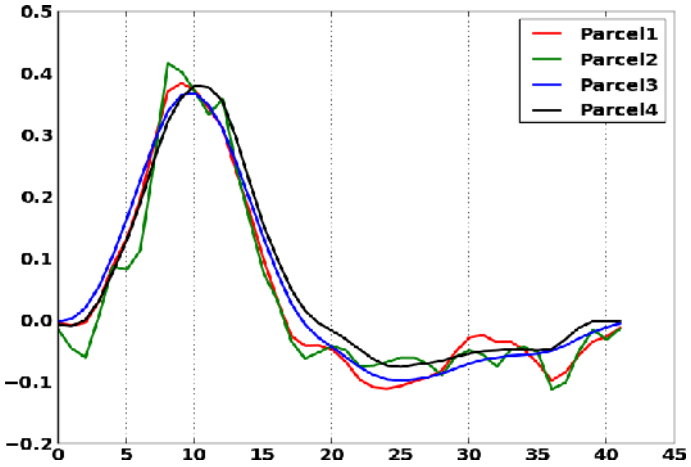

(a) $(\sigma_h^G)^2 = 0.2$

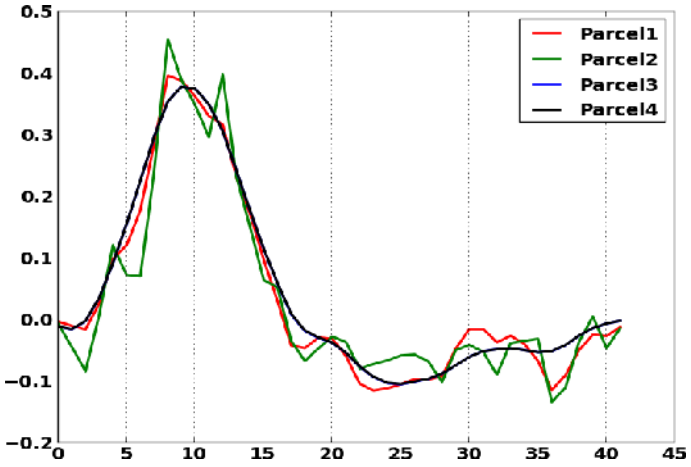

(b) $(\sigma_h^G)^2 = 0.5$

Figure 6.12: The estimated HRF shapes for different values of $(\sigma_h^G)^2$.

Table 6.7: The estimated TTP for running the same group experiment using the MS-JPDE model with different values of $(\sigma_h^G)^2$.

	$(\sigma_h^G)^2 = 0.2$	$(\sigma_h^G)^2 = 0.5$
HRF. 1	5.4	4.8
HRF. 2	4.8	4.8
HRF. 3	6.0	5.4
HRF. 4	6.0	5.4

6.6 Conclusion

In this chapter, we proposed a new model for a multi-subject analysis of fMRI data (MS-JPDE). This model allowed the estimation of the group-level parcellation and HRF profiles for the involved individuals as well as a detection task indicating wether the voxels were activated or not in response to stimuli. The MS-JPDE model was firstly validated using synthetic data experiments. The results showed the ability of the proposed model to obtain group-level estimates with high accuracy. However, the NRL estimates of the individuals were slightly affected when compared to the JPDE model. In a second step, we validated the proposed model via a real data experiment. The considered ROI was the right motor cortex and ten individuals were involved in the same experimental paradigm. The data collected from all the individuals were processed simultaneously using the MS-JPDE model. The parcellation and HRF estimates obtained with this model allowed us to interpret the analysis results at the group-level. The obtained HRF estimates obtained with the MS-JPDE were similar to the canonical HRF shape which was coherent with previous studies on this region of the brain (these studies indicated that HRFs in the motor cortex are very similar in shape to the canonical one). However, we noticed that the hyperparameter $(\sigma_h^G)^2$ had a significant effect on the smoothness of the HRF profiles. Repeating the same experiment but using different values for this hyperparameter, we showed the changes in the smoothness and the resulting changes in the estimated TTP of the HRFs of the estimated parcels. To overcome the drawbacks revealed in the MS-JPDE model, we propose in the next chapter a new model for multi-subject analysis. This model performs a joint inter and intra subject analysis which is a very interesting approach that allowing parcellation and HRF estimates at the subject and group levels.

CHAPTER 7

Hybrid Multi-Subject Joint Parcellation Detection Estimation

Contents

7.1 Introduction

In this chapter, we propose a new model for group-level analysis to overcome the limitations of the MS-JPDE model which was introduced in Chapter 6. This model allows the HRF variability across brain regions at the subject and group levels to be studied. This objective is accomplished by performing an inter and intra subject analysis to achieve parcellation and HRF estimation at the group and subject levels. In what follows, this model is referred to as the HMS-JPDE model. The observation equation for the HMS-JPDE is the same as in Section 6.2[6.1]. However, the two models differ in the way the voxel-dependent HRFs are expressed. Indeed, the MS-JPDE model assumes that the HRF at voxel j for subject s is expressed conditionally

to a group-level HRF class that it belongs to. The HMS-JPDE model assumes that the HRF at voxel j for subject s is expressed conditionally to a subject-level HRF class which in turn is expressed to a group-level HRF class. Assuming that there are K HRF groups, in the HMS-JPDE each of the analyzed subjects has K HRF profiles that represent the parcels for this specific subject. Moreover, K group-level HRF profiles are estimated that represent the group-level parcels of all the subjects. The MS-JPDE does not allow this variability at the subject-level. Considering K HRF groups for the MS-JPDE, all the subjects have the same parcellation, thus sharing the same HRF profiles.
The rest of this chapter is organized as follows. The hierarchy of the HMS-JPDE model is introduced in Section 7.2. Then, the inference strategy adopted for the HMS-JPDE model is described in Section 7.3. An experimental validation is conducted in Section 7.4. Finally, some conclusions are drawn in Section 7.5.

7.2 Hierarchical Bayesian model

The HMS-JPDE model shares some of its hierarchy terms with the MS-JPDE model (namely, Likelihood, neural response levels and activation classes). The reader can refer to Section 6.3(i)-(iii) for more details on these mutual hierarchical terms. However, one of the main differences between the two models is that the HMS-JPDE model considers both the subject and group level parcellations and HRFs contrary to the MS-JPDE model where the group-level parcellation and HRFs are only considered. This difference is described below.

(i) **Subject-level HRF patterns**
The HMS-JPDE model assumes that the voxel-dependent HRF $\boldsymbol{h}_j^s$ is expressed conditionally to a subject-level HRF class label z_j^s (see Subsection 3.2.2 (i)) contrary to the MS-JPDE model which assumes $\boldsymbol{h}_j^s$ is expressed conditionally to the group-level HRF class label z_j^G. Following this assumption $\boldsymbol{H}^s$ can be expressed as

$$p(\boldsymbol{H}^s|\boldsymbol{z}^s) = \prod_{j\in\boldsymbol{\mathcal{P}}} p(\boldsymbol{h}_j^s \mid z_j^s). \qquad [7.1]$$

As a consequence $\boldsymbol{h}_j^s$ is a stochastic perturbation of a subject-level HRF pattern $\bar{\boldsymbol{h}}_k^s$ of HRF group $\#k^s$, *i.e.*, $\boldsymbol{h}_j^s$ is assigned a Gaussian prior

distribution $p(\boldsymbol{h}_j^s \,|\, z_j^s = k) \sim \mathcal{N}(\bar{\boldsymbol{h}}_k^s, \bar{\boldsymbol{\Sigma}}_k^s)$ where $\bar{\boldsymbol{\Sigma}}_k^s = \nu_k^s \boldsymbol{I}_D$ adjusts the stochastic perturbations around $\bar{\boldsymbol{h}}_k^s$ via the value of the hyperparameter ν_k^s.

Remark. Each subject s has its own set of HRF profiles $\bar{\boldsymbol{h}}^s = \left(\bar{\boldsymbol{h}}_k^s\right)_{1 \leq k \leq K}$. These subject-level HRF profiles are characterized by Gaussian distributions such that $\bar{\boldsymbol{h}}_k^s \sim \mathcal{N}(\bar{\boldsymbol{h}}_k^G, (\sigma_h^s)^2 \boldsymbol{R})$ where $\bar{\boldsymbol{h}}_k^s$ is related to the group-level HRF profile $\bar{\boldsymbol{h}}_k^G$. The group-level HRF profile $\bar{\boldsymbol{h}}_k^G$ is a priori assigned a zero mean Gaussian distribution, *i.e.*, $\bar{\boldsymbol{h}}_k^G \sim \mathcal{N}(\boldsymbol{0}, (\sigma_h^G)^2 \boldsymbol{R})$ and $\boldsymbol{R} = (\Delta t)^4 \, (\boldsymbol{D}_2^{\mathrm{t}} \boldsymbol{D}_2)^{-1}$. The second-order finite difference matrix is denoted as $\boldsymbol{D}_2$. Note that the hyperparameters $(\sigma_h^s)^2$ and $(\sigma_h^G)^2$ are fixed and that $\bar{\boldsymbol{h}}_k^s$ in the JPDE model is assigned a zero mean Gaussian distribution. Moreover, $\bar{\boldsymbol{h}}_{k0}^s = \bar{\boldsymbol{h}}_{kD\Delta t}^s = 0$ and $\bar{\boldsymbol{h}}_{k0}^G = \bar{\boldsymbol{h}}_{kD\Delta t}^G = 0$ as in (Makni et al., 2008; Vincent et al., 2010; Chaari et al., 2011). Hence, $\bar{\boldsymbol{h}}_k^s, \bar{\boldsymbol{h}}_k^G \in \mathbb{R}^{D-1}$.

(ii) **Subject-level HRF groups**

For $s = 1, \ldots, S$, the prior $p\left(\boldsymbol{z}^s \mid \boldsymbol{z}^G\right)$ is an MRF whose parameters depends on $\boldsymbol{z}^G$ where $\boldsymbol{z}^G = \{z_j^G, j = 1, \ldots, N\}$ is a label vector associated with a common group-level parcellation. The label distribution $p(\boldsymbol{z}^s \mid \boldsymbol{z}^G)$ can be written as

$$p\left(\boldsymbol{z}^s \mid \boldsymbol{z}^G\right) \propto \exp\left(\sum_{j=1}^{N} \alpha_{j,z_j^s}\left(\boldsymbol{z}^G\right) + \beta_z^s \sum_{i \sim j} I\left(z_i^s = z_j^s\right)\right), \qquad [7.2]$$

where β_z^s is the interaction parameter and $\alpha_{j,k}\left(\boldsymbol{z}^G\right)$ is the external field parameter of the MRF. For $j = 1, \ldots, N$ and for $k = 1, \ldots, K$, this parameter can be defined as

$$\alpha_{j,k}\left(\boldsymbol{z}^G\right) = \eta \sum_{i \in \mathcal{R}(j)} I\left(z_i^G = k\right), \qquad [7.3]$$

where η is a positive scalar parameter adjusting the strength of the external field and $\mathcal{R}(j)$ is a region of voxels around j including the voxel j. Moreover, $\mathcal{R}(j)$ could also be larger or smaller , *i.e.*, $\mathcal{R}(j) = \{j\}$. Note that in this case, the $\alpha_{j,k}\left(\boldsymbol{z}^G\right)$ acts as an external field that depends on voxel j and on the global parcellation at this voxel and around it. This model has the particularity to mix inside the same MRF model informations coming from the subject and group level parcellations.

Remark. $\mathcal{R}(j) = \{j\}$ means that we favor all parcellations $\boldsymbol{z}^s, \quad s \in \{1 \ldots, S\}$ to be equal to $\boldsymbol{z}^G$ the global one. In this case, the value of η should be large enough to give more weight to the information coming from the group-level parcellation in the external field.

Remark. $\alpha_{j,k}\left(\boldsymbol{z}^G\right)$ is a voting rule system, the voxels in $\mathcal{R}(j)$ are the voters for voxel j and η is the voting weight. Instead of a single value of η, we can have one value for each voxel in $\mathcal{R}(j)$, *i.e.*, $\boldsymbol{\eta} = \{\eta_i, i \in \mathcal{R}(j)\}$. Typically, one can put more weight on the group-level parcellation at voxel j and less on $i \in \mathcal{R}(j)_{\setminus j}$ to favor the information coming from the group-level parcellation at voxel j.

Remark. One can notice that this kind of MRF priors that allows us to account for informations about the parcellation from both the subject and group level is neither used in the JPDE model nor in the MS-JPDE model.

(iii) **Group-level HRF groups**
To guarantee the connexity of the group-level parcellation, a K-class Potts model is used with interaction parameter β_z^G such that

$$p\left(\boldsymbol{z}^G\right) \propto \exp\left(\beta_G \sum_{i \sim j} I\left(z_i^G = z_j^G\right)\right). \qquad [7.4]$$

Using this prior forces the neighbouring voxels to belong to the same HRF group and thus to share the same HRF pattern. The same Potts model was used for the JPDE and MS-JPDE models (see Subsection 3.2.2 (iii) and Section 6.3 (v), respectively) to promote spatial connexity.

In what follows, the set of all parameters for one subject is denoted as $\boldsymbol{\Theta}^s = \left\{\boldsymbol{\Gamma}^s, \boldsymbol{L}^s, \boldsymbol{\theta}^s_{\{1:M\}}, \beta_z^s, (\sigma_h^s)^2, (\bar{\boldsymbol{h}}_k^s, \nu_k^s)_{1 \leq k \leq K}\right\}$. The global parcellation parameters are gathered in the vector $\boldsymbol{\omega} = \{\beta_z^G, (\sigma_h^G)^2, (\bar{\boldsymbol{h}}_k^G)_{1 \leq k \leq K}\}$ and $\boldsymbol{\Phi} = \{\{\boldsymbol{\Theta}^s\}^{1:S}, \boldsymbol{\omega}\}$.
The graphical model shown in Fig. 7.1 illustrates the hierarchy of the HMS-JPDE model and the dependencies between the observations and unknown variables. To summarize, the graphical model in Fig. 7.1 preserves the hierarchical terms of the JPDE model which are illustrated in Fig. 3.2. However,

extra layers of hierarchy are added in order to consider the group-level parcellations and HRFs as in the graphical model of the MS-JPDE in Fig. 6.1. The variables and parameters associated with these layers are gathered in a block labelled as G in Fig. 7.1. More precisely, the variable of the subject-level parcellation label z_j^s depends on the group-level parcellation label z_j^G. Furthermore, the subject-level HRF pattern $\bar{\boldsymbol{h}}_k^s$ at parcel $\#k$ depends on the hyperparameter $\bar{\boldsymbol{h}}_k^G$, which is the group-level HRF pattern.

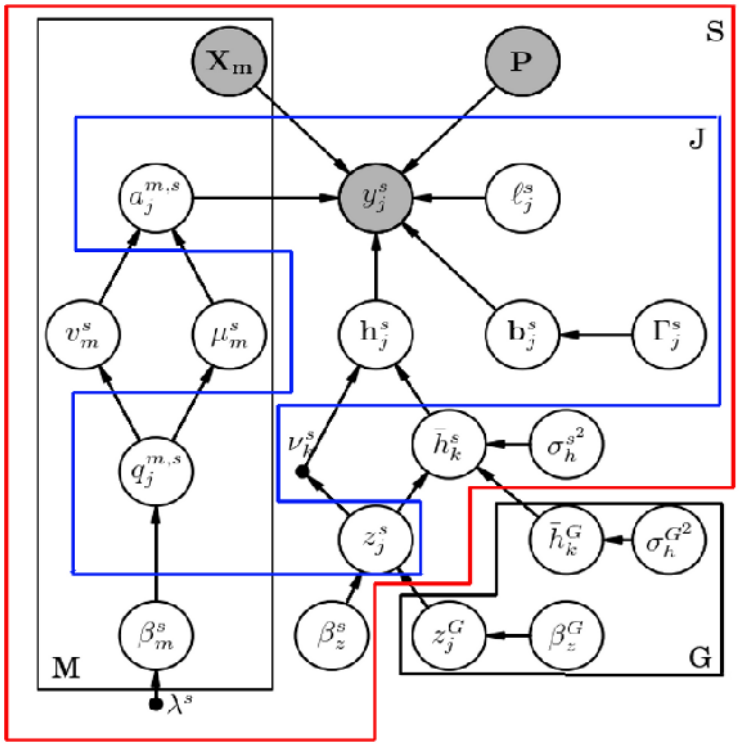

Figure 7.1: Graphical model describing the hierarchy of the HMS-JPDE model.

7.3 Variational expectation maximization

We denote the BOLD time series $\boldsymbol{Y}$ and the unknown variables ($\boldsymbol{H}, \boldsymbol{A}, \boldsymbol{Q}$, and $\boldsymbol{z}$) from all the individuals involved in the fMRI experiment as $\mathbb{Y} = \{\boldsymbol{Y}^s\}^{s=1:S}$, $\mathbb{H} = \{\boldsymbol{H}^s\}^{s=1:S}$, $\mathbb{A} = \{\boldsymbol{A}^s\}^{s=1:S}$, $\mathbb{Q} = \{\boldsymbol{Q}^s\}^{s=1:S}$ and $\mathbb{Z} = \{\boldsymbol{z}^s\}^{s=1:S}$, respectively. The resulting joint distribution of the model can be

written as

$$p(\mathbb{Y},\mathbb{A},\mathbb{H},\mathbb{Q},\mathbb{Z},\boldsymbol{z}^G) \propto \prod_{s=1}^{S} [p\left(\boldsymbol{Y}^s \mid \boldsymbol{A}^s,\boldsymbol{H}^s\right) p\left(\boldsymbol{A}^s \mid \boldsymbol{Q}^s\right) p\left(\boldsymbol{Q}^s\right) p\left(\boldsymbol{H}^s \mid \boldsymbol{z}^s\right) \times p\left(\boldsymbol{z}^s \mid \boldsymbol{z}^G\right)] \, p\left(\boldsymbol{z}^G\right) \quad [7.5]$$

where the term factorizing over the subjects in the joint distribution is similar to the one in the standard JPDE model except that a different prior of $\boldsymbol{z}^s$ is used. The probability $p(\boldsymbol{z}^G)$ comes from the group-level parcellation.
We rely on a VEM strategy to compute the Bayesian estimates associated with the intractable posterior of the HMS-JPDE model. As a result, the target posterior distribution can be approximated as

$$\tilde{p}(\mathbb{A},\mathbb{H},\mathbb{Q},\mathbb{Z},\boldsymbol{z}^G \mid \mathbb{Y}) = \tilde{p}_A(\mathbb{A})\tilde{p}_H(\mathbb{H})\tilde{p}_Q(\mathbb{Q})\tilde{p}_Z(\mathbb{Z})\tilde{p}_{z^G}(\boldsymbol{z}^G). \quad [7.6]$$

An iterative algorithm is used to compute these variables by alternating maximization of the following free energy with respect to $\tilde{p}$ and $\boldsymbol{\Phi}$

$$\mathcal{F}(\tilde{p},\boldsymbol{\Phi}) \;=\; \mathrm{E}_{\tilde{p}}\big[\log p(\mathbb{Y},\mathbb{A},\mathbb{H},\mathbb{Q},\mathbb{Z},\boldsymbol{z}^G \,|\, \boldsymbol{\Phi})\big] + \mathcal{G}(\tilde{p}) \quad [7.7]$$

where $\tilde{p} \in \mathcal{D}$, $\mathcal{D}$ is the set of all probability distributions on $\mathcal{A}\times\mathcal{H}\times\mathcal{Q}\times\mathcal{Z}\times z^G$ where $\mathcal{A},\mathcal{H},\mathcal{Q},\mathcal{Z},z^G$ are the probability spaces associated with $\mathbb{A},\mathbb{H},\mathbb{Q},\mathbb{Z}$ and $\boldsymbol{z}^G$ respectively, and $\mathcal{G}(\tilde{p}) = -\mathrm{E}_{\tilde{p}}\big[\log \tilde{p}(\mathbb{A},\mathbb{H},\mathbb{Q},\mathbb{Z},\boldsymbol{z}^G)\big]$ is the entropy of $\tilde{p}$. At the r-th iteration, the current value of the unknown parameters is denoted by $\boldsymbol{\Phi}^{(r-1)}$. The alternating procedure proceeds as follows

$$\textbf{E-step: } \tilde{p}^{(r)}_{\mathbb{A},\mathbb{H},\mathbb{Q},\mathbb{Z},\boldsymbol{z}^G} = \arg\max_{\tilde{p}\in\mathcal{D}} \; \mathcal{F}(\tilde{p},\boldsymbol{\Phi}^{(r-1)}) \quad [7.8]$$

$$\textbf{M-step: } \boldsymbol{\Phi}^{(r)} = \arg\max_{\Phi\in\underline{\boldsymbol{\Phi}}} \; \mathcal{F}(\tilde{p}^{(r)}_{\mathbb{A},\mathbb{H},\mathbb{Q},\mathbb{Z},\boldsymbol{z}^G},\boldsymbol{\Phi}). \quad [7.9]$$

The resulting five E-steps are the E-$\mathbb{A}$, E-$\mathbb{H}$, E-$\mathbb{Q}$, E-$\mathbb{Z}$ and E-$\boldsymbol{z}^G$ and they can be expressed as

$$\textbf{VE-}\mathbb{H}\textbf{:}\quad \widetilde{p}^{(r)}_{\mathbb{H}}(\mathbb{H}) \propto \exp\left(\mathrm{E}_{\widetilde{p}^{(r-1)}_{\mathbb{A}}\widetilde{p}^{(r-1)}_{\mathbb{Z}}}\left[\log p(\mathbb{H}\,|\,\mathbb{Y},\mathbb{A},\mathbb{Z};\boldsymbol{\Phi}^{(r-1)}\right]\right), \tag{7.10}$$

$$\textbf{VE-}\mathbb{A}\textbf{:}\quad \widetilde{p}^{(r)}_{\mathbb{A}}(\mathbb{A}) \propto \exp\left(\mathrm{E}_{\widetilde{p}^{(r)}_{\mathbb{H}}\widetilde{p}^{(r-1)}_{\mathbb{Q}}}\left[\log p(\mathbb{A}\,|\,\mathbb{Y},\mathbb{H},\mathbb{Q};\boldsymbol{\Phi}^{(r-1)})\right]\right), \tag{7.11}$$

$$\textbf{VE-}\mathbb{Q}\textbf{:}\quad \widetilde{p}^{(r)}_{\mathbb{Q}}(\mathbb{Q}) \propto \exp\left(\mathrm{E}_{\widetilde{p}^{(r)}_{\mathbb{A}}}\left[\log p(\mathbb{Q}\,|\,\mathbb{Y},\mathbb{A};\boldsymbol{\Phi}^{(r-1)})\right]\right), \tag{7.12}$$

$$\textbf{VE-}\mathbb{Z}\textbf{:}\quad \widetilde{p}^{(r)}_{\mathbb{Z}}(\mathbb{Z}) \propto \exp\left(\mathrm{E}_{\widetilde{p}^{(r)}_{\mathbb{H}}\widetilde{p}^{(r-1)}_{\boldsymbol{z}^G}}\left[\log p(\mathbb{Z}\,|\,\mathbb{Y},\mathbb{H},\boldsymbol{z}^G;\boldsymbol{\Phi}^{(r-1)})\right]\right), \tag{7.13}$$

$$\textbf{VE-}\boldsymbol{z}^G\textbf{:}\ \widetilde{p}^{(r)}_{\boldsymbol{z}^G}(\boldsymbol{z}^G) \propto \exp\left(\mathrm{E}_{\widetilde{p}_{\mathbb{Z}^{(r)}}}\left[\log p(\boldsymbol{z}^G\,|\,\mathbb{Y},\mathbb{Z};\boldsymbol{\Phi}^{(r-1)})\right]\right). \tag{7.14}$$

It is worth noticing that each of the first four E-steps consists of S sub-steps. Moreover, the computations of VE-$\mathbb{H}$, VE-$\mathbb{A}$ and VE-$\mathbb{Q}$ steps are the same as in the standard JPDE model (Chaari et al., 2012, 2015) (see Subsection 3.2.3 [3.18]-[3.25] for more details) and they proceed by iterating over individuals. The two new steps are the VE-Z^s and VE-Z^G steps. Further details regarding the new steps are provided in what follows.

(i) **VE**-$\mathbb{Z}$ step
This step is divided into S steps one for each subject such that $\tilde{p}_{\mathbb{Z}}(\mathbb{Z}) = \prod_{s=1}^{S}\tilde{p}_{\boldsymbol{z}^s}(\boldsymbol{z}^s)$. Each $\tilde{p}_{\boldsymbol{z}^s}(\boldsymbol{z}^s)$ includes J sub-steps resulting from a product approximation, *i.e.*, $\tilde{p}_{\boldsymbol{z}^s}(\boldsymbol{z}^s) = \prod_{j=1}^{J}\tilde{p}_{z_j^s}(z_j^s)$. The posterior $\tilde{p}_{z_j^s}(z_j^s)$ can be approximated as

$$\begin{aligned}\widetilde{p}_{z_j^s}(z_j^s) &\propto \exp\left(\mathrm{E}_{\widetilde{p}_{h_j^s}\widetilde{p}_{z_j^s}\widetilde{p}_{z^G}}\left[\log p\left(h_j^s \mid z_j^s\right) + \log p\left(\boldsymbol{z}^s \mid \boldsymbol{z}^G\right)\right]\right),\\ &\propto \exp\left(\underbrace{\mathrm{E}_{\widetilde{p}_{h_j^s}}\left[\log p\left(h_j^s \mid z_j^s\right)\right]}_{\mathrm{A}} + \underbrace{\mathrm{E}_{\widetilde{p}_{z^s_{\setminus j}}\widetilde{p}_{z^G}}\left[\log p\left(\boldsymbol{z}^s \mid \boldsymbol{z}^G\right)\right]}_{\mathrm{B}}\right),\end{aligned} \tag{7.15}$$

where part A of the equation is the same as in the standard JPDE model [3.27] and part B is computed as

$$\begin{aligned}\mathrm{E}_{\widetilde{p}_{z_j^s}\widetilde{p}_{\boldsymbol{z}^G}}\left[\log p\left(\boldsymbol{z}^s \mid \boldsymbol{z}^G\right)\right] =& \mathrm{E}_{\widetilde{p}_{z^s_{\setminus j}}\widetilde{p}_{\boldsymbol{z}^G}}\Big[\sum_{j=1}^{N}\alpha_{j,z_j^s}\left(\boldsymbol{z}^G\right) + \beta_z^s\sum_{i\sim j}I(z_i^s = z_j^s)\\ &- \log\mathcal{K}\left(\boldsymbol{z}^G,\beta_z^G\right)\Big],\end{aligned} \tag{7.16}$$

where $\mathcal{K}(\boldsymbol{z}^G, \beta_z^G)$ is the group-level Markov random field in [7.4] which is independent of z_j^s. Straightforward computations of [7.16] lead to

$$\begin{aligned} \mathrm{E}_{\tilde{p}_{z_{\setminus j}^s} \tilde{p}_{\boldsymbol{z}^G}} \left[\log p \left(\boldsymbol{z}^s \mid \boldsymbol{z}^G \right) \right] &= \mathrm{E}_{\tilde{p}_{\boldsymbol{z}^G}} \left[\alpha_{j, z_j^s} \left(\boldsymbol{z}^G \right) \right] + \beta_z^s \sum_{i \in \mathcal{N}(j)} \tilde{p}_{z_i^s} \left(z_j^s \right), \\ &= \eta \sum_{i \in \mathcal{R}(j)} \tilde{p}_{z_i^G} \left(z_j^s \right) + \beta_z^s \sum_{i \in \mathcal{N}(j)} \tilde{p}_{z_i^s} \left(z_j^s \right). \end{aligned} \quad [7.17]$$

The posterior in [7.15] is then equivalent to

$$\tilde{p}_{z_j^s} \left(z_j^s = k \right) \propto \exp \left(\mathrm{E}_{\tilde{p}_{\boldsymbol{h}_j^s}} \left[\log \mathcal{N} \left(\boldsymbol{h}_j^s; \bar{\boldsymbol{h}}_k^s, \bar{\boldsymbol{\Sigma}}_k^s \right) \right] + \eta \sum_{i \in \mathcal{R}(j)} \tilde{p}_{z_i^G} (k) + \beta_z^s \sum_{i \in \mathcal{N}(j)} \tilde{p}_{z_i^s} (k) \right). \quad [7.18]$$

From the previous equations, we can notice that for subject s, the probability that voxel j belongs to parcel k depends on the number of neighbouring voxels in $\mathcal{N}(j)$ in the same subject and neighbouring voxels in $\mathcal{R}(j)$ in the group-level parcellation that also belong to parcel k.

(ii) **VE**-Z^G step
Assuming a product approximation over voxels, the VE-Z^G is split into J sub-steps, *i.e.*, $\tilde{p}_{\boldsymbol{z}^G}(\boldsymbol{z}^G) = \prod_{j=1}^J \tilde{p}_{z_j^G}(z_j^G)$ where $\tilde{p}_{z_j^G}(z_j^G)$ can be written as

$$\tilde{p}_{z_j^G}(z_j^G) \propto \exp\left(\mathrm{E}_{\tilde{p}_{\boldsymbol{z}\{s=1,\ldots,S\}}\tilde{p}_{z_j^G}}\Big[\sum_{s=1}^{S}\log p\left(\boldsymbol{z}^s \mid \boldsymbol{z}^G\right)+\log p\left(z_j^G \mid z_{N(j)}^G\right)\Big]\right),$$

$$\propto \exp\left(\sum_{s=1}^{S}\sum_{i=1}^{J}\mathrm{E}_{\tilde{p}_{z_i^s}\tilde{p}_{z_j^G\setminus j}}\left[\alpha_{i,z_i^s}\left(\boldsymbol{z}^G\right)\right]+\mathrm{E}_{\tilde{p}_{z_{N(j)}^G}}\Big[\beta_z^G\sum_{i\in N(j)}I\left(z_i^G=z_j^G\right)\Big]\right),$$

$$\propto \exp\left(\underbrace{\eta\sum_{s=1}^{S}\sum_{i=1}^{J}\mathrm{E}_{\tilde{p}_{z_i^s}}\Big[\sum_{l\in\mathcal{R}(i)}\tilde{p}_{z_l^G}\left(z_i^s\right)\Big]}_{\mathrm{A}}+\beta_z^G\sum_{i\in N(j)}\tilde{p}_{z_i^G}\left(z_j^G\right)\right). \quad [7.19]$$

Part A of [7.19] can be computed as

$$A=\eta\sum_{s=1}^{S}\sum_{i=1}^{J}\sum_{k=1}^{K}\tilde{p}_{z_i^s}(k)\left(\sum_{l\in\mathcal{R}(i)}\tilde{p}_{z_l^G}(k)\right), \quad [7.20]$$

$$=\sum_{s=1}^{S}\sum_{i=1}^{J}\mathrm{E}_{\tilde{p}_{z_i^s}\tilde{p}_{\boldsymbol{z}^G\setminus j}}\Big[\eta\sum_{l\in\mathcal{R}(i)}I\left(z_l^G=z_i^s\right)\Big], \quad [7.21]$$

$$=\sum_{s=1}^{S}\sum_{i=1}^{J}\sum_{k=1}^{K}\eta\,\tilde{p}_{z_i^s}(k)\underbrace{\mathrm{E}_{\tilde{p}_{z_j^G\setminus j}}\Big[\sum_{l\in\mathcal{R}(i)}I\left(z_l^G=k\right)\Big]}_{\mathrm{W}}, \quad [7.22]$$

whereas part W can be computed according to following condition

$$\mathrm{W}=\begin{cases}\sum_{l\in\mathcal{R}(i)}\tilde{p}_{z_i^G}(k), & \text{if} \quad j\notin\mathcal{R}(i)\\ \sum_{l\in\mathcal{R}(i)\setminus j}\tilde{p}_{z_l^G}(k)+I(z_j^G=k), & \text{if} \quad j\in\mathcal{R}(i).\end{cases}$$

Straightforward computations lead to

$$\mathrm{W}=\eta\sum_{s=1}^{S}\sum_{i\in\bar{\mathcal{R}}(j)}\sum_{k=1}^{K}\tilde{p}_{z_i^s}(k)I\left(z_j^G=k\right), \quad [7.23]$$

where $\sum_{k=1}^{K} \tilde{p}_{z_i^s}(k) I\left(z_j^G = k\right) = \tilde{p}_{z_i^s}(z_j^G)$. Finally, we end up with the following expression of $\tilde{p}_{z_j^G}(z_j^G = k)$

$$\tilde{p}_{z_j^G}(z_j^G = k) \propto \exp\left(\eta \sum_{s=1}^{S} \sum_{i \in \bar{\mathcal{R}}(j)} \tilde{p}_{z_i^s}(k) + \beta_z^G \sum_{i \in N(j)} \tilde{p}_{z_i^G}(k)\right). \quad [7.24]$$

On the other hand, the M-step of the algorithm can be written as follows

$$\textbf{VM:} \quad \boldsymbol{\Phi}^{(r)} = \arg\max_{\Phi \in \underline{\boldsymbol{\Phi}}} \mathrm{E}_{\tilde{p}_{\mathbb{A}}^{(r)} \tilde{p}_{\mathbb{H}}^{(r)} \tilde{p}_{\mathbb{Q}}^{(r)} \tilde{p}_{\mathbb{Z}}^{(r)} \tilde{p}_{\boldsymbol{z}^G}^{(r)}} \left[\log p(\mathbb{Y}, \mathbb{A}, \mathbb{H}, \mathbb{Q}, \mathbb{Z}, \boldsymbol{z}^G; \boldsymbol{\Phi})\right], \quad [7.25]$$

or equivalently

$$\begin{aligned} \boldsymbol{\Phi}^{(r)} = \arg\max_{\Phi \in \underline{\boldsymbol{\Phi}}} & \left[\mathrm{E}_{\tilde{p}_{\mathbb{A}} \tilde{p}_{\mathbb{H}}}\left[\log p(\mathbb{Y} \mid \mathbb{A}, \mathbb{H}; \boldsymbol{\Phi})\right] + \mathrm{E}_{\tilde{p}_{\mathbb{A}} \tilde{p}_{\mathbb{Q}}}\left[\log p(\mathbb{A} \mid \mathbb{Q}; \boldsymbol{\Phi})\right]\right. \\ & + \mathrm{E}_{\tilde{p}_{\mathbb{Z}} \tilde{p}_{\boldsymbol{z}^G}}\left[\log p(\mathbb{Z} \mid \boldsymbol{z}^G; \boldsymbol{\Phi})\right] + \mathrm{E}_{\tilde{p}_{\boldsymbol{z}^G}}\left[\log p(\boldsymbol{z}^G; \boldsymbol{\Phi})\right] \\ & \left. + \mathrm{E}_{\tilde{p}_{\mathbb{H}} \tilde{p}_{\mathbb{Z}}}\left[\log p(\mathbb{H} \mid \mathbb{Z}; \boldsymbol{\Phi})\right] + \log p(\bar{\boldsymbol{h}}; \boldsymbol{\Phi}) + \log p(\bar{\boldsymbol{h}}^G; \boldsymbol{\Phi})\right]. \end{aligned} \quad [7.26]$$

Comparing [7.26] to the maximization equation [3.17] in the standard JPDE model, we can notice that the modification in the hierarchy of the HMS-JPDE model results in two new maximization sub-steps associated with the parameters $\bar{\boldsymbol{h}}$ and $\bar{\boldsymbol{h}}^G$.

(i) **VM-$\bar{\boldsymbol{h}}^s$ step**
The maximization of $\bar{\boldsymbol{h}}^s$ can be obtained by solving the following problem

$$\bar{\boldsymbol{h}}^s = \arg\max_{\bar{\boldsymbol{h}}^s} \left[\mathrm{E}_{\tilde{p}_{H^s} \tilde{p}_{z^s}}\left[\log p(\boldsymbol{H}^s \mid \boldsymbol{z}^s; \bar{\boldsymbol{h}}^s, \boldsymbol{\nu})\right] + \log p(\bar{\boldsymbol{h}}^s; \bar{\boldsymbol{h}}^G, (\sigma_h^s)^2)\right]. \quad [7.27]$$

For $s = 1, \ldots, S$, a single HRF pattern $\bar{\boldsymbol{h}}_k^s$ is estimated for parcel k^s. Differentiating with respect to $\bar{\boldsymbol{h}}_k^s$ yields

$$\bar{\boldsymbol{h}}_k^s = \left(\frac{\sum_{j=1}^{J} \tilde{p}_{z_j^s}(k) \boldsymbol{\Sigma}_k^{s\,-1} \boldsymbol{m}_{H_j}}{\sum_{j=1}^{J} \tilde{p}_{z_j^s}(k) \boldsymbol{\Sigma}_k^{s\,-1} + \boldsymbol{R}^{-1}/(\sigma_h^s)^2}\right) + \left(\frac{\bar{\boldsymbol{h}}_k^G \boldsymbol{R}^{-1}/(\sigma_h^s)^2}{\sum_{j=1}^{J} \tilde{p}_{z_j^s}(k) \boldsymbol{\Sigma}_k^{s\,-1} + \boldsymbol{R}^{-1}/(\sigma_h^s)^2}\right). \quad [7.28]$$

(ii) **VM-$\bar{\boldsymbol{h}}^G$** step
This maximization step can be formulated as follows

$$\bar{\boldsymbol{h}}^G = \arg\max_{\bar{\boldsymbol{h}}^G} \left[\sum_{s=1}^{S} p(\bar{\boldsymbol{h}}^s; \bar{\boldsymbol{h}}^G, (\sigma_h^s)^2) + \log p(\bar{\boldsymbol{h}}^G; (\sigma_h^G)^2) \right]. \quad [7.29]$$

For the group-level HRF profiles, a single HRF pattern is estimated for each parcel. Differentiating [7.29] with respect to $\bar{\boldsymbol{h}}_k^G$ yields

$$\bar{\boldsymbol{h}}_k^G = \frac{\sum_{s=1}^{S} \bar{\boldsymbol{h}}_k^s ((\sigma_h^s)^2 \boldsymbol{R})^{-1}}{((\sigma_h^G)^2 \boldsymbol{R})^{-1} + \sum_{s=1}^{S} ((\sigma_h^s)^2 \boldsymbol{R})^{-1}}. \quad [7.30]$$

For further details about the rest of the expectation and maximization steps refer to Subsection 3.2.3 (v)(a),(v)(b) and (v)(c). The steps of the HMS-JPDE model are described in Algorithm 7.1.

Algorithm 7.1 The HMS-JPDE algorithm. The subscript (r) refers to the current iteration.

Initialization:
  $\tilde{p}^{(0)}_{z^G}(\boldsymbol{z}^G)$ is initialized from the initial parcellation.
  for all s **do**
    $\tilde{p}^{(0)}_{z^s}(\boldsymbol{z}^s)$ is initialized from the initial parcellation.
    $\tilde{p}^{(0)}_{Q^s}(\boldsymbol{Q}^s)$ such that $\tilde{p}^{(0)}_{Q^s_j}(q^{m,s}_j) \in \{0,1\}$.
    for all j **do**
      - $\boldsymbol{m}^{(0)}_{H^s_j}$ is initialized from the canonical HRF.
      - $\boldsymbol{m}^{(0)}_{A^s_j}$ is initialized with zeros.
    end for
  end for
    Initialize with some $\boldsymbol{\Phi}^{(0)}$.
$r = 1$
repeat
  Expectation step:
    for all s **do**
      - Compute $\tilde{p}^{(r)}_{H^s}(\boldsymbol{H}^s)$ according to [3.18].
      - Compute $\tilde{p}^{(r)}_{A^s}(\boldsymbol{A}^s)$ according to [3.19].
      - Compute $\tilde{p}^{(r)}_{Q^s}(\boldsymbol{Q}^s)$ according to [3.24].
      - Compute $\tilde{p}^{(r)}_{z^s}(\boldsymbol{z}^s)$ according to [7.18].
    end for
    - Compute $\tilde{p}^{(r)}_{z^G}(\boldsymbol{z}^G)$ according to [7.24].
  Maximization step:
    Compute $\boldsymbol{\Phi}^{(r)}$ according to [7.26].
  set $r \leftarrow r + 1$
until convergence

7.4 Experimental validation

The HMS-JPDE was validated using synthetic and real data experiments via appropriate comparisons to assess its performance. These experiments are described in this section.

7.4.1 Synthetic fMRI time series

The fMRI time series were generated under the same considerations as in Subsection 6.5.1 and the same initial parcellation was used (see Subsection 6.5.1 for more details). The HMS-JPDE was used to analyze these time series in order to obtain parcellation and HRF estimates for each subject (contrary to the MS-JPDE in Chapter 6) as well as the corresponding group-level estimates. The subject-level and group-level parcellation estimates obtained by analyzing the generated fMRI time series of the four subjects are depicted in Fig. 7.2. From a visual point of view, the results in this figure are close to the ground truth parcellations in Fig. 6.2(a-e).
More precisely, the parcellation error values between the reference and estimated parcellations are reported in Tab. 7.1. These error percentages are relatively small which confirm that the HMS-JPDE model is able to obtain accurate parcellation estimates at the subject and the group level. Moreover, the parcellation error obtained with the HMS-JPDE is identical to the one obtained using the MS-JPDE in Subsection 6.5.1. This allows us to conclude that both models are able to provide similar and accurate group-level parcellation estimates. To further investigate the performance of the HMS-JPDE model in the parcellation task, we computed the confusion matrices between the reference and estimated parcellations in Tabs. 7.2-7.6 which show major intersections between the estimated parcels and their ground truths. The lowest and the highest true positive rate were 0.82 and 1.0, respectively which prove that the HMS-JPDE model is able to establish accurate parcels when compared to the reference ones. This precision gain is due to considering both the group and subject level parcellation layers which allows more variability of the estimated parcellation for the individuals. This variability at the subject-level parcellation allows more reliable group-level parcellation estimates.

As regards the HRF estimates, this model provides us with subject and group level HRF profiles. The estimated HRF profiles for the individuals

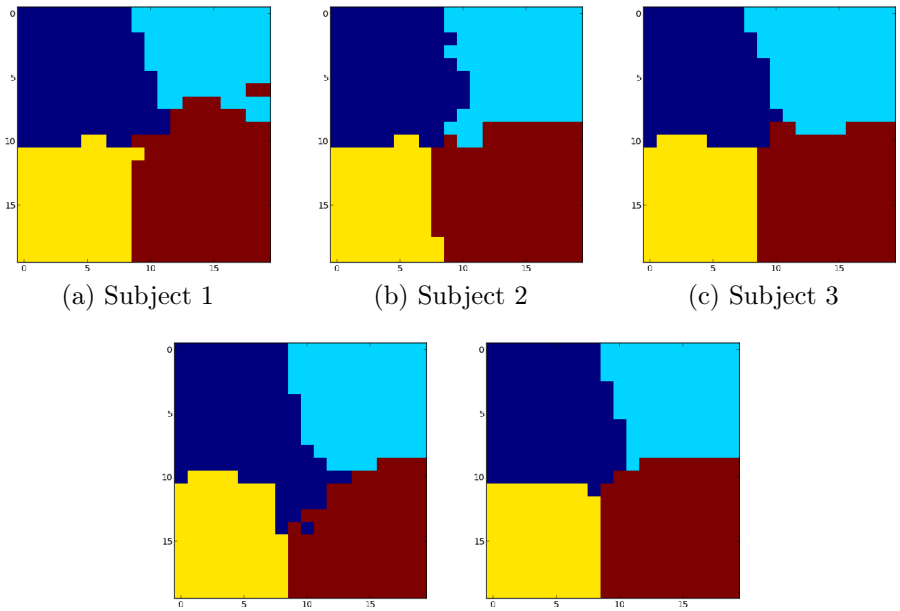

(a) Subject 1 (b) Subject 2 (c) Subject 3

(d) Subject 4 (e) Group-level

Figure 7.2: Subject-level and group-level parcellation estimates using the HMS-JPDE model.

Table 7.1: Error probabilities between the reference parcellations and their corresponding parcellation estimates.

Parcellation	Error probability
Subject.1	4.5%
Subject.2	1.0%
Subject.3	5.5%
Subject.4	2.0%
Group-level	4.25%

Table 7.2: Confusion matrix between reference (RP) and estimated (EP) for subject 1 using the HMS-JPDE model.

EP \ RP	Parcel 1	Parcel 2	Parcel 3	Parcel 4
Parcel 1	**0.98**	0.0	0.01	0.05
Parcel 2	0.02	**1.0**	0.0	0.06
Parcel 3	0.0	0.0	**0.99**	0.04
Parcel 4	0.0	0.0	0.0	**0.85**

Table 7.3: Confusion matrix between reference (RP) and estimated (EP) for subject 2 using the HMS-JPDE model.

EP \ RP	Parcel 1	Parcel 2	Parcel 3	Parcel 4
Parcel 1	**0.96**	0.02	0.01	0.01
Parcel 2	0.04	**0.98**	0.0	0.01
Parcel 3	0.0	0.0	**0.99**	0.0
Parcel 4	0.0	0.0	0.0	**0.98**

Table 7.4: Confusion matrix between reference (RP) and estimated (EP) for subject 3 using the HMS-JPDE model.

EP \ RP	Parcel 1	Parcel 2	Parcel 3	Parcel 4
Parcel 1	**0.97**	0.02	0.01	0.0
Parcel 2	0.03	**0.98**	0.0	0.02
Parcel 3	0.0	0.0	**0.82**	0.0
Parcel 4	0.0	0.026	0.17	**0.98**

Table 7.5: Confusion matrix between reference (RP) and estimated (EP) for subject 4 using the HMS-JPDE model.

EP \ RP	Parcel 1	Parcel 2	Parcel 3	Parcel 4
Parcel 1	**0.95**	0.01	0.0	0.0
Parcel 2	0.01	**0.98**	0.0	0.02
Parcel 3	0.01	0.0	**0.99**	0.0
Parcel 4	0.03	0.01	0.01	**0.98**

Table 7.6: Confusion matrix between reference (RP) and estimated (EP) for the group-level using the HMS-JPDE model.

EP \ RP	Parcel 1	Parcel 2	Parcel 3	Parcel 4
Parcel 1	**0.95**	0.0	0.0	0.01
Parcel 2	0.03	**0.96**	0.0	0.01
Parcel 3	0.0	0.0	**0.99**	0.03
Parcel 4	0.02	0.04	0.01	**0.95**

and their group-level HRF profiles are depicted in Fig. 7.3 along with their reference HRFs. One can visually notice that the estimated HRFs are similar to their ground truths.

To further investigate the performance of the HMS-JPDE model in estimating the subject and group level HRFs, the MSEs between the ground truth HRFs and the corresponding HRF estimates are reported in Tabs. 7.7. In general, these values are relatively small and confirm the previous visual observation. To be more specific, the HMS-JPDE model outperforms the MS-JPDE in estimating group-level HRFs which can be obvious by comparing the MSEs in the last column of Tab. 7.7 to those in Tab. 6.2 obtained using the MS-JPDE model.

Table 7.7: MSEs between reference and estimated subject and group level HRF profiles using HMS-JPDE model.

HRF	Subject 1	Subject 2	Subject 3	Subject 4	Group-level
HRF 1	4.9×10^{-5}	1.0×10^{-5}	1.9×10^{-5}	1.4×10^{-5}	5.63×10^{-5}
HRF 2	4.0×10^{-5}	3.5×10^{-5}	3.9×10^{-5}	3.8×10^{-5}	3.71×10^{-5}
HRF 3	4.0×10^{-5}	5.9×10^{-5}	1.38×10^{-5}	6.0×10^{-5}	6.92×10^{-5}
HRF 4	3.0×10^{-5}	8.8×10^{-5}	3.1×10^{-5}	3.7×10^{-5}	1.0×10^{-4}

Furthermore, we tested the performance of the HMS-JPDE model in estimating the NRLs and detecting the activation. The computed MSE values between the reference and the estimated NRLs and activation labels are reported in Tab. 7.8. These values are relatively small when compared to those of the MS-JPDE model in Tab. 6.3 and they are closer to those of the JPDE model in Tab. 6.4 which confirm that the HMS-JPDE model outperforms the MS-JPDE and is able to retain the robust performance of the JPDE model in the detection task. Moreover, we tested the proposed model for different Sig-

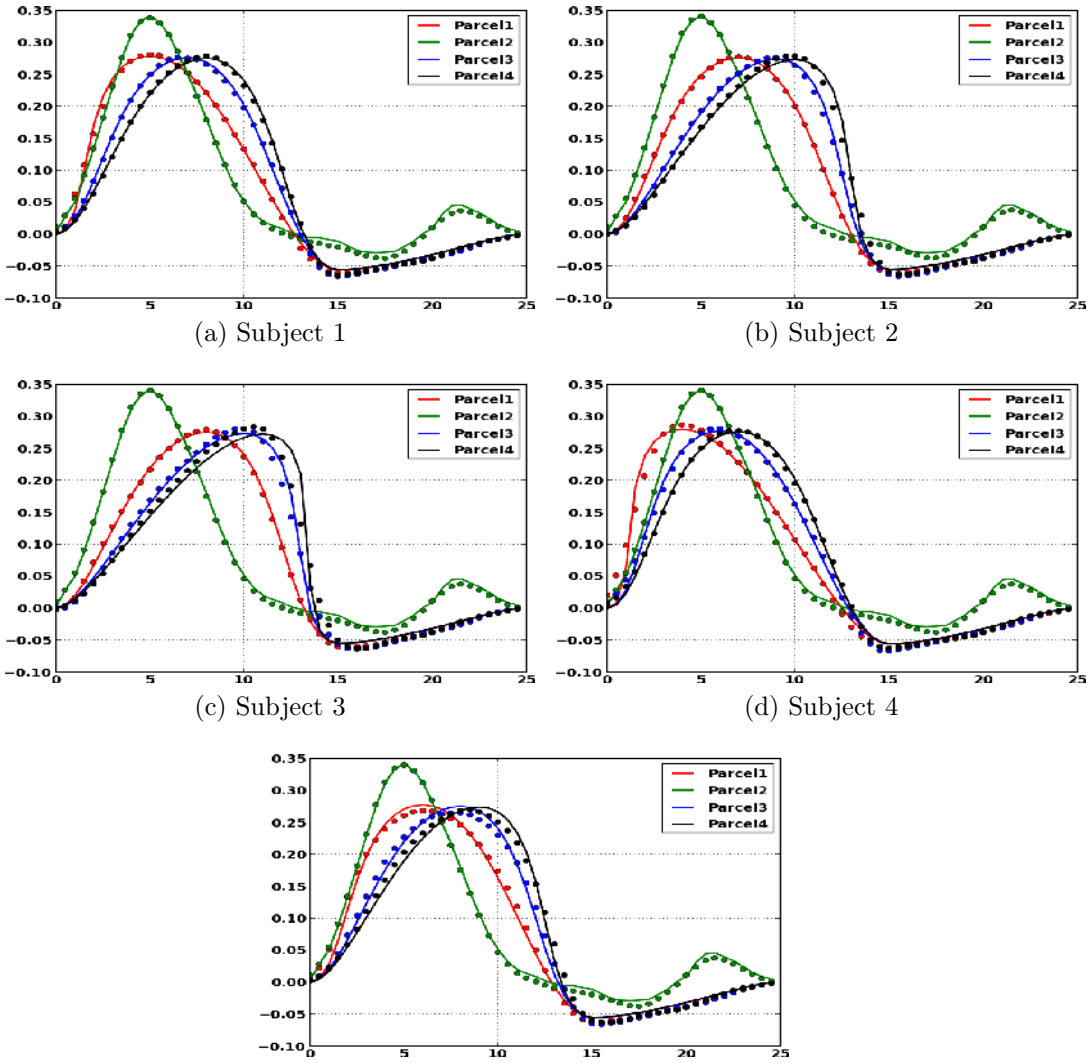

(a) Subject 1 (b) Subject 2

(c) Subject 3 (d) Subject 4

(e) Group-level

Figure 7.3: Estimated (dotted line) and ground truth (continuous line) group and subject level HRF profiles using HMS-JPDE model.

Table 7.8: MSEs between reference and estimated NRLs and activation labels.

		Subject 1	Subject 2	Subject 3	Subject 4
NRLs	$m = 1$	0.016	0.017	0.017	0.016
	$m = 2$	0.011	0.010	0.010	0.011
Labels	$m = 1$	0.002	0.002	0.002	0.002
	$m = 2$	0.003	0.003	0.002	0.002

nal to Noise Ratios (SNR). Twenty experiments were run for different noise variances ranging from 0.01 to 0.2 with 0.01 increment for each experiment. The mean parcellation error and the standard deviation for the estimated subject and group level parcellations are shown in Fig. 7.4. The average parcellation errors over the subjects and for the group-level parcellation in the twenty experiments were 2.15% and 3.35% respectively. The average subject-level parcellation error ranges between 1.0% and 2.8%. These results prove that the HMS-JPDE model is able to obtain accurate estimates of the group and subject level parcellations for high SNR.

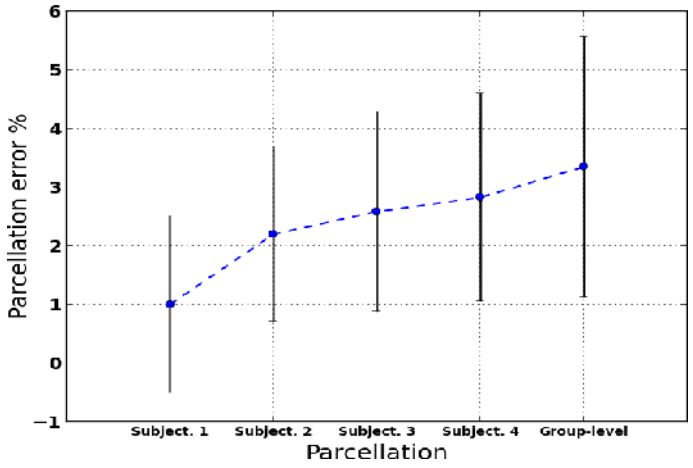

Figure 7.4: The evolution of the mean parcellation error and standard deviation on the estimated subject-level and group-level parcellations for 20 experiments with different SNRs.

7.4.2 Real data

The real data experiment was carried out under the same considerations in Subsection 6.5.2 with fMRI data from the same individuals and the same ROI. We fixed $\beta_z^s = 0.9$, $(\sigma_h^s)^2 = 0.5$ for $s = 1, \ldots, S$, $\beta_G = 0.9$ and $((\sigma_h^G)^2 = 0.5)$[1].
For the ease of exposure, we separate the analysis results of the real data experiment into two parts. The first part is devoted to the subject-level analysis and the comparison with the results obtained by analyzing each individual using the JPDE model. The second one is dedicated to the group-level analysis and the comparison with the MS-JPDE model.

(i) **Subject-level analysis**
The subject-level results were obtained after analyzing the fMRI data coming from all the subjects simultaneously. These results are compared with those obtained by analyzing the individuals using the JPDE model. The parcellation estimates using both models are depicted in Figs. 7.5-7.14. The displayed parcellations for the individuals in Figs. 7.5-7.14 show some similarities between the estimated subject-level parcellations using the HMS-JPDE and standard JPDE models, which is confirmed by the confusion matrices between these estimates in Tabs. 7.9-7.18. To be more specific, the first and the fourth estimated parcels using the HMS-JPDE are very similar with their counterparts obtained using the JPDE model for most of the individuals while some of the voxels in parcels 2 (respectively parcel 3) obtained using the JPDE model may actually exist in parcel 3 (respectively parcel 2) of the HMS-JPDE model. These results indicate that the HMS-JPDE and the standard JPDE models provide coherent parcellation results at the subject-level. However, the standard JPDE model is not adequate for obtaining the group-level analysis results, which will be discussed in the next part.

[1]These parameters were adjusted using cross validation

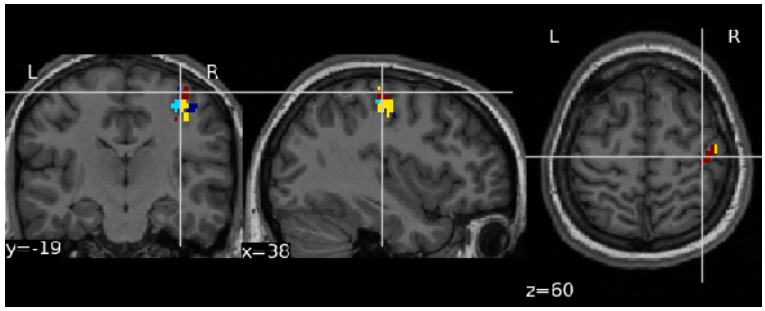

(a) HMS-JPDE

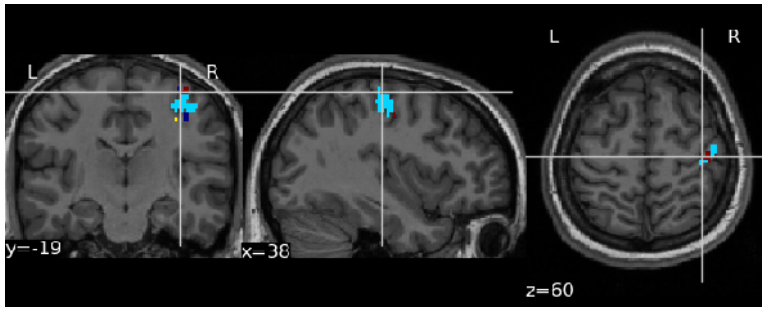

(b) JPDE

Figure 7.5: Slices of the parcellation estimates for subject 1 using the HMS-JPDE and JPDE models.

Table 7.9: Confusion matrix between the parcellation estimates for subject 1 using the HMS-JPDE and JPDE models.

HMS-JPDE \ JPDE	Parcel 1	Parcel 2	Parcel 3	Parcel 4
Parcel 1	0.06	0.0	0.1	0.0
Parcel 2	**0.62**	**0.96**	**0.9**	0.46
Parcel 3	0.23	0.04	0.0	0.04
Parcel 4	0.08	0.0	0.0	**0.5**

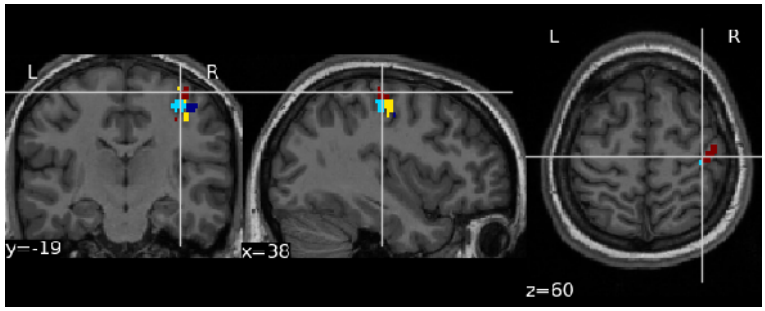

(a) HMS-JPDE

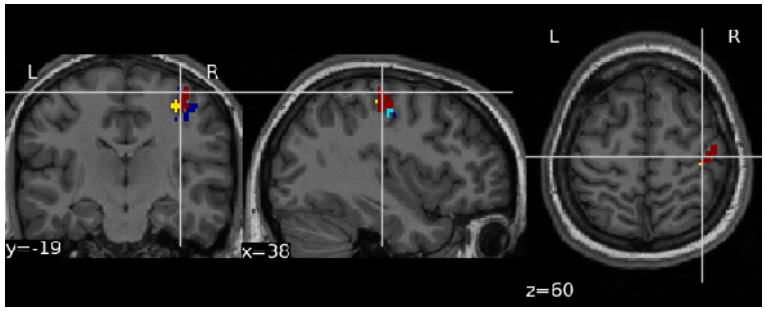

(b) JPDE

Figure 7.6: Slices of the parcellation estimates for subject 2 using the HMS-JPDE and JPDE models.

Table 7.10: Confusion matrix between the parcellation estimates for subject 2 using the HMS-JPDE and JPDE models.

HMS-JPDE \ JPDE	Parcel 1	Parcel 2	Parcel 3	Parcel 4
Parcel 1	**0.8**	0.0	0.12	0.04
Parcel 2	0.0	**0.72**	0.0	0.0
Parcel 3	0.02	0.0	**0.52**	0.0
Parcel 4	0.18	0.28	0.36	**0.96**

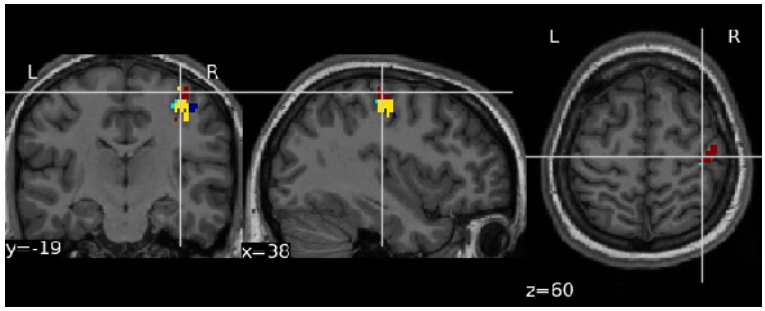

(a) HMS-JPDE

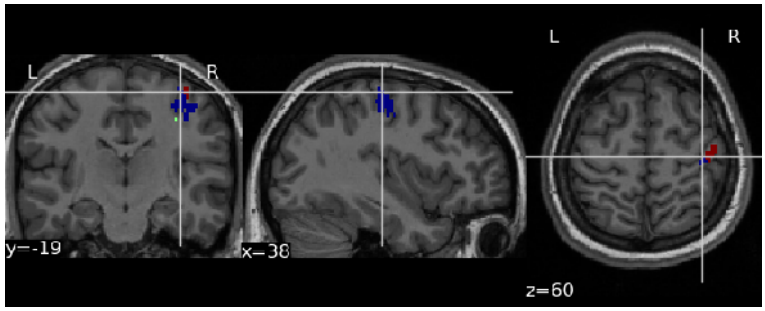

(b) JPDE

Figure 7.7: Slices of the parcellation estimates for subject 3 using the HMS-JPDE and JPDE models.

Table 7.11: Confusion matrix between the parcellation estimates for subject 3 using the HMS-JPDE and JPDE models.

HMS-JPDE \ JPDE	Parcel 1	Parcel 2	Parcel 3	Parcel 4
Parcel 1	0.0	0.0	0.0	0.0
Parcel 2	**0.92**	**1.0**	0.0	0.26
Parcel 3	0.06	0.0	**1.0**	0.04
Parcel 4	0.02	0.0	0.0	**0.70**

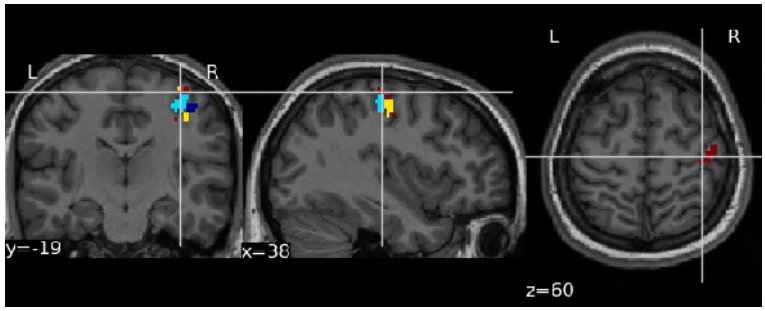

(a) HMS-JPDE

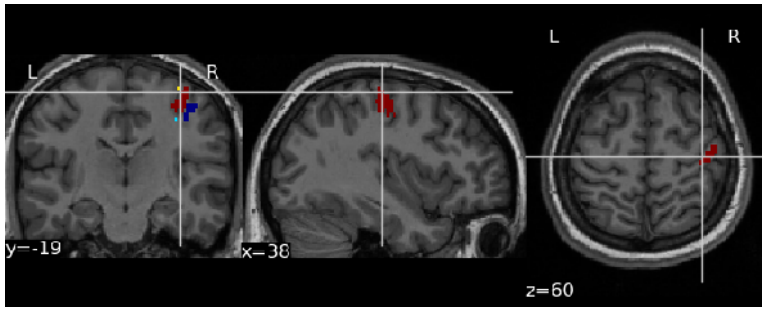

(b) JPDE

Figure 7.8: Slices of the parcellation estimates for subject 4 using the HMS-JPDE and JPDE models.

Table 7.12: Confusion matrix between the parcellation estimates for subject 4 using the HMS-JPDE and JPDE models.

HMS-JPDE \ JPDE	Parcel 1	Parcel 2	Parcel 3	Parcel 4
Parcel 1	**0.82**	0.02	0.20	0.0
Parcel 2	0.0	**0.65**	0.0	0.04
Parcel 3	0.05	0.0	**0.76**	0.0
Parcel 4	0.13	0.33	0.04	**0.96**

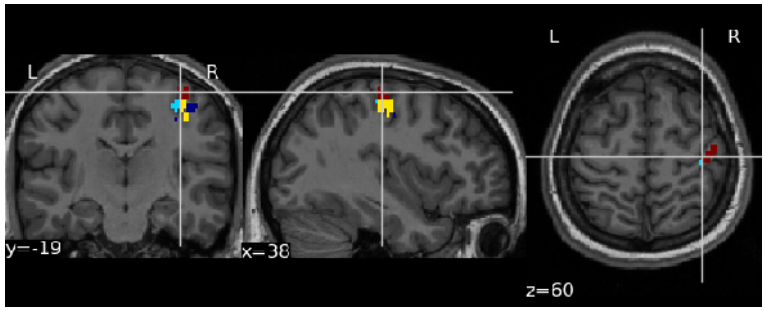

(a) HMS-JPDE

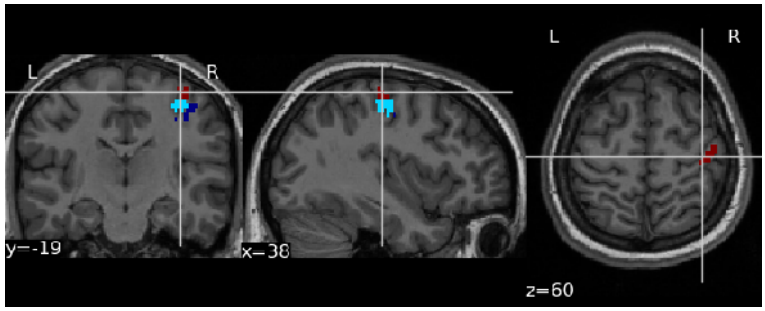

(b) JPDE

Figure 7.9: Slices of the parcellation estimates for subject 5 using the HMS-JPDE and JPDE models.

Table 7.13: Confusion matrix between the parcellation estimates for subject. 5 using the HMS-JPDE and JPDE models.

HMS-JPDE \ JPDE	Parcel 1	Parcel 2	Parcel 3	Parcel 4
Parcel 1	**0.83**	0.04	0.17	0.0
Parcel 2	0.17	**0.89**	**0.83**	0.0
Parcel 3	0.05	0.0	0.0	0.0
Parcel 4	0.13	0.07	0.0	**1.0**

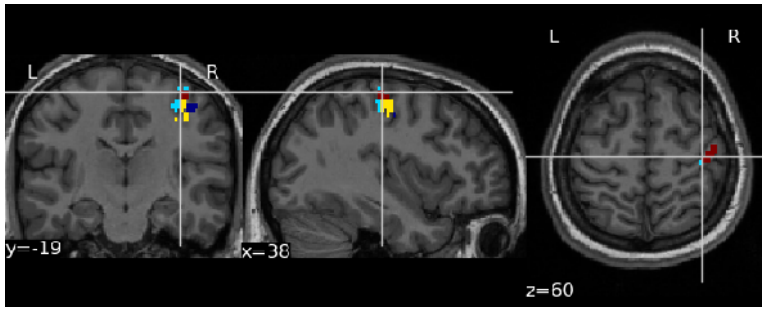

(a) HMS-JPDE

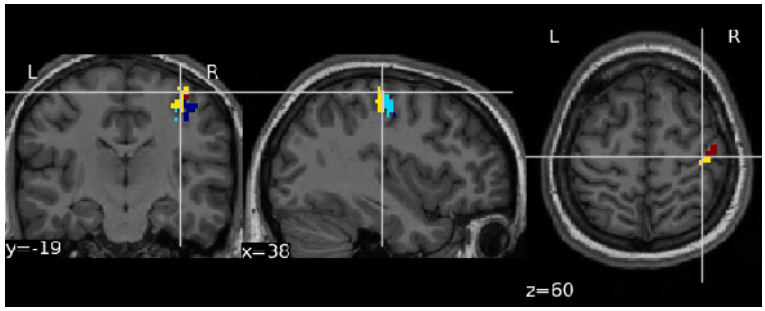

(b) JPDE

Figure 7.10: Slices of the parcellation estimates for subject 6 using the HMS-JPDE and JPDE models.

Table 7.14: Confusion matrix between the parcellation estimates for subject. 6 using the HMS-JPDE and JPDE models.

HMS-JPDE \ JPDE	Parcel 1	Parcel 2	Parcel 3	Parcel 4
Parcel 1	**0.98**	0.0	0.27	0.0
Parcel 2	0.0	0.03	**0.64**	0.04
Parcel 3	0.02	**0.97**	0.06	0.20
Parcel 4	0.0	0.0	0.03	**0.76**

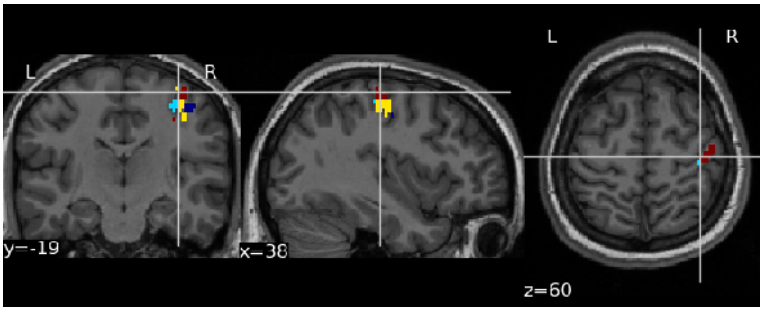

(a) HMS-JPDE

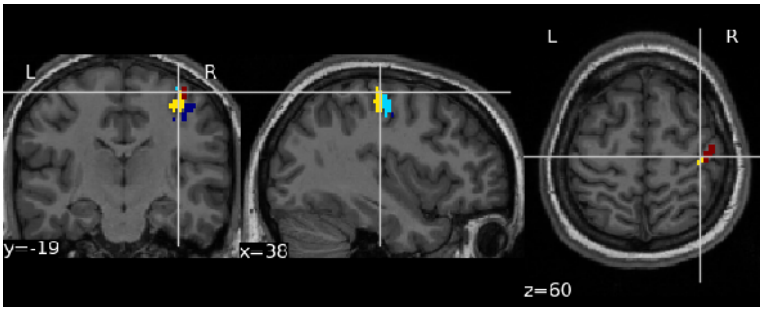

(b) JPDE

Figure 7.11: Slices of the parcellation estimates for subject 7 using the HMS-JPDE and JPDE models.

Table 7.15: Confusion matrix between the parcellation estimates for subject 7 using the HMS-JPDE and JPDE models.

HMS-JPDE \ JPDE	Parcel 1	Parcel 2	Parcel 3	Parcel 4
Parcel 1	**0.88**	0.0	0.20	0.04
Parcel 2	0.0	0.0	0.20	0.04
Parcel 3	0.09	**1.0**	**0.60**	0.10
Parcel 4	0.03	0.0	0.0	**0.82**

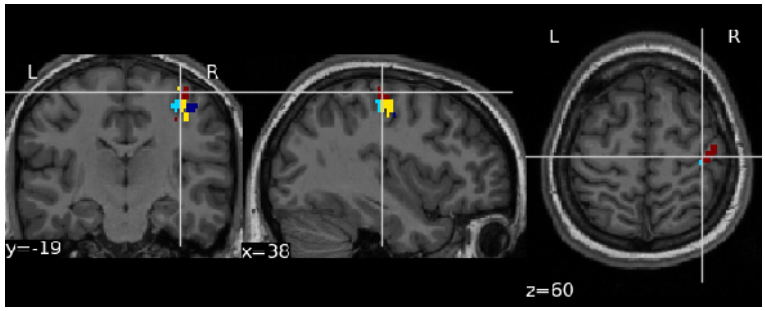

(a) HMS-JPDE

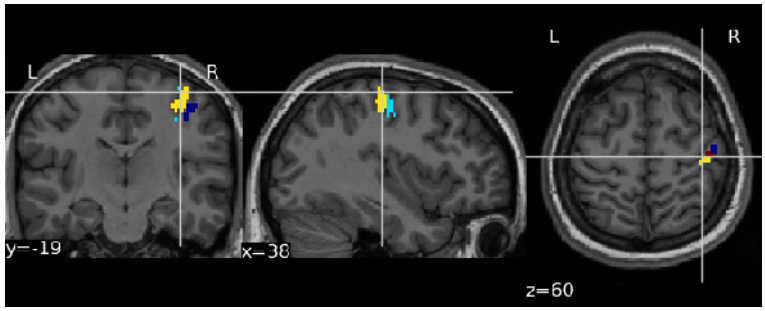

(b) JPDE

Figure 7.12: Slices of the parcellation estimates for subject 8 using the HMS-JPDE and JPDE models.

Table 7.16: Confusion matrix between the parcellation estimates for subject 8 using the HMS-JPDE and JPDE models.

HMS-JPDE \ JPDE	Parcel 1	Parcel 2	Parcel 3	Parcel 4
Parcel 1	**0.78**	0.0	0.22	0.32
Parcel 2	0.22	0.07	**0.55**	0.06
Parcel 3	0.0	**0.93**	0.23	0.12
Parcel 4	0.0	0.0	0.0	**0.50**

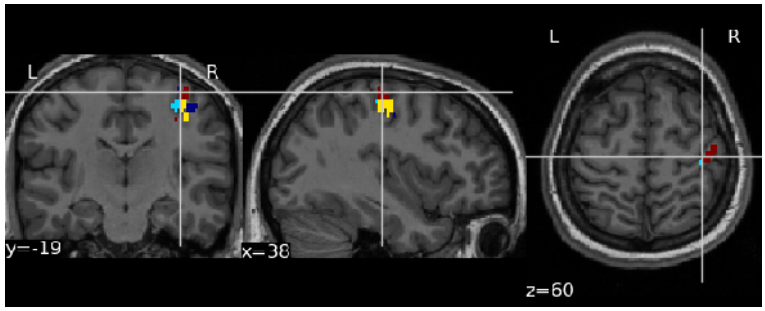

(a) HMS-JPDE

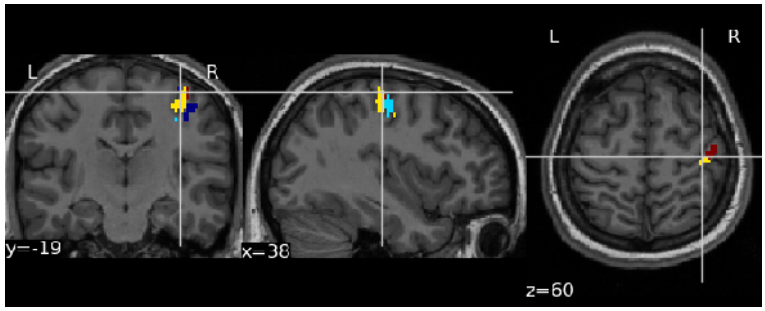

(b) JPDE

Figure 7.13: slices of the parcellation estimates for subject 9 using the HMS-JPDE and JPDE models.

Table 7.17: Confusion matrix between the parcellation estimates for subject 9 using the HMS-JPDE and JPDE models.

HMS-JPDE \ JPDE	Parcel 1	Parcel 2	Parcel 3	Parcel 4
Parcel 1	**0.67**	0.0	0.16	0.0
Parcel 2	0.10	0.0	**0.58**	0.08
Parcel 3	0.04	**1.0**	0.22	0.24
Parcel 4	0.19	0.0	0.04	**0.68**

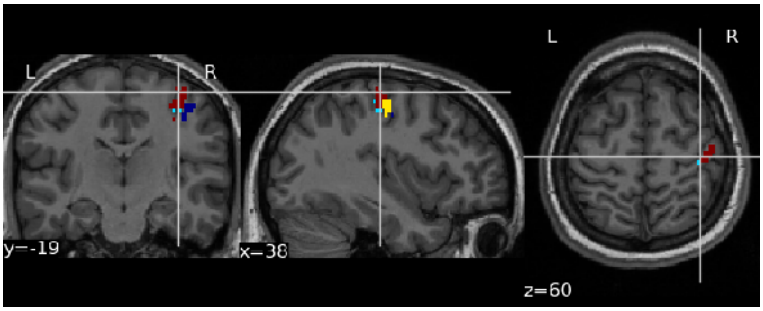

(a) HMS-JPDE

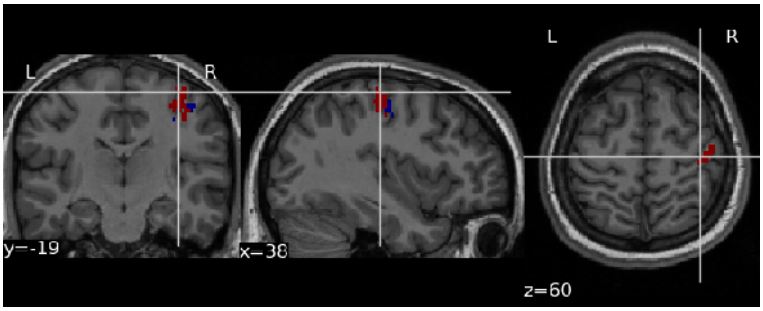

(b) JPDE

Figure 7.14: Slices of the parcellation estimates for subject 10 using the HMS-JPDE and JPDE models.

Table 7.18: Confusion matrix between the parcellation estimates for subject 10 using the HMS-JPDE and JPDE models.

HMS-JPDE \ JPDE	Parcel 1	Parcel 2	Parcel 3	Parcel 4
Parcel 1	0.09	0.0	0.16	0.0
Parcel 2	0.33	0.06	**0.57**	0.03
Parcel 3	0.0	0.0	0.0	0.0
Parcel 4	**0.58**	**0.94**	0.43	**0.97**

The HRF estimates obtained using the HMS-JPDE and JPDE models as well as the canonical HRFs are depicted in Figs. 7.15-7.19. From a visual point of view we can notice some similarities in their shapes. However, some of the HRF profiles estimated using the HMS-JPDE model are closer in shape to the canonical HRF which is the case of the HRF in the motor cortex. We further explored these HRF profiles by calculating their TTP and FWHM. These results are reported in Tabs. 7.19 and 7.20, respectively. The TTPs for the estimated HRFs using the HMS-JPDE and JPDE models range between 5.4 to 6.6 s and 4.8 to 7.8 s, respectively. Regarding the FWHMs, they range between 3.6 to 6.0 s for the HRF estimated using the HMS-JPDE model and 4.8 to 9.0 s for those obtained by the JPDE model. Moreover, we computed the Euclidean distances between the estimated HRFs using both models and the canonical HRF in Tab. 7.21. The average Euclidean distance between the estimated HRF using the HMS-JPDE and the JPDE models and the canonical HRF are 0.46 and 0.47, respectively which indicate that the two models gives coherent results in estimating these HRF profiles at the subject-level. However, these Euclidean distances combined with estimated TTPs and FWHMs in Tabs. 7.19 and 7.20 allow the interpretation that the HRF estimates using the HMS-JPDE model are closer to the canonical HRF than those estimated using the JPDE model, which is coherent with the previous conclusions in Subsections 4.3.2 and 5.4.2 and the study conducted in (Badillo et al., 2013b) which demonstrated that the HRF in the motor cortex strongly departs from the canonical shape. Hence, the HMS-JPDE model outperforms the JPDE model for this specific dataset in obtaining accurate HRF estimates that are close to the canonical shape.

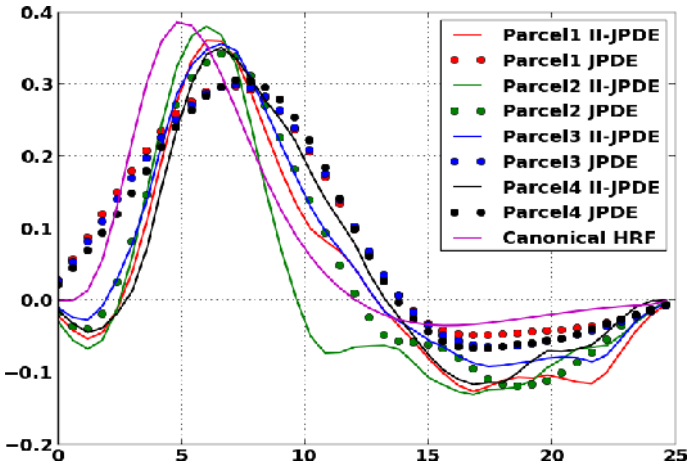

(a) Subject 1

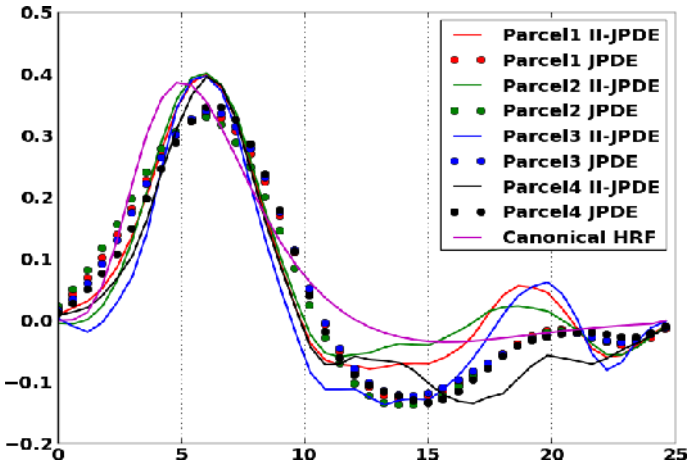

(b) Subject 2

Figure 7.15: HRF estimates for subjects 1 and 2 using the HMS-JPDE and JPDE models in the right motor cortex.

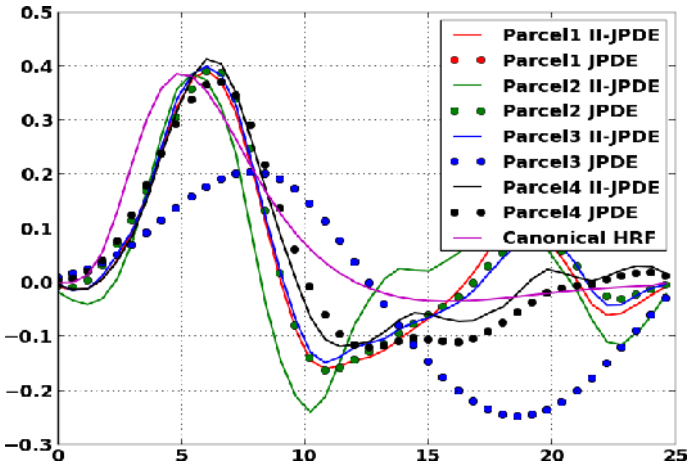

(a) Subject 3

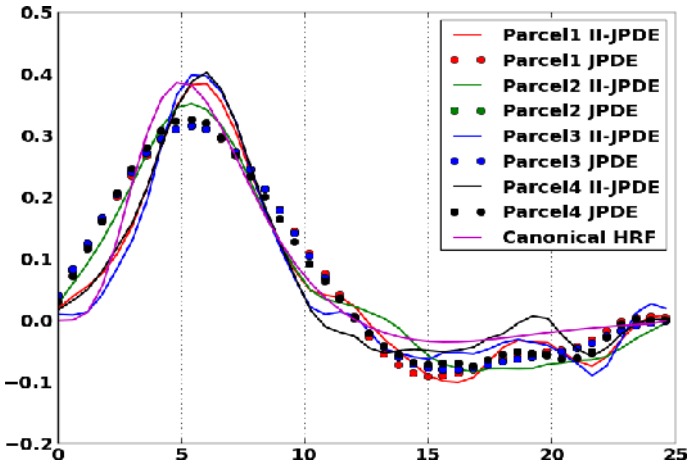

(b) Subject 4

Figure 7.16: HRF estimates for subjects 3 and 4 using the HMS-JPDE and JPDE models in the right motor cortex.

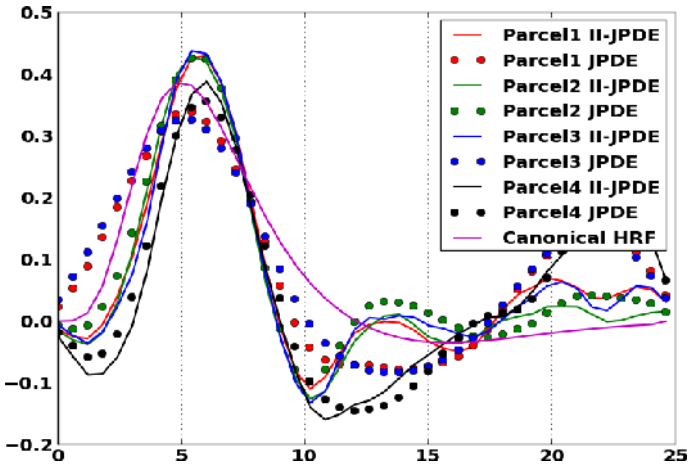

(a) Subject 5

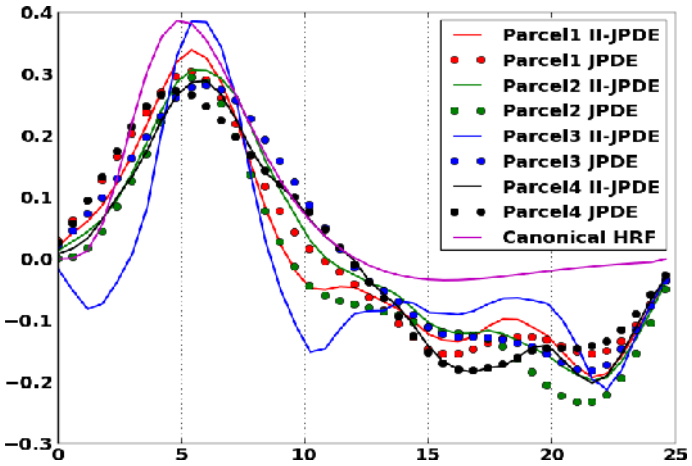

(b) Subject 6

Figure 7.17: HRF estimates for subjects 5 and 6 using the HMS-JPDE and JPDE models in the right motor cortex.

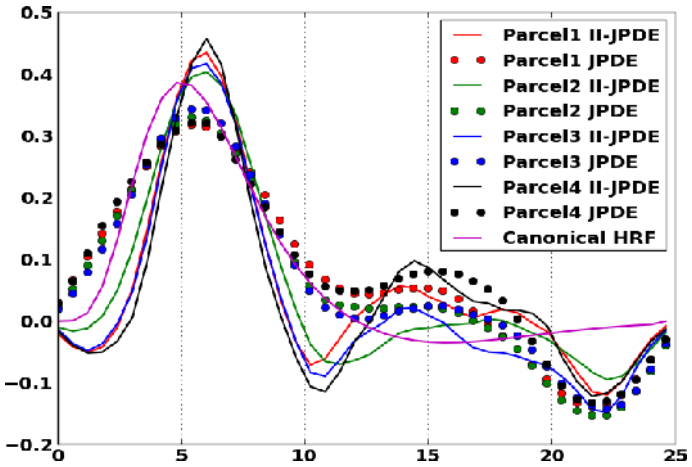

(a) Subject 7

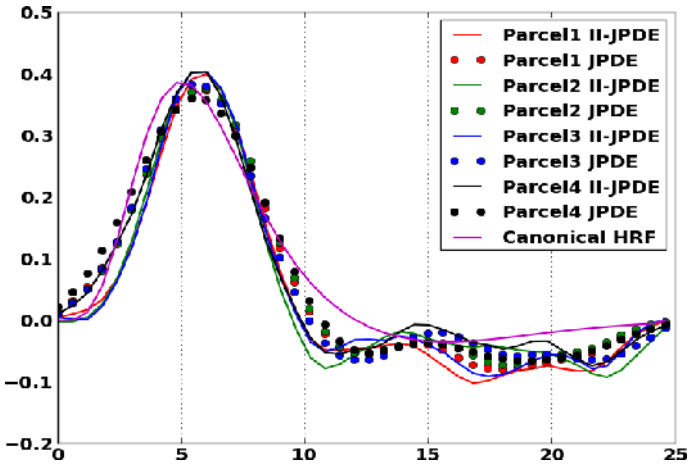

(b) Subject 8

Figure 7.18: HRF estimates for subjects 7 and 8 using the HMS-JPDE and JPDE models in the right motor cortex.

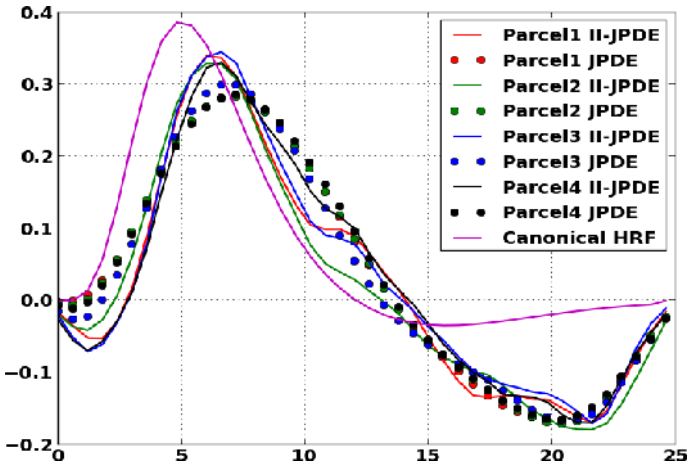

(a) Subject 9

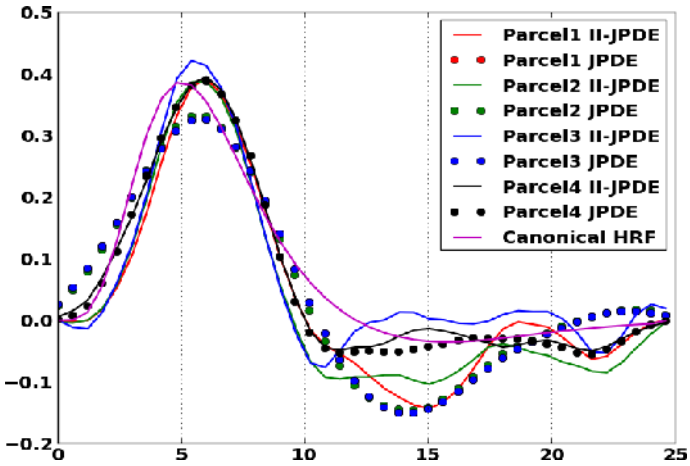

(b) Subject 10

Figure 7.19: HRF estimates for subjects 9 and 10 using the HMS-JPDE and JPDE models in the right motor cortex.

Table 7.19: The estimated TTP for the HRFs estimated using HMS-JPDE and JPDE models.

Model	Subject 1				Subject 2			
	HRF 1	HRF 2	HRF 3	HRF 4	HRF 1	HRF 2	HRF 3	HRF 4
HMS-JPDE	**6.0**	**6.0**	**6.6**	**6.6**	6.0	6.0	6.0	6.0
JPDE	7.2	6.6	7.2	7.2	6.0	6.0	6.0	6.6
Model	Subject 3				Subject 4			
	HRF 1	HRF 2	HRF 3	HRF 4	HRF 1	HRF 2	HRF 3	HRF 4
HMS-JPDE	**6.0**	**5.4**	**6.0**	**6.0**	6.0	5.4	5.4	6.0
JPDE	7.8	6.0	7.8	6.6	**5.4**	5.4	5.4	**5.4**
Model	Subject 5				Subject 6			
	HRF 1	HRF 2	HRF 3	HRF 4	HRF 1	HRF 2	HRF 3	HRF 4
HMS-JPDE	6.0	5.4	5.4	6.0	5.4	5.4	**5.4**	6.0
JPDE	**5.4**	5.4	5.4	6.0	5.4	5.4	6.0	**4.8**
Model	Subject 7				Subject 8			
	HRF 1	HRF 2	HRF 3	HRF 4	HRF 1	HRF 2	HRF 3	HRF 4
HMS-JPDE	6.0	6.0	6.0	6.0	6.0	6.0	6.0	6.0
JPDE	**5.4**	**5.4**	**5.4**	**5.4**	6.0	6.0	**5.4**	**5.4**
Model	Subject 9				Subject 10			
	HRF 1	HRF 2	HRF 3	HRF 4	HRF 1	HRF 2	HRF 3	HRF 4
HMS-JPDE	**6.0**	**6.0**	**6.6**	**6.6**	6.0	6.0	**5.4**	6.0
JPDE	7.2	7.2	7.2	7.2	6.0	6.0	6.0	6.0

Table 7.20: The estimated FWHM for the HRFs estimated using HMS-JPDE and JPDE models.

Model	Subject 1				Subject 2			
	HRF 1	HRF 2	HRF 3	HRF 4	HRF 1	HRF 2	HRF 3	HRF 4
HMS-JPDE	**5.1**	**4.2**	**5.4**	**6.0**	**4.8**	**4.8**	**4.2**	**4.2**
JPDE	9.0	6.0	8.4	7.8	6.6	6.0	6.6	6.0
Model	Subject 3				Subject 4			
	HRF 1	HRF 2	HRF 3	HRF 4	HRF 1	HRF 2	HRF 3	HRF 4
HMS-JPDE	**4.2**	**3.6**	**4.2**	**4.2**	**4.8**	**5.4**	**4.2**	4.8
JPDE	7.2	4.2	7.2	4.8	7.8	7.8	7.8	7.2
Model	Subject 5				Subject 6			
	HRF 1	HRF 2	HRF 3	HRF 4	HRF 1	HRF 2	HRF 3	HRF 4
HMS-JPDE	**3.6**	**3.6**	**3.6**	**3.6**	**4.2**	5.4	**3.6**	**4.8**
JPDE	6.0	4.2	6.0	6.0	6.0	**4.2**	6.6	6.6
Model	Subject 7				Subject 8			
	HRF 1	HRF 2	HRF 3	HRF 4	HRF 1	HRF 2	HRF 3	HRF 4
HMS-JPDE	**4.2**	**4.2**	**4.2**	**3.0**	**4.2**	**4.8**	**4.2**	**4.8**
JPDE	7.2	6.6	6.0	6.6	4.8	5.4	4.8	6.0
Model	Subject 9				Subject 10			
	HRF 1	HRF 2	HRF 3	HRF 4	HRF 1	HRF 2	HRF 3	HRF 4
HMS-JPDE	**5.4**	**4.8**	**5.4**	**5.4**	**4.2**	**4.8**	**4.2**	4.8
JPDE	7.2	7.2	6.6	7.2	6.0	6.0	6.0	4.8

Table 7.21: Euclidean distance between the HRFs estimated using HMS-JPDE and JPDE models and the canonical HRF.

Model	Subject 1				Subject 2			
	HRF 1	HRF 2	HRF 3	HRF 4	HRF 1	HRF 2	HRF 3	HRF 4
HMS-JPDE	0.53	0.50	**0.44**	0.59	0.35	**0.30**	0.52	0.43
JPDE	**0.45**	**0.48**	0.47	**0.50**	0.35	0.37	**0.34**	**0.39**
Model	Subject 3				Subject 4			
	HRF 1	HRF 2	HRF 3	HRF 4	HRF 1	HRF 2	HRF 3	HRF 4
HMS-JPDE	**0.60**	0.79	**0.54**	**0.42**	**0.24**	**0.24**	**0.25**	**0.22**
JPDE	0.90	**0.56**	0.90	0.43	0.30	0.30	0.30	0.26
Model	Subject 5				Subject 6			
	HRF 1	HRF 2	HRF 3	HRF 4	HRF 1	HRF 2	HRF 3	HRF 4
HMS-JPDE	**0.46**	0.45	0.50	**0.78**	**0.56**	**0.56**	0.74	0.63
JPDE	0.51	**0.40**	0.50	0.79	0.56	0.74	**0.57**	**0.60**
Model	Subject 7				Subject 8			
	HRF 1	HRF 2	HRF 3	HRF 4	HRF 1	HRF 2	HRF 3	HRF 4
HMS-JPDE	0.50	**0.35**	**0.36**	0.63	0.34	0.34	0.32	0.26
JPDE	**0.42**	0.40	0.51	**0.46**	**0.24**	**0.23**	**0.24**	**0.21**
Model	Subject 9				Subject 10			
	HRF 1	HRF 2	HRF 3	HRF 4	HRF 1	HRF 2	HRF 3	HRF 4
HMS-JPDE	**0.64**	**0.58**	0.62	0.68	**0.39**	0.40	**0.33**	**0.23**
JPDE	0.65	0.65	0.62	**0.66**	0.40	0.40	0.40	0.25

(ii) **Group-level analysis**
This part compares the group-level estimates obtained using the HMS-JPDE and the MS-JPDE models. Starting with the group-level parcellation, Fig. 7.20 shows different slices of the parcellation estimates using the HMS-JPDE model. To compare the group-level parcellation estimates of the HMS-JPDE model with those obtained using the MS-JPDE model, Tab. 7.22 displays the confusion matrix between these estimates using the two models. These results show important similarities between the corresponding estimated parcels using the two models. It is worth recalling that the group-level parcellation estimator obtained using the HMS-JPDE model is directly derived from the subject-level parcellations contrary to the MS-JPDE model where the group-level parcellation is derived from the subject-level voxel-dependent HRFs. As a result, the HMS-JPDE model allows more flexibility in the parcellation at the subject-level since each subject has its own parcellation. Thus, the group-level parcellation estimates obtained using the HMS-JPDE model are considered to be more reliable from a theoretical point of view.

Table 7.22: Confusion matrix for group-level parcellation estimates obtained using the HMS-JPDE and JPDE models.

HMS-JPDE \ MS-JPDE	Parcel 1	Parcel 2	Parcel 3	Parcel 4
Parcel 1	**0.75**	0.0	0.14	0.0
Parcel 2	0.25	**1.0**	0.30	0.45
Parcel 3	0.0	0.0	**0.56**	0.04
Parcel 4	0.25	0.0	0.0	**0.51**

The group-level HRF estimates for both models are shown along with the canonical HRF shape in Fig. 7.21-7.24. From a visual point of view, we can notice that the HRF estimates using the two models are similar and they are close to the canonical HRF shape. More precisely, we computed the Euclidean distances between the HRF estimates obtained with the HMS-JPDE and the canonical HRF in Tab. 7.23. Generally speaking, these results are close to those in Tab. 6.5 for the HRF estimates obtained using the MS-JPDE model and there are no significant differences between the reported values. Furthermore, the TTP and FWHM for the obtained HRF estimates are computed in Tab. 7.24.

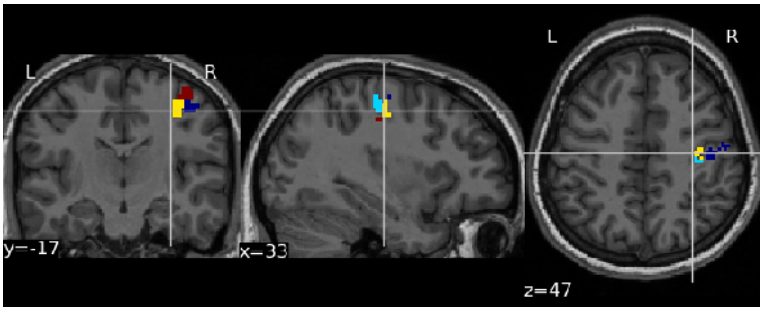

(a) Slice 1

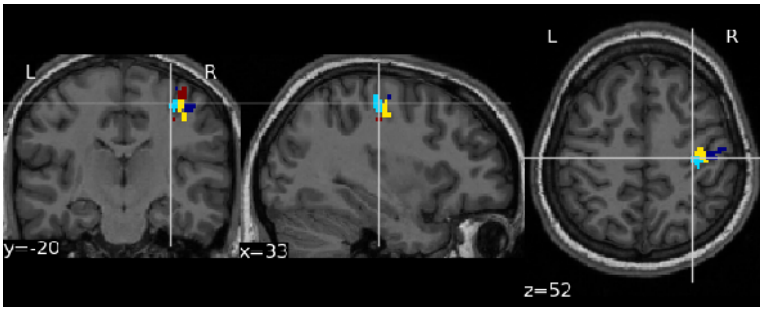

(b) Slice 2

Figure 7.20: Different slices of the estimated parcellation using HMS-JPDE model.

Comparing these results with the ones in Tab. 6.6, we can notice some similarities in the computed TTP values for the corresponding HRFs. As discussed in Subsection 6.5.2, the estimated HRFs using the MS-JPDE model are affected by the value of the hyperparameter $(\sigma_h^G)^2$ which can be clear in Fig. 6.12. It is worth noticing that $(\sigma_h^G)^2$ was adjusted to 0.5 in the setting of the real data experiment conducted using the HMS-JPDE model which does not have any effect on the smoothness of the group-level HRFs when compared to those obtained with the MS-JPDE model under the same experimental setting. However, $(\sigma_h^G)^2$ could be included in the MS-JPDE model and this estimated with the other model parameters.

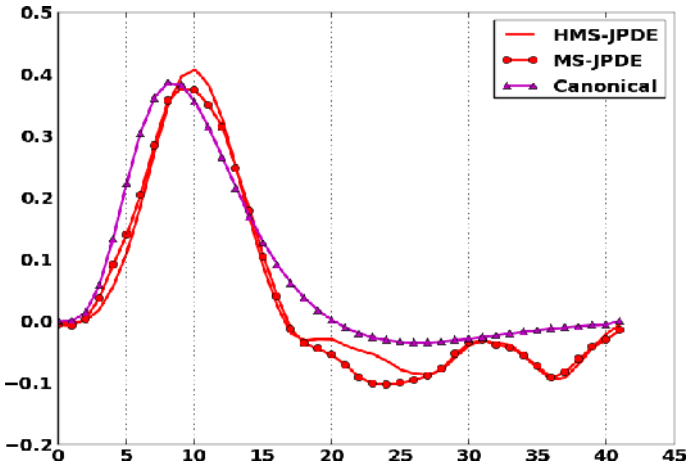

Figure 7.21: Group-level HRF estimates of parcel 1 using the HMS-JPDE and MS-JPDE models in the right motor cortex along with the canonical HRF.

Table 7.23: Euclidean distances between the estimated HRFs obtained using the HMS-JPDE model and the canonical HRF.

	Euclidean distance
HRF. 1	0.32
HRF. 2	0.38
HRF. 3	0.27
HRF. 4	0.29

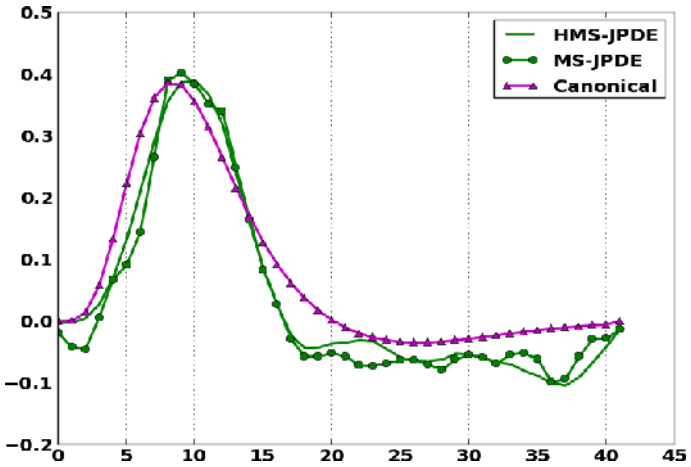

Figure 7.22: Group-level HRF estimates of parcel 2 using the HMS-JPDE and MS-JPDE models in the right motor cortex along with the canonical HRF.

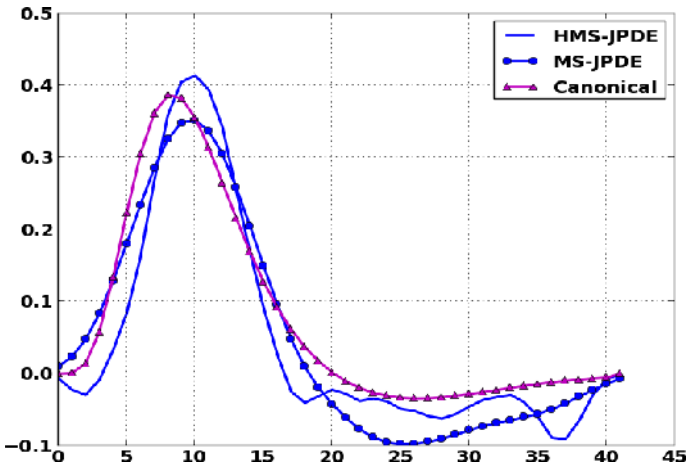

Figure 7.23: Group-level HRF estimates of parcel 3 using the HMS-JPDE and MS-JPDE models in the right motor cortex along with the canonical HRF.

Table 7.24: The estimated TTP and FWHM for the HRF estimates obtained using the HMS-JPDE model.

	TTP	FWHM
HRF. 1	6.0	4.2
HRF. 2	6.0	4.8
HRF. 3	6.0	4.2
HRF. 4	6.0	4.2

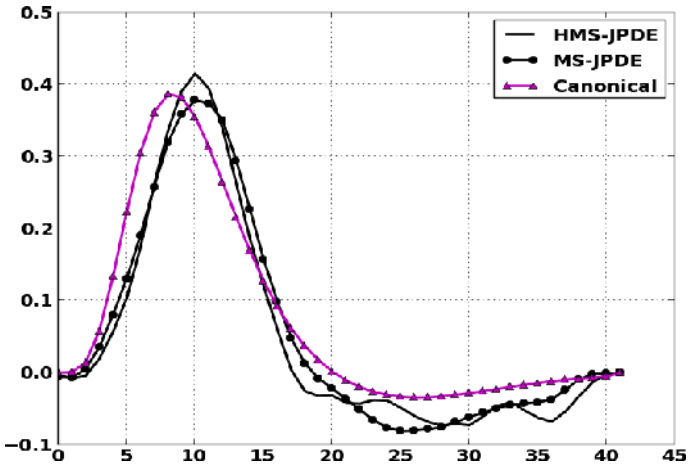

Figure 7.24: Group-level HRF estimates for parcel 4 using the HMS-JPDE and MS-JPDE models in the right motor cortex along with the canonical HRF.

7.4.3 Discussion

This section described the validation of the HMS-JPDE model via synthetic and real data experiments. Via synthetic data experiments, the HMS-JPDE model showed a robust performance in estimating the subject and group level parcellations with different SNRs. Moreover, the HMS-JPDE model provided similar results to the JPDE model and outperformed the MS-JPDE model in providing accurate NRL estimates. Via real data experiment, the performance of the HMS-JPDE model was compared with the JPDE model at the subject-level and the MS-JPDE model at the group level. At the subject-level, the HMS-JPDE model managed to provide HRF estimates that were closer to the canonical HRF shape than those provided by the JPDE model in the right motor cortex as it has been proven that the HRF in the motor cortex departs from the canonical shape (see (Badillo et al., 2013b)). This conclusion was based on the computed TTP, FWHM of the HRF estimates and their Euclidean distances with the canonical HRF. At the group-level, the parcellation estimates using the HMS-JPDE and MS-JPDE models were similar which was confirmed by computing the confusion matrix between them. The HRF estimates using both models were close to the canonical shape. However, the ones provided by the HMS-JPDE model were smoother than those obtained using the MS-JPDE model and their smoothness was not sensitive to the hyperparameter $(\sigma_h^G)^2$ as in the MS-JPDE model. Note that

a comparison for the proposed multi-subject models with the multi-subject model in (Badillo et al., 2014) is essential. However, this comparison is not included in the framework of this thesis due to the limited time and will be conducted for further validation of these models. To finish, the properties of the HMS-JPDE, MS-JPDE and JPDE models are briefly summarized in Tab. 7.25.

Table 7.25: A breif comparison between the JPDE, MS-JPDE and HMS-JPDE models .

Aspect	JPDE	MS-JPDE	HMS-JPDE
Subject-level analysis	HRF estimates Parcellation estimates Activation labels NRL estimates	N/A N/A Activation labels NRL estimates	HRF estimates Parcellation estimates Activation labels NRL estimates
Group-level analysis	N/A	HRF estimates Parcellation	HRF estimates Parcellation
HRF smoothness	Not affected by $(\sigma_h^s)^2$ $\sigma_h^{s^2}$ fixed or estimated	Affected by $(\sigma_h^G)^2$ $(\sigma_h^G)^2$ fixed	Not affected by $(\sigma_h^G)^2$ $(\sigma_h^G)^2$ fixed
NRL estimates accuracy	Not affected Coherent with the HMS-JPDE	Slightly affected	Not affected Coherent with the JPDE

7.5 Conclusion

A novel approach for group-level fMRI analysis (HMS-JPDE) was proposed in this chapter. This model performs a joint inter and intra subject parcellation and estimation along with the detection task that iterated over individuals contrary to the MS-JPDE in Chapter 6 which only allows for the group-level estimates. The hierarchy of the HMS-JPDE model and its variational inference were described in details and the model was then validated using synthetic and real data experiments. A thorough comparison for the HMS-JPDE model with the JPDE and MS-JPDE models showed competitive results for the proposed HMS-JPDE strategy at the subject and group levels. Moreover, the HMS-JPDE model is one of the first models that study the variability of the HRFs across different brain regions at the subject and group levels simultaneously.

CHAPTER 8

Conclusion and Future Work

fMRI is a powerful non-invasive imaging technique that indirectly measures neural activity from the BOLD signal which reflects the variations in the blood oxygenation level induced by oxygen consumption of neural population during task performance. Task-related fMRI focuses on the detection of the evoked activity in brain areas in response to a given stimulus and the estimation of brain dynamics (HRF) associated with such activation. Classical fMRI analyses focus on the detection of the activity in the brain and ignore the variability of the HRF by considering a constant canonical HRF. However, the HRF has been proven to vary between regions and sessions within subject, across subjects and groups. Moreover, a robust HRF estimation increases the reliability of the detection task. The JPDE model is one of the approaches that jointly performs the detection and estimation tasks along with the hemodynamic parcellation of the brain such that each of the estimated hemodynamic parcels has its own HRF shape. Although the JPDE is able to estimate the parcellation of the brain, it still requires a proper initialization and the number of parcels to be fixed which can be complicated when no prior information about the optimum number of parcels is available. The contributions of this PhD can be classified into two main parts; the first one focuses on the subject-level analysis and the second one is concerned with the multi-subject analysis. In the subject-level analysis the PhD contributed in developing new techniques and algorithms to estimate the number of parcels and the parcellation online without previous knowledge about the parcels and their shape. As a start, we introduced the JPDE model and its proposed variational model selection procedure in chapter 3 which relied on the free energy calculation. However, this model selection procedure is computationally intensive since it requires to be run for all the candidate models. As a result, a new approach for hemodynamic brain parcellation was proposed in Chapter 4. This approach relies on a Bayesian non-parametric approach in which a combination of a hidden Markov random field and a

Dirichlet process mixture model was used in order to automatically estimate the parcellation. The hidden Markov random field promoted spatial connexity on the neighbouring voxels while the Dirichlet processes allowed an unbounded number of parcels to be considered. This model was mathematically proven and the its inference strategy was illustrated in details. Due to the deep hierarchy and computational complexity of the previous model, Chapter 5 explored an interesting approach that incorporates the adaptive mean shift algorithm in the VEM framework of the JPDE model. The adaptive mean shift was first introduced. Then, it was applied to the estimation of the hemodynamic parcellation. More precisely, the adaptive mean shift algorithm replaced the maximization of the HRF patterns and an approximation E-$\boldsymbol{z}$ step was used since there was no prior over the variable of the parcellation labels $\boldsymbol{z}$.

All of these approaches managed to automatically estimate the number of parcels in addition to the parcels themselves and their corresponding HRF profiles. Nonetheless, the experiments conducted during this thesis showed that the best choice to estimate these parcels is the NP-JPDE model. For instance, when the NP-JPDE model is compared to the JPDE with the model selection procedure, the NP-JPDE model was less computationally intensive since it estimates the parcellation using a single run. Moreover, the parcels estimated using the NP-JPDE model were spatially consistent contrary to those obtained with the AMS-JPDE model where the parcels could be disconnected due to the existence of outlier voxels. Finally, the NP-JPDE model also managed to discriminate parcels with different HRF characteristics (e.g., different FWHMs) in contrast to the AMS-JPDE model which failed to discriminate the different parcels in the right motor cortex.

At the group-level, two models were proposed in this PhD. The first one was the multi-subject joint parcellation detection estimation (MS-JPDE) proposed in Chapter 6 that can jointly estimates the group-level parcellation and HRF profiles. However, the experimental validation on synthetic and real data proved that the NRL estimates obtained using this model were slightly affected and that the HRF estimates were sensitive to the value of one of the hyperparameters, which in turn affected the characteristics of the HRF profiles. As a result, Chapter 7 introduced an hyprid multi-subject joint parcellation detection estimation (HMS-JPDE) model, which enabled the estimation of the group and subject level parcellations and HRF profiles. This model was compared to the standard JPDE model at the subject-level where it managed to give closer HRF estimates to the canonical shape. At the

group-level, the HMS-JPDE model was compared to the MS-JPDE model. This comparison showed that the estimated NRLs obtained with the HMS-JPDE model at the subject-level were improved when compared to those obtained with the MS-JPDE model and were closer to the NRL estimates obtained using the JPDE model. Furthermore, the group-level HRF profiles estimated by the HMS-JPDE model were smoother than those obtained using the MS-JPDE model, which proved that the HMS-JPDE model managed to eliminate the sensitivity of the HRFs arising from the hyperparameters.
Both models allow obtaining the group-level estimates and give coherent results under specific considerations of some parameters. However, the HMS-JPDE model has the interesting advantage of capturing the HRF variability across brain regions at both the subject and group levels, which is not achievable in the MS-JPDE model. This inter and intra subject framework also increases the computational complexity of the HMS-JPDE model if compared to the MS-JPDE model. One additional advantage of the HMS-JPDE model is that a user does not have to precisely adjust the hyperparameter $\sigma_h^{G^2}$. This is in contrast with the MS-JPDE model, where a user may need to run the same experiment more than once with different values of $\sigma_h^{G^2}$ to obtain the best results. After all, one can choose any of these two models depending on whether the interest is to study the HRF variability at both the subject and group level or only at the group-level.
The main contributions of this thesis can be specified in:

(i) The variational model selection procedure for the JPDE model that computes the free energy associated with different candidate models characterized by different numbers of parcels and selects the one maximizing the free energy as the best fit for the data.

(ii) The NP-JPDE model which uses the properties of the Dirichlet process mixture model and the hidden Markov random field to estimate the parcellation online from the fMRI data without any previous initialization for the parcellation. Our experiments showed the ability of the NP-JPDE model to distinguish HRFs with different FWHM and TTP. Our proposed algorithm is one of the first approaches that relies on non-parametric techniques for estimating the hemodynamic parcellations.

(iii) The AMS-JPDE model makes use of the well known adaptive mean shift algorithm and includes it in the VEM framework to estimate the

parcellation. The parcellation is formulated as a clustering issue with this algorithm where one only needs to set the number of k-nearest neighbours required for the mean-shift algorithm.

(iv) The group-level approaches for fMRI analysis. The first one is the multi-subject joint parcellation detection estimation model that allows the estimation of group-level parcellation and HRF profiles. This model is able to analyze data from multiple subjects and for all parcels involved in a region of interest. Additional hierarchical levels are introduced in the Bayesian framework of the JPDE model to jointly and non-parametrically asses common global hemodynamic responses for all estimated parcels in the global parcellation for all individuals. The second is the inter and intra subject joint parcellation detection estimation model that performs a joint subject and group level analysis. This model allows estimating group and subject level parcellations and HRF profiles along with the detection task for each subject separately. To the best of our knowledge, very few approaches have been proposed to tackle the parcellation and the HRF estimation at the group-level making these two models very interesting and innovative for fMRI analysis.

The accomplished contributions in this PhD are associated with some perspectives to be considered in future work:

(i) **The estimation of the interaction parameter of the Potts model in the NP-JPDE**
Future work will focus on finding a more efficient approach to estimate the parameter β_z of the Potts model in the NP-JPDE model to avoid the computational complexity of the theoretical estimation provided in Chapter 4.

(ii) **The extension of the NP-JPDE model to group-level analysis**
Following the line of the JPDE model and its extensions to multi-subject analysis, it would be interesting to extend the NP-JPDE model for the same purpose. By doing so, we might consider a non-parametric framework that allows estimating the parcellation of a group of subjects without any prior knowledge about the optimum number of parcels. Note that additional layers of hierarchy have to be added to the Bayesian model of the NP-JPDE in order to account for data coming from multiple subjects.

(iii) **Increasing the robustness of the AMS-JPDE model**
As noticed in the synthetic data experiments of Chapter 5, the existence of outlier voxels in the parcellation estimates using the AMS-JPDE model causes disconnection in the estimated parcels. Two different approaches can be used to eliminate these outliers. The first approach consists of adding spatial priors to guarantee the connexity of the neighbouring voxels. Another possible way is to use postprocessing techniques to eliminate the outlier voxels.

(iv) **Conducting a study for the hemodynamic variability**
As a first step, further validation of the proposed multi-subject models can be performed by using different ROIs. Moreover, a comparison with the multi-subject approach in (Badillo et al., 2014) seems essential. Knowing that the multi-subject model in (Badillo et al., 2014) assumes a priori fixed parcellation, this allows analyzing the effect of estimating a group-level parcellation on the group-level HRF estimates. This comparison was not carried out in the framework of this thesis due to the limited time. As a second step, it is important to verify the reproducibility of the parcellation and HRF estimates of Chapters 6 and 7. The latter objective can be accomplished by conducting a study on another group of subjects with similar characteristics to the one used in this thesis.

(v) **The establishment of a hemodynamic atlas**
This can be accomplished by analyzing data from a large cohorts of subjects using one of the proposed multi-subject models. This hemodynamic atlas can be an alternative to the functional anatomical one. Brain structure mapping is widely used in neuro-anatomy to identify common brain structures among individuals. One can mention the approach investigated in (Perrot et al., 2009) in which the mapping methods consider the normalization and the identification of the structures. This type of atlas is widely used in cerebral morphometry. A Bayesian framework has also been proposed in (Perrot et al., 2011) to automatically identify 60 sulcal labels per hemisphere based on a probabilistic atlas. This is similar to the combination between anatomical parcellation and the functional information to refine this parcellation (Mazziotta et al., 1995; Thompson and Toga, 1997; Shattuck et al., 2008). Analyzing data belong to a specific group of interest with one of

our proposed approaches for group-level analysis will allow the use of the voxel-dependent HRF estimates to identify common brain regions with similar hemodynamic properties.

Bibliography

Aguirre, G., Zarahn, E., D'esposito, M., 1998. The variability of human, BOLD hemodynamic responses. Neuroimage 8 (4), 360–369.

Albughdadi, M., Chaari, L., Forbes, F., Tourneret, J.-Y., Ciuciu, P., Sept 2014. Model selection for hemodynamic brain parcellation in fMRI. In: Proc. EUSIPCO. Lisbon, Portugal, pp. 31–35.

Albughdadi, M., Chaari, L., Forbes, F., Tourneret, J.-Y., Ciuciu, P., April 2016a. Multi-subject joint parcellation detection estimation in functional MRI. In: Proc. 13th IEEE International Symposium on Biomedical Imaging (ISBI'13). Prague, Czech Republic.
URL https://hal.inria.fr/hal-01261982

Albughdadi, M., Chaari, L., Tourneret, J.-Y., Aug. 2016b. Adaptive mean shift based hemodynamic brain parcellation in fMRI, accepted in the 7th International Conference on Medical Imaging and Augmented Reality.

Albughdadi, M., Chaari, L., Tourneret, J.-Y., Forbes, F., Ciuciu, P., Feb 2016c. Hemodynamic Brain Parcellation Using A Non-Parametric Bayesian Approach, submitted to Medical Image Analysis.
URL https://hal.inria.fr/hal-01275622

Amaro, E., Barker, G., 2006. Study design in fMRI: basic principles. Brain and cognition 60 (3), 220–232.

Andersson, J., Hutton, C., Ashburner, J., Turner, R., Friston, K., 2001. Modeling geometric deformations in EPI time series. Neuroimage 13 (5), 903–919.

Attias, H., 2000. A variational Bayesian framework for graphical models. In: Proc. Advances in Neural Information Processing Systems 12. MIT Press, Denver, Colorado, United States, pp. 209–215.

Badillo, S., Desmidt, S., Ginisty, C., Ciuciu, P., June 2014. Multi-subject Bayesian joint detection and estimation in fMRI. In: Proc. Workshop Pattern Recognition in Neuroimaging. Tübingen, Germany, pp. 1–4.

Badillo, S., Varoquaux, G., Ciuciu, P., June 2013a. Hemodynamic estimation based on consensus clustering. In: Proc. PRNI. Philadelphia, USA, pp. 211–215.

Badillo, S., Vincent, T., Ciuciu, P., 15 Nov. 2013b. Group-level impacts of within- and between-subject hemodynamic variability in fMRI. Neuroimage 82, 433–448.

Bakhous, C., 2013. Modèles d'encodage parcimonieux de l'activité cérébrale mesurée par IRM fonctionnelle. Ph.D. thesis, University of Grenoble.

Berger, A., 2002. How does it work?: Magnetic resonance imaging. BMJ: British Medical Journal 324 (7328), 35.

Besag, J., 1974. Spatial interaction and the statistical analysis of lattice systems. Journal of the Royal Statistical Society. Series B (Methodological), 192–236.

Blei, D. M., Jordan, M. I., et al., 2006. Variational inference for Dirichlet process mixtures. Bayesian Analysis 1 (1), 121–143.

Bowman, F., 2007. Spatiotemporal models for region of interest analyses of functional neuroimaging data. Journal of the American Statistical Association 102 (478), 442–453.

Bowman, F., Guo, Y., Derado, G., 2007. Statistical approaches to functional neuroimaging data. Neuroimaging Clinics of North America 17 (4), 441–458.

Boynton, G. M., Engel, S. A., Glover, G. H., Heeger, D. J., 1996. Linear systems analysis of functional magnetic resonance imaging in human v1. The Journal of Neuroscience 16 (13), 4207–4221.

Brett, M., Penny, W., Kiebel, S., 2004. An introduction to random field theory. Human brain function 2.

Brown, W., Cheng, Y.-C., Haacke, E., Thompson, M., Venkatesan, R., 2014. Magnetic resonance imaging: physical principles and sequence design. John Wiley & Sons.

Buxton, R. B., Frank, L., 1997. A model for the coupling between cerebral blood flow and oxygen metabolism during neural stimulation. Journal of Cerebral Blood Flow & Metabolism 17 (1), 64–72.

Calhoun, V., Golay, X., Pearlson, G., 2000. Improved fMRI slice timing correction: interpolation errors and wrap around effects. In: Proc., ISMRM, 9th annual meeting. Denver, USA, p. 810.

Celeux, G., Forbes, F., Peyrard, N., 2003. EM procedures using mean field-like approximations for Markov model-based image segmentation. Pattern Recognition 36, 131–144.

Chaari, L., Badillo, S., Vincent, T., Dehaene-Lambertz, G., Forbes, F., Ciuciu, P., Nov. 2015. Hemodynamic-Informed Parcellation of fMRI Data in a Joint Detection Estimation Framework, submitted to IEEE Transactions on Medical Imaging.

Chaari, L., Ciuciu, P., Mériaux, S., Pesquet, J.-C., 2014. Spatio-temporal wavelet regularization for parallel mri reconstruction: application to functional mri. Magnetic Resonance Materials in Physics, Biology and Medicine (MAGMA)DOI: 10.1007/s10334-014-0436-5.

Chaari, L., Forbes, F., Vincent, T., Ciuciu, P., 2012. Hemodynamic-informed parcellation of fMRI data in a variational joint detection estimation framework. In: et al., N. A. (Ed.), Medical Image Computing and Computer-Assisted Intervention. Vol. 7512. Springer, pp. 180–188.

Chaari, L., Forbes, F., Vincent, T., Dojat, M., Ciuciu, P., 2011. Variational solution to the joint detection estimation of brain activity in fMRI. In: Fichtinger, G., Martel, A., Peters, T. (Eds.), Medical Image Computing and Computer-Assisted Intervention. Vol. 6892. Springer, pp. 260–268.

Chaari, L., Vincent, T., Forbes, F., Dojat, M., Ciuciu, P., 2013. Fast joint detection-estimation of evoked brain activity in event-related fMRI using a variational approach. IEEE Transactions on Medical Imaging 32 (5), 821–837.

Chatzis, S. P., Tsechpenakis, G., 2010. The infinite hidden Markov random field model. IEEE Transactions on Neural Networks 21 (6), 1004–1014.

Chickering, D. M., Heckerman, D., 1997. Efficient approximations for the marginal likelihood of Bayesian networks with hidden variables. Machine Learning 29 (2-3), 181–212.

Ciuciu, P., Idier, J., Roche, A., Pallier, C., Apr. 2004. Outlier detection for robust region-based estimation of the hemodynamic response function in event-related fMRI. In: IEEE International Symposium on Biomedical Imaging. Arlington, VA USA, pp. 392–395.

Ciuciu, P., Poline, J., Marrelec, G., Idier, J., Pallier, C., Benali, H., Oct 2003. Unsupervised robust non-parametric estimation of the hemodynamic response function for any fMRI experiment. IEEE Transactions on Medical Imaging 22 (10), 1235–1251.

Comaniciu, D., Meer, P., 2002. Mean shift: A robust approach toward feature space analysis. IEEE Transactions on Pattern Analysis Machine Intelligence 24 (5), 603–619.

Degras, D., Lindquist, M., 2014. A hierarchical model for simultaneous detection and estimation in multi-subject fMRI studies. NeuroImage 98, 61–72.

Deneux, T., Faugeras, O., 2006. Using nonlinear models in fMRI data analysis: model selection and activation detection. Neuroimage 32 (4), 1669–1689.

Dervin, J., 1 1990. Co-planar stereotaxic atlas of the human brain 3-dimensional proportional system: An approach to cerebral imaging 1988 by j. talairich and p. tournoux m. rayport g. thieme verlag. The Journal of Laryngology and Otology 104, 72–72.
URL http://journals.cambridge.org/article_S0022215100111879

D'Esposito, M., Aguirre, G., Zarahn, E., Ballard, D., Shin, R., Lease, J., 1998. Functional MRI studies of spatial and nonspatial working memory. Cognitive Brain Research 7 (1), 1–13.

D'Esposito, M., Deouell, L. Y., Gazzaley, A., Nov. 2003. Alterations in the BOLD fMRI signal with ageing and disease: a challenge for neuroimaging. Neuroimage 4 (11), 863–872.

Donaldson, D., 2004. Parsing brain activity with fMRI and mixed designs: what kind of a state is neuroimaging in? Trends in Neurosciences 27 (8), 442–444.

Duda, R., Hart, P., et al., 1973. Pattern classification and scene analysis. Vol. 3. Wiley New York.

Eickhoff, S., Bzdok, D., Laird, A., Roski, C., Caspers, S., Zilles, K., Fox, P., 2011. Co-activation patterns distinguish cortical modules, their connectivity and functional differentiation. Neuroimage 57 (3), 938–949.

Escobar, M. D., West, M., 1995. Bayesian density estimation and inference using mixtures. Journal of the American Statistical Association 90 (430), 577–588.

Ferguson, T. S., 1973. A Bayesian analysis of some nonparametric problems. The Annals of Statistics, 209–230.

Flandin, G., Kherif, F., Pennec, X., Rivière, D., Ayache, N., Poline, J.-B., 2002. A new representation of fMRI data using anatomo-functional constraints. In: Proc. Neuroimage (HBM'02). Sendai, Japan.

Fouque, A.-L., Ciuciu, P., Risser, L., April 2009. Multivariate spatial Gaussian mixture modeling for statistical clustering of hemodynamic parameters in functional MRI. In: Proc. ICASSP. Taipei, Taiwan, pp. 445–448.

Fox, P., Mintun, M., Raichle, M., Miezin, F., Allman, J., Van Essen, D., 1986. Mapping human visual cortex with positron emission tomography. Nature 323, 806–809.

Frahm, J., Bruhn, H., Merboldt, K.-D., Hänicke, W., 1992. Dynamic MR imaging of human brain oxygenation during rest and photic stimulation. Journal of Magnetic Resonance Imaging 2 (5), 501–505.

Frau-Pascual, A., Vincent, T., Forbes, F., Ciuciu, P., May 2014. Hemodynamically informed parcellation of cerebral fMRI data. In: Proc. ICASSP. Florence, Italy, pp. 2079–2083.

Friston, K. J., Holmes, A. P., Poline, J.-B., Grasby, P. J., Williams, S. C. R., Frackowiak, R. S. J., Turner, R., 1995. Analysis of fMRI time-series revisited. Neuroimage 2 (1), 45–53.

Friston, K. J., Mechelli, A., Turner, R., Price, C. J., 2000. Nonlinear responses in fMRI: the Balloon model, Volterra kernels, and other hemodynamics. Neuroimage 12 (4), 466–477.

Georgescu, B., Shimshoni, I., Meer, P., 2003. Mean shift based clustering in high dimensions: A texture classification example. In: Proc. ICCV. IEEE, Nice, France, pp. 456–463.

Glover, G. H., 1999. Deconvolution of impulse response in event-related BOLD fMRI. Neuroimage 9 (4), 416–429.

Golland, P., Golland, Y., Malach, R., 2007. Detection of spatial activation patterns as unsupervised segmentation of fMRI data. In: Medical Image Computing and Computer-Assisted Intervention. Springer, pp. 110–118.

Grubb, R., Raichle, M., Eichling, J., Ter-Pogossian, M., 1974. The effects of changes in paco2 cerebral blood volume, blood flow, and vascular mean transit time. Stroke 5 (5), 630–639.

Handwerker, D., Gonzalez-Castillo, J., D'Esposito, M., Bandettini, P., 2012. The continuing challenge of understanding and modeling hemodynamic variation in fMRI. Neuroimage 62 (2), 1017–1023.

Handwerker, D. A., Ollinger, J., D'Esposito, M., Apr. 2004. Variation of BOLD hemodynamic responses across subjects and brain regions and their effects on statistical analyses 21, 1639–1651.

Henson, R. N. A., Rugg, M. D., Friston, K. J., 2001. The choice of basis functions in event-related fMRI. Neuroimage 13 (6), 149.

Huettel, S., Song, A., McCarthy, G., 2004. Functional magnetic resonance imaging. Vol. 1. Sinauer Associates Sunderland.

Hyder, F., Rothman, D., Shulman, R., 2002. Total neuroenergetics support localized brain activity: implications for the interpretation of fMRI. Proceedings of the National Academy of Sciences 99 (16), 10771–10776.

Kao, M.-H., et al., 2009. Multi-objective optimal experimental designs for ER-fMRI using MATLAB. Journal of Statistical Software 30 (11), 1–13.

Kershaw, J., Ardekani, B. A., Kanno, I., 1999. Application of Bayesian inference to fMRI data analysis. IEEE Transactions on Medical Imaging 18 (12), 1138–1153.

Kim, S., Smyth, P., Stern, H., 2006. A nonparametric bayesian approach to detecting spatial activation patterns in fmri data. In: International Conference on Medical Image Computing and Computer-Assisted Intervention. Springer, pp. 217–224.

Kriegeskorte, N., Goebel, R., Bandettini, P., 2006. Information-based functional brain mapping. Proceedings of the National Academy of Sciences of the United States of America 103 (10), 3863–3868.

Kriegeskorte, N., Mur, M., Bandettini, P., 2008. Representational similarity analysis-connecting the branches of systems neuroscience. Frontiers in systems neuroscience 2, 4.

Kwong, K., Belliveau, J., Chesler, D., Goldberg, I., Weisskoff, R., Poncelet, B., Kennedy, D., Hoppel, B., Cohen, M., Turner, R., 1992. Dynamic magnetic resonance imaging of human brain activity during primary sensory stimulation. Proceedings of the National Academy of Sciences 89 (12), 5675–5679.

Larkman, D., Hajnal, J., Herlihy, A., Coutts, G., Young, I., Ehnholm, G., 2001. Use of multicoil arrays for separation of signal from multiple slices simultaneously excited. Journal of Magnetic Resonance Imaging 13 (2), 313–317.

Lashkari, D., Sridharan, R., Vul, E., Hsieh, P.-J., Kanwisher, N., Golland, P., 2012. Search for patterns of functional specificity in the brain: a nonparametric hierarchical Bayesian model for group fMRI data. Neuroimage 59 (2), 1348–1368.

Lashkari, D., Vul, E., Kanwisher, N., Golland, P., 2010. Discovering structure in the space of fMRI selectivity profiles. Neuroimage 50 (3), 1085–1098.

Lindquist, M., Wager, T., 2014. Principles of functional magnetic resonance imaging. In: Handbook of Neuroimaing Data Analysis. CRC Press.

Lindquist, M., Zhang, C.-H., Glover, G., Shepp, L., 2008a. Rapid three-dimensional functional magnetic resonance imaging of the initial negative BOLD response. Journal of Magnetic Resonance 191 (1), 100–111.

Lindquist, M., et al., 2008b. The statistical analysis of fMRI data. Statistical Science 23 (4), 439–464.

Lindquist, M. A., Loh, J. M., Atlas, L. Y., Wager, T. D., 2009. Modeling the hemodynamic response function in fMRI: efficiency, bias and mis-modeling. Neuroimage 45 (1), S187–S198.

Lund, T., Madsen, K., Sidaros, K., Luo, W.-L., Nichols, T., 2006. Non-white noise in fMRI: Does modelling have an impact? Neuroimage 29 (1), 54–66.

Lustig, M., Donoho, D., Pauly, J., 2007. Sparse MRI: The application of compressed sensing for rapid MR imaging. Magnetic Resonance in Medicine 58 (6), 1182–1195.

Makni, S., Idier, J., Vincent, T., Thirion, B., Dehaene-Lambertz, G., Ciuciu, P., 2008. A fully Bayesian approach to the parcel-based detection-estimation of brain activity in fMRI. Neuroimage 41 (3), 941–969.

Malonek, D., Grinvald, A., 1996. Interactions between electrical activity and cortical microcirculation revealed by imaging spectroscopy: implications for functional brain mapping. Science 272 (5261), 551.

Mazziotta, J., Toga, A., Evans, A., Fox, P., Lancaster, J., 1995. A probabilistic atlas of the human brain: theory and rationale for its development: The international consortium for brain mapping (ICBM). Neuroimage 2 (2), 89–101.

Mechelli, A., Penny, W., Price, C., Gitelman, D., Friston, K., 2002. Effective connectivity and intersubject variability: using a multisubject network to test differences and commonalities. Neuroimage 17 (3), 1459–1469.

Miezin, F., Maccotta, L., Ollinger, J., Petersen, S., Buckner, R., 2000. Characterizing the hemodynamic response: effects of presentation rate, sampling procedure, and the possibility of ordering brain activity based on relative timing. Neuroimage 11 (6), 735–759.

Moeller, S., Yacoub, E., Olman, C., Auerbach, E., Strupp, J., Harel, N., Uğurbil, K., 2010. Multiband multislice GE-EPI at 7 Tesla, with 16-fold acceleration using partial parallel imaging with application to high spatial and temporal whole-brain fMRI. Magnetic Resonance in Medicine 63 (5), 1144–1153.

Ng, A., Jordan, M., Weiss, Y., et al., 2002. On spectral clustering: Analysis and an algorithm. Advances in neural information processing systems 2, 849–856.

Ogawa, S., Lee, T.-M., Kay, A. R., Tank, D. W., 1990a. Brain magnetic resonance imaging with contrast dependent on blood oxygenation. Proc. Natl. Acad. Sci. 87 (24), 9868–72.

Ogawa, S., Lee, T.-M., Nayak, A., Glynn, P., 1990b. Oxygenation-sensitive contrast in magnetic resonance image of rodent brain at high magnetic fields. Magnetic Resonance in Medicine 14 (1), 68–78.

Ogawa, S., Tank, D., Menon, R., Ellermann, J., Kim, S., Merkle, H., Ugurbil, K., 1992. Intrinsic signal changes accompanying sensory stimulation: functional brain mapping with magnetic resonance imaging. Proceedings of the National Academy of Sciences 89 (13), 5951–5955.

Otten, L., Henson, R., Rugg, M., 2002. State-related and item-related neural correlates of successful memory encoding. Nature neuroscience 5 (12), 1339–1344.

Pauling, L., Coryell, C. D., 1936. The magnetic properties and structure of hemoglobin, oxyhemoglobin and carbonmonoxyhemoglobin. Proceedings of the National Academy of Sciences 22 (4), 210–216.
URL http://www.pnas.org/content/22/4/210.short

Perrot, M., Rivière, D., Mangin, J.-F., 2011. Cortical sulci recognition and spatial normalization. Medical Image Analysis 15 (4), 529–550.

Perrot, M., Rivière, D., Tucholka, A., Mangin, J.-F., 2009. Joint Bayesian cortical sulci recognition and spatial normalization. In: Information Processing in Medical Imaging. Springer, pp. 176–187.

Petcharunpaisan, S., Ramalho, J., Castillo, M., 2010. Arterial spin labeling in neuroimaging. World Journal of Radiology 2 (10), 384–398.

Petersen, S., Dubis, J., 2012. The mixed block/event-related design. Neuroimage 62 (2), 1177–1184.

Pinel, P., Thirion, B., Mériaux, S., Jobert, A., Serres, J., Le Bihan, D., Poline, J.-B., Dehaene, S., 2007. Fast reproducible identification and large-scale databasing of individual functional cognitive networks. BMC Neuroscience 8 (1), 91.

Poline, J.-B., Kherif, F., 2007. Contrasts and classical inference. Statistical Parametric Mapping: The Analysis of Functional Brain Images 1, 126.

Pruessmann, K., Weiger, M., Scheidegger, M., Boesiger, P., et al., 1999. Sense: sensitivity encoding for fast MRI. Magnetic Resonance in Medicine 42 (5), 952–962.

Riera, J. J., Watanabe, J., Kazuki, I., Naoki, M., Aubert, E., Ozaki, T., Kawashima, R., 2004. A state-space model of the hemodynamic approach: nonlinear filtering of BOLD signals. Neuroimage 21 (2), 547–567.

Shattuck, D., Mirza, M., Adisetiyo, V., Hojatkashani, C., Salamon, G., Narr, K., Poldrack, R., Bilder, R., Toga, A., 2008. Construction of a 3D probabilistic atlas of human cortical structures. Neuroimage 39 (3), 1064–1080.

Shi, J., Malik, J., 2000. Normalized cuts and image segmentation. IEEE Transactions on Pattern Analysis and Machine Intelligence 22 (8), 888–905.

Sodickson, D., Manning, W., 1997. Simultaneous acquisition of spatial harmonics (SMASH): fast imaging with radiofrequency coil arrays. Magnetic Resonance in Medicine 38 (4), 591–603.

Sprawls, P., 2000. Magnetic Resonance Imaging: Principles, Methods, and Techniques. Medical Physics Publising, Wisconsin, USA.

Tahmasebi, A., Abolmaesumi, P., Zheng, Z., Munhall, K., Johnsrude, I., 2009. Reducing inter-subject anatomical variation: effect of normalization method on sensitivity of functional magnetic resonance imaging data analysis in auditory cortex and the superior temporal region. NeuroImage 47 (4), 1522–1531.

Thirion, B., Flandin, G., Pinel, P., Roche, A., Ciuciu, P., Poline, J.-B., 2006. Dealing with the shortcomings of spatial normalization: Multi-subject parcellation of fMRI datasets. Human Brain Mapping 27 (8), 678–693.

Thirion, B., Varoquaux, G., Dohmatob, E., Poline, J.-B., 2014. Which fMRI clustering gives good brain parcellations? Frontiers in neuroscience 8.

Thompson, P., Toga, A., 1997. Detection, visualization and animation of abnormal anatomic structure with a deformable probabilistic brain atlas based on random vector field transformations. Medical Image Analysis 1 (4), 271–294.

Thulborn, K., Waterton, J., Matthews, P., Radda, G., 1982. Oxygenation dependence of the transverse relaxation-time of water protons in whole-blood at high-field. Biochimia et Biophysica Acta 714, 265–270.
URL http://dx.doi.org/10.1016/0304-4165(82)90333-6

Turner, R., Bihan, D., Moonen, C., Despres, D., Frank, J., 1991. Echo-planar time course MRI of cat brain oxygenation changes. Magnetic Resonance in Medicine 22 (1), 159–166.

Turner, R., Jezzard, P., Wen, H., Kwong, K., Le Bihan, D., Zeffiro, T., Balaban, R., 1993. Functional mapping of the human visual cortex at 4 and 1.5 Tesla using deoxygenation contrast EPI. Magnetic Resonance in Medicine 29 (2), 277–279.

Uludag, K., Dubowitz, D., Buxton, R., 2006. Basic principles of functional MRI. In: Edelman, R., Hesselink, J., Zlatkin, M. (Eds.), Clinical Magnetic Resonance Imaging, 3rd Edition. Pa: Saunders Elsevier.

Vincent, T., Badillo, S., Risser, L., Chaari, L., Bakhous, C., Forbes, F., Ciuciu, P., 2014. Flexible multivariate hemodynamics fMRI data analyses and simulations with PyHRF. Frontiers in Neuroscience 8 (67).

Vincent, T., Risser, L., Ciuciu, P., 2010. Spatially adaptive mixture modeling for analysis of fMRI time series. IEEE Transactions on Medical Imaging 29 (4), 1059–1074.

Waldorp, L., 2009. Robust and unbiased variance of GLM coefficients for misspecified autocorrelation and hemodynamic response models in fMRI. Journal of Biomedical Imaging 2009, 15.

Ward, J., Joe, H., 1963. Hierarchical grouping to optimize an objective function. Journal of the American statistical association 58 (301), 236–244.

Witjes, H., Rijpkema, M., Van Der Graaf, M., Melssen, W., Heerschap, A., Buydens, L., 2003. Multispectral magnetic resonance image analysis using principal component and linear discriminant analysis. Journal of Magnetic Resonance Imaging 17 (2), 261–269.

Woods, R., Grafton, S., Watson, J., Sicotte, N., Mazziotta, J., 1998. Automated image registration: II. Intersubject validation of linear and nonlinear models. Journal of Computer Assisted Tomography 22 (1), 153–165.

Woolrich, M. W., Ripley, B. D., Brady, M., Smith, S. M., 2001. Temporal autocorrelation in univariate linear modeling of fMRI data. Neuroimage 14 (6), 1370–1386.

Yaron, U., Bernard, S., 2004. Mean shift theory and applications. http://www.wisdom.weizmann.ac.il/~vision/courses/2004_2/files/mean_shift/mean_shift.ppt.

Zhang, T., Li, F., Beckes, L., Coan, J., 2013. A semi-parametric model of the hemodynamic response for multi-subject fMRI data. NeuroImage 75, 136–145.